CANADIAN THESES ON MICROFICHE

I.S.B.N.

THESES CANADIENNES SUR MICROFICHE

National Library of Canada
Collections Development Branch

Canadian Theses on
Microfiche Service

Ottawa, Canada
K1A 0N4

Bibliothèque nationale du Canada
Direction du développement des collections

Service des thèses canadiennes
sur microfiche

NOTICE

The quality of this microfiche is heavily dependent upon the quality of the original thesis submitted for microfilming. Every effort has been made to ensure the highest quality of reproduction possible.

If pages are missing, contact the university which granted the degree.

Some pages may have indistinct print especially if the original pages were typed with a poor typewriter ribbon or if the university sent us a poor photocopy.

Previously copyrighted materials (journal articles, published tests, etc.) are not filmed.

Reproduction in full or in part of this film is governed by the Canadian Copyright Act, R.S.C. 1970, c. C-30. Please read the authorization forms which accompany this thesis.

THIS DISSERTATION
HAS BEEN MICROFILMED
EXACTLY AS RECEIVED

AVIS

La qualité de cette microfiche dépend grandement de la qualité de la thèse soumise au microfilmage. Nous avons tout fait pour assurer une qualité supérieure de reproduction.

S'il manque des pages, veuillez communiquer avec l'université qui a conféré le grade.

La qualité d'impression de certaines pages peut laisser à désirer, surtout si les pages originales ont été dactylographiées à l'aide d'un ruban usé ou si l'université nous a fait parvenir une photocopie de mauvaise qualité.

Les documents qui font déjà l'objet d'un droit d'auteur (articles de revue, examens publiés, etc.) ne sont pas microfilmés.

La reproduction, même partielle, de ce microfilm est soumise à la Loi canadienne sur le droit d'auteur, SRC 1970, c. C-30. Veuillez prendre connaissance des formules d'autorisation qui accompagnent cette thèse.

LA THÈSE A ÉTÉ
MICROFILMÉE TELLE QUE
NOUS L'AVONS REÇUE

NL-339 (r. 82/08)

Canadä

0-315-19363-8

(15)

National Library
of Canada

Canadian Theses Division

Ottawa, Canada
K1A 0N4

Bibliothèque nationale
du Canada

Division des thèses canadiennes

67271

PERMISSION TO MICROFILM — AUTORISATION DE MICROFILMER

- Please print or type — Écrire en lettres moulées ou dactylographier

Full Name of Author — Nom complet de l'auteur

Doug S. Phillips

Date of Birth — Date de naissance 20 April 1954	Country of Birth — Lieu de naissance Canada

Permanent Address — Résidence fixe

5420 - 37 St. S.W.
Calgary, Alberta
T3E 5M5

Title of Thesis — Titre de la thèse

Terrain-shape effects on surface pressure and drag for steady, linear, hydrostatic mountain airflow

University — Université

Univ. of Alberta

Degree for which thesis was presented — Grade pour lequel cette thèse fut présentée

Ph.D

Year this degree conferred — Année d'obtention de ce grade 1984	Name of Supervisor — Nom du directeur de thèse E. R. Reinelt

Permission is hereby granted to the NATIONAL LIBRARY OF CANADA to microfilm this thesis and to lend or sell copies of the film.

The author reserves other publication rights, and neither the thesis nor extensive extracts from it may be printed or otherwise reproduced without the author's written permission.

L'autorisation est, par la présente, accordée à la BIBLIOTHÈQUE NATIONALE DU CANADA de microfilmer cette thèse et de prêter ou de vendre des exemplaires du film.

L'auteur se réserve les autres droits de publication; ni la thèse ni de longs extraits de celle-ci ne doivent être imprimés ou autrement reproduits sans l'autorisation écrite de l'auteur.

Date 19 April 1984	Signature Doug S. Phillips

NL-91 (4/77)

THE UNIVERSITY OF ALBERTA

TERRAIN-SHAPE EFFECTS ON SURFACE PRESSURE AND DRAG FOR STEADY, LINEAR, HYDROSTATIC, MOUNTAIN AIRFLOW

by

© DOUGLAS STANLEY PHILLIPS

A THESIS
SUBMITTED TO THE FACULTY OF GRADUATE STUDIES AND RESEARCH
IN PARTIAL FULFILMENT OF THE REQUIREMENTS FOR THE DEGREE
OF DOCTOR OF PHILOSOPHY
IN
METEOROLOGY

DEPARTMENT OF GEOGRAPHY

EDMONTON, ALBERTA
SPRING 1984

THE UNIVERSITY OF ALBERTA

RELEASE FORM

NAME OF AUTHOR DOUGLAS STANLEY PHILLIPS

TITLE OF THESIS TERRAIN-SHAPE EFFECTS ON SURFACE PRESSURE AND DRAG FOR STEADY, LINEAR, HYDROSTATIC, MOUNTAIN AIRFLOW

DEGREE FOR WHICH THESIS WAS PRESENTED DOCTOR OF PHILOSOPHY

YEAR THIS DEGREE GRANTED SPRING 1984

Permission is hereby granted to THE UNIVERSITY OF ALBERTA LIBRARY to reproduce single copies of this thesis and to lend or sell such copies for private, scholarly or scientific research purposes only.

The author reserves other publication rights, and neither the thesis nor extensive extracts from it may be printed or otherwise reproduced without the author's written permission.

Doug S. Phillips

PERMANENT ADDRESS:

5420 37 Street, S.W.,
CALGARY, ALBERTA,
T3E 5M5

DATED 17 April 1984

THE UNIVERSITY OF ALBERTA

FACULTY OF GRADUATE STUDIES AND RESEARCH

The undersigned certify that they have read, and recommend to the Faculty of Graduate Studies and Research, for acceptance, a thesis entitled TERRAIN-SHAPE EFFECTS ON SURFACE PRESSURE AND DRAG FOR STEADY, LINEAR, HYDROSTATIC, MOUNTAIN AIRFLOW submitted by DOUGLAS STANLEY PHILLIPS in partial fulfilment of the requirements for the degree of DOCTOR OF PHILOSOPHY in METEOROLOGY.

E R Reinelt

Supervisor

Gordon Rostoker

Edward Lozowski

Han-Ru Cho

External Examiner

Date 6 April 1984

DEDICATION

TO MY PARENTS
FOR WAITING SO LONG

AND

TO LESLIE
FOR SEEING ME TO THE END

ABSTRACT

After a brief review of theories and observations of lee cyclogenesis, an analysis of the preferred regions for lee cyclone formation in Western Canada is presented. The question is raised as to whether or not details in the pattern of cyclogenesis locations have a physical origin or are statistical fluctuations due to a small sample size.

The bulk of the thesis involves the study of a linear, hydrostatic model of the steady flow of stably stratified air over three-dimensional mountains with elliptical horizontal cross-sections. Analytical expressions for the surface pressure perturbation are used to examine the differences between two- and three-dimensional flows. The maximum pressure perturbation due to a hill with a circular cross-section is about 30% less than that for an infinitely-long ridge perpendicular to the mean flow. For a barrier three to four times as wide across the wind as along the mean flow, the assumption of two-dimensional flow, in vertical planes, leads to an extreme pressure perturbation differing from the three-dimensional solution by only about 10%. For an elliptical barrier with an axis parallel to the mean flow, the maximum difference between the pressure fields for two- and three-dimensional flows occurs along that axis, rather than in the region of the maximum velocity component perpendicular to the mean flow. The horizontal divergence and lateral streamline deflection associated with this velocity component are also considered. For a ridge curved in a horizontal plane, the pressure perturbation was found to be enhanced on the convex side and weakened on the concave side.

Within the context of the same linear, hydrostatic model, the force exerted by the air on the terrain surface is studied. The reaction force, or drag, of a unit length of the barrier on the flow is calculated for a variety of infinitely-extended crosswind ridges and for isolated three-dimensional mountains with elliptical horizontal cross-sections. In addition, the drag per unit length is determined for barrier shapes which have been smoothed by application of a differential operator or by truncation of a spectral series for the terrain height. Also, the total force exerted on an elliptical mountain by the incoming airstream is found as a function of the barrier eccentricity and orientation. If the upstream flow is not parallel to a symmetry axis of the terrain, there is a transverse force on the air which can be an appreciable fraction of the drag force acting in the direction opposite to the mean wind.

Finally, the application of the linear model to flow over a realistic representation of the topography in Western Canada is considered.

ACKNOWLEDGMENTS

It is with pleasure that I thank some of the people who have made this thesis possible. Dr. E. R. Reinelt, who initiated my study of lee cyclogenesis, was always available to discuss this and other aspects of my thesis as it progressed. Dr. R. B. Smith is due thanks for suggesting a comparison between the three-dimensional and two-dimensional slice flow solutions. I appreciate the efforts of the examiners, Drs. E. P. Lozowski, R. B. Charlton, H.-R. Cho, and G. Rostoker, in reading this thesis at a busy time of year.

A special word of thanks is given to Leslie D. Stovel, for the important roles she played in the production of this work. These include the reading of a preliminary version of the thesis, helping with typing and drafting, and continual encouragement.

Generous financial assistance, in the form of a 1967 Science Scholarship from the National Research Council of Canada, an Izaak Walton Killam Memorial Scholarship and a University of Alberta Graduate Fellowship, was greatly appreciated. Computing and photographic support was provided through the Department of Geography at the University of Alberta.

TABLE OF CONTENTS

PAGE

LIST OF TABLES xi

LIST OF FIGURES xii

NOTATION xvi

CHAPTER

1 INTRODUCTION 1

1.1 Motivation 1

1.2 Previous studies of lee troughs and cyclones 3

2 LEE CYCLOGENESIS FREQUENCY PER UNIT AREA 15

2.1 Counts of lee cyclogenesis events 15

2.2 Smoothing contour maps of cyclogenesis frequency per unit area 19

2.3 Lee cyclogenesis frequency maps for special classes of lows 26

3 A STEADY, LINEAR, HYDROSTATIC, AIRFLOW MODEL 32

3.1 Introduction 32

3.2 Model equations and their solution 36

4 ELLIPTICAL TERRAIN SHAPE 46

5 ANALYTICAL SURFACE PRESSURE PERTURBATION 54

5.1 Three-dimensional flow 54

5.2 Two-dimensional slice flow 64

6 PRESSURE PERTURBATION FOR FLOW OVER CURVED RIDGES 73

6.1 Introduction 73

6.2 Parabolically curved ridge 76

6.3 Sinusoidally curved ridge 84

7 TRANSVERSE PERTURBATION VELOCITY, STREAMLINE DEFLECTION, AND HORIZONTAL DIVERGENCE 89

8 INTRODUCTION TO MOUNTAIN WAVE DRAG AND TRANSVERSE FORCE 99

8.1 Introduction 99

8.2 Basic expressions for wave drag and transverse force 101

9 DRAG PER UNIT CROSSWIND LENGTH 104

9.1 Drag per unit crosswind length for infinitely-extended ridges 104

9.2 Drag per unit crosswind length for sinusoidally modulated ridges 115

9.3 Drag per unit crosswind length for double ridges 120

9.4 Drag per unit crosswind length for isolated three-dimensional barriers 125

10 TOTAL FORCE ON THE BARRIER 130

11 EFFECT OF TERRAIN SMOOTHING ON SURFACE DRAG AND TRANSVERSE FORCE 140

11.1 Introduction to terrain smoothing 140

11.2 Differential smoothing 140

11.3 Smoothing by spectral truncation 152

12 APPLICATION OF THE LINEAR MODEL TO REALISTIC TERRAIN 163

12.1 Model limitations 163

12.2 Realistic terrain 167

13 SUMMARY AND POSSIBILITIES FOR FUTURE STUDY 185

13.1 Summary 185

13.2 Possibilities for future study 192

BIBLIOGRAPHY 196

APPENDIX

A JUSTIFICATION OF THE NEGLECT OF CERTAIN EFFECTS OF THE VERTICAL VARIATION OF DENSITY 207

B DIMENSIONLESS VARIABLES AND INTEGRAL FORMULAE 212

C HORIZONTAL SCALE TRANSFORMATION 215

D ANALYTICAL RESULTS FOR SINGLE RIDGES AND ELLIPTICAL HILLS 216

D.1 Terrain-height Fourier transforms 216

D.2 Pressure fields 217

E ANALYTICAL RESULTS FOR A SEPARABLE AGNESI TERRAIN FORM 234

E.1 Three-dimensional pressure field 234

E.2 Total drag 236

F PERTURBATION FIELDS NEAR R=0 238

G PRESSURE PERTURBATION FAR FROM THE BARRIER 242

H LIMIT OF AN INFINITELY-EXTENDED CROSSWIND RIDGE 246

I LIMIT OF AN INFINITELY-EXTENDED RIDGE PARALLEL TO THE WIND 253

J FAST FOURIER TRANSFORM CALCULATION OF THE PRESSURE FIELD 256

K DRAG PER UNIT CROSSWIND LENGTH 261

L ANALYTICAL RESULTS FOR SINUSOIDALLY MODULATED RIDGES 267

M ANALYTICAL RESULTS FOR DOUBLE RIDGES 269

N TOTAL DRAG 272

O FORCE ON THE BARRIER IN TWO-DIMENSIONAL SLICE FLOW 276

P INTEGRALS ARISING FROM TERRAIN SMOOTHING 280

P.1 Differential smoothing 280

P.2 Truncated spectral series 280

Q ELLIPTIC INTEGRALS 285

LIST OF TABLES

TABLE PAGE

1 Maxima of cyclogenesis frequency per unit area as a function of the smoothing parameter, ϵ 25

2 Normalized terrain-height Fourier transform, $\hat{H}(\kappa;Y)$, for elliptical terrain 217

3 Normalized terrain-height Fourier transform, $\hat{H}(\rho)$, for elliptical terrain 218

4 Normalized surface pressure perturbation, P_2, for flow over a μ-type infinite ridge 220

5 Normalized surface pressure perturbation, P_{3c}, for flow over a μ-type circular hill 221

6 Normalized surface pressure perturbation, P_{2s}, for two-dimensional slice flow over a ν-type elliptical barrier 229

7 Normalized surface pressure perturbation, P_{3c}, for flow over a ν-type circular hill 230

8 Normalized drag per unit crosswind length, d_{2s}, for two-dimensional slice flow over an elliptical barrier 262

9 Normalized total drag, $D_{2s}=G$, for two-dimensional slice flow over an elliptical barrier 273

10 Terrain smoothing integrals, s_n 281

11 Terrain smoothing integrals, S_n 281

LIST OF FIGURES

FIGURE		PAGE
1	Contour maps of lee cyclogenesis frequency per unit area for smoothing radius (a) ϵ=200 km and (b) ϵ=300 km	23
2	Contour maps of lee cyclogenesis frequency per unit area for (a) mobile and (b) local cyclones	27
3	Contour maps of lee cyclogenesis frequency per unit area for (a) with-parent and (b) without-parent cyclones	29
4	Terrain height vs. position for μ-type ridges	49
5	Terrain-height Fourier transform vs. radial wave number for μ-type elliptical terrain	53
6	Surface pressure perturbation, P_2, for flow over infinitely-extended μ-type ridges	58
7	Surface pressure perturbation, P_{3c}, along Y=0, for flow over a μ-type circular hill	58
8	Contour maps of terrain height and surface pressure perturbation for several orientations of barriers with μ=2, γ=1/2	62
9	Contour maps for comparison of three-dimensional and two-dimensional slice flow pressure perturbation for a μ=3/2, γ=1/2 elliptical barrier	65
10	As in Fig. 9, except γ=1/4	66
11	Magnitude, P_{3m}, and position, X_m, of the extreme pressure perturbation vs. scaling ratio, γ, for μ-type barriers	68
12	Surface pressure perturbation for three-dimensional flow and the difference in pressure for two- and three-dimensional flow, vs. X, along Y=0, for several values of γ and μ	71
13	Surface pressure perturbation vs. X, along Y=0, for flow over a parabolically curved Agnesi ridge	79

FIGURE PAGE

14 Comparison of Fast Fourier Transform and Simpson's rule calculation of the pressure perturbation for flow over a parabolically curved Agnesi ridge 82

15 Contour plot of the pressure perturbation field for parabolically curved Agnesi ridges 83

16 Contour plot of the pressure perturbation field for a sinusoidally curved Agnesi ridge 87

17 Normalized horizontal divergence and other derivatives of the horizontal velocity components at the peak of an elliptical barrier 91

18 Horizontal divergence vs. position, X, along Y=0, for flow over an infinite ridge and a circular hill 93

19 Terrain height vs. position, and drag per unit crosswind length, d_2, for flow over μ, ν and exponential type infinite ridges 108

20 As in Fig. 19, except for logarithmic and arccot barriers 110

21 As in Fig. 19, except for a variety of ridges having the same drag per unit crosswind length 112

22 Drag per unit crosswind length, d_2, vs. the maximum pressure perturbation, P_{2m}, for flow over various infinitely-extended single ridges 114

23 Drag per unit crosswind length, d_2, vs. frequency for sinusoidally modulated Agnesi and Gaussian ridges 116

24 As in Fig 22, except for infinitely-extended double ridges of various types 122

25 Drag per unit crosswind length, d_2, vs. a normalized separation distance, ϵ/X_m, for double arccot ridges 124

FIGURE PAGE

26 Comparison of the drag per unit crosswind length for two-dimensional slice flow, d_{2s}, and three-dimensional flow over a circular hill, d_{3c}, as a function of Y 127

27 Drag per unit crosswind length, d_3, at Y=0, vs. the horizontal scaling ratio, γ, for flow over various elliptical barriers 129

28 Total drag and transverse force for three-dimensional flow and two-dimensional slice flow over an elliptical barrier as a function of the scaling ratio, γ, and orientation, ψ 134

29 Ratio, T_3/D_3, of the transverse to drag force components as a function of scaling ratio, γ, and orientation, ψ 137

30 Terrain height contours for μ-type elliptical barriers smoothed with a Laplacian operator and unsmoothed 142

31 Effect of Laplacian smoothing on the total drag and maximum terrain height for an unrotated elliptical barrier with $\gamma=1/2$ and a circular barrier 148

32 Terrain height contours for a ν-type elliptical barrier, smoothed with a Laplacian operator 151

33 Effect of Laplacian smoothing on the total transverse force and maximum terrain height for a rotated elliptical barrier with $\gamma=1/2$ 153

34 Terrain height vs. position for spectral series approximations to an Agnesi barrier 157

35 Effect of spectral truncation on the drag per unit crosswind length and maximum terrain height for Agnesi and sinusoidally modulated Gaussian ridges 158

36 As in Fig. 34, except for a sinusoidally modulated Gaussian ridge 162

37 Contour plot of total pressure (mean plus perturbation) for flow over an elliptical barrier 166

FIGURE PAGE

38 Terrain-height cross-sections in Western Canada 169

39 Maps showing the orientation of the cross-sections in Fig. 38 and the areas for the pressure perturbation as displayed in Figs. 40-44 170

40 Topographic contours and pressure perturbation for a mean flow at an angle, $\bar{\psi}$=35° north of east, for the Southern Alberta region 174

41 Pressure perturbations for westerly ($\bar{\psi}$=0) and southerly ($\bar{\psi}$=90°) flow over the Southern Alberta region 176

42 As in Fig. 40, except $\bar{\psi}$=-35° 177

43 As in Fig. 40, except for the Northeastern B.C. region ($\bar{\psi}$=35°) 179

44 As in Fig. 41, except for the Northeastern B.C. region ($\bar{\psi}$=0 and 90°) 181

45 Total pressure field for the Southern Alberta region (mean field plus perturbation based on Fig. 40) for buoyancy frequency $\bar{N}$=.01 s^{-1} and .02 s^{-1} 182

46 Surface isobars and 500 mb geopotential height contours for a typical southwesterly flow across the Rocky Mountains in Western Canada 184

47 Comparison of the pressure perturbation, P_3, its approximation, P_{3A}, given by (H.10), and the two-dimensional slice flow perturbation, P_{2S}, for flow over an elliptical barrier 250

48 Pressure perturbation vs. position for flow over an Agnesi ridge, as calculated by a discrete Fourier transform, for several values of grid spacing 259

NOTATION

Before referring to the list of symbols that is given below, the reader may find it helpful to note the following guidelines that were employed in choosing the notation used throughout the thesis.

For some of the most frequently occurring variables, a subscript, 2 or 2S, is used to denote the special case of two-dimensional flow (in a vertical plane) over an infinite ridge, or over an isolated barrier, respectively. Also, the subscript, 3 or 3C, is used for the cases of three-dimensional flow over barriers with elliptical or circular horizontal cross-sections, respectively. The subscript, m, in most cases, is used to denote the magnitude of the extreme value of a variable. Subscripts are also used to denote differentiation (see Chapter 3). To simplify the list of symbols that follows, a separate entry is not included for each subscripted variation of a quantity. Also, variables which appear only in the intermediate stages of a calculation are not included in the symbol table. For several variables, appearing with a prime (′), a corresponding dimensionless form is defined without the prime. The most important dimensionless variables are defined in Appendix B. In another context, a prime denotes a quantity referred to a barrier which has been rotated from a standard position. An overbar is used to denote variables describing the mean flow. Angular brackets around a variable, V, as in <V>, are used to indicate that the quantity refers to a case in which the barrier shape has been modified by curvature in a horizontal plane (Chapter 6) or by smoothing (Chapter 11).

SYMBOL	DEFINITION
a	- horizontal length scale, usually along the x axis
A	- intense, mobile cyclone type (Chapter 2) - x-z cross-sectional area of a barrier (Chapter 4) - amplitude of sinusoidal ridge displacements (Chapter 6) - amplitude of constant factor in sinusoidal modulation of terrain height (Chapter 9)
A_1, A_2	- type A cyclone with one or two periods of intensification, respectively
$\hat{A}$	- Fourier transform (with respect to y) of barrier cross-sectional area
b	- horizontal length scale, usually along the y axis
B	- local cyclone type of moderate intensity (Chapter 2) - amplitude of sinusoidal modulation of terrain height (Chapter 9) - factor appearing in expression for the total force on an elliptical barrier (Chapters 10, 11)
B_n	- an elliptic integral, defined in (Q.1)
BF	- Byrd and Friedman (1971), a reference for elliptic integrals
$\bar{c}$	- speed of sound in the mean flow, defined by (3.8)
C	- weak, mobile cyclone type (Chapter 2) - factor appearing in expression for the total force on an elliptical barrier (Chapters 10, 11)
C_n	- an elliptic integral, defined in (Q.1)

d - drag per unit crosswind length of a barrier

D - weak, local cyclone type (Chapter 2)
- total drag on a barrier (Chapters 8, 10)

e - the number 2.718+

E - complete elliptic integral of the second kind

f - Coriolis parameter

$\vec{f}'$ - force per unit crosswind length on a barrier

$F(\alpha,\beta,\gamma;z)$ - hypergeometric function

$\vec{F}'$ - the total force on a barrier

g - acceleration due to gravity

G - factor appearing in expressions for the total force on a barrier, defined by (10.5)

GR - Gradshteyn and Ryzhik (1965), a mathematical reference

h - barrier height (dimensionless forms appear in upper case)

h_o - amplitude factor in barrier height and vertical scaling factor

h_n - spectral expansion coefficients for the height field (Chapter 11)

$\tilde{h}$ - Fourier transform of terrain height with respect to x alone, defined by (3.22) or (3.26) (dimensionless forms appear in upper case)

$\hat{h}$ - Fourier transform of terrain height with respect to x and y, defined by (3.17) (dimensionless forms appear in upper case)

H_n - Hermite polynomial

$\mathbf{H}_n$ - Struve function

$\overline{H}_o$ - scale height for the mean-flow density, defined in (3.9)

i - a square root of -1

I - factor, defined by (F.3), appearing in the normalization for the horizontal divergence for flow over an elliptical barrier

J_n - Bessel function

k - horizontal wave number component (corresponding to the x coordinate in the physical domain)
- modulus of elliptic integral

K - complete elliptic integral of the first kind

K_μ - Bessel function of imaginary argument

ℓ - horizontal wave number component (corresponding to the y coordinate in the physical domain)

L - horizontal length scale in the direction parallel to the mean flow

m - vertical wave number, defined by (3.19) (with the + sign), or (3.24)

M - number of points used in a discrete Fourier transform

N - truncation limit for a spectral expansion

N_o - Bessel function of the second kind

$\overline{N}$ - Brunt-Väisälä or buoyancy frequency

p' - pressure perturbation (dimensionless form in upper case)

$\overline{P}$ - pressure associated geostrophically with the mean flow

P_T - total pressure ($p'+\overline{P}$)

R - gas constant for dry air (Chapters 1 and 3)
- dimensionless radial elliptical polar coordinate, defined by (B.1)

R_c - normalized radius of curvature, defined by (6.13)

R_d - dimensionless measure comparing the drag per unit length of a smoothed barrier to that expected from a quadratic dependence on height

R_e - mean radius of the Earth=6371 km

R_D - as R_d, except for total drag

R_T - as R_d, except for total transverse force

S - smoothing operator defined by (11.2) or (11.8)

s_n, S_n - integrals defined by (11.13) and (11.16), respectively, arising in the calculation of the force on a smoothed barrier

t - time variable
- transverse force on a barrier per unit crosswind length

T - transverse component of the total force on a barrier

$\bar{T}$ - temperature of the mean flow

u' - x component of velocity perturbation

$\bar{U}$ - mean flow speed (mean wind vector is along the positive x direction, unless otherwise noted)

v' - y component of velocity perturbation

V - terrain volume

w' - vertical (z) component of velocity perturbation

x - horizontal Cartesian coordinate, increasing towards the right in most figures

X - normalized coordinate = x/a

X_m - distance from the terrain peak to the position of the extreme pressure perturbation

y - horizontal Cartesian coordinate, increasing towards the top in most figures

Y - normalized coordinate = y/b

z - vertical Cartesian coordinate, increasing upwards

α - parameter determining the overall horizontal scale of a barrier (see Appendix C)

β - Rossby parameter = $\partial f/\partial y$ (Chapter 1)
- parameter appearing in a spectral expansion of the terrain height (Eq. 11.21)

γ - ratio of horizontal scaling lengths ($=a/b$)

γ_o - ratio of specific heats ($=1.4$)

Γ - gamma function

δ - Dirac delta function (Chapter 3)
- lateral displacement of a streamline (Chapter 7)
- terrain-shape parameter appearing in the logarithmic type of barrier, defined in (9.2)

δ_i - parameter taking the value 0 or 1 according to approximations made in Chapter 3

ΔX - grid spacing for a discrete Fourier transform

ϵ - parameter specifying the degree of smoothing of lee cyclogenesis frequency per unit area maps (Chapter 2)
- eccentricity of an elliptical barrier, defined by (4.5)
- separation of double ridges (Section 9.3)

ζ - vertical component of vorticity, defined at the end of Chapter 3

η - cyclogenesis frequency per unit area (Chapter 2)
- vertical displacement of a streamline (Chapters 3, 7)

θ - unit step function (0 or 1 according to whether its argument is negative or positive, respectively)
- angular elliptical polar coordinate, defined in (B.1)

κ - dimensionless wave number variable $(=ka)$

λ - longitude (Chapters 2 and 12)
- dimensionless wave number coordinate $(=\ell b)$

μ - a terrain-shape parameter, defined in (4.1)

ν - a parameter entering the probability density assumed for the location of cyclogenesis events (Chapter 2)
- a terrain-shape parameter defined in (9.2)

ξ - $= 1/(8\tau\gamma^2)$ (Chapter 6)

π - the number 3.14159+

Π - elliptic integral of the third kind

ρ - radial elliptical polar coordinate in the wave number domain, defined in (B.2)

ρ' - density perturbation

$\bar{\rho}$ - density of mean flow, defined by (3.9)

$\bar{\rho}_o$ - value of $\bar{\rho}$ at $z=0$

σ - parameter controlling the degree of smoothing by a differential operator (Chapter 11)

τ - parameter controlling the degree of curvature of parabolic terrain (Chapter 6)

ϕ - latitude (Chapters 2 and 12)
- angular elliptical polar coordinate in the wave number domain, defined in (B.2)

ψ - counterclockwise angle through which a barrier is rotated relative to some standard orientation

$\bar{\psi}$ - counterclockwise angle between the mean wind vector and the x axis (east)

ω - terrain-shape parameter appearing in the arccot type of barrier, defined in (9.2)

ω_n - quadratic form in smoothing coefficients, defined by (11.12)

Ω - angular frequency of sinusoidal modulation of ridgeline displacement (Chapter 6) or terrain height (Chapter 9)

∇^2 - two-dimensional Laplacian operator $(\partial^2/\partial x^2+\partial^2/\partial y^2)$

CHAPTER 1

INTRODUCTION

1.1 Motivation

The original goal of my thesis research was to improve our understanding of lee cyclogenesis, the formation of a low-pressure center on the downwind side of a mountain range, through the technique of numerical modelling. However, like an airstream approaching a mountain of finite length, the easiest path to take may be to skirt around the edges of the obstacle blocking one's way. The work summarized in this thesis represents a rather large deviation from the proposed course of action.

As a first step in my study of mountain airflow, an examination was made of the statistics compiled by Chung (1972) on the frequency of occurrence of cyclogenesis in the lee of the Rocky Mountains of Western Canada as a function of geographic location. As is discussed in Chapter 2, there are preferred regions for cyclone formation which appear to be closely related to the upstream topography. One is led to consider which terrain features are responsible for the observed clustering of the cyclogenesis locations. The mean barrier height is likely the most important factor, but the lengths of the mountain range in the crosswind and streamwise directions, overall orientation of the range, terrain slope and curvature of the ridge in a horizontal plane are all geometrical parameters that could be considered.

Spatial variations in the roughness of the terrain surface, and its thermal properties, could also be reflected in the preferred positions of new low-pressure centers.

As part of a review of the extensive literature on mountain airflow, calculations were performed to clarify some results of Smith (1980), who used a steady, linear, hydrostatic model to study mountain waves. Exact analytical solutions were discovered for the surface pressure and winds for flow over a three-dimensional elliptical hill. Although this steady-state theory seemed of little relevance to the intrinsically time-dependent phenomenon of lee cyclogenesis, it was decided that the analytical results themselves were sufficiently interesting to pursue further. Note, however, that for any airflow over a barrier, the pressure field can be resolved into a time-independent part, produced by a mean flow interacting with the fixed mountain, plus a time-dependent 'residual' (which may or may not be small compared to the time-independent term). Without a more detailed knowledge, one might expect the average position of lee cyclone formation to depend principally on the time-independent part of the flow. The results obtained using the analytical model for flow over an idealized barrier are presented in Chapters 3 through 7. Topics covered include the surface pressure and wind fields, and the associated streamline deflection and horizontal divergence. The force exerted by the barrier on the airstream is calculated in Chapters 8 through 10. The subject of Chapter 11 is the change in this force when the barrier is artificially smoothed. In Chapter 12, the model is applied, in numerical form, to flow over a representation of the terrain of the Canadian Rockies. A summary and some suggestions for future work appear in Chapter 13. Some of the mathematical details are given in the Appendices.

1.2 Previous studies of lee troughs and cyclones

Following Chung et al. (1976), it seems reasonable to define lee cyclogenesis as the initial formation of a low-pressure center in the lee of a mountain range. This is a more restrictive definition than commonly appears in the meteorological literature, where the term is used to include intensification of a cyclone after it has formed (Petterssen, 1956, p. 50). Speranza (1975) makes the further distinction of excluding the formation of weak, stationary low-pressure areas from the lee cyclogenesis category. He argues that such systems do not have a developed cyclonic circulation and, therefore, should not be called cyclones. The flow near the mountain can be highly ageostrophic so the pressure field may not be a good indicator of the winds. Although Speranza's suggested terminology will not be used here, it is agreed that there are different types of low-pressure areas in the lee, including troughs, regions with closed isobars which remain weak and shallow (many localized with respect to the barrier), and fully developed mobile cyclonic systems occupying the entire depth of the troposphere (Schallert, 1962; Chung et al., 1976).

Smith (1979a) outlines some conceptual models for explaining the formation of lee cyclones, including arguments based on potential vorticity (discussed below), the effects of friction, flow transience, variation of the Coriolis parameter with latitude, and low-level blocking of the flow on the windward side of the barrier. Other review papers, which deal more directly with observed characteristics of lee cyclogenesis will be mentioned later.

One of the simplest and most widely used rationales for the observed tendency of low-pressure centers to develop in the lee of major mountain ranges is based on some form of potential vorticity equation. Examples include Hess and Wagner (1948), Bolin (1950), Kasahara (1966), and Holton (1972). For frictionless, adiabatic flow this equation expresses the constancy of the ratio of an average vertical component of absolute vorticity of an air column, Q, to the pressure difference, Δp, between two surfaces of constant potential temperature (Petterssen, 1956, p. 134):

$$\frac{D}{Dt}\left(\frac{Q}{\Delta p}\right) = 0 \quad ; \quad Q = \zeta + f \ . \qquad (1.1)$$

Here ζ is the relative vorticity of the air and f is the Coriolis parameter or planetary vorticity. To apply the conservation of potential vorticity, assumptions are made about how the depth of an air column changes as it passes over a barrier. Generally, it is proposed that there is a vertical shortening of the column immediately above the mountain, causing a compensating horizontal divergence (to conserve mass). The Coriolis force acts to deflect the diverging air (to the right of its original path, in the Northern Hemisphere), producing an anticyclonic circulation or reduction in the (cyclonic) vorticity. In the lee of the barrier it is assumed that an air column will be stretched vertically and the original vorticity may be restored. On the basis of such arguments it has often been suggested that a westerly flow will be diverted towards the southeast in crossing a mountain range. Smith (1979a, 1979c), however, has indicated that permanent anticyclonic deflection should not be present in some simplified atmospheric models. Specifically, in a Boussinesq model of stratified flow, the mountain influence aloft extends upstream, such that the incident flow is stretched before it reaches the barrier. This causes a cyclonic deflection of the flow on the windward side of the mountain. This lateral motion is not shown in the discussion by Holton (1972), for example, but is a common feature of the real atmosphere (Smith, 1982). If the upstream effect is included, it compensates for the anticyclonic turning over the barrier so that the flow returns to its original direction far downstream. However, Smith goes on to show that a permanent deflection in the lee is obtained in a homogeneous model or in a vertically unbounded compressible one.

The way in which these ideas have been applied to the effect of mountains on the atmosphere depends on the horizontal scale of the motion. First consider a relatively large scale (several thousand kilometres, for example), such that the variation of the Coriolis parameter with latitude has an appreciable effect on air trajectories. Orographic influences on this scale have been reviewed by Kasahara (1980). Although Sutcliffe (1951) has argued that the thermal contrast between continents and oceans is sufficient to explain the mean positions of planetary-scale waves, early theoretical studies by Charney and Eliassen (1949) and Bolin (1950) showed orographic effects to be important also. More recent numerical experiments with general circulation models, such as those by Manabe and Terpstra (1974) and Kasahara et al. (1973), have confirmed that both thermal and direct orographic forcing are needed to explain observed large-scale features of the atmosphere. However, Dickinson (1980) cautions that the relative contributions of the two types of forcing are 'now too poorly known for precise quantitative comparisons to be made'.

Potential absolute vorticity arguments can be used to justify large-scale mountain airflow as a generation mechanism for long Rossby waves if it is assumed that the flow experiences a net anticyclonic turning in passing the barrier. In such a case a westerly flow incident on the Rockies would acquire a component towards the south in the lee. To conserve absolute vorticity, the decreasing

Coriolis parameter is countered by an increasing relative vorticity of the flow. This tends to deflect the airstream back to the north. The broad trough over the eastern portion of North America, at about 80°W longitude, that is a prominent feature of the mean 500mb chart (for example, see Kasahara, 1980, or Bolin, 1950) could be qualitatively explained in this way.

It is not clear how relevant this sort of argument may be to lee cyclogenesis because the scale of the trough generated by the variation of the Coriolis parameter with latitude (the 'β effect'), is much larger than that of the low-pressure centers initiated in the lee of the Rockies. Smith (1979a) comments that the 'restoring force for Rossby waves is not just β, however, but the gradient in the background potential vorticity'. As a consequence, the mountain initiated wave could have a shorter wavelength than for a uniform flow situation. Also see Pedlosky (1979, pp. 111, 428).

Another way in which potential vorticity conservation arguments can be used in an attempt to understand Rocky Mountain lee cyclogenesis is by noting that a large fraction of the lee cyclones are associated with a 'parent' on the windward side of the barrier (Chung, 1972). As the parent low moves on to the west coast it may fill, giving up some low-level vorticity, while the associated upper trough carries on across the barrier. As the flow is stretched in the lee, the low-level vorticity reappears in the form of a new low. This description is certainly oversimplified and does not explain cases in which the lee cyclone acquires a greater intensity than the parent or in which the parent low is absent. Also, Chung shows cases where more than one lee cyclone is associated with a single parent. Zishka and Smith (1980) show areal frequency statistics based on 28 years of data for January cyclolysis and cyclogenesis events in and near North America. Their Fig. 2 shows a maximum of cyclolysis frequency (counted in 2° latitude by 2° longitude areas) near the Washington coast. The magnitude of this extremum is comparable to the maxima of cyclogenesis frequency seen in the Southern Alberta - Montana and Southeastern Colorado regions. However, the total number of cyclolysis events off the coast appears to be less than half of the number of cyclogenesis events in the western half of the North American continent. (See Peyrefitte and Astling, 1981, for comments on the Zishka and Smith paper).

If mechanisms were proposed that led to a net cyclonic vorticity production in the passage of an air parcel over a barrier, then it would be easier to understand why the formation of low-pressure centers is associated with mountain ranges. Smith (1979a) lists blocking of the windward flow at low levels and the action of surface friction as two such processes. In discussing the model of Buzzi and Tibaldi (1977), which incorporated an Ekman layer parameterization of friction, Smith indicates that the anticyclonic circulation induced by the barrier is opposed by the frictional force, leading to an effective increase in the cyclonic vorticity. Petterssen (1956, pp. 257-266) discusses the role of friction as a source of vorticity in surface high-pressure regions but neglects it in the section on the effect of mountains. The circulation around a mountain in quasi-geostrophic flow is similar to that around a cold-core anticyclone (Smith, 1979a), so Petterssen's comments about the role of friction in vorticity export from the Antarctic are also relevant here.

Synoptically-based studies of lee cyclogenesis have concentrated on the Alps in Europe and the Rocky Mountains in North America. Speranza (1975) reviewed some of the early work in the Alpine region. This was updated by Tibaldi (1979, 1980) to include results of numerical modelling efforts to simulate cyclogenesis. A more complete discussion of one particular modelling attempt is given by Tibaldi et al. (1980). McGinley (1982) presents a recent diagnostic study. Further results may be forthcoming, based on analysis of data from the Alpex Subprogram of the Global Atmospheric Research Program.

A typical case of Alpine lee cyclogenesis occurs in conjunction with a well-developed upper trough and associated surface cold front approaching the Alps from the northwest. The interaction of this system with the mountains occurs in a two-step process. In the first stage there is a localized increase in low-level vorticity in the lee. In the second stage, the continuing advance of the upper trough causes its associated positive vorticity advection and divergence regions to overtake the initial orographic disturbance. The surface low then develops by baroclinic processes in a manner similar to storms which are not directly influenced by mountains. Fons (1979) illustrates various synoptic situations that can lead to cyclogenesis in the Alpine region. For further details on lee development sequences the articles previously mentioned should be consulted.

The initial formation of a low in the lee of the Alps and its relation to blocking of the low-level cold air is partially explained by Tibaldi (1980). He presents a diagnostic relation between the temperature, T, and the geostrophic relative vorticity, ζ_g:

$$\frac{\partial \zeta_g}{\partial \ln p} = -\frac{R}{f} \nabla^2 T \quad . \qquad (1.2)$$

Here p is the pressure, f is the Coriolis parameter and R is the gas constant. The Laplacian on the right side of (1.2) includes only horizontal derivatives taken at constant pressure. This equation can be derived by taking the curl (at constant pressure) of the thermal wind relation given by Holton (1972, p. 49). Because there is a relative maximum of temperature in the lee at low levels (caused by the deflection of the cold air to the sides of the convex face that the Alps present to the incident flow), $\nabla^2 T<0$ in this region and decreases with height. Eq. (1.2) then implies that the geostrophic vorticity increases with pressure. This is consistent with the existence of a shallow low-pressure system in the lee. Note, however, that the argument is only qualitative because the flow can be highly ageostrophic. For example, Newton (1956) found for an intense cyclogenesis case in the lee of the Rockies, that the vorticity computed from the actual surface winds was only about one-sixth that obtained geostrophically.

Now consider research on North American lee cyclogenesis. Palmén and Newton (1969) have summarized some of the early work (including Hess and Wagner, 1948, and others) on this phenomenon by describing a typical development sequence, appropriate for a relatively intense lee cyclone case. As with the Alpine case, this conceptual model has two phases. First, a 'parent' cyclone in the Pacific approaches the coast and begins to fill as it is deflected northward. Flow from the southeast quadrant of this low passes over the mountains, generating or strengthening a shallow lee trough. McClain (1960) attributes an important role in forming this trough to compressional warming due to adiabatic descent below 700mb. Newton (1956) has found that friction can also act to increase the low-level circulation during the initial hours of lee cyclone development. Godson (1948) also briefly discusses lee trough formation. Carlson (1961) has attempted to describe the thermal ridges connected with these low-pressure areas using an equivalent barotropic model. Note that the area of relatively warm surface air is initially closely tied to the topography, but may subsequently be broadened towards the east by advection. Even so, the width of the trough is hundreds of kilometres rather than the thousands that would be appropriate for the topographically induced, continental-scale Rossby wave mentioned earlier.

In the second stage of development, an area of upper-level divergence ahead of an advancing upper cold low or trough (originally associated with the parent low) crosses into the lee. Because the low-level baroclinic zone (lee trough) is held quasi-stationary (Hage, 1961) through its tie to the topography, it is overtaken by the upper system and further development can occur. The overall process is rather similar to the Alpine case, except for the manner in which the initial low-level circulation develops.

In many cases the upper-level divergence can be identified with a region of positive vorticity advection (for example, if the air speed is much greater than the speed of movement of the vorticity pattern (Petterssen, 1956, p. 302)). In such an instance lee-side development as just described is a realization of the Petterssen hypothesis (Petterssen et al., 1955 and Petterssen, 1955), which relates the occurrence of surface cyclogenesis in a baroclinic zone to the approach of a region of positive vorticity advection aloft. However, Schallert (1962) and Chung (1972) have indicated that there is a class of relatively weak, short-lived, orographic disturbances, comprising a significant fraction of all lee cyclones, which form without a direct association with an advancing upper trough. In one of the few attempts at numerical modelling of airflow over the Rocky Mountains (excepting operational weather prediction) Egger (1974) concluded that in his simulation of a relatively weak case of cyclogenesis in the lee of a highly idealized barrier, the vorticity advection aloft played a small role. Also, note that in a sample of lee cyclones studied by Hovanec and Horn (1975), those with a lifetime greater than 72 hours displayed a statistically significant correlation with the wind speed at 300mb, whereas shorter-lived lows did not. Jurčec (1981) advocated the study of weak, shallow cyclones in the lee of the Alps. Previous investigators have tended to concentrate on the more intense cases.

There are many other aspects of lee cyclogensis research that have not yet been mentioned. Some references are listed here for those who would like to pursue the subject further. Papers dealing specifically with the frequency and positions of occurence of lee cyclogenesis are considered in Chapter 2. Fawcett and Saylor (1965) studied the precipitation and severe weather associated with Colorado cyclogenesis events. Hage (1961) and Chung (1977b) examined structural changes in upper cold lows as they pass over a mountain barrier. Chung and Reinelt (1973) and Vickers (1975) found about 80% of lee cyclogenesis events are associated with difluent upper flow patterns. Charette (1971), Hopkinson (1972) and Schram (1974) have done diagnostic studies of orographically induced vertical motion. Because of the frequent association of chinook (foehn) conditions with lee cyclogenesis (for example, see McClain, 1960) much of the literature on chinook airflow may be relevant to the study of lee troughs and the initial stages of lee cyclone formation. Examples include McClain (1952), Cook and Topil (1952), Brinkmann and Ashwell (1968), and Lester (1976).

The steady, linear, hydrostatic airflow model which is the basis for most of this thesis includes the adiabatic compression mechanism thought to be important for the maintenance of a small-scale lee trough. However, because of the use of the Boussinesq approximation and the neglect of the Coriolis force, it can be shown that the vertical component of vorticity is zero everywhere in the model (see Chapter 3). Therefore, the model cannot be used to describe a lee cyclone as defined by Speranza (1975), since he requires the presence of cyclonic vorticity. It might be used, however, to give a qualitative indication of some features of a standing lee trough.

CHAPTER 2

LEE CYCLOGENESIS FREQUENCY PER UNIT AREA

2.1 Counts of lee cyclogenesis events

Numerous papers have been published giving positions or counts of low-pressure centers or cyclogenesis events in a given region. The results of Petterssen (1956), based on daily surface analyses for the years 1899 through mid-1939, are among the most comprehensive and widely quoted. He found that there exist preferred locations for cyclone formation, which he explained with reference to orographic influences, among others. Petterssen grouped his data to show areal density of cyclogenesis frequency in the winter and summer seasons only. Klein (1957) extended these results by showing a month by month analysis based on the years 1909-1914 and 1924-1937. In general terms, it was found that the regions of formation of both highs and lows are farthest north in August and farthest south in February. Cyclogenesis is found in the lee of barriers while anti-cyclogenesis is associated with the higher terrain itself. Klein presents a detailed bibliography of earlier work on the tracks of pressure centers and their points of origin.

While Petterssen and Klein analyzed data for the whole Northern Hemisphere, recent work has concentrated on more limited regions, and in many cases a much more limited time period also. Radinović (1965) counted cyclone formations in a portion of Europe. Chung (1977a) has studied cyclogenesis in the lee of the Andes. Chung et al. (1976) present results for East Asia and the lee side of the Canadian Rocky Mountains. The latter area has also been considered by Vickers (1975). Reitan (1974) presented maps of cyclogenesis frequency per unit area for North American cases for five different months of the year. Schallert (1962) and Hovanec and Horn (1975) show the positions of formation for a number of 'Colorado' lows (including those found in several other states to the south and east of Colorado). In a recent paper, Zishka and Smith (1980) claim that there has been a significant decrease in the number of cyclones and anticyclones in and near North America during the 28-year period (ending in 1977) included in their study. It has subsequently been pointed out, by Peyrefitte and Astling (1981), that the data set used by Zishka and Smith is not a homogeneous one. Apparently, during the first five years of the period studied, the surface pressure fields were analyzed at an interval of 3mb, rather than the 4mb used later. Zishka and Smith (1981) remain unconvinced that this is sufficient to explain the trend in the number of pressure centers that they reported.

Besides this unresolved problem, there are other obstacles to comparing the different results on cyclogenesis frequency and its areal density. For example, the synoptic analyses on which Radinović based his results were at a 5mb resolution, Chung used 2.5mb for his Asian studies but 2mb for North America, while Schallert used a 1mb interval.

Another source of difference arises from the temporal resolution in the data sets. Petterssen and Klein had access to only one map per day, whereas in many of the other studies four maps were available. Chung (1972) reports that he referred to maps analyzed at 3 hour intervals on occasion. A lack of temporal resolution would tend to smear out the observed maxima in cyclogenesis frequency per unit area because of motion of the cyclones in the intervals between their formation and the succeeding map time. Vickers (1975) suggested this as a possible explanation of differences between his results and those of Chung (1972). It seems likely that the different resolutions used in the pressure field analyses (4mb for Vickers and 2mb for Chung) would also have contributed to the larger spatial scale characteristic of the cyclogenetic regions found by Vickers.

Two other sources of difficulty in the quantitative comparison of the various research results are the subject of this chapter. The first of these is related to the size of the areas within which the cyclogenesis counts are made. For example, Klein (1957) counted cyclogenesis events in quadrangles defined by latitude circles and meridians, averaging about 200,000 km^2, Reitan (1975) and Chung (1972) used regions of about 550,000 km^2 and 28,000 km^2, respectively. If the sampling area is too large the resulting fields of cyclogenesis frequency per unit area will be too smooth. As a consequence, potentially useful information could be lost. Although the cyclogenesis frequency per unit area will not be calculated in quite the same manner as in the studies mentioned, it will be shown, at least for relatively small sample sizes, that the degree of smoothing has an appreciable effect on the magnitude of the areal density of cyclogenesis frequency.

The second idea to be explored in this chapter is whether or not different types of low-pressure systems show distinct preferred regions of formation. There has been a tendency in previous studies to ignore some types of lows. For example, because Klein (1957) was primarily interested in the tracks of mobile cyclones, lows judged to be 'thermal' were excluded from his analyses. Speranza (1975) and others have distinguished between weak low-pressure centers which tend to remain almost fixed with respect to a mountain barrier and more vigorous mobile cyclones. Schallert (1962) identified four types of lee cyclone on the basis of their maximum intensity (weak, moderate, or intense) and mobility with respect to the lee region of the Colorado Rocky Mountains (migratory or local). Mobile cyclones which acquired 'moderate' or greater intensity were designated as type A. This group was further subdivided into types A_1 and A_2, according to whether there was a single period of intensification or two periods, respectively. A few type A cyclones could not be clearly placed in either the A_1 or A_2 category. Type B cyclones were defined as those of moderate intensity which remained local. Weak lows were labelled C or D according to whether they were migratory or local, respectively. Schallert concentrated his efforts on the A and B type cyclones, finding a clustering of the positions of type A_2 lows at the time of onset of the first period of intensification and in the positions of type B lows. He attributed this localization to orographic influences. Chung (1972), in his analysis of cyclones in the lee of the Canadian Rockies also used the classification scheme of Schallert. Chung included all lows having a closed isobar lasting at least 24 hours on consecutive maps at 6 hour intervals assuming that the surface pressure was analyzed at a 2mb resolution. Because he included maps showing the positions of formation for all the cyclone types, it was possible to use Chung's data to examine differences between the types.

2.2 Smoothing contour maps of cyclogenesis frequency per unit area

In this section, a method is presented for constructing maps of cyclogenesis frequency per unit area which differs from the traditional method of counting cyclogenesis events on a grid. The procedure is then applied to study the effect of smoothing on the cyclogenesis frequency per unit area.

Assume that an estimate of the position of each cyclogenesis event in a given unit time is known. The location of the ith event is specified as $\vec{r}_i = (\phi_i, \lambda_i)$, where ϕ_i is latitude and λ_i is longitude. Because of uncertainty in determining the location of a lee cyclone, the new low may not have formed precisely at $\vec{r}_i$. For the purpose of constructing a map of the cyclogenesis frequency per unit area, it is convenient to assume that there is a finite probability that the cyclogenesis event actually occurred within a circle of radius ϵ about $\vec{r}_i$. If η is the number of cyclogenesis events per unit area per unit time at the point $\vec{r}$, it is assumed to be representable in the form

$$\eta(\vec{r}) = \sum_i \eta_i(|\vec{r}-\vec{r}_i|) \quad , \qquad (2.1)$$

where

$$\eta_i(d) = \frac{\nu+1}{\pi\varepsilon^2}\left(1 - \frac{d^2}{\varepsilon^2}\right)^{\nu} \theta(\varepsilon-d) \qquad (2.2)$$

is a convenient, but otherwise arbitrarily chosen probability density function used to describe the precision with which an individual cyclogenesis event can be located. $\theta(\epsilon-d) = 1$ if $d<\epsilon$ and 0 otherwise. The parameter ν was introduced to increase the flexibility of the definition of η. If $\nu=\infty$ then the cyclone position is known with infinite precision. For decreasing ν the distribution becomes progressively broader. For the maps to be presented in the following, $\nu=2$ was used. Except for the normalization factor, the form of η_i is the same as the function plotted in Fig. 19 in Chapter 9. The normalization chosen in (2.2) ensures that the integral of η_i over a circle of radius ϵ is unity, that is, cyclogenesis event i is 'counted' only once.

Note that the functional form of η_i is taken to be independent of i.

This representation for η was chosen on the basis of simplicity, not on detailed knowledge of the uncertainties of position involved. In fact, the distribution of position about $\vec{r}_i$ is probably not circularly symmetric for points near the barrier because of the tendency for lows to form on the lee side and to move southeastward thereafter. Furthermore, the precision with which a lee cyclone can be identified and located depends on the spatial arrangement of the observing stations and the resolution at which the surface pressure analysis is completed. An estimate of a typical distance between observing stations in South-central Alberta is 150 km to 200 km, but is substantially larger in the northern half of the province. One might argue that ϵ should be increased in regions of low station density. The definition of η by (2.1) and (2.2) should be regarded as an artifice to smooth the scattered cyclogenesis locations so that clustering of the points can be seen more clearly. As already stated, it is not a representation firmly based on the nature of the uncertanties in identifying the positions of lee cyclones.

By expressing $\vec{r}=(\phi,\lambda)$ and $\vec{r}_i=(\phi_i,\lambda_i)$ in terms of Cartesian components in a coordinate system established at the center of the Earth, for example, one can show that

$$|\vec{r}-\vec{r}_i| = R_e \left\{\cos(\lambda-\lambda_i)\cos\phi\cos\phi_i + \sin\phi\sin\phi_i\right\} \quad , \qquad (2.3)$$

where R_e is the radius of the Earth. An alternative would be to use the distance from $\vec{r}$ to $\vec{r}_i$ along the curved surface of the Earth, but this would result in a negligible change for the small inter-point distances involved here. Given (ϕ_i,λ_i), one can substitute (2.3) into (2.1) to obtain the cyclogenesis frequency per unit area, η, at an arbitrary point, $\vec{r}$. In actual application to the maps presented in this chapter, η was calculated at points corresponding to a uniform grid on a polar stereographic projection map, true at 60°N latitude. The Surface II Graphics Package (Sampson, 1978) was used for all the figures requiring contouring in this thesis.

To test the effect of varying the parameter ϵ (which controls the degree of smoothing of the η field), the preceding analysis was applied to the data of Chung (1972). Chung's data includes 146 cyclones seen in a one-year period (1958) in the lee of the Rocky Mountains in Canada and Montana, including representatives of all of Schallert's types. Positions of cyclone initiation were measured from Chung's Figs. 12 and 13. Some discrepancies were found in the positions of several type A_1 cyclones between Chung's Figs. 12 and 14, amounting to 2° of latitude in the worst case. Comments to follow would not be changed had the alternative positions been used.

In Fig. 1, the number of lee cyclones formed per unit area per unit time, η, is compared for ϵ=200 km (Fig. 1a) and ϵ=300 km (Fig. 1b), both with ν=2. The contour interval

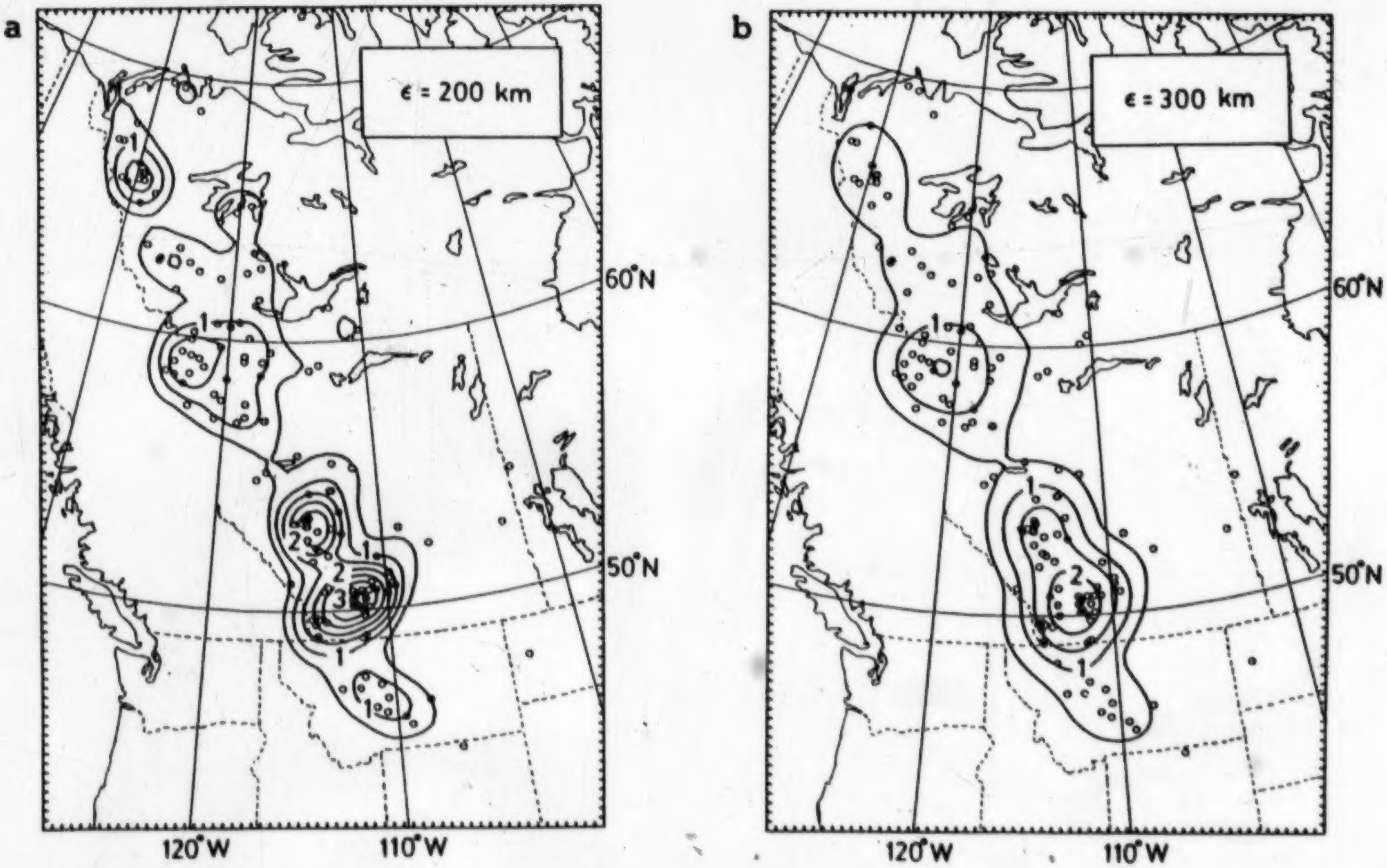
a
ϵ = 200 km
b
ϵ = 300 km
60°N
50°N
120°W
110°W
1
2
3

Figure 1. Contour maps of cyclogenesis events per unit area per unit time, in units of 10^{-4} km^{-2} yr^{-1}, for the smoothing radius, ϵ=200 km (Fig. 1a) and ϵ=300 km (Fig. 1b). The contour interval is 0.5 units. Individual cyclogenesis events are marked by the small circles (146 cases).

is 0.5, in units of 10^{-4} km^{-2} yr^{-1}. Positions of individual cyclones are marked with small circles. Chung used a unit area of $(1.5° \text{ latitude})^2 \approx 2.78 \times 10^4$ km^2 so that numerical values obtained from Chung's Fig. 11 should be divided by 2.78 before comparison with Fig. 1 here. Chung's results are similar to those presented in Fig. 1, although using ϵ=150 km gives a closer match to his numerical values. Also, because of the unrealistic circular symmetry of the assumed probability distribution near the Continental Divide, the contours on the maps presented here extend too far to the west near the barrier.

Examining Fig. 1a, it is seen that there are separate maxima in the lee of the Mackenzie Mountains directly to the west of Great Bear Lake, in Northeastern British Columbia, in South-central Alberta, in Southern Alberta and in Montana. Increasing the smoothing parameter, ϵ, to 300 km, as in Fig. 1b, leaves only the Northeastern B. C. and Southern Alberta maxima well defined by the contours. The magnitude of the Southern Alberta maximum has been significantly decreased by the increase in ϵ but that of the one in Northeastern B. C. is more nearly maintained. This is an indication of the relatively large length scale characterizing the cyclogenesis positions in B. C. and Northern Alberta compared to the stronger clustering seen in Southern Alberta. To see the effect on η of changing ϵ in a more quantitative manner refer to Table 1, which shows the values of the relative maxima in some of the regions.

Table 1. Relative maxima of cyclogenesis frequency per unit area, η, in events per year per $(100\ \text{km})^2$, as a function of the smoothing parameter, ϵ, by region.

ϵ (km)	Mackenzie	Northeastern B. C.	South-central Alberta	Southern Alberta
100	4.2	3.2	7.1	8.0
150	2.7	2.6	4.1	5.0
200	1.8	2.0	3.0	3.6
300	1.0	1.5	1.8	2.4

The table illustrates that the magnitude of cyclogenesis frequency per unit area is strongly dependent on the value of ϵ. This sensitivity is likely a reflection of the small number of data points on which the calculation is based. This leads to excessively high values of η for small ϵ. Except possibly in Northeastern B. C., the η values may be too small for $\epsilon=300$ km because this smoothing length is comparable to the length scale characterizing the clustering in the data. As a compromise, the value $\epsilon=200$ km was used for the remainder of the plots in this chapter. Besides the general decline of the maximum η values as ϵ increases, note from Table 1 that the Mackenzie maximum is larger than that in Northeastern B. C. for $\epsilon\leq150$ km, but is smaller for $\epsilon\geq200$ km. Thus one cannot make a one-to-one correspondence between the maximum η values and the barrier heights, for example. A significantly larger data sample might be useful in finding relations between the pattern of preferred locations for cyclogenesis and terrain shape features.

2.3 Lee cyclogenesis frequency maps for special classes of lows

The maps of the areal density of cyclogenesis frequency in Fig. 1 include all the cyclones in Chung's (1972) sample. Some results obtained by partitioning the cyclones according to Schallert's (1962) types will now be presented. All the maps in this section were constructed using $\nu=2$ and $\epsilon=200$ km in (2.2). In Fig. 2, a comparison is made between the cyclogenesis frequency per unit area for the mobile cyclones (types A and C) and the local lows (types B and D). Fig. 2a, showing the 109 mobile cases, is very similar in appearance to the map in Fig. 1a. Each maximum seen in Fig. 2a has a corresponding one in Fig. 1a, but with a reduced magnitude (especially the Southern Alberta maximum). On the other hand, Fig. 2b, showing the 37 lows that remained in the lee of the barrier, is quite different in appearance. The only regions with a significant number of lows of the local type are the Northeastern B. C. and Southern Alberta areas. Note that the contour interval in Fig. 2b is half that of Fig. 2a. Based on the number of cyclones that appear in the South-central and Southern Alberta clusters in Fig. 1a (about 20 and 30 lows, respectively, out of the sample of 146), one would expect about 5

A

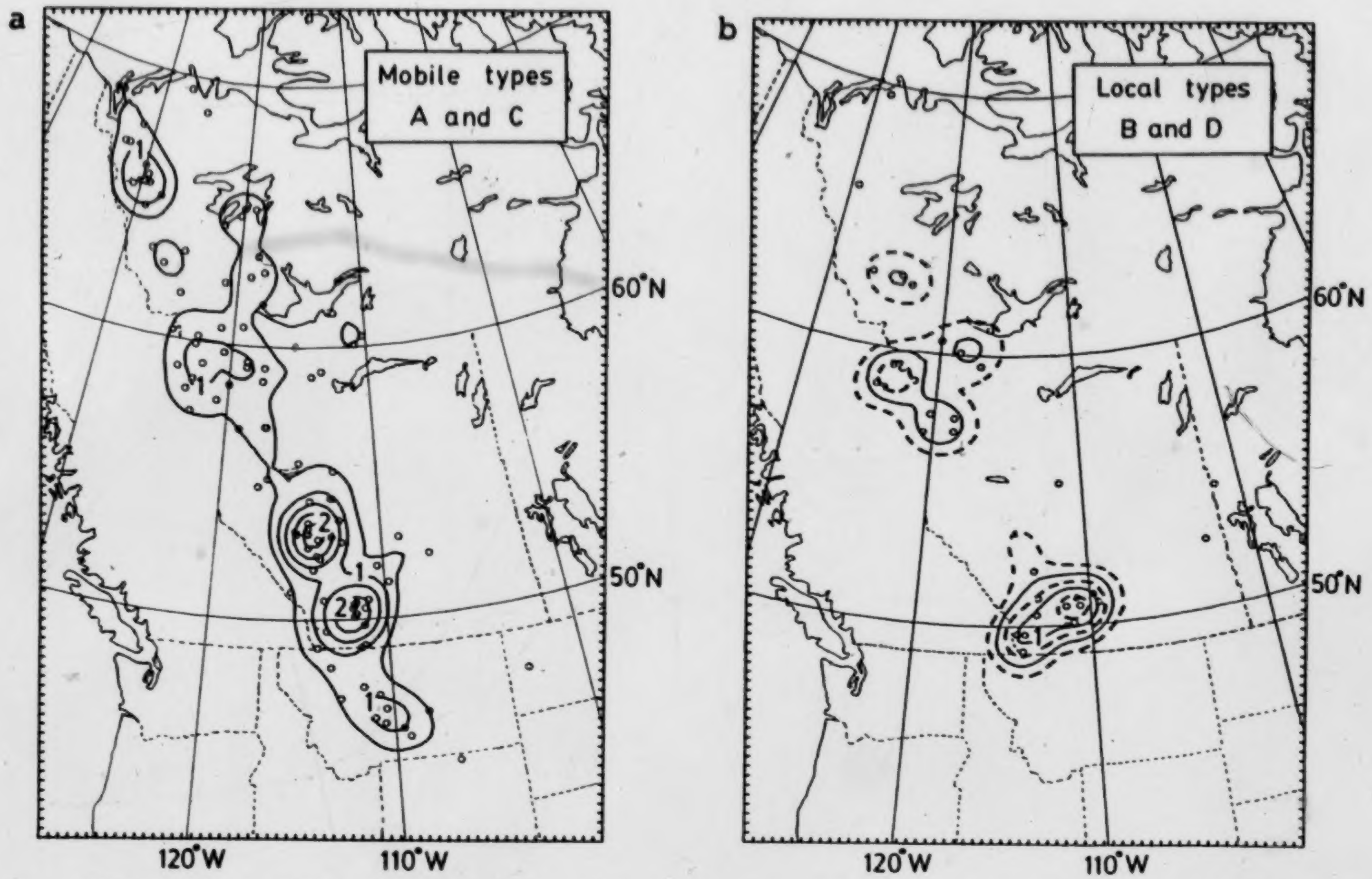
a
Mobile types
A and C
b
Local types
B and D
60°N
50°N
120°W
110°W
1
2
2.8

Figure 2. Contour maps of cyclogenesis events per unit area per unit time, in units of 10^{-6} km^{-2} yr^{-1}, using smoothing radius, ϵ=200 km, for mobile cyclones (Fig. 2a - 109 cases) and for local cyclones (Fig. 2b - 37 cases). The contour interval is 0.5 units in (a) and 0.25 units in (b). Contours 0.25, 0.75, and 1.25 appear dashed. All closed contours outline relative maxima.

lows in South-central Alberta and 7 or 8 in Southern Alberta in Fig. 2b. The actual counts in this figure are about 2 and 13, respectively.

The lee cyclones were classified in one additional way. Although he did not explicitly define the terms, Chung (1972) makes a distinction between lee cyclones that are associated with a 'parent' low on the upstream side of the barrier and those which seem to be independent developments. On his Figs. 14 through 17, trajectories are shown for the parent lows. Cases for which Chung did not include an upstream trajectory were classified as being without a parent cyclone. Examination of upper-air charts for the no-parent cases showed that the development of some of these lows occurred in association with travelling waves aloft. Apparently, however, the influence of these mid-level disturbances was not great enough to be detectable at the surface on the upstream side of the barrier. Of the 34 no-parent cases identified from Chung's data, 18 became migratory (9 of type A_1 and 9 of type C), but no detailed check was made to see if this motion was tied to the approach of an upper-level wave. Of the mobile no-parent cases that acquired appreciable intensity (the A_1 cases), 6 of these occurred north of 60°N, but, as yet, no particular significance has been attached to this.

The cyclogenesis frequency per unit area is shown in Figs. 3a and 3b for the 112 with-parent cases and 34 without-parent cases, respectively. Again note that the

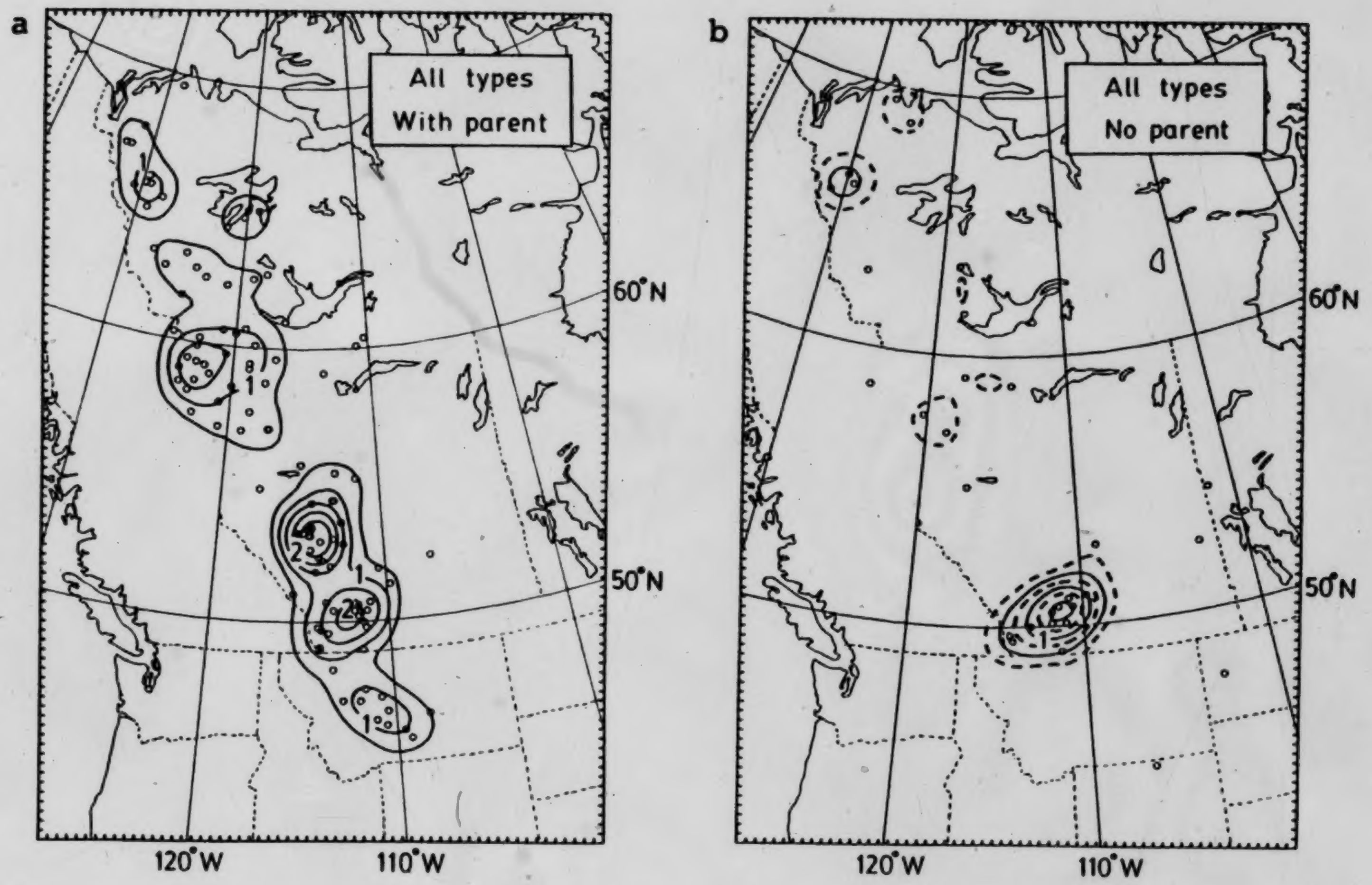
a
All types
With parent
60°N
50°N
120°W
110°W
1
2
b
All types
No parent
60°N
50°N
120°W
110°W
1

Figure 3. As in Fig. 2, except for cyclones with an upstream parent (Fig. 3a - 112 cases) and without a parent (Fig. 3b - 34 cases).

contour interval is not the same for the two parts of the figure. Even more clearly than in Fig. 2, the main feature that stands out as a result of the classification of the cyclones is the lack of a South-central Alberta maximum in the second half of the figure. Instead of the 4 or 5 lows that might be expected in this region on the basis of the proportion of no-parent lows to the total sample, no lows appear.

Chung (1972) has expressed the opinion that the maxima of lee cyclogenesis frequency in the South-central and Southern Alberta regions would probably merge given a larger data set. The results presented here, however, showing an unusual distribution of the local and no-parent types of lee cyclones, suggest that a closer look is warranted into the question of whether the separation into two maxima has a demonstrable physical basis. There are many factors which might contribute to a spatial variation in cyclogenesis frequency, including differences in surface friction, upstream terrain shape, and thermal effects. The upstream barrier profile is examined in Chapter 12 but no definite answer to the question considered here comes out of that analysis. With regard to thermal influences, note that Southeastern Alberta is significantly warmer (McKay, undated) and remains snow-free for a greater proportion of the winter season than the central part of the province. These factors would favour the maintainence of weak thermal lows in Southeastern Alberta through surface heating effects. Note, however, that if the separation of the frequency maxima is not an artifact of the small sample size then an explanation may be required for both the large number of no-parent and local lows in Southern Alberta and the unexpectedly low number in the South-central region.

It is hoped that future students will take up the task of clarifying these issues. It is recomended that particular attention be paid to identifying the positions of lee cyclones as early as possible in their lifecycle. The time of day that a low-pressure area first appears is a potentially useful datum, especially in the cases of weak lows, where solar heating or tidal influences could be important. An objective definition of whether or not a lee development is associated with a parent low would be helpful. It might prove necessary to classify the lows according to the degree of association with an upstream system. More emphasis on cyclolysis on the windward side of the barrier could ultimately provide insight into cyclogenetic processes in the lee.

CHAPTER 3

A STEADY, LINEAR, HYDROSTATIC, AIRFLOW MODEL

3.1 Introduction

The research summarized in the remainder of this thesis was motivated by a recent paper by Smith (1980). He applied linear, hydrostatic theory to the flow of stratified air over a mountain having a circular horizontal cross-section, and also to the flow near the end of a long ridge lying across the wind. In his discussion of the surface pressure and wind fields, Smith presented analytical results for the circular ('bell-shaped') barrier, but not for the ridge. In the present study it is shown that closed-form analytical solutions for the surface fields can also be obtained for mountains with elliptical horizontal cross-sections. This allows systematic exploration of some aspects of the transition between the fully three-dimensional circular barrier case and the two-dimensional limit of an infinitely-extended ridge, as the eccentricity of the elliptical cross-section is varied.

In addition to excluding nonlinear and non-hydrostatic effects, the theoretical model used here is restricted to inviscid, dry, steady flow over a non-rotating surface. A Boussinesq-type of approximation is also made. As a final simplification, the air far upstream of the barrier is assumed to have uniform velocity and temperature. Authors who have used a uniform incoming flow such as this in a linear model include Lyra (1943) and Queney (1947,1948) for two-dimensional barriers, and Wurtele (1957) and Crapper (1959) in three dimensions. As appears to be the case in much of the previous theory of mountain airflow, most of the simplifications in the present work were introduced to make the mathematics tractable. Note, however, that Blumen (1965), Klemp and Lilly (1975), and Blumen and McGregor (1976), for example, have shown that the wave amplitude and related wave drag are rather sensitive functions of the vertical profile of the upstream flow. One must bear this in mind when considering the results of this thesis, in which the vertical structure is very simple.

There is an extensive literature based on attempts to remove one or more of the restrictions implied by the above assumptions. One can refer to articles by Queney et al. (1960), Smith (1979a), and Klemp and Lilly (1980) for an overview, but some references are indicated in the following. Multilevel three-dimensional models, for non-hydrostatic, trapped waves, incorporating vertical variations of upstream wind speed and static stability have been studied by Sawyer (1962), Crapper (1962), and Marthinsen (1980). Blumen and McGregor (1976) and Blumen and Dietze (1981) incorporated horizontal wind shear in their hydrostatic models. Barcilon et al. (1979,1980) and Smith and Lin (1982), have considered the effect of moisture in two-dimensional models. In a particularly detailed numerical modelling study, Durran and Klemp (1983) found that the inclusion of moisture led to a significant reduction in the amplitude of mountain waves. The effect of the Earth's rotation on mesoscale waves was treated by Queney (1947,1948), Smith (1979b), and Somieski (1981). Nonlinear and time-dependent processes were incorporated into the numerical simulations of two-dimensional non-hydrostatic flows by Clark and Peltier (1977) and Peltier and Clark (1979), while the hydrostatic case was treated by Klemp and Lilly (1978). The effect of using nonlinear lower boundary conditions was also studied by Lilly and Klemp (1979).

Due to the neglect of the Earth's rotation, and of nonlinear and non-hydrostatic effects in the present model, there are certain restrictions on the vertical scale of the barrier, h, and the downwind horizontal scale, L, in relation to the incoming air speed, $\overline{U}$, and the static stability, (as measured by the Brunt-Väisälä frequency, $\overline{N}$). The rotation of the Earth is unimportant when the Rossby number, $\overline{U}/Lf \gg 1$, where f is the Coriolis parameter. The linearity and hydrostatic assumptions are expected to be applicable when $\overline{U}/h\overline{N} \gg 1$ and $\overline{U}/L\overline{N} \ll 1$, respectively. The reader is referred to Smith (1980) for a discussion of these criteria. Substituting typical mid-latitude, mid-tropospheric values of $\overline{U} = 10 \text{ m s}^{-1}$, $\overline{N} = 0.01 \text{ s}^{-1}$, and $f = 0.0001 \text{ s}^{-1}$, gives $h \ll 1 \text{ km} \ll L \ll 100 \text{ km}$. These can be regarded only as crude estimates of the limitations on the barrier dimensions. In practice there may be a somewhat greater range of applicability, depending on particular circumstances. For example, Queney (1948) suggested linear theory could be useful for 'any typical mountain range as high as 1 or 2 km, if its total width is not less than 10 km'.

The hydrostatic approximation is essential to the derivation of the analytical solutions to be presented, but, there is also a physical basis for an interest in the hydrostatic scales of motion with $\bar{N}L/\bar{U} \approx 10$. An important distinguishing feature of the hydrostatic mountain waves in the 10-100 km region is their efficiency in transporting energy and momentum vertically, as compared to waves of both smaller and larger horizontal scale (Klemp and Lilly, 1980). Non-hydrostatic effects are important for the production of extended trains of short lee waves and the transport of energy downstream, but are unnecessary complications when examining other aspects of mountain airflow. Vergeiner (1971) suggested that the severe downslope winds in the lee of the Rocky Mountains in Colorado are nearly hydrostatic in nature. Subsequent numerical simulations by Klemp and Lilly (1975) support this conclusion. Recently, Smith (1981) has applied the hydrostatic, linear theory to an analysis of the Hood Canal Bridge collapse in Washington State.

The equations of the model and integral expressions for the surface pressure and wind fields are given later in this chapter. Details of the particular type of elliptical terrain used are in Chapter 4. The analytical results for the surface pressure perturbation due to this topography are presented in Chapter 5. The deviation of the fully three-dimensional flow solution from one in which the air is confined to move in vertical planes is also examined. In Chapter 6, another effect of terrain shape on the pressure field is explored, as ridges having curvature in a horizontal plane are considered. Chapter 7 is devoted to a discussion of the transverse velocity perturbation and horizontal divergence caused by air forced to move laterally, around the ends of the barrier.

For the analytical work, extensive use has been made of the mathematical reference Gradshteyn and Ryzhik (1965). This is indicated as GR in the following. A standard reference for elliptic integrals is Byrd and Friedman (1971), which is abbreviated as BF.

3.2 Model equations and their solution

The inviscid, dry, steady flow assumed in this study is described by horizontal momentum, hydrostatic, continuity and adiabatic equations linearized about an isothermal upstream state having a constant speed, $\overline{U}$, in the +x direction. If u', v', and w' are the x, y, and z components, respectively, of the velocity perturbation to the incoming flow due to a mountain barrier, with ρ' and p' as the corresponding deviations from the upstream density, $\overline{\rho}$, and pressure, $\overline{p}$, then the model equations are

$$\overline{\rho}\,\overline{U}\,u'_x + p'_x = 0 \quad , \tag{3.1}$$

$$\overline{\rho}\,\overline{U}\,v'_x + p'_y = 0 \quad , \tag{3.2}$$

$$g\rho' + p'_z = 0 \quad , \tag{3.3}$$

$$\overline{\rho}\left(u'_x + v'_y + w'_z\right) + \delta_1\overline{U}\,\rho'_x + \delta_2\overline{\rho}_z\,w' = 0 \quad , \tag{3.4}$$

$$\delta_3\overline{U}\,p'_x + \overline{p}_z\,w' - \overline{c^2}\left(\overline{U}\,\rho'_x + \overline{\rho}_z\,w'\right) = 0 \quad . \tag{3.5}$$

The symbols δ_1, δ_2, and δ_3, which take the value 0 or 1 according to whether the corresponding terms in the equations are neglected or retained, have been introduced to facilitate an examination of the effect of certain approximations to be made later. The subscripts on the perturbation fields denote differentiation, g is the acceleration due to gravity (assumed constant), and $\overline{c}$ is the speed of sound in the undisturbed flow. The variables describing the mean flow are related by the hydrostatic equation, the ideal gas law and the definition of the speed of sound:

$$\overline{p}_z = -\,\overline{\rho}\,g \quad , \tag{3.6}$$

$$\overline{p} = \overline{\rho}\,R\,\overline{T} \quad , \tag{3.7}$$

$$\overline{c^2} = \gamma_o R\,\overline{T} \quad , \tag{3.8}$$

where $\overline{T}$ is the (constant) absolute temperature, $\gamma_0 \simeq 1.4$ is the ratio of specific heats and $R \simeq 287$ J kg^{-1} K^{-1} is the gas constant for dry air. If $\overline{\rho}_0$ is the density at z=0, then combining (3.6) and (3.7) gives

$$\overline{\rho} = \overline{\rho}_o \, e^{-z/\overline{H}_o} \quad , \tag{3.9}$$

where $\overline{H}_0 = R\overline{T}/g$ is the density scale height.

The system of governing equations (3.1-3.5) is to be solved subject to the constraint that the air follows the contours of the terrain at the lower boundary. For ease of applying this boundary condition, the vertical displacement, η, of a streamline from its upstream position, is introduced and related to the vertical velocity by a linearized Lagrangian derivative, as in Smith (1980):

$$w' = \frac{D\eta}{Dt} = \overline{U} \, \eta_x \quad . \tag{3.10}$$

At the terrain surface the vertical displacement of a streamline is equal to the terrain height, h, so $\eta(z=h)=h$. However, in this study, a linearized version of this equation is used:

$$\eta(z=0) = h \quad . \tag{3.11}$$

This boundary condition is applied to a wave equation for η which will now be derived.

Eliminating w' and ρ' from the adiabatic equation (3.5), using (3.3) and (3.10), gives

$$\delta_3 \frac{g}{c^2} p' + p_z' = - \overline{\rho} \, \overline{N^2} \eta \quad , \tag{3.12}$$

where

$$\overline{N^2} = -g \left(\frac{g}{c^2} + \frac{\overline{\rho}_z}{\overline{\rho}} \right) = \left(1 - \frac{1}{\gamma_o} \right) \frac{g}{\overline{H}_o} \tag{3.13}$$

is the square of the Brunt-Väisälä, or buoyancy, frequency.

The $g/\bar{c}^2$ term in $\bar{N}^2$ was neglected by Smith (1980) and by Wurtele (1957), who, however, arbitrarily restores it in his final results. It will be retained here, since $g/\bar{c}^2 = 1/\gamma_o\bar{H}_o$ does make a significant contribution to $\bar{N}^2$ in a compressible atmosphere. In addition, Smith (1980) neglects the $g/\bar{c}^2$ terms in (3.12) ($\delta_3=0$), although he indicates that the corresponding term in (3.5) is important for fast acoustic waves (Smith, 1979a). In mountain wave theory it is also common to make a Boussinesq approximation. This involves the neglect of the compressibilty terms in (3.4) ($\delta_1=\delta_2=0$) and of the vertical variation of $\bar{\rho}$ in all equations except the definition of buoyancy frequency (3.13). To follow the consequences of this approximation, write

$$\bar{\rho} = \bar{\rho}_o\, e^{-[\frac{z}{\bar{H}_o} \delta_4]} \qquad (3.14)$$

in place of (3.9), where δ_4 can take the value 0 or 1.

Next, differentiate the continuity equation (3.4) with respect to x and express the other variables in terms of p' using (3.1-3.3), (3.12) and (3.14), to give

$$p'_{xxzz} + \left\{ \frac{\delta_1 + \delta_4(1-\delta_2)}{\bar{H}_o} + (\delta_3-\delta_1)\frac{g}{\bar{c}^2} \right\} p'_{xxz} \qquad (3.15)$$
$$+ \frac{\delta_3\delta_4(1-\delta_2)}{\bar{H}_o}\frac{g}{\bar{c}^2}\, p'_{xx} + \frac{\bar{N}^2}{\bar{U}^2}\left(p'_{xx} + p'_{yy}\right) = 0 \ .$$

Operating with $\{\delta_3 g/\bar{c}^2 + \partial/\partial z\}$ on (3.15) and substituting from (3.12) and (3.14) gives an equation for η, to which the boundary condition (3.11) can be applied:

$$\begin{aligned} &\eta_{xxzz} + \left(\frac{\delta_1 - \delta_4(1+\delta_2)}{\overline{H}_o} + (\delta_3-\delta_1)\frac{g}{c^2} \right) \eta_{xxz} \\ &\quad + \frac{\delta_4}{\overline{H}_o} \left(\frac{(\delta_2\delta_4-\delta_1)}{\overline{H}_o} + (\delta_1-\delta_2\delta_3)\frac{g}{c^2} \right) \eta_{xx} + \frac{\overline{N}^2}{\overline{U}^2}\left(\eta_{xx} + \eta_{yy}\right) = 0 \quad . \end{aligned} \tag{3.16}$$

Examining (3.16), one finds that retention of all the terms ($\delta_1=\delta_2=\delta_3=\delta_4=1$) leads to exactly the same equation for η as obtained if one neglects the compressibility terms in the continuity equation ($\delta_1=\delta_2=0$) and the pressure fluctuation term in the adiabatic equation ($\delta_3=0$), while retaining the density stratification effects ($\delta_4=1$). A similar relationship between isothermal and incompressible models has been noted by Gossard and Hooke (1975, p. 77). They comment that 'the principal consequence of the assumption of incompressibilty is the absence of the acoustic solutions from the wave equation', so that an incompressible model 'contains much of the physics of wave motion in the (compressible) atmosphere'.

For the remainder of the thesis, attention is restricted to the simplified model in which density stratification and compressibility enter only through the buoyancy frequency, $\overline{N}$. Specifically, $\delta_1=\delta_2=\delta_3=\delta_4=0$ will be assumed throughout. In Appendix A, it is shown that retaining all the terms in the governing equations changes the pressure field by less than 10% of the maximum perturbation, in most circumstances.

To solve (3.16) for the vertical displacement, we employ the Fourier transform method used by Queney (1948) in two dimensions and by Wurtele (1957) and Smith (1980) in three. Using the notation of Smith, introduce the Fourier transform, $\hat{h}(k,\ell)$, of the terrain height, $h(x,y)$:

$$\hat{h}(k,\ell) = \frac{1}{4\pi^2} \int_{-\infty}^{\infty} \int_{-\infty}^{\infty} h(x,y)\, e^{-i(kx+\ell y)} dx\, dy \quad . \qquad (3.17)$$

Representing η in the form

$$\eta(x,y,z) = \int_{-\infty}^{\infty} \int_{-\infty}^{\infty} \hat{h}(k,\ell)\, e^{i(kx+\ell y+mz)} dk\, d\ell \quad , \qquad (3.18)$$

one finds that the boundary condition (3.11) and the wave equation (3.16) are satisfied, provided the vertical wave number, m, is determined as a function of k and ℓ by:

$$m = \pm \frac{\overline{N}}{\overline{U}} \frac{(k^2+\ell^2)^{\frac{1}{2}}}{k} \quad . \qquad (3.19)$$

The solution is thereby uniquely determined, except for the sign in the expression for m. As discussed by Smith (1979a), the + sign is the correct choice here since this corresponds to a propagation of wave energy upward from the mountain by each Fourier component. This 'radiation condition', as it is known, is appropriate for the present problem because there is no wave energy source at high levels in the model atmosphere, and the simple vertical structure of the upstream flow prevents reflection of upwardly propagating waves. The solution given by choosing the + sign is also the one that would be obtained in the large time limit of a time-dependent generalization of the present problem or one in which a small frictional force is introduced. See Crapper (1959) for more detail on this point.

In Appendix A, the adiabatic relation (3.12) is integrated with respect to z, to give the pressure perturbation. With $\delta_3=\delta_4=0$ in (A.2), one finds

$$p'(x,y,z) = i\,\bar{\rho}_o \bar{N}^2 \int_{-\infty}^{\infty}\int_{-\infty}^{\infty} \frac{\hat{h}(k,\ell)}{m(k,\ell)}\, e^{i(kx+\ell y+mz)}\, dk\, d\ell \quad , \qquad (3.20)$$

where $\bar{\rho}_0$ is the value of $\bar{\rho}(z)$ at z=0.

In calculations of the pressure and wind perturbations, values at the terrain surface, z=h(x,y), will be approximated by the corresponding values at z=0, in a manner similar to the linearization of the boundary condition (3.11). Consequently, the surface pressure perturbation is given by

$$p'(x,y) = i\,\bar{\rho}_o \bar{N}^2 \int_{-\infty}^{\infty}\int_{-\infty}^{\infty} \frac{\hat{h}(k,\ell)}{m(k,\ell)}\, e^{i(kx+\ell y)}\, dk\, d\ell \quad . \qquad (3.21)$$

The three-dimensional nature of the present problem enters the expression for p′ through the dependence of the terrain Fourier transform, $\hat{h}(k,\ell)$, and the vertical wave number, $m(k,\ell)$, on the lateral wave number, ℓ. In the special case of a ridge, h(x), infinitely-extended in the y direction, the wave motion is two-dimensional in the sense that it is confined to x-z planes and the surface pressure perturbation depends only on x. To confirm this, note that the terrain height Fourier transform simplifies in this case to

$$\hat{h}(k,\ell) = \tilde{h}(k)\;\delta(\ell) \quad ,$$

$$\tilde{h}(k) = \frac{1}{2\pi}\int_{-\infty}^{\infty} h(x)\, e^{-ikx}\, dx \quad , \qquad (3.22)$$

where $\delta(\ell)$ is a Dirac delta function, which is non-zero only for $\ell=0$ (see Byron and Fuller, 1969, p. 224, for example). Substituting this expression into (3.21), the ℓ integration can be done immediately to give the 'two-dimensional' solution

$$p'(x,y) = p'(x) = i\,\bar{\rho}_o \bar{N}^2 \int_{-\infty}^{\infty} \frac{\tilde{h}(k)}{m(k)}\, e^{ikx}\, dk \quad , \tag{3.23}$$

where, from (3.19) one has

$$m(k) = m(k,0) = \frac{\bar{N}}{\bar{U}}\, \mathrm{sign}(k) \quad . \tag{3.24}$$

Even if the terrain is fully three-dimensional, there are cases in which the motion occurs nearly in vertical planes, and the transverse perturbation velocity, v', is negligible. In such cases the ℓ dependence in $m(k,\ell)$ can also be neglected, so that the vertical wave number, m, again simplifies to the form (3.24). The surface pressure perturbation becomes

$$p'(x,y) = i\,\bar{\rho}_o \bar{N}^2 \int_{-\infty}^{\infty} \frac{\tilde{h}(k;y)}{m(k)}\, e^{ikx}\, dk \quad , \tag{3.25}$$

where the integration over ℓ in (3.21) has been performed and

$$\tilde{h}(k;y) = \frac{1}{2\pi} \int_{-\infty}^{\infty} h(x,y)\, e^{-ikx}\, dx \quad . \tag{3.26}$$

Unlike the infinite ridge case, p' still depends on both x and y because of the change in terrain cross-section with y. For any fixed lateral position, y = constant, however, the solution obtained is the same as for an infinitely-extended ridge having the same x-z cross-section. (Compare

(3.22-3.23) with (3.25-3.26)). The expression (3.25) will be termed the 'two-dimensional slice' approximation to the full three-dimensional solution.

Having obtained the pressure perturbation, p', one can derive various other quantities. For example, integration of (3.1) with respect to x, assuming that all perturbations vanish far upstream ($x=-\infty$), gives the x component of the velocity perturbation:

$$u'(x,y,z) = -\frac{p'(x,y,z)}{\bar{\rho}\,\bar{U}} \quad . \tag{3.27}$$

Similarly, from (3.2) and (3.20), one finds that the transverse velocity perturbation, v', is given by

$$\begin{aligned} v'(x,y,z) &= -\frac{1}{\bar{\rho}\,\bar{U}} \int_{-\infty}^{x} p_y(x',y,z)\,dx' \\ &= \frac{\bar{N}^2}{\bar{U}} \int_{-\infty}^{\infty}\int_{-\infty}^{\infty} \frac{\hat{h}(k,\ell)}{i\,m(k,\ell)}\,\frac{\ell}{k}\,e^{i(kx+\ell y+m(k,\ell)z)}\,dk\,d\ell \quad . \end{aligned} \tag{3.28}$$

An interesting expression for the surface perturbation $v'(x,y) = v'(x,y,z=0)$ can be obtained in the hydrostatic approximation using the result

$$\frac{m(k,\ell)}{\ell} = \frac{m(\ell,k)}{k} \quad , \tag{3.29}$$

which follows from (3.19). Using (3.29) in (3.28), interchanging the order of the integrations and relabelling the variables k and ℓ, gives

$$v'(x,y) = \frac{\bar{N}^2}{\bar{U}} \int_{-\infty}^{\infty}\int_{-\infty}^{\infty} \frac{\hat{h}(\ell,k)}{i\,m(k,\ell)}\,e^{i(ky+\ell x)}\,dk\,d\ell \quad . \tag{3.30}$$

Comparing (3.30) and (3.21) one sees that

$$v'(x,y) = -\frac{1}{\bar{\rho}_o \bar{U}} p_R'(y,x) \quad , \qquad (3.31)$$

where $p_R'(x,y)$ is the pressure perturbation due to a terrain field, $h_R(x,y)$, obtained from the original field, $h(x,y)$, by reflection about the line $x=y$:

$$h_R(x,y) = h(y,x) \quad . \qquad (3.32)$$

Some deductions about the transverse perturbation velocity, v', based on (3.31) are presented in Chapter 7.

From the first equality in (3.28), together with (3.27), it follows immediately that the vertical component of the perturbation vorticity, $\zeta=\partial v'/\partial x-\partial u'/\partial y$, is identically zero. The horizontal divergence, another combination of the derivatives of the velocity components, is considered in Chapter 7.

CHAPTER 4

ELLIPTICAL TERRAIN SHAPE

A variety of three-dimensional terrain forms have been used in mountain airflow studies, including an infinite plateau of finite crosswind extent by Wurtele (1957), a Gaussian hill with height $h(x,y) = h_0\exp(-x^2/a^2-y^2/b^2)$ by Crapper (1962) and Marthinsen (1980), and the 'circular' hill with $h(x,y) = h_0[1+(x^2+y^2)/a^2]^{-3/2}$ employed by Crapper (1959) and Smith (1980). Recently, Blumen and Dietze (1981) have studied a class of barrier which includes considerable variation in planform, from quasi-circular to quasi-elliptical. The mountain shape used for much of the present work allows a similar flexibility, but has terrain height contours which are exact ellipses of arbitrary eccentricity. Specifically, we choose the terrain height field as

$$h(x,y) = \frac{h_0}{\left[1 + \left(\frac{x}{a}\right)^2 + \left(\frac{y}{b}\right)^2\right]^{\mu}} , \qquad (4.1)$$

where h_0, a, b, and μ are constant parameters. Note that a=b, μ=3/2 corresponds to the terrain of Crapper and of Smith mentioned above, while a=b, μ=1/2 was studied by Palm (1958). Clark and Gall (1982) used the elliptical case (a≠b), with μ=1, in their numerical experiments on airflow over Elk Mountain, Wyoming. The special case b=∞, μ=1 gives the two-dimensional ridge introduced by Queney (1947,1948) and used by Vergeiner (1971), Smith (1976), and others.

When the analytical portion of this thesis was initiated, a mountain shape different from (4.1) had been chosen:

$$h(x,y) = \frac{h_o}{\left[1 + \left(\frac{x}{a}\right)^2\right] \left[1 + \left(\frac{y}{b}\right)^2\right]} \quad . \tag{4.2}$$

The separable form of (4.2) is a slight convenience, but, in general, the derivation of solutions for the surface pressure perturbation involves about the same amount of algebraic manipulation as for (4.1). It should be noted, however, that use of (4.1) leads to expressions containing elliptic integrals, whereas (4.2) does not. See Appendix E for analytical results pertaining to (4.2). Because (4.1) seemed a better representation of naturally occurring terrain and includes cases appearing in previous research, it was used more extensively than (4.2) in the current work.

At times it will be convenient to use dimensionless variables, scaled by the terrain amplitude, h_o, and the parameters, a and b, controlling the decay of the barrier height in the x and y directions, respectively. Define dimensionless Cartesian coordinates, (X,Y), and elliptical polar coordinates, (R,θ), by

$$\left.\begin{aligned} R &= (X^2+Y^2)^{\frac{1}{2}} \quad , \\ X = \frac{x}{a} = R\cos\theta \quad &, \quad Y = \frac{y}{b} = R\sin\theta \quad . \end{aligned}\right\} \tag{4.3}$$

Dimensionless forms for the terrain-height Fourier transforms and pressure integrals of Chapter 3, based on (4.3) and analogous quantities in wave number space (4.9), are summarized in Appendix B. Using (4.3) in (4.1) gives a normalized terrain height:

$$H(R) = \frac{h(x,y)}{h_0} = \frac{1}{\left(1 + R^2\right)^{\mu}} \quad . \tag{4.4}$$

The terrain height contours are the ellipses R=constant. The eccentricity, ϵ, of these contours is given by

$$\epsilon = \begin{cases} \left(1 - \gamma^2\right)^{1/2} & , \gamma \leq 1 \\ \left(1 - \frac{1}{\gamma^2}\right)^{1/2} & , \gamma \geq 1 \quad . \end{cases} \tag{4.5}$$

where $\gamma=a/b$ is the ratio of the horizontal scaling lengths.

The parameter μ appearing in (4.4) specifies the rate at which the height declines with distance far from the barrier peak. It will be termed the terrain exponent. However, μ is also related to the extent to which the mountain is broad or peaked and, therefore, could be considered as a measure of terrain steepness. For example, one finds that the maximum terrain slope, along the Y=0 axis, occurs at $|X|=(2\mu+1)^{-1/2}$ and its magnitude goes as $\mu^{-1/2}$ for $\mu>>1$. As μ increases, the characteristic size of the barrier, as measured by the half-width at maximum slope, also behaves as $\mu^{-1/2}$ and the hill becomes steeper and more sharply peaked. Although calculations are performed for general μ where convenient, some of the more complicated results are obtained only for the particular values $\mu=1/2$, 1, 3/2, and 2. A vertical cross-section of terrain as a function of X along Y=0 for these four μ values is shown in Fig. 4.

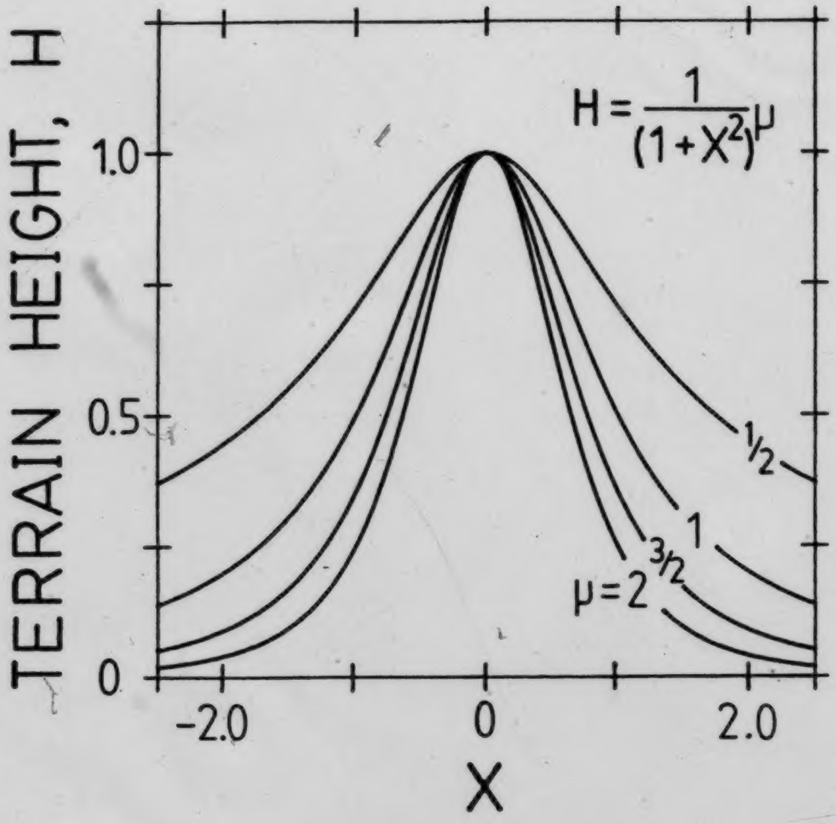

Figure 4. Normalized terrain height, $H=1/(1+X^2)^\mu$, vs. dimensionless position, $X=x/a$, along $Y=0$, for terrain exponent $\mu=1/2$, 1, 3/2, and 2.

Calculations of the x-z cross-sectional area of the terrain, A(y), and the mountain volume, V, show that the cases $\mu=1/2$ and $\mu=1$ have special significance. The cross-sectional area is defined by

$$A(y) = \int_{-\infty}^{\infty} h(x,y)\,dx = a\,h_0 \int_{-\infty}^{\infty} \frac{dX}{(1 + X^2 + Y^2)^{\mu}} ,$$

$$= \frac{\Gamma(1/2)\,\Gamma(\mu-1/2)}{\Gamma(\mu)} \frac{a\,h_0}{(1 + Y^2)^{\mu-1/2}} , \quad (\mu > 1/2). \qquad (4.6)$$

where the second form, involving gamma functions, can be obtained from standard integral tables, such as GR (p. 295). Note that the cross-section has infinite area in the case $\mu=1/2$, whereas it is finite for the larger values of μ.

Similarly, one finds that $\mu=1$ is the largest value of μ for which the terrain volume is not finite. Specifically, V is given by

$$V = \int_{-\infty}^{\infty}\int_{-\infty}^{\infty} h(x,y)\,dx\,dy = h_0 ab \int_{0}^{2\pi}\int_{0}^{\infty} R\,H(R)\,dR\,d\theta \quad . \qquad (4.7)$$

where the dimensionless variables (4.3) have been used in the second expression. The integration is easily done to obtain

$$V = \frac{\pi}{\mu-1} h_0 ab \quad , (\mu > 1) \quad . \qquad (4.8)$$

Therefore, the terrain for the $\mu=1/2$ case has infinite cross-sectional area and volume, the $\mu=1$ case gives a finite cross-section but infinite volume, whereas in the $\mu=3/2$ and

$\mu=2$ cases both quantities are finite.

In the calculation of the surface pressure perturbation, as given by (3.21), the Fourier transform of the height field is required. Consider the general case of terrain with elliptical height contours, so that $h(x,y) = h_o H(R)$, where $H(R)$ is an arbitrary positive function of the radial elliptical polar coordinate. Introducing the dimensionless wave number variables

$$\left.\begin{array}{c} \rho = (\kappa^2+\lambda^2)^{\frac{1}{2}} \quad , \\ \kappa = ka = \rho\cos\phi \quad , \quad \lambda = \ell b = \rho\sin\phi \quad . \end{array}\right\} \tag{4.9}$$

and transforming (3.17) to the (R,θ) coordinates, one finds that the terrain Fourier transform is a function, $\hat{H}(\rho)$, of the wave number magnitude, ρ, alone:

$$\begin{aligned} \hat{H}(\rho) = \frac{\hat{h}(k,\ell)}{h_0 ab} &= \frac{1}{4\pi^2}\int_0^{2\pi}\int_0^{\infty} H(R)\, e^{-i\rho R\cos(\theta-\phi)}\, R\, dR\, d\theta \quad , \\ &= \frac{1}{2\pi}\int_0^{\infty} R\, H(R)\, J_0(\rho R)\, dR \quad , \end{aligned} \tag{4.10}$$

where the θ integration has been done (GR, p. 953), giving rise to the Bessel function, J_o.

Specializing again to the particular height field given by (4.4), the remaining integral in (4.10) can be evaluated (GR, p. 686) to give

$$\hat{H}(\rho) = \frac{1}{2\pi}\left(\frac{\rho}{2}\right)^{\mu-1}\frac{K_{\mu-1}(\rho)}{\Gamma(\mu)} \quad , \quad (\mu > \tfrac{1}{2}) \quad , \tag{4.11}$$

where $K_{\mu-1}(\rho)$ is a Bessel function of imaginary argument.

In Table 2 of Appendix D, explicit expressions are given for $\hat{H}(\rho)$ for other terrain shapes.

Fig. 5 shows the normalized Fourier transform, $\hat{H}(\rho)$, as a function of ρ for the cases $\mu=1/2$, 1, 3/2, and 2. The flattening of the curves as μ increases reflects the fact that the terrain is more peaked for large μ, and the low wave numbers become less important. From the properties of Bessel functions (Abramowitz and Stegun, 1965, p. 375) one can show that as $\rho \to 0$, $\hat{H}(\rho)$ becomes infinite like $(2\pi\rho)^{-1}$ for $\mu=1/2$ and like $-(\ln\rho)/2\pi$ for $\mu=1$. This singular behaviour is closely related to the result that the terrain volume, V, is infinite for these cases. Comparing (4.7) and (4.10), one sees that $\hat{H}(0)=V/(4\pi^2 h_0 ab)$. In a similar manner, the terrain-height Fourier transform, $\tilde{h}(k;y)$, involved in the two-dimensional slice approximation, is related to the terrain cross-sectional area, A, by $\tilde{h}(0;y)=A(y)/2\pi$. This is shown by comparing (3.26) and (4.6).

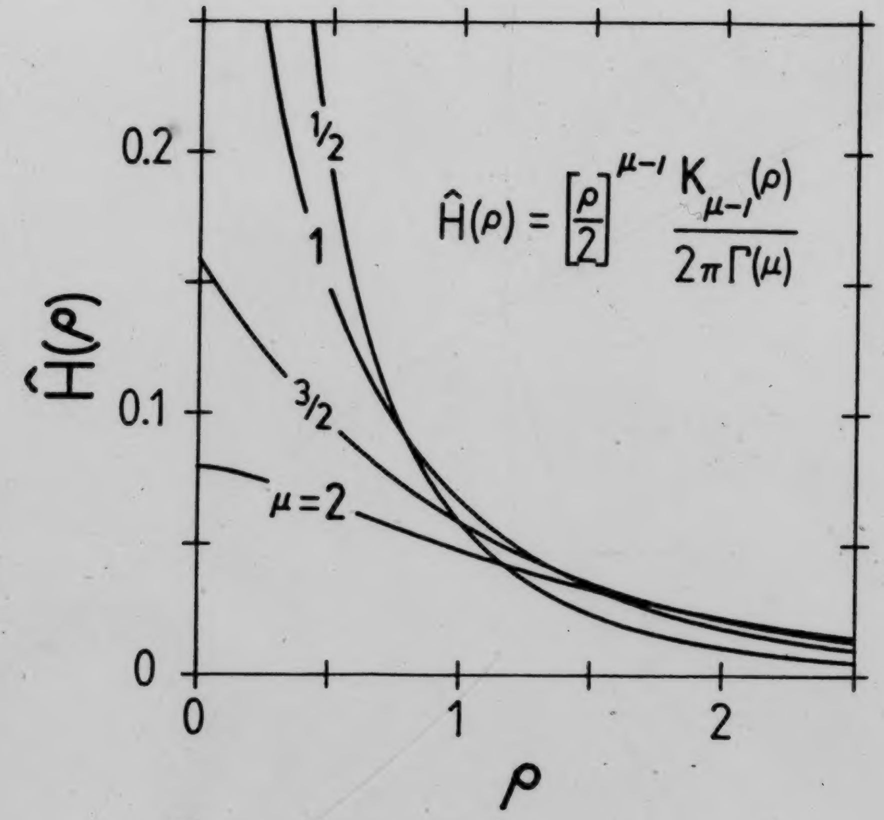

Figure 5. Normalized terrain height Fourier transform, $\hat{H}(\rho)$, vs. dimensionless radial wave number, ρ, for terrain exponent $\mu=1/2$, 1, 3/2, and 2. For $\mu=1/2$ and 1, $\hat{H}(0)$ is infinite.

CHAPTER 5

ANALYTICAL SURFACE PRESSURE PERTURBATION

5.1 Three-dimensional flow

Analytical results for the surface pressure perturbation, p', given by (3.21), are derived in this section for the terrain shape (4.1). The dependence of the pressure field on the horizontal scaling lengths, a and b, of the terrain, is discussed. The transition from two-dimensional flow over an infinitely-extended ridge to the three-dimensional flow over a circular barrier is considered.

For any elliptical terrain, $h(x,y) = h_0 H(R)$, the normalized Fourier transform, $\hat{H}(\rho)$, of the height field is a function only of the radial wave number coordinate, ρ, defined in (4.9). Therefore, it is convenient to transform the double integral (3.21) to polar coordinates, (ρ,ϕ). Using the hydrostatic vertical wave number expression (3.19), one obtains a dimensionless surface pressure perturbation, $P_3(X,Y)$, given by

$$P_3(X,Y) = \frac{p'(x,y)}{\bar{\rho}_o \bar{U}\,\bar{N}\,h_o} = i \int_0^{2\pi} \int_0^{\infty} \frac{\cos\phi \; e^{i\rho R\cos(\phi-\theta)}}{(\cos^2\phi+\gamma^2\sin^2\phi)^{\frac{1}{2}}}\, \rho\, \hat{H}(\rho)\, d\rho\, d\phi \quad , \qquad (5.1)$$

where $X=R\cos\theta$, $Y=R\sin\theta$, and $\gamma=a/b$. With $\bar{\rho}_0 = 1$ kg m^{-3}, $\bar{N} = 0.01$ s^{-1}, $\bar{U} = 10$ m s^{-1}, and $h_0 = 1$ km, the normalization factor $\bar{\rho}_0 \bar{U}\,\bar{N}\,h_0 = 100$ Pa (= 1 mb).

There are two special barriers for which an exact analytical result can be found for the ϕ integral, namely an infinitely-extended ridge and a hill of circular horizontal cross-section. In the ridge case, which corresponds to $b \to \infty$ in (4.1), the terrain height depends only on X, since $Y = y/b \to 0$ for finite y. Also, $\gamma = a/b \to 0$ so that the ϕ integral to be evaluated is

$$\int_0^{2\pi} \operatorname{sign}(\cos\phi)\, e^{i\rho X\cos\phi}\, d\phi \quad . \tag{5.2}$$

Using some symmetry arguments the integral reduces to

$$4i \int_0^{\pi/2} \sin(\rho X\cos\phi)\, d\phi = 2\pi i\, H_0(\rho X) \quad , \tag{5.3}$$

where the last form is given in GR (p. 402) and H_0 is a Struve function. Therefore, the normalized pressure perturbation, $P_3(X,Y)$, for the two-dimensional ridge case, which will be denoted by $P_2(X)$, is given by

$$P_2(X) = -2\pi \int_0^{\infty} \rho\, H_0(\rho X)\, \hat{H}(\rho)\, d\rho \quad . \tag{5.4}$$

The other special case to be considered is that in which $\gamma=1$ (a=b) so that the hill is circular in horizontal cross-section. The ϕ integral becomes

$$\int_0^{2\pi} \cos\phi\, e^{i\rho R\cos(\phi-\theta)}\, d\phi \quad . \tag{5.5}$$

Making the change of variable, $\phi=\theta+\xi$, and examining the periodicity properties of the integrand, one can show from

GR (p. 402) that (5.5) reduces to

$$2i \cos\theta \int_0^{\pi} \cos\xi \sin(\rho R\cos\xi)\, d\xi = 2\pi i \cos\theta\, J_1(\rho R) \quad , \qquad (5.6)$$

where J_1 is a Bessel function. Denoting the normalized pressure perturbation for the circular barrier case by $P_{3C}(X,Y)$, and using (5.6) in (5.1), gives

$$P_{3C}(X,Y) = -2\pi \cos\theta \int_0^{\infty} \rho\, J_1(\rho R)\, \hat{H}(\rho)\, d\rho \quad . \qquad (5.7)$$

To make further progress we now restrict attention to the particular terrain shape (4.1) having a normalized Fourier transform, $\hat{H}(\rho)$, given by (4.11). Other barrier profiles are treated in Appendix D. The surface pressure perturbation for the infinite ridge, the two-dimensional slice approximation for an elliptical barrier, and the full three-dimensional flow solution for the circular barrier case can all be obtained in a straightforward manner.

Substituting (4.11) into the integral (5.4) for the ridge case gives

$$P_2(X) = -\frac{\Gamma(\mu+1/2)}{\Gamma(3/2)\,\Gamma(\mu)}\, X\, F(1,\mu+\tfrac{1}{2};\tfrac{3}{2};-X^2) \quad , \qquad (5.8)$$

using a result from GR (p. 781), where $F(\alpha,\beta;\gamma;z)$ is a hypergeometric function. As it stands, (5.8) is useful only for $|X|<1$, but transformation formulae, such as given in GR (p. 1043), allow one to obtain expressions valid for all X. For example,

$$F(1,\mu+\tfrac{1}{2};\tfrac{3}{2};-X^2) = \frac{1}{1+X^2}\, F(1,1-\mu;\tfrac{3}{2};\tfrac{X^2}{1+X^2}) \quad . \tag{5.9}$$

In the particular cases where μ is half of a positive integer, the hypergeometric function can be reduced to a combination of elementary functions. The resulting expressions for $\mu=1/2$, 1, 3/2, and 2 are given in Table 4 of Appendix D, along with the position and magnitude of the maximum pressure perturbation. Fig. 6 shows the pressure perturbation as a function of X for these same values of μ. As indicated in Chapter 4, as μ increases the barrier becomes more sharply peaked and its width effectively decreases. This is reflected in the results for the pressure perturbation. From Table 4 or Fig. 6 one can see that, as μ increases, the extreme pressure perturbation increases in magnitude and shifts toward the barrier.

The normalized surface pressure perturbation for the two-dimensional slice flow, denoted by $P_{2S}(X,Y)$, can be obtained from the infinite-ridge solution by some simple transformations in (3.25) and (3.26). One obtains

$$P_{2S}(X,Y) = \frac{1}{(1+Y^2)^{\mu}}\, P_2\left[\frac{X}{(1+Y^2)^{\frac{1}{2}}}\right] \quad . \tag{5.10}$$

Using (5.8)-(5.10) gives

$$P_{2S}(X,Y) = -\,\frac{\Gamma(\mu+1/2)}{\Gamma(3/2)\,\Gamma(\mu)}\;\frac{X}{(1+Y^2)^{\mu-\frac{1}{2}}\,(1+R^2)}\;F(1,1-\mu;\tfrac{3}{2};\tfrac{X^2}{1+R^2}) \quad . \tag{5.11}$$

Note $P_{2S}(X,0) = P_2(X)$ so Fig. 6 applies equally well to the

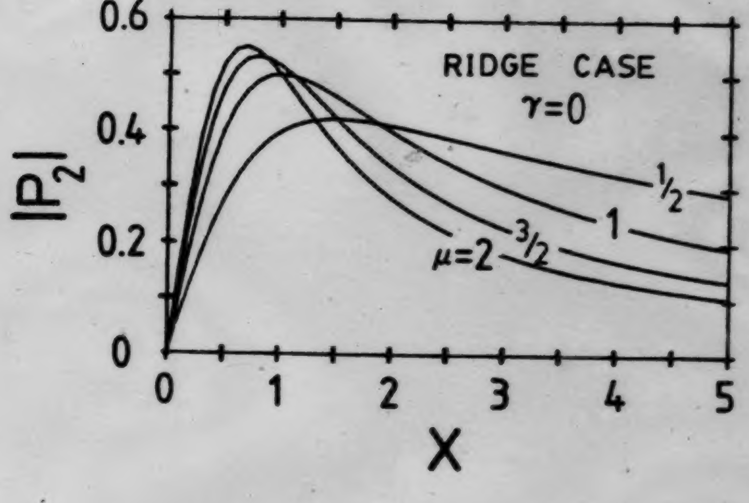

Figure 6. Magnitude of the normalized surface pressure perturbation, $|P_2(X)|$, for flow over an infinitely-extended ridge with the vertical cross-section shown in Fig. 4, vs. dimensionless position, $X=x/a$, for terrain exponent $\mu=1/2$, 1, 3/2, and 2.

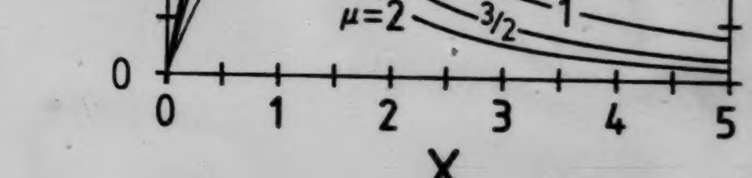

Figure 7. As in Fig. 6, except showing the magnitude of the normalized surface pressure perturbation, $|P_{3c}(X,Y)|$, along $Y=0$, for flow over an isolated circular hill.

two-dimensional slice flow along Y=0 and to the corresponding infinite ridge. An example of the full X-Y variation of $P_{2S}(X,Y)$ will be discussed later in this section.

Next consider the circular barrier case. Substituting (4.11) into (5.7), using an integral tabulated in GR (p. 693), gives the normalized pressure perturbation

$$P_{3C}(X,Y) = -\frac{\Gamma(\mu+1/2)\ \Gamma(3/2)}{\Gamma(\mu)}\ X\ F(\tfrac{3}{2},\mu+\tfrac{1}{2};2;-R^2)$$

$$= -\frac{\Gamma(\mu+1/2)\ \Gamma(3/2)}{\Gamma(\mu)}\ \frac{X}{(1+R^2)^{3/2}}\ F(\tfrac{3}{2},\tfrac{3}{2}-\mu;2;\tfrac{R^2}{1+R^2}) \quad . \tag{5.12}$$

Table 5 in Appendix D gives the functional form for $P_{3C}(X,Y)$ in the special cases μ=1/2, 1, 3/2, and 2. Note that the result for μ=3/2 agrees with that given by Smith (1980). The extreme value of the pressure perturbation is found to lie along the Y=0 axis. This value and the X coordinate at which it occurs are also given in Table 5. Fig. 7 shows the full variation with X along Y=0. Comparing Figs. 6 and 7, it is seen that the variation with the terrain exponent, μ, is qualitatively similar in the infinite ridge and circular hill cases. However, for a fixed value of μ the maximum value of the hydrostatic pressure perturbation is nearly 30% lower for the circular hill case than for the ridge case. In contrast, for non-hydrostatic waves, Crapper (1959) found that, under some conditions, the circular barrier can produce waves of greater amplitude along Y=0 than an infinite ridge of the same vertical cross-section.

Now return to (5.1) and consider the solution in the general elliptical case, where the ratio of the horizontal length scales, γ, is not restricted to 0 or 1. In this case, a closed-form result for the ϕ integration has not been found, although symmetry arguments can be made to show that the imaginary part of P_3 vanishes. If attention is restricted to the terrain shape (4.1), then the ρ integration can be done first and the ϕ integration completed afterwards. Expanding the exponential in (5.1) and substituting for $\hat{H}(\rho)$ from (4.11) allows the ρ integral to be written as

$$\int_0^\infty \sin\bigl(\rho R\cos(\phi-\theta)\bigr)\, \rho\hat{H}(\rho)\, d\rho = \frac{1}{\pi 2^\mu \Gamma(\mu)} \int_0^\infty \rho^\mu K_{\mu-1}(\rho) \sin\bigl(\rho R\cos(\phi-\theta)\bigr)\, d\rho$$

$$= \frac{\Gamma(\mu+1/2)}{4\,\Gamma(3/2)\,\Gamma(\mu)} \frac{R\cos(\phi-\theta)}{\bigl(1+R^2\cos^2(\phi-\theta)\bigr)^{\mu+\frac{1}{2}}} , \qquad (5.13)$$

where the last form is obtained from GR (p. 749). From (5.1) one then finds

$$P_3(X,Y) = -\frac{\Gamma(\mu+1/2)}{4\,\Gamma(3/2)\,\Gamma(\mu)} R \int_0^{2\pi} \frac{\cos(\phi-\theta)\cos\phi}{\bigl(1+R^2\cos^2(\phi-\theta)\bigr)^{\mu+\frac{1}{2}} (\cos^2\phi+\gamma^2\sin^2\phi)^{\frac{1}{2}}}\, d\phi . \qquad (5.14)$$

The ϕ integration can be done analytically in terms of elliptic integrals if μ is half a positive integer. Explicit expressions for the cases μ=1/2, 1, 3/2, and 2 are presented in Appendix D.

As a typical example of the surface pressure field obtained in this model, some results for the μ=2 case are shown in Fig. 8. In Fig. 8a, the upstream flow is perpendicular to the major axis of the ellipse ($\gamma=1/2$), whereas in Fig. 8b it is parallel ($\gamma=2$). In both cases the pressure field is antisymmetric about the X=0 axis with high pressure on the upstream side of the barrier and low pressure downstream. However, the extreme pressure perturbation is about 1.5 times larger when the long axis of the ridge is perpendicular to the incoming stream, than when it is parallel. The extreme perturbations are found to lie on the Y=0 axis in both cases, with the maximum pressure gradient occurring directly over the barrier at X=Y=0. An analytical expression for the maximum pressure gradient as a function of the terrain exponent, eccentricity, and orientation is presented in Appendix F. From (F.6), one finds the maximum gradient is over 2.8 times larger in the case of Fig. 8a than in Fig. 8b.

From the results for the barriers of Figs. 8a and 8b, one can easily derive the pressure field for a hill with an intermediate orientation, such as is shown in Fig. 8c. In this example, the barrier of Fig. 8a has been rotated counterclockwise by 45°. To obtain the pressure field, $P_{ROT}(X,Y)$, for a rotated barrier, one resolves the upstream velocity into two perpendicular components (for example, along the symmetry axes of the elliptical terrain) and sums the pressure field corresponding to each component. If ψ is the (counterclockwise) angle through which the barrier has been rotated, then

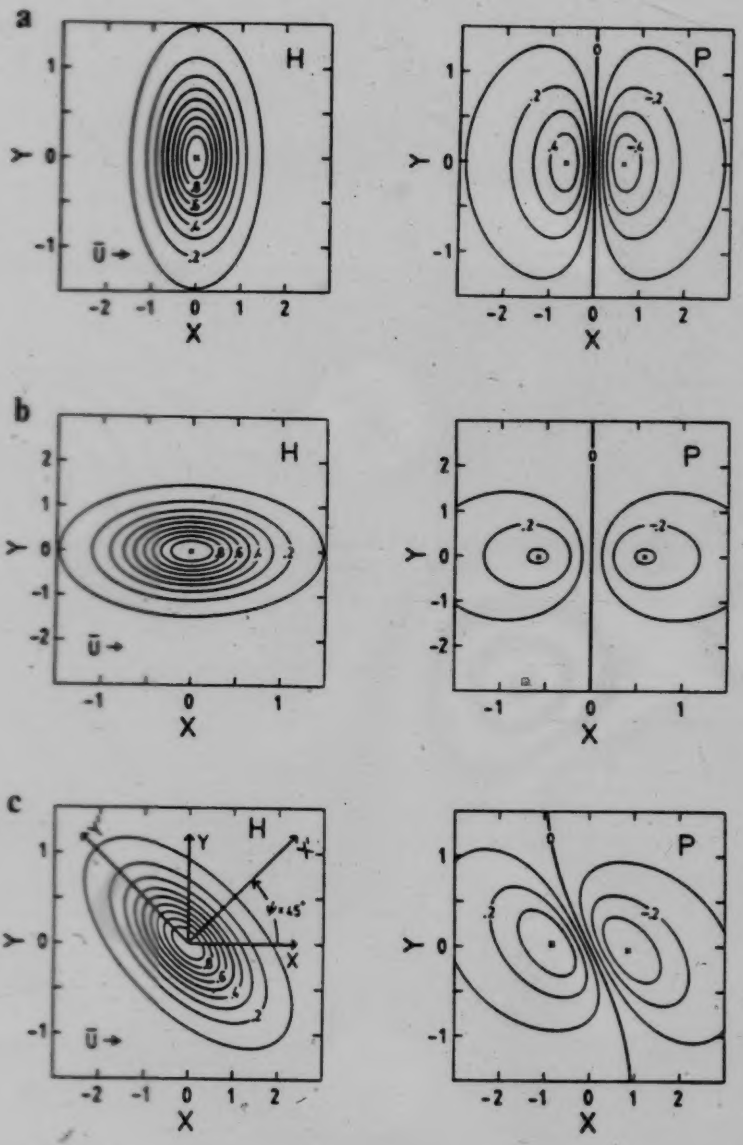

Figure 8. Contours of normalized surface pressure perturbation, $P_3(X,Y)$, (right panels) and terrain height, $H(X,Y)$, (left panels) for terrain exponent $\mu=2$, and horizontal scale ratio $\gamma=1/2$ (Figs. 8a and 8c) and $\gamma=2$ (Fig. 8b). Fig. 8c shows a rotated barrier case with $\psi=45°$. The mean wind, $\bar{U}$, is from left to right. Axes are labelled by dimensionless coordinates, (X,Y), but each figure shows the same physical area. The extreme perturbations, and their positions, indicated by the small crosses, are $\pm P_3$ = .470, .309 and .400, at $\mp(X,Y)$ = (.636,0.), (.583,0.) and (.826,-.030), for Figs. 8a, 8b and 8c, respectively.

$$P_{ROT}(X,Y) = \cos\psi \; P_3(X',Y';\gamma) + \sin\psi \; P_3(-Y',X';\tfrac{1}{\gamma}) \quad , \qquad (5.15)$$

where $P_3(X=x/a, Y=y/b; \gamma=a/b)$ is the normalized pressure field for an 'unrotated' barrier, with a and b measured along the x and y axes, respectively. Here

$$\left.\begin{aligned} X' &= x'/a = X\cos\psi + \frac{Y}{\gamma}\sin\psi \\ Y' &= y'/b = -\gamma X\sin\psi + Y\cos\psi \end{aligned}\right\} \qquad (5.16)$$

are normalized coordinates along the x′ and y′ axes shown in Fig. 8c. In this figure it is seen that there is some tendency for the pressure pattern to 'rotate with the barrier', but through a smaller angle. The pressure contours near the origin (X=Y=0), for example, are no longer aligned with an axis of the barrier, as in Figs. 8a and 8b. In Appendix F, an expression is derived for the orientation of the zero pressure perturbation contour at the origin for an arbitrary elliptical barrier, $h(x,y) = h_0H(R)$. The result is independent of the function H, depending only on the orientation of the barrier and its eccentricity. For the case of Fig. 8c, for example, it is calculated from (F.7) that this contour makes an angle of 25.6° with respect to the Y axis.

Another feature to note about the pressure perturbation field for the 45° rotated barrier is that the extreme values do not occur exactly along the Y=0 axis as in Figs. 8a and 8b, but are displaced slightly into the second and fourth quadrants. This displacement is more pronounced for barriers with large eccentricity.

5.2 Two-dimensional slice flow

To highlight the properties of flow around a three-dimensional barrier, the surface pressure field for an isolated elliptical mountain is compared to the 'two-dimensional slice' flow introduced in Chapter 3. In the latter case the pressure is calculated as if the air moved in vertical planes over a barrier of the same x-z cross-section but infinitely-extended in the Y direction. Figs. 9 and 10 show normalized fields of the terrain height, H, given by (4.4), surface pressure perturbation for three-dimensional flow, P_3, calculated from (5.1), that for two-dimensional slice flow, P_{2S}, from (5.10) and their difference P_3-P_{2S}. In Fig. 9, the ratio of the characteristic distances a and b, in the x and y directions, respectively, is $\gamma=1/2$, whereas in Fig. 10 the width of the barrier has been halved, so $\gamma=1/4$. Results are presented here for $\mu=3/2$ only, but those obtained for $\mu=1/2$, 1, and 2 are qualitatively similar. The axes in the figures are scaled so that the same dimensional distance is shown in the x and y directions, but the labelling is in terms of the normalized coordinates, $X=x/a$ and $Y=y/b$. All diagrams are restricted to the quadrant $X\geq0$, $Y\geq0$, but no information is lost because the pressure fields are symmetric in Y and antisymmetric in X.

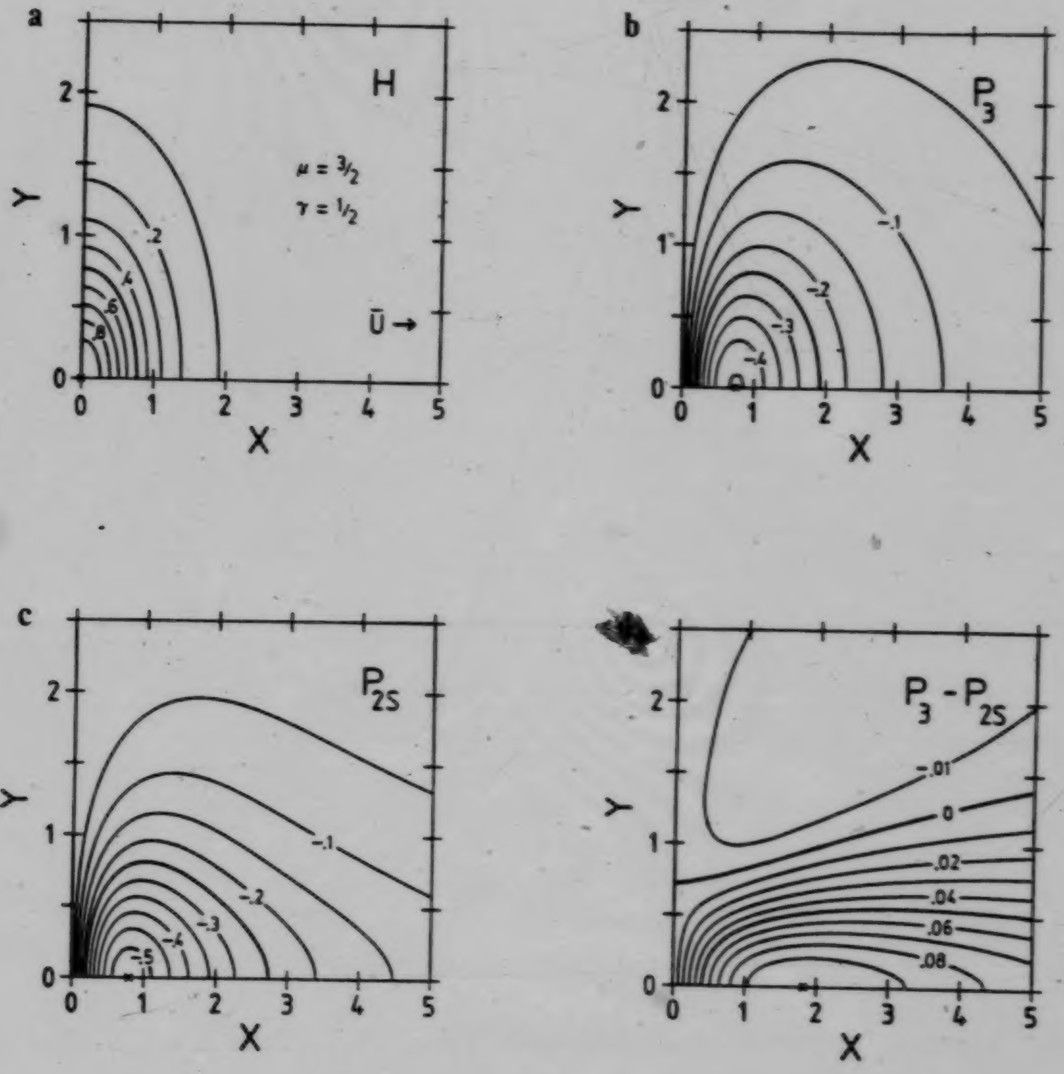

Figure 9. Contours of normalized terrain height, H, for $\mu=3/2$ and $\gamma=1/2$ (Fig 9a), three-dimensional flow pressure perturbation, P_3 (Fig. 9b), two-dimensional slice flow pressure perturbation, P_{2s} (Fig. 9c), and the difference, P_3-P_{2s} (Fig. 9d). The extreme values of P_3, P_{2s} and P_3-P_{2s} are -.454, -.533 and .100, and occur along $Y=0$ at $X = .740$, .797 and 1.80, respectively.

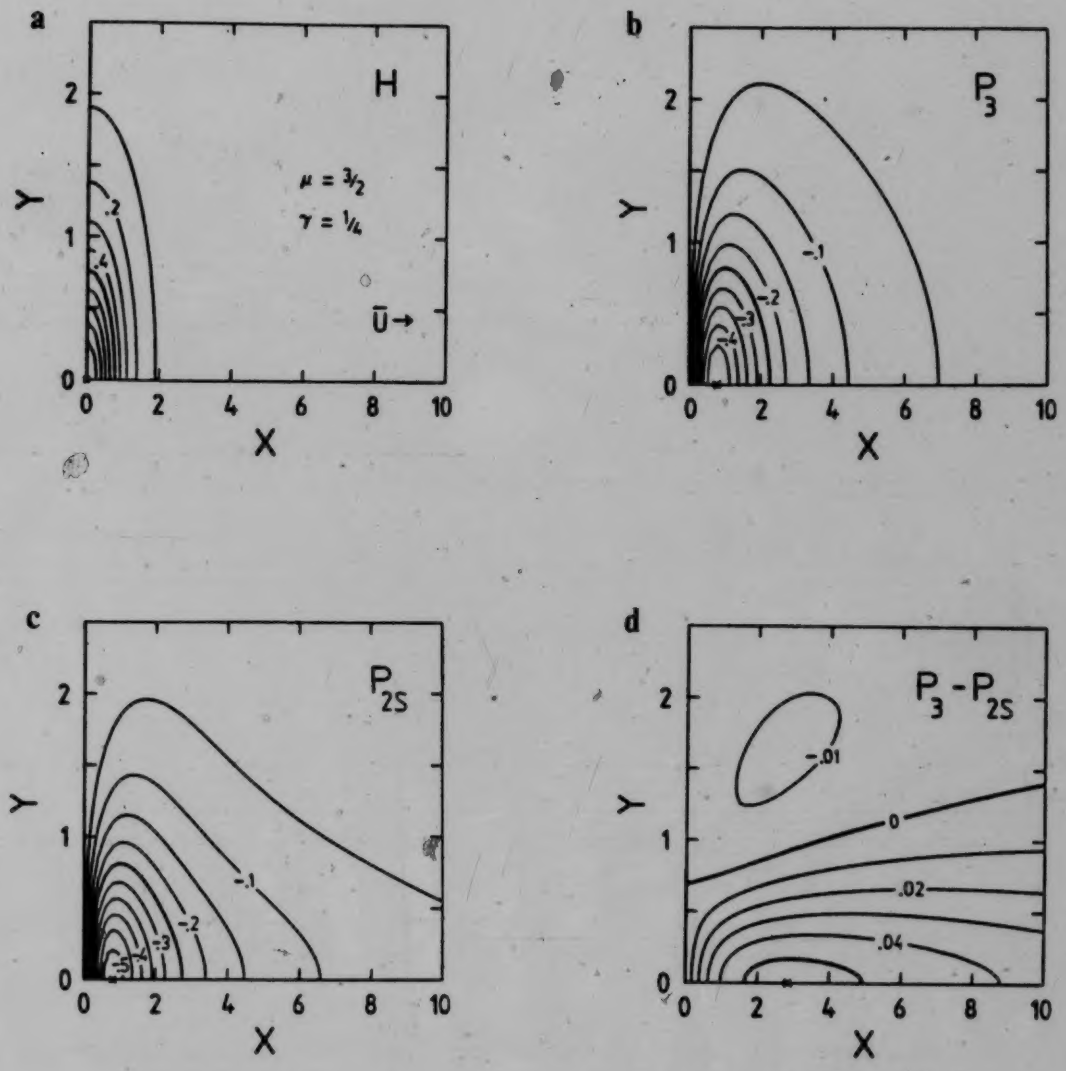

Figure 10. As in Fig. 9, but with $\gamma=1/4$. Extreme values of P_3, P_{2s} and P_3-P_{2s} are -.498, -.533 and .054, at X = .767, .797 and 2.82, respectively.

In Figs. 9 and 10 it is seen that the magnitude of the pressure perturbation in the three-dimensional flow is generally less than would occur if the motion were treated as two-dimensional. The difference, P_3-P_{2S}, is smaller in Fig. 10, as one would expect, since the barrier in that case is closer to being 'two-dimensional', having a larger length to width ratio. Also from these figures, note that the maximum perturbation occurs closer to the ridgeline for the three-dimensional barrier, compared to an infinite ridge of the same vertical cross-section. These features are also shown in Figs. 11a and 11b, in which the magnitudes of the extreme pressure perturbation, and its dimensionless position, P_{3m} and X_m, respectively, are plotted as a function of γ for various values of the terrain exponent, μ. Recall that $\gamma=0$ corresponds to the two-dimensional flow over an infinitely-extended crosswind ridge, $\gamma=1$ to a circular barrier, and $\gamma>1$ to a barrier with its long axis parallel to the wind. As γ increases, the pressure perturbation decreases monotonically, with a $\ln\gamma/\gamma$ behaviour for $\gamma>>1$. This result is derived in Appendix I.

As the terrain exponent, μ, increases and the barrier becomes more localized and sharply peaked, the maximum pressure perturbation increases, but tends to a finite value as $\mu\rightarrow\infty$. The position of the maximum pressure tends to the constant value $(2\mu)^{-1/2}$ as γ increases. By way of comparison, note that the maximum terrain slope occurs at $|X|=(2\mu+1)^{-1/2}$. So, for relatively broad barriers, such as

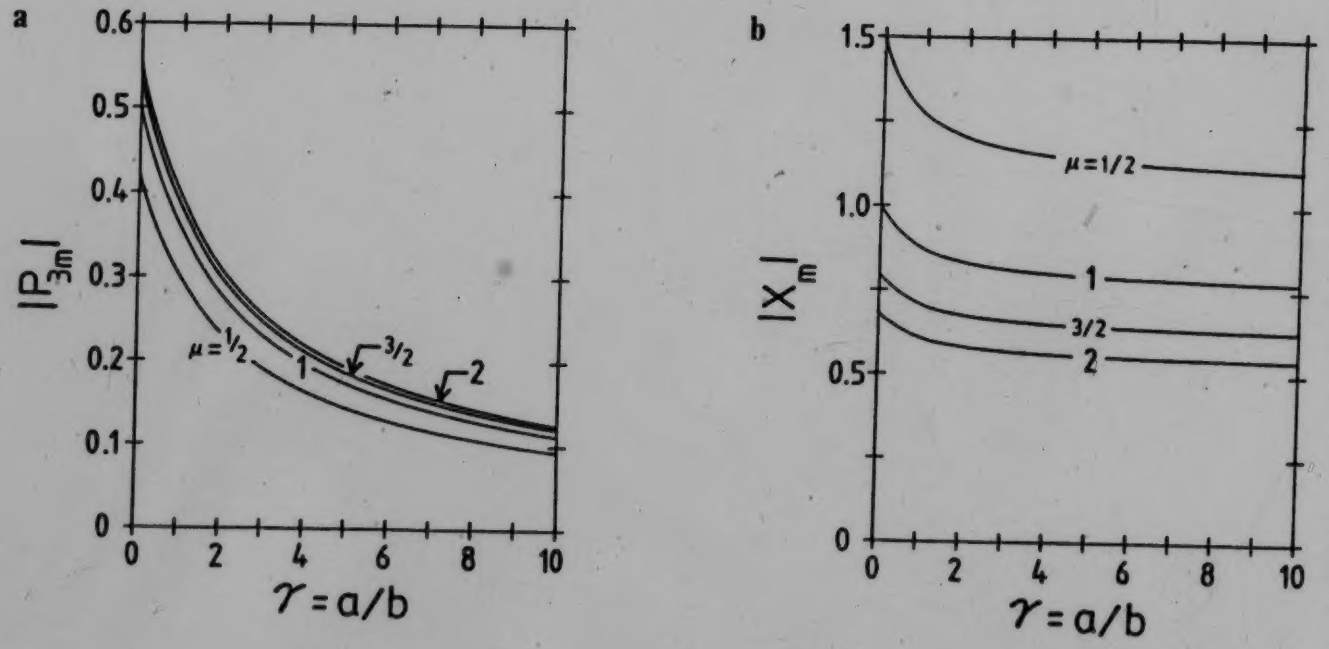

Figure 11. Magnitude of the extreme pressure perturbation, P_{3m} (Fig. 11a), and its position, X_m (Fig. 11b), vs. horizontal length scale ratio, $\gamma=a/b$, for terrain exponent $\mu=1/2$, 1, 3/2, and 2.

$\mu=1$, the position of the greatest pressure perturbation is somewhat farther from the barrier top than the position of maximum slope. For more peaked barriers, with $\mu>>1$, the two positions nearly coincide.

Turning once again to Figs. 9 and 10, note that the perturbation in the three-dimensional case falls off more rapidly with distance downstream of the barrier than in the two-dimensional flow. For example, in Fig. 9, the -0.25 pressure contour for P_3 intersects the $Y=0$ axis at $X=1.9$, whereas for P_{2S} it extends to $X=2.7$. In Appendix F, asymptotic expansions of the pressure fields as $X\to\infty$ are derived. The leading terms in such expansions are found to be closely related to the barrier cross-sectional area, A, and to the terrain volume, V, (introduced in Chapter 4) in the infinite ridge and isolated hill cases, respectively. In the $\mu=3/2$ case, where both A and V are finite, the two-dimensional flow pressure perturbation falls off as X^{-1}, whereas the three-dimensional solution goes as X^{-2}, as $X\to\infty$. If A or V is infinite, as can occur for smaller μ values, the fields decay more slowly. See Appendix F for details. Because P_{2S} falls off slowly with X compared to P_3, the maximum difference between these fields is displaced well downstream relative to the position where P_{2S} or P_3 has its extreme value. For example, if $\mu=3/2$ and $\gamma=1/4$, as in Fig. 10, the maximum pressure perturbation is about 0.5 and occurs at $|X|=0.8$, at which point the terrain height field $H=0.5$, whereas the maximum value of $|P_3-P_{2S}|=0.054$ at

$|X|=2.82$, with $H=0.037$.

The manner in which the pressure field changes with the eccentricity of the elliptical terrain is now examined in more detail. In Fig. 12a, the magnitude of the pressure perturbation along the $Y=0$ axis is shown for $\gamma=1$ (circular barrier), 1/2, 1/4, 1/8, and 0 (two-dimensional flow). The cases presented are for the terrain exponent $\mu=1$ and 2. The shape of the pressure curve and its variation with γ is qualitatively the same for each μ. Fig. 12b shows the difference, P_3-P_2, between the pressure field near an isolated three-dimensional barrier ($\gamma>0$) and an infinite ridge ($\gamma=0$). Note that the ordinates of Figs. 12a and 12b are not plotted to the same scale.

In Appendix H, an expansion (H.11) is derived to determine the nature of the limit as $\gamma\to0$. It is found that the three-dimensional pressure perturbation, P_3, can be expressed as the sum of the two-dimensional slice pressure field, P_{2S}, plus a correction term (H.12) that vanishes as $\gamma^2\ln\gamma$ as $\gamma\to0$. Some numerical examples are now considered to see how small γ needs to be in practice for the two-dimensional slice solution to serve as a good approximation to the three-dimensional one. For $\gamma=1$, one finds from Fig. 12 (recalling that $P_{2S}(X,0)=P_2(X)$) that the maximum of P_3-P_{2S} amounts to 25-35% of the maximum of P_3, with the exact percentage depending on μ. This relative difference drops to about 10% for a barrier four times as long crosswind as downwind ($\gamma=1/4$) and to about 5% for $\gamma=1/8$. If one is

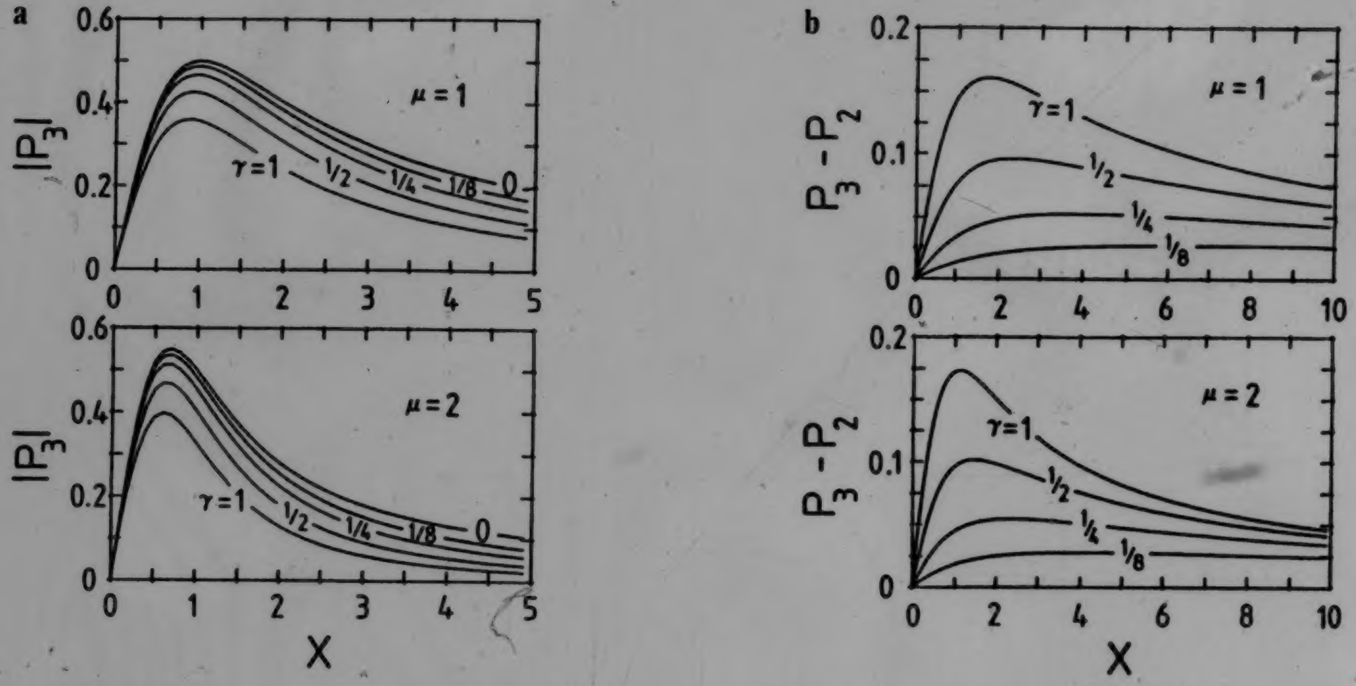

Figure 12. (a) Magnitude of the surface pressure perturbation, $|P_3|$, vs. X, the dimensionless distance from the terrain peak, along Y=0, for terrain exponent $\mu=1$ and 2, and $\gamma=1$ (circular hill), 1/2, 1/4, 1/8 and 0 (infinite ridge).
(b) The difference in pressure perturbation, P_3-P_2, between the isolated hill ($\gamma>0$) and infinite ridge ($\gamma=0$) cases in Fig. 12a. ($P_2(X)=P_3(X,Y=0,\gamma=0)$).

interested only in the extent to which P_{2S} reproduces the maximum value of P_3, rather than where the maximum occurs, then γ need not be as small in order to get an acceptable approximation. For example, from a higher resolution version of Fig. 11 it was found that the maximum value of P_{2S} exceeds the maximum value of P_3 by about 10% when $\gamma=1/3$ and by 5% for $\gamma=1/5$. These values are almost independent of the terrain exponent, μ.

In summary, one can say that for the calculation of the surface pressure field, the flow across an isolated hill can be considered essentially two-dimensional if the crosswind extent of the barrier is greater than about four times its width in the direction of the mean wind.

CHAPTER 6

PRESSURE PERTURBATION FOR FLOW OVER CURVED RIDGES

6.1 Introduction

In the preceding chapter, the pressure perturbation induced by flow over an elliptical mountain was calculated as a function of the barrier orientation and eccentricity. In the present chapter, another geometrical variable is introduced. Here, the effect of curvature (in a horizontal plane) of an extended mountain ridge on the pressure field is investigated.

Very few papers in the meteorological literature address the question of whether or not the large-scale curvature of terrain features has a systematic effect on cyclone development. On the scale of lee waves, it has been reported (Gerbier and Berenger, 1961) that 'wave effects are more pronounced' for flow over a ridge which is concave to the wind and less pronounced for the convex case. In a mesoscale numerical modelling study, Ballentine (1980) found enhanced precipitation was predicted in regions where the coastline presents a concave arc to the low-level flow. Petterssen (1956) mentions variations in wind speed attributable to shoreline curvature effects. However, these coastal effects appear to be a consequence of the distribution of surface heating rather than a dynamical effect of terrain shape. On a larger scale, Carpenter (1945), on the basis of data for two winter months each year from 1920 to

1938, suggested that low-pressure centers crossing the west coast of North America in regions of concave shoreline tend to develop whereas those approaching convex coasts weaken. Godev (1971) attempted to explain Carpenter's result, and a similar observation in Europe, in terms of a parameterization of boundary layer turbulence. Because Godev's arguments do not seem particularly convincing, the details will not be presented here. To mention just one difficulty, he implicitly assumes that there exists a definite relation between curvature of the vertical profile of the terrain and its curvature in a horizontal plane. A more complete dynamical model than considered by Godev was used by Tibaldi et al. (1980) to study cyclogenesis in the lee of the Alps. In their numerical model, a straight barrier leads to a weaker cyclogenesis than a mountain which is convex to the incident flow. They conclude that 'the arc shape of the Alps is favorable for cyclogenesis, but is not strictly necessary'. However, it would be difficult to justify application of this result to the development of low-pressure centers in the lee of extended barriers such as the Rockies. The present work will address the much more limited question of what effect ridge curvature has on the magnitude of pressure perturbations in a steady, linear, hydrostatic model. There is certainly room for more study to determine the extent to which terrain curvature effects enhance or inhibit development.

Given a barrier shape, $H(X,Y)$, curvature effects can be introduced by translation of the barrier along the X axis, by amounts specified by a function $X_0(Y)$. Variables referring to the differentially translated ('curved') barrier will be denoted by angular brackets, so,

$$\langle H(X,Y)\rangle = H(X-X_o(Y),Y) \quad . \tag{6.1}$$

From the definition of the Fourier transforms in (B.3), one can easily show that

$$\langle\tilde{H}(\kappa;Y)\rangle = e^{-i\kappa X_o}\,\tilde{H}(\kappa;Y) \tag{6.2}$$

and

$$\langle\hat{H}(\kappa,\lambda)\rangle = \frac{1}{2\pi}\int_{-\infty}^{\infty} e^{-i(\kappa X_o+\lambda Y)}\,\tilde{H}(\kappa;Y)\,dY \quad . \tag{6.3}$$

Although some progress can be made in the case of an isolated barrier for which H contains a factor of $\exp(-Y^2)$, results are presented in this chapter only for flow over an infinite ridge. If an uncurved ridge is parallel to the Y axis, then, $\tilde{H}(\kappa;Y) = \tilde{H}(\kappa)$ is independent of Y and can be taken outside the integral in (6.3). Two types of curved barriers will be discussed, a parabolic case with $X_0 = \tau Y^2$ and a sinusoidal case, $X_0 = A\cos\Omega Y$, where τ, A and Ω are parameters controlling the degree of curvature. For the most part, results will be limited to the Agnesi ridge profile, $\dot{H} = 1/1+X^2$. The parabolic case is considered first.

6.2 Parabolically curved ridge

For the case of $X_0 = \tau Y^2$, the integral (6.3) can be explicitly evaluated for an arbitrary infinite ridge. From GR (p. 395) one obtains

$$<\hat{H}(\kappa,\lambda)> = \frac{\tilde{H}(\kappa)}{2\,\left(\pi|\kappa\tau|\right)^{\frac{1}{2}}}\, e^{i\left(\frac{\lambda^2}{4\kappa\tau} - \frac{\pi}{4}\,\mathrm{sign}(\kappa\tau)\right)} \quad . \tag{6.4}$$

Substituting (6.4) into (B.5) gives a complicated double integral for the pressure <P>. Further progress was made, however, in the special case of an Agnesi barrier, and along Y=0 for an arbitrary one.

In the Y=0 case, the λ integration can be done (GR, p 428) in terms of Bessel functions, J_0 and N_0 :

$$<P(X,0)> =$$

$$-\mathrm{sign}(\tau)\left(\frac{\pi|\xi|}{2}\right)^{\frac{1}{2}} \int_{-\infty}^{\infty} |\kappa|^{\frac{1}{2}}\, \tilde{H}(\kappa)\left\{J_0\left(|\xi\kappa|\right) + isN_0\left(|\xi\kappa|\right)\right\} e^{i\left(\kappa(X-\xi)-\pi s/4\right)}\, d\kappa \quad , \tag{6.5}$$

where $s=\mathrm{sign}(\kappa\tau)$ and

$$\xi = \frac{1}{8\tau\gamma^2} \quad . \tag{6.6}$$

For the singular barrier, $H=1/\sqrt{X}$, (6.5) can be explicitly evaluated in terms of elementary functions but the results will not be presented here. Instead, consider the Agnesi ridge case, $H = 1/(1+X^2)$, with Fourier transform $\tilde{H}(\kappa) = \exp(-|\kappa|)/2$. For this ridge profile, an analytical expression for the pressure was found only at the point ($X=\xi, Y=0$). From GR (p. 711), $<P(\xi,0)>$ can be written in terms of hypergeometric functions, which, in turn, are found to reduce to elliptic integrals (GR, pp.1016, 1019, 1045). The result obtained is

$$\langle P(\xi,0)\rangle = \frac{-X^{1/2}}{2(1+X^2)^{3/4}}\left\{2\left(E(k_+)+E(k_-)\right) - K(k_+) - K(k_-)\right\} , \qquad (6.7)$$

where

$$k_\pm^2 = \frac{1}{2}\left(1 \pm \frac{1}{(1+X^2)^{\frac{1}{2}}}\right) . \qquad (6.8)$$

Although (6.7) refers only to a single point, it serves as a useful check on answers obtained numerically by other means.

In another attempt to evaluate the pressure field for the Agnesi barrier, the double integral obtained by substituting (6.4) into (B.5) was transformed using the elliptical polar coordinates (B.2). Carrying out the ρ integration (GR, p. 317), and introducing a new variable, ω, by

$$\sinh\omega = \gamma \tan\phi \quad , \qquad (6.9)$$

the pressure perturbation can be expressed as

$$\langle P(X,Y)\rangle = -\frac{1}{4\gamma|\tau|^{\frac{1}{2}}}\int_0^\infty \left(f(X,Y;\omega) + f(X,-Y;\omega)\right) d\omega \quad , \qquad (6.10)$$

where

$$f(X,Y;\omega) = \frac{\sin\left(\frac{3}{2}\arctan\eta - \frac{\pi}{4}\,\mathrm{sign}\,\tau\right)}{(1+\eta^2)^{3/4}} \quad , \qquad (6.11)$$

and

$$\eta = \frac{(\sinh\omega + 2\tau\gamma Y)^2}{4\tau\gamma^2} + X - \tau Y^2 \quad . \qquad (6.12)$$

To study the behavior of the pressure field as the parameter, τ, (and hence the curvature of the ridge) is varied, the expression (6.10) was evaluated numerically using a 200 point Simpson's rule (see, for example, Gerald, 1978, p. 214) with $\omega=5$ as the upper integration limit. Test runs with 1000 points and an upper limit of 10 gave results differing only by one unit in the fifth place after the decimal. First consider the pressure perturbation along the Y=0 axis. Results to be shown here are based on (6.10), although some calculations were done using (6.5) as well. Both methods took about the same amount of computer time.

In Fig. 13, <P> is plotted as a function of X for the uncurved ridge, $\tau=0$ (dashed curve) and the parabolically curved cases, $\tau\gamma^2=1/32$, 1/8, and 1/2. The special points, $X=\xi$, defined by (6.6), for which <P> can be checked using (6.7), are marked on the $\tau>0$ curves. Note that positive values of τ correspond to a barrier which is convex to the incoming flow. The concave case is obtained simply by changing the signs of P and X. On the lee (concave) side of the barrier (X>0), there is a monotonic progression to perturbations of smaller magnitude as τ increases.

On the upstream (convex) side of the ridge, the variation with τ is not so simple. For small values of τ, the pressure is slightly larger than for a straight barrier ($\tau=0$), with the extreme perturbation occurring closer to the ridgeline. The maximum extreme value (about .567) is attained for $\tau\gamma^2$ near 1/8, with smaller maxima for larger

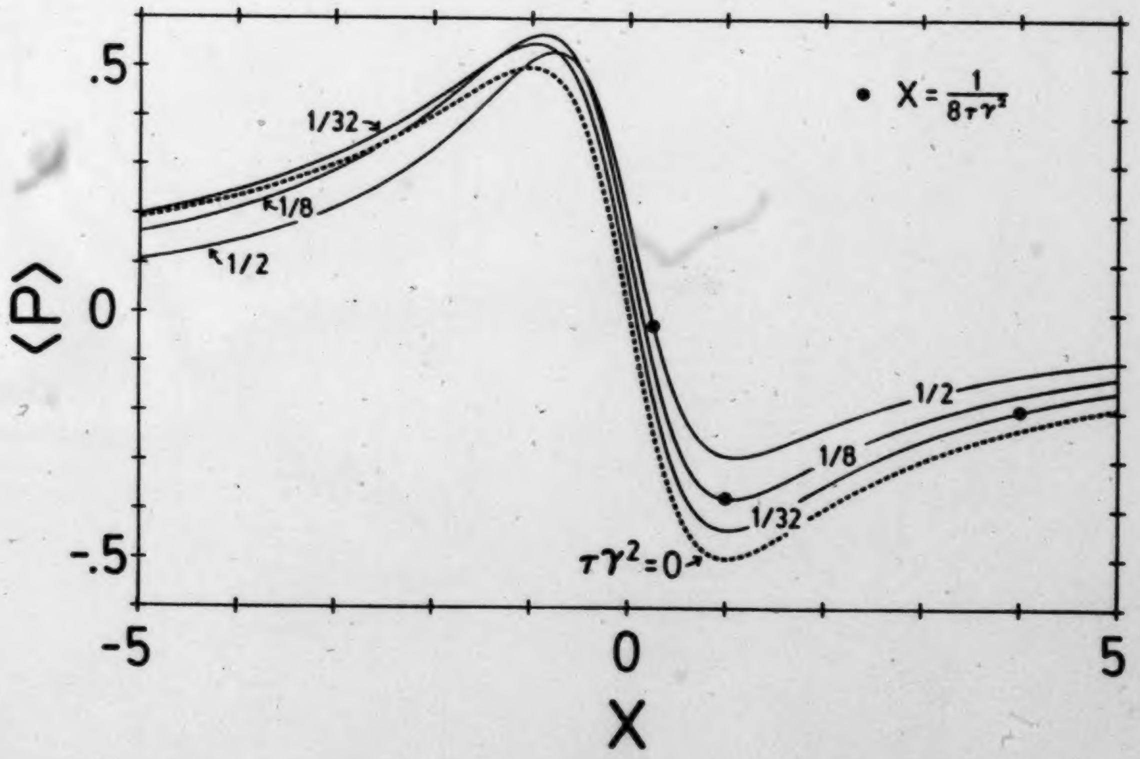

Figure 13. Normalized pressure perturbation, <P>, vs. dimensionless position, X, along Y=0 for an infinitely-extended crosswind Agnesi ridge (τ=0, dashed curve), and the parabolically curved ridges (concave on lee side), $\tau\gamma^2$=1/32, 1/8, and 1/2. The points $X=1/(8\tau\gamma^2)$, for which the pressure is given in (6.7), are marked by circles.

values of τ. For the $\tau\gamma^2=1/2$ case, the pressure perturbation is noticeably less than for the straight ridge case if X is less than about 1. The magnitude of the change in the pressure field induced by ridgeline curvature is greatest on the concave side of the barrier.

If the ridgeline is given by $X=X_0(Y)$, then the radius of curvature of the ridge, normalized by the length scale, a, is defined by

$$R_c = \frac{\left[1 + \gamma^2\left(\frac{dX_o}{dY}\right)^2\right]^{3/2}}{\gamma^2\frac{d^2X_o}{dY^2}} \; . \qquad (6.13)$$

For the particular case, $X_0=\tau\gamma^2$, the radius of curvature is

$$R_c = \frac{\left[1 + (2\tau\gamma Y)^2\right]^{3/2}}{2\tau\gamma^2} \; . \qquad (6.14)$$

The minimum value of R_c is $R_{cm}=1/(2\tau\gamma^2)$ which occurs at $Y=0$. For $\tau\gamma^2$ greater than about 1/2, this minimum radius of curvature is comparable to the streamwise horizontal scale of the ridge. For such sharply curved ridges, the cross-section presented to the incident flow is relatively small. Consequently, the ridge affects the flow in a manner comparable to a barrier extended along, rather than across, the mean wind. This produces a general reduction in the magnitude of the pressure perturbation, as $\tau\gamma^2$ is increased beyond 1/2. For example, for $\tau\gamma^2=1$, the maximum perturbation is less than 0.5, the value for a straight ridge.

Although (6.10) is convenient for calculating <P> at a given point or small set of points, it is unnecessarily expensive for two-dimensional arrays of points. Instead, a discrete Fourier transform method (the 'Fast Fourier Transform') can be used to approximate the Fourier integrals defining <P> for a lattice of points in the X-Y plane. The basic procedure is outlined in Appendix J. In the cases to be discussed, the calculations were done on a mesh of 256 by 256 points with a grid spacing of 0.1 in both X and Y directions.

To examine the accuracy of the calculation, the discrete Fourier transform result is compared to that based on a Simpson's rule evaluation of (6.10) in Fig. 14. The figure illustrates <P(X,Y)> vs. X along the cross-sections Y=0 and Y=3, for the case of $\tau\gamma^2=1/8$. Along both lines, the discrete Fourier transform integration underestimates the Simpson's rule result. The latter of the two is thought to be the most accurate for the parameter values chosen. The maximum difference between the values given by the two methods is about 5% of the maximum perturbation.

In Fig. 15a, the full X-Y variation of <P> is shown for the $\tau\gamma^2=1/8$ case, based on the discrete Fourier transform calculation on a 256 by 256 point grid. Fig. 15b illustrates the $\tau\gamma^2=1/4$ case. The region shown in the figures corresponds to the innermost 61 by 61 points, where contamination due to discontinuities at the boundary of the computational grid is minimized. The contour interval for

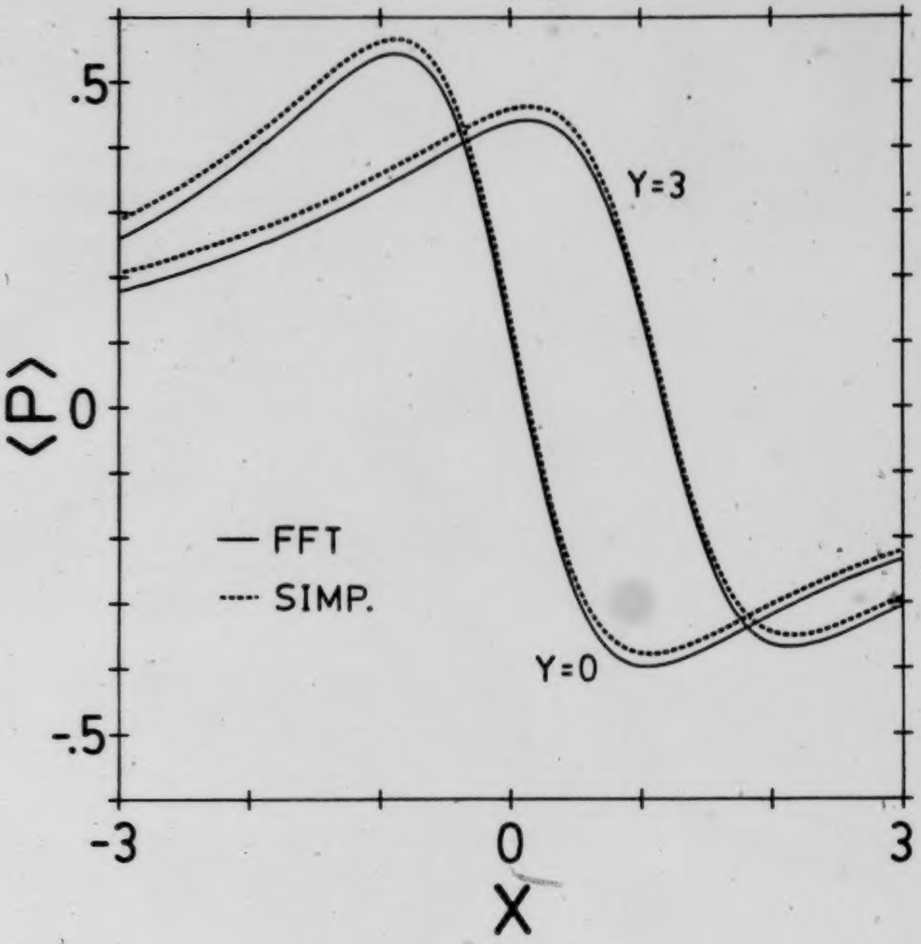

Figure 14. Comparison of the pressure perturbation, <P>, vs. dimensionless position, X, along the lines Y=0 and Y=3, for flow over a parabolically curved Agnesi ridge, as calculated by a Fast Fourier Transform method (solid curves) or Simpson's Rule integration of (6.10) (dashed curves).

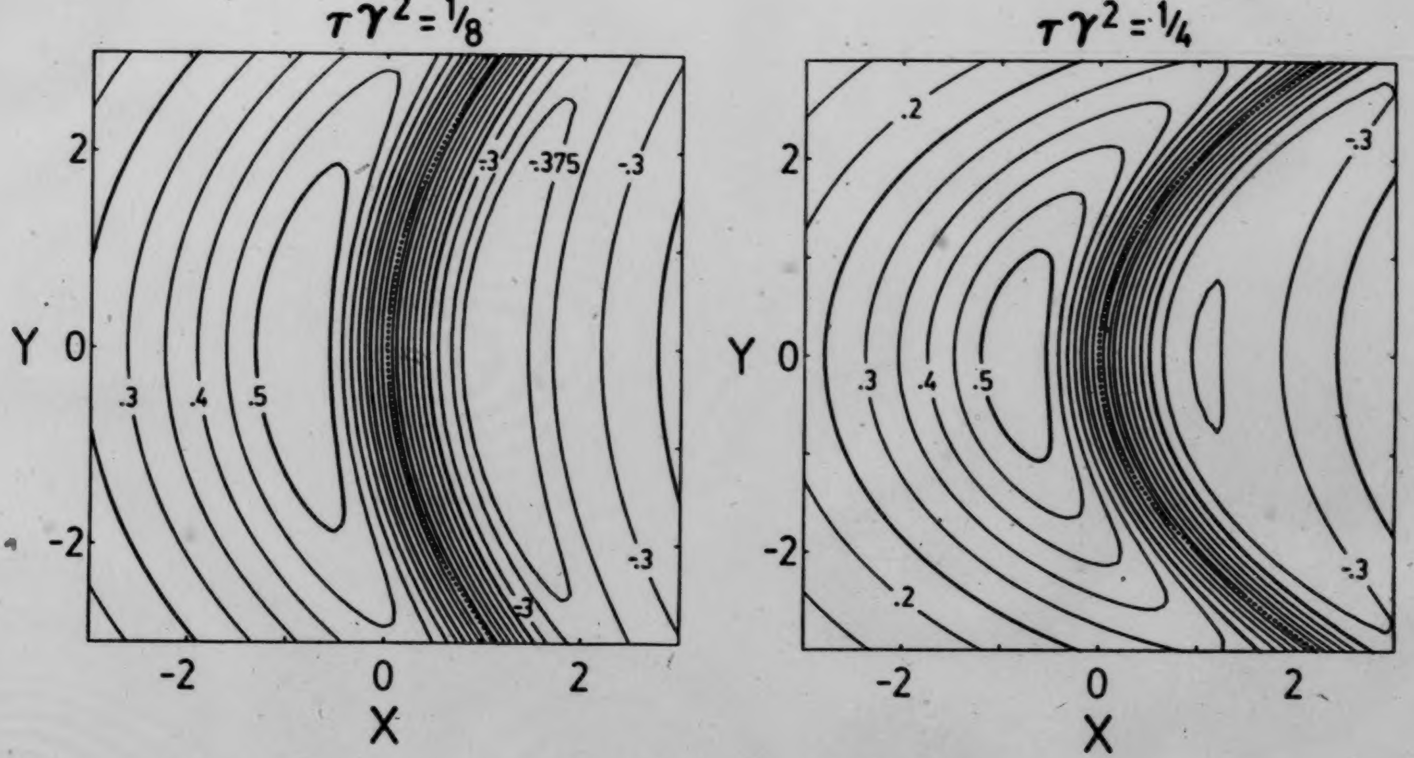

Figure 15. Approximate pressure perturbation, <P>, contoured at an interval of 0.05, for the parabolically curved Agnesi ridges (a) $\tau\gamma^2=1/8$, and (b) $\tau\gamma^2=1/4$, defined by $X_0=\tau Y^2$ in (6.1). An extra contour level, -0.375, appears in (a). The ridgeline of the height field is shown as a dashed curve.

the plots is 0.05, except for an extra contour level of -0.375 to delineate the minimum pressure more clearly in Fig. 15a. The dashed curves indicate the ridgeline of the height field, $X=\tau Y^2$. If the barrier did not induce any transverse velocity, then the isobars would be congruent to the ridge in the height field and the magnitude of the extreme perturbation would be the same (0.5) on both sides of the barrier. However, from the figures, it is seen that the isobars show slightly less curvature than the topographic contour. Also, as mentioned previously, the effect of curvature on the extreme perturbation is greatest on the concave side of the ridge. Finally, note that a comparison of the two figures shows the decrease in crosswind length scale (for example, compare the sizes of the 0.5 isobars) with increasing τ, as has been discussed.

6.3 Sinusoidally curved ridge

The second type of ridge that was studied is a sinusoidally curved one, with

$$X_o = A\cos\Omega Y \quad . \tag{6.15}$$

Employing the expansion (GR, p. 973)

$$e^{iz\cos\phi} = \sum_{n=-\infty}^{\infty} i^n J_n(z)\, e^{in\phi} \quad , \tag{6.16}$$

in (6.3), in the infinite ridge case ($\tilde{H}(\kappa;Y)=\tilde{H}(\kappa)$), the integration over ϕ can be performed using (O.11) to give the terrain-height Fourier transform

$$\langle\hat{H}(\kappa,\lambda)\rangle = \bar{H}(\kappa) \sum_{n=-\infty}^{\infty} i^{n} J_{n}(-\kappa A)\, \delta(n\Omega-\lambda) \quad . \qquad (6.17)$$

Substituting this result into (B.5), the λ integration is easily done. Assuming that the remaining integration and summation operations can be interchanged, this leaves the pressure perturbation in the form

$$\langle P(X,Y)\rangle = \sum_{n=-\infty}^{\infty} i^{n+1}\, e^{in\Omega Y} \int_{-\infty}^{\infty} \frac{\kappa\, \bar{H}(\kappa)}{(\kappa^{2}+\gamma^{2}n^{2}\Omega^{2})^{\frac{1}{2}}}\, J_{n}(-\kappa A)\, e^{i\kappa X}\, d\kappa \quad . \qquad (6.18)$$

This is an interesting form, in that periodicity in Y, that one would expect on the basis of the height field, is explicit. However, no progress was made with the integral in (6.18), except for the n=0 term. The infinite summation can be eliminated in favour of an integral by using (GR, p. 732):

$$\frac{1}{(\kappa^{2}+\gamma^{2}n^{2}\Omega^{2})^{\frac{1}{2}}} = \frac{2}{\pi} \int_{0}^{\infty} K_{0}\{|\kappa|t\}\, \cos(\gamma n\Omega t)\, dt \quad . \qquad (6.19)$$

Expressing the cosine in (6.19) as a sum of complex exponentials, one finds upon substitution into (6.18) that the summation over n takes the form (6.16), with the result:

$$\langle P(X,Y)\rangle = \frac{i}{\pi} \int_{-\infty}^{\infty} \int_{-\infty}^{\infty} \kappa\, \bar{H}(\kappa)\, K_{0}\{|\kappa t|\}\, e^{i\kappa\chi}\, d\kappa\, dt \quad , \qquad (6.20)$$

where

$$\chi = X - X_{0}(Y+\gamma t) \quad . \qquad (6.21)$$

By substituting (6.3) into (B.5) and carrying out the λ integration, one can show that an expression of the form (6.20) holds generally, not just for X_0 given by (6.15). In addition, $\tilde{H}(\kappa)$ can be replaced by $\tilde{H}(\kappa;Y)$ in (6.20).

For certain terrain forms, the κ integral in (6.20) can be evaluated analytically. However, that would leave a final integration which would likely have to be done numerically, as in the $X_0=\tau\gamma^2$ example. In view of this, it was decided to abandon attempts to determine $\langle P(X,Y)\rangle$ based on (6.18) and (6.20), and to proceed to use the Fast Fourier Transform method employed in the previous section. The periodicity of the terrain height implied by (6.15) is an added advantage to using the Fourier transform approach, as the height field need be sampled only for one wavelength in the Y direction. The grid used for the calculation had 256 points at a spacing of 0.1 in the X direction and 64 points at a spacing of 0.0625 in the Y direction. The result for the choice of parameters, $A=0.5$ and $\Omega=\pi/2$ (which implies a wavelength of 4 units in the Y direction), is plotted in Fig. 16. As in Fig. 15, the ridgeline of the terrain is shown as a dashed curve. The ridge shown in Fig. 16 is somewhat more sharply curved than the examples in Fig. 15. One can show from (6.15) in (6.13) that the minimum (positive) radius of curvature is $R_{cm}=1/(A\Omega^2)$. For the present case, $R_{cm}=8/\pi^2\simeq.81$ intermediate to the values of $R_{cm}=1$ and 1/2 corresponding, respectively, to the $\tau\gamma^2=1/2$ and 1 parabolic ridges.

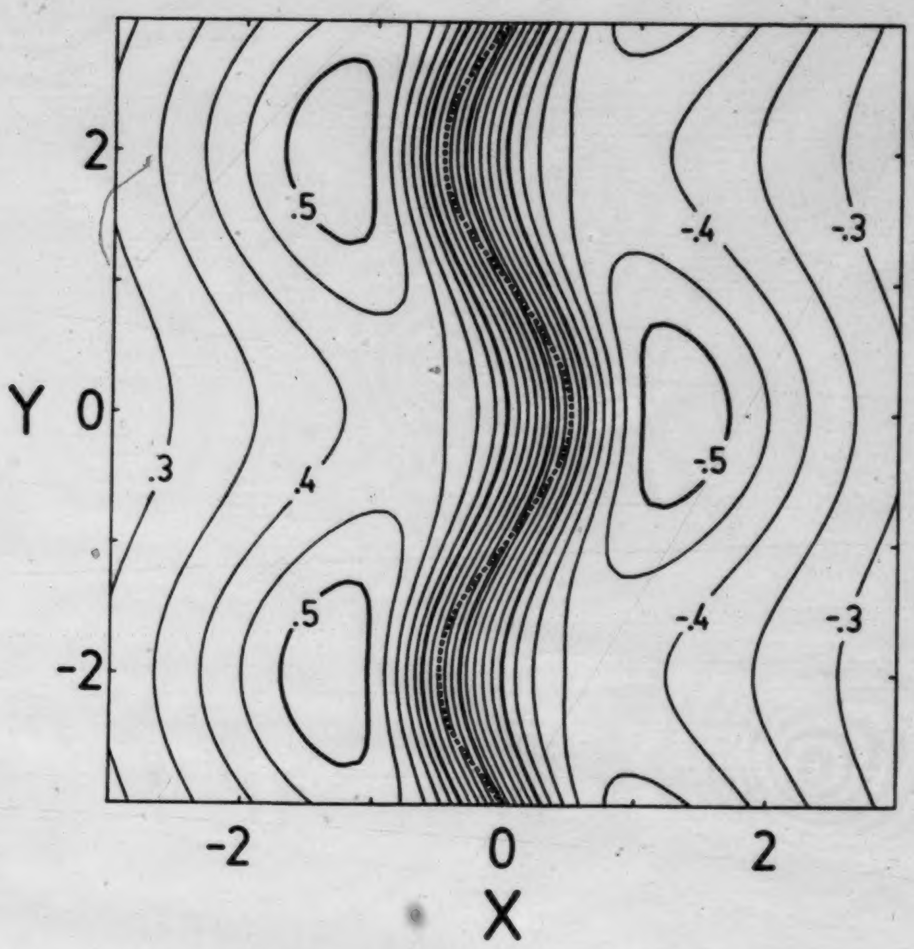

Figure 16. As in Fig. 15, except, for the sinusoidal ridge, defined by $X_0=A\cos\Omega Y$ in (6.1), with $A=0.5$ and $\Omega=\pi/2$.

On the convex side of the areas of strong curvature of the ridge, the appearance of the isobars is qualitatively similar to Fig. 15. In the concave regions, however, there are more prominent differences between the parabolic and sinusoidal ridges. In the former case, there is a closed pressure contour in each concavity, but, in the latter case there is only a saddle point. For the example of Fig. 16, the magnitude of the perturbation at this point is about .42, a larger value than comparably curved parabolic barriers. For example, the magnitude of the extreme perturbation on the convex side of the barrier is only about .3 and .25 for $\tau\gamma^2=1/2$ and 1, respectively. Therefore, one must consider the pattern of curvature along a ridge, not just the maximum curvature, in estimating the effect of horizontal deformations of the ridge on the pressure perturbation.

In the context of a simple model, this study of barrier curvature effects has shown that the perturbation is slightly enhanced on the convex side of a moderately curved ridge segment. However, if the radius of curvature is so small as to be comparable to the length scale of the terrain parallel to the mean flow, then there can be a decrease in the magnitude of the extreme perturbation. The effect of ridge curvature was found to be stronger on the concave side of the barrier, with the strength of the perturbation decreasing as the curvature increases.

CHAPTER 7

TRANSVERSE PERTURBATION VELOCITY, STREAMLINE DEFLECTION AND HORIZONTAL DIVERGENCE

An important difference between flow over an isolated three-dimensional hill and that over an extended ridge is the existence of a non-zero transverse velocity, v', in the former case. Perhaps the most interesting aspect of the comparison of the two- and three-dimensional pressure perturbations in Chapter 5 is that the maximum difference occurs along the $Y=0$ axis, even though the transverse velocity is zero there, for an unrotated barrier ($\psi=0$). Because of the lateral symmetry of the barrier, the motion occurs in a vertical plane along $Y=0$ even for the fully three-dimensional barrier. However, the quantity $\partial v'/\partial y$ is not zero for the three-dimensional case, and so can be used as a measure of the departure from two-dimensional flow (where $\partial v'/\partial y=0$). Another convenient parameter to study is the horizontal divergence, D_H, which is defined as

$$D_H = \frac{\partial u'}{\partial x} + \frac{\partial v'}{\partial y} \quad . \qquad (7.1)$$

A non-zero value for $\partial v'/\partial y$ changes the vertical motion field, relative to the two-dimensional case, through the continuity equation (3.4), and ultimately the pressure field, through the adiabatic equation (3.12). As will be seen shortly, $\partial u'/\partial x$ is also different in the two- and three-dimensional flows.

Each of the terms, $\partial u'/\partial x$ and $\partial v'/\partial y$, and consequently, D_H, attains its maximum value directly over the barrier, at $R=0$. This is intimately related to the fact, mentioned previously, that the pressure gradient is also a maximum there. This follows from the relation between the velocity and pressure fields given in (3.27) and (3.31) or in the horizontal momentum equations (3.1) and (3.2). For the particular barrier (4.1), analytical results for the velocity derivatives and divergence could be obtained using the explicit expressions for the pressure derived in Appendix D. However, for the most part, in the present study it will be sufficient to examine the region near $R=0$ where calculation is considerably simplified and tedious differentiations of the pressure field need not be done.

Evaluation of $\partial u'/\partial x$, $\partial v'/\partial y$, and D_H at $R=0$, for an arbitrary elliptical barrier is considered in Appendix F. The horizontal divergence at $R=0$ is found to be independent of the barrier orientation angle, ψ, but the relative contributions of $\partial u'/\partial x$ and $\partial v'/\partial y$ to the divergence vary with both ψ and the measure of eccentricity, γ. Fig. 17 shows the divergence and velocity derivatives for the unrotated case, $\psi=0$, normalized by the divergence for an infinite ridge having the same downwind scale, a, as a function of $\gamma=a/b$. The stretching of the flow along the direction of the incident wind, as measured by $\partial u'/\partial x$, is seen to decrease as the crosswind extent, b, of the barrier decreases (that is, as γ increases). At the same time, the

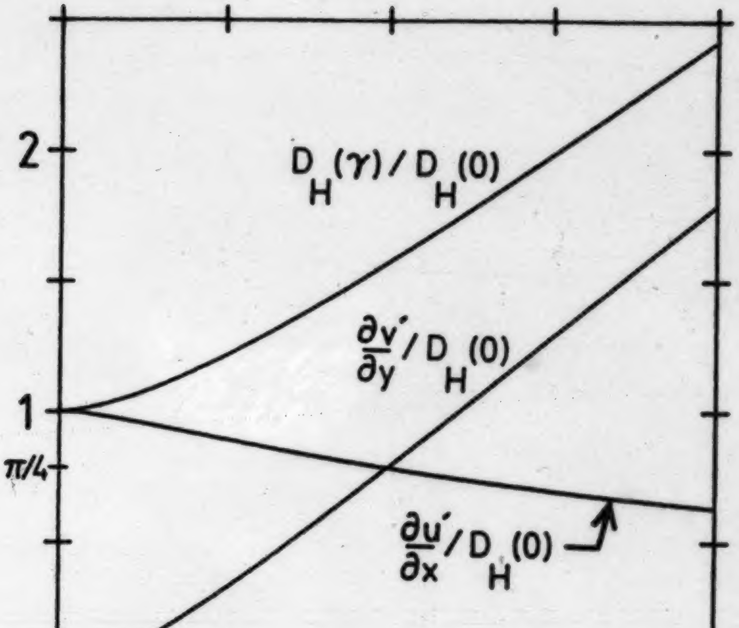

Figure 17. Horizontal divergence, $D_H(\gamma)$, and the velocity derivatives, $\partial u'/\partial x$ and $\partial v'/\partial y$, at the terrain peak ($R=0$), normalized by the value, $D_H(0)=I\bar{N}h_0/a$ (see Eq. F.11), of divergence for the infinite ridge case ($\gamma=0$), vs. the horizontal length scale ratio, $\gamma=a/b$.

contribution to divergence from the transverse velocity, $\partial v'/\partial y$, increases, until, for a circular barrier ($\gamma=1$) the stretching is equal along the x and y axes ($\partial u'/\partial x = \partial v'/\partial y$). For a very narrow ridge ($\gamma\to\infty$) the horizontal divergence becomes indefinitely large.

As a further comparison of the divergence field in the two- and three-dimensional flow situations, Fig. 18 illustrates the horizontal divergence along the Y=0 axis for the circular hill ($\gamma=1$) and infinite ridge ($\gamma=0$) cases with terrain exponent $\mu=3/2$. The divergence is normalized by the factor $\overline{N}h_o/a$, which has the value 10^{-3} s^{-1} for $\overline{N} = 0.01$ s^{-1}, $h_o = 1$ km, and $a = 10$ km.

To see the effect of the different distributions of horizontal divergence on the vertical movement of an air parcel crossing the barrier, one can integrate the continuity equation (3.4) with respect to x (dropping the compressibility terms). Then using (3.10) one obtains the rate of change of the streamline displacement in the vertical:

$$\eta_z(x,y) = -\frac{1}{\overline{U}} \int_{-\infty}^{x} D_H(x',y)\, dx' \quad . \tag{7.2}$$

Substituting for the horizontal divergence from (7.1) gives

$$\eta_z = -\left(\frac{u'}{\overline{U}} + \delta_y\right) \quad . \tag{7.3}$$

Here, following Smith (1980), the crosswind displacement, δ, of a surface streamline from its upstream position has been introduced, being defined by

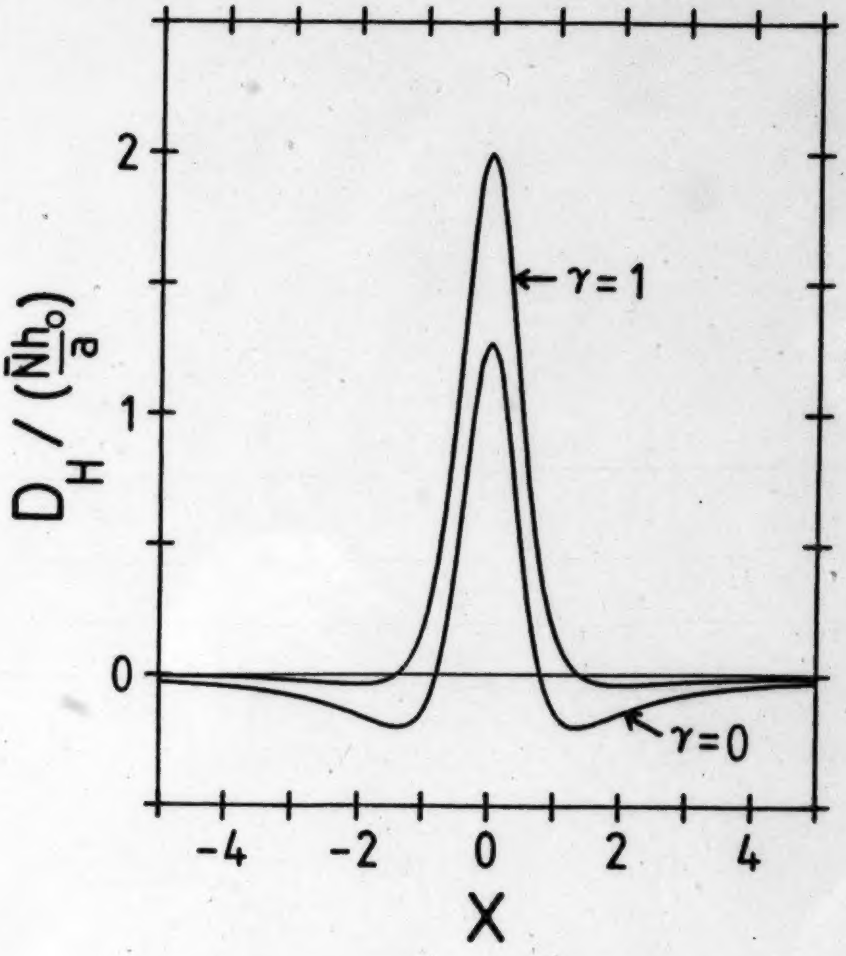

Figure 18. Horizontal divergence, D_H, vs. dimensionless position, X, along Y=0, for the circular hill ($\gamma=1$) and infinite ridge ($\gamma=0$) cases, normalized by the factor $\bar{N}h_o/a$.

$$\delta(x,y) = \frac{1}{U} \int_{-\infty}^{x} v'(x',y)\, dx' \quad . \qquad (7.4)$$

From (7.2), it is seen that η_z is proportional to the area under a plot of horizontal divergence, such as given in Fig. 18.

Far downstream of the barrier ($x \to \infty$), the x component of the perturbation velocity, u', vanishes, so that (7.2) and (7.3) reduce to

$$\delta_y(x=\infty,y) = -\eta_z(x=\infty,y) = \int_{-\infty}^{\infty} D_H(x',y)\, dx' \quad . \qquad (7.5)$$

For the circular barrier case, Smith (1980) obtained a positive value for the integral (7.5) near $y=0$. He showed this to be an indication that surface air parcels traversing the barrier suffer a horizontal deflection which persists infinitely-far downstream, with a compensating descent of air from above. For two-dimensional flows however, there is no lateral deflection of streamlines or permanent sinking of air far downstream. As a consequence, the integral (7.5) vanishes: Fig. 18 provides a visual indication of the cancellation of divergence and convergence as an air parcel passes the barrier in the two-dimensional flow situation. In the three-dimensional, case the increased divergence over the mountain dominates the weaker convergence away from the peak so as to give a net positive result for (7.5), as indicated above.

Additional information about the transverse perturbation velocity, v', and the deflection, δ, can be obtained from results already presented for the pressure field by using the relation (3.31). This equation implies that for flow over an unrotated elliptical barrier, characterized by a ratio of horizontal length scales $\gamma=a/b$, the velocity perturbation is expressible directly in terms of the pressure field for a barrier for which γ has been replaced by $1/\gamma$. For the symmetric terrain considered here, this is equivalent to rotating the mountain by 90°. So, for example, Fig. 11, showing the position and magnitude of the maximum pressure perturbation, also gives the corresponding quantities for the normalized transverse velocity, $v'/\overline{N}h_0$, if one replaces γ with $1/\gamma$. Similarly, the x-y plot of pressure given in Fig. 8a ($\gamma=1/2$) can be interpreted as a plot of $v'/\overline{N}h_0$ (rotated 90°) for the barrier of Fig. 8b ($\gamma=2$).

For an elliptical barrier, with axes along the x and y directions, the pressure field is positive or negative according to whether x is negative or positive, respectively. The relation (3.31) then implies that, for three-dimensional flow, the surface transverse velocity is positive for $y>0$ and negative for $y<0$. This is certainly what one would expect on the upwind side of the barrier but may not be intuitively obvious on the lee side. Since v' is found to have the same sign in the entire half plane, $y>0$, the integral (7.4) for the lateral streamline deflection, δ, is a monotonically increasing function of x and the maximum deflection is attained at $x=\infty$. Smith (1980) stated an equivalent result for the circular barrier case with $\mu=3/2$, but the above argument shows that the essential nature of the streamline deflection is unchanged if one generalizes to elliptical mountains having a single low-pressure region in the lee.

Smith (1980) also presented a formula for the streamline deflection far downstream, $\delta(x=\infty,y)$, in terms of the Fourier transform, $\hat{A}(\ell)$, of the x-z cross-sectional area, A(y), of the terrain:

$$\hat{A}(\ell) = \frac{1}{2\pi}\int_{-\infty}^{\infty} e^{-i\ell y}\, A(y)\, dy \quad , \tag{7.6}$$

$$\delta(x=\infty,y) = -i\,\frac{\overline{N}}{\overline{U}}\int_{-\infty}^{\infty} \mathrm{sign}(\ell)\, \hat{A}(\ell)\, e^{i\ell y}\, d\ell \quad . \tag{7.7}$$

For the particular barrier (4.1), A(y) is given by (4.6) and from GR (p. 426) one finds

$$\hat{A}(\ell) = \frac{abh_0}{\Gamma(\mu)}\left(\frac{|\lambda|}{2}\right)^{\mu-1} K_{\mu-1}\big(|\lambda|\big) \quad , \qquad \lambda = \ell b \quad . \tag{7.8}$$

Substituting this into (7.7) gives

$$\delta(x=\infty,y) = \frac{2\overline{N}ah_0}{\overline{U}}\, Y\, F(1,\mu;\tfrac{3}{2};-Y^2) \quad , \qquad (\mu>\tfrac{1}{2}) \quad . \tag{7.9}$$

The deflection is seen to be directly proportional to the downwind width of the barrier, a. The distance, b, characterizing the crosswind extent of the mountain, enters the expression only through the coordinate $Y=y/b$. In the limit of a long crosswind ridge, b tends to infinity. As a consequence, $Y\to0$ for any finite y, which in turn implies that

that $\delta(x=\infty,y)\to 0$. This is the expected result as the two-dimensional flow limit is approached.

Note that the hypergeometric function appearing in (7.9) is almost the same as that giving the two-dimensional pressure perturbation, $P_2(X)$, so that expressions for δ in terms of elementary functions for some special values of μ can be obtained from Table 4 in Appendix D. For example, for $\mu=3/2$ the simplified form is

$$\delta(x=\infty,y) = \frac{2\overline{N}ah_0}{\overline{U}} \frac{Y}{1+Y^2} \quad . \tag{7.10}$$

This is consistent with the result given by Smith (1980) for the circular barrier (a=b).

The case in which the terrain exponent $\mu=1/2$ is somewhat exceptional, for then the derivation of (7.9) based on Fourier transformation fails. This is because the barrier cross-sectional area, $A(y)$, becomes infinite, as indicated in Chapter 4 (see (4.6)). However, direct integration of the transverse velocity perturbation, as in (7.4), in the circular barrier case, shows that the formula (7.9) actually does apply for $\mu=1/2$ if a=b. The hypergeometric function in this case becomes

$$F(1,\tfrac{1}{2};\tfrac{3}{2};-Y^2) = \frac{\arctan(Y)}{Y} \quad , \tag{7.11}$$

so that (7.9) reduces to

$$\delta(x=\infty,y) = \frac{2\overline{N}ah_0}{\overline{U}} \arctan(Y) \quad , \qquad (\mu=\tfrac{1}{2}) \quad . \tag{7.12}$$

Note that for $\mu=1/2$, the maximum deflection at $x=\infty$ occurs as

$y \to \infty$, even though the lateral velocity, v', tends to zero in this limit. For larger values of μ, the terrain height falls off more quickly away from the peak, and the lateral deflection has a maximum at a finite value of Y.

CHAPTER 8

INTRODUCTION TO MOUNTAIN WAVE DRAG AND TRANSVERSE FORCE

8.1 Introduction

Even in the absence of friction, stably stratified air flowing over a barrier can experience a net retarding force, or drag, due to momentum transferred to the surface by mountain waves. This drag is associated with the asymmetrical surface pressure distribution, discussed in Chapter 5, with high pressure on the upwind side of the barrier and low pressure in the lee. As indicated in Chapter 3, the hydrostatic theory employed in this thesis is intended to be applied to barriers with a horizontal length scale, L, such that $\overline{N}L/\overline{U} \simeq 10$. For typical atmospheric values of $\overline{U}$ and $\overline{N}$, this criterion suggests a mountain half-width of the order of 10 km, or somewhat greater. As it happens, hydrostatic waves generated by flow over barriers of this scale are particularly efficient in transporting energy and momentum vertically (Klemp and Lilly, 1980). In view of the special physical role of hydrostatic mountain waves, it was decided to study the relation between the force on the terrain surface and some geometrical features of the terrain, using the simple model considered in previous chapters.

For a linear, non-hydrostatic flow over a series of infinitely-extended crosswind ridges, each having a half-width of 2 km, Sawyer (1959) calculated that the wave drag can be comparable to the frictional drag due to the roughness of the surface. Blumen (1965) extended this sort of calculation to three dimensions, using ridges parallel or perpendicular to the mean wind, formed by superimposing a series of circular barriers of the type studied by Crapper (1959). By numerically computing the drag for an airflow with realistic vertical profiles of wind and stability over a region of complex terrain in Wales, Bretherton (1969) was able to confirm the order of magnitude of the wave momentum flux suggested by the earlier studies. While it is important to understand the effect on the drag of a superposition of individual mountains (which gives a realistically complex barrier), there is still much to be learned using the simpler terrain forms and flow of the present study.

In the following, the drag on a linear, hydrostatic flow over a variety of elliptical mountains is determined as a function of the barrier steepness, eccentricity, and orientation. It is also shown that the force exerted by a mountain on the air can have a significant component perpendicular to the incoming flow for some barrier orientations. The basic formulae for the force components are presented in the next section. In an attempt to clarify the dependence of the drag on the vertical profile of the barrier, calculations for two-dimensional flow over infinitely-extended crosswind ridges are presented in Chapter 9. Isolated three-dimensional hills are treated in Section 9.4 and Chapter 10, which deal with the drag per unit crosswind length and the total force, respectively.

Increased understanding of the momentum flux associated with mountain waves was a goal of the ALPEX (Alpine Experiment) Subprogram of the Global Atmospheric Research Program of the World Meteorological Organization (Kuettner and O'Neill, 1981). The inclusion of such fluxes, in parameterized form, in large scale numerical weather prediction models, is also of current interest (Klemp and Lilly, 1980). Since terrain necessarily appears in numerical models in an idealized, usually smoothed, form, the effect of terrain smoothing on wave drag is also considered in the present work, in Chapter 11.

8.2 Basic expressions for wave drag and transverse force

In this section, basic integral formulae are presented for the drag and related quantities for unsheared, linear, hydrostatic flow.

Let $\vec{F}'=(D',T')$ be the horizontal force exerted by an airstream on a mountain, due to the pressure perturbation associated with mountain waves. D' is termed the wave drag because $D'>0$ implies a force on the air in the direction opposite to the incoming uniform airflow. T' is the force component transverse to the mean flow. Neglecting small quadratic terms involving the terrain slope, $\vec{\nabla}h=(\partial h/\partial x,\partial h/\partial y)$, $\vec{F}'$ is defined by

$$\vec{F}' = \int_{-\infty}^{\infty} \vec{f}'(y)\, dy = \int_{-\infty}^{\infty}\int_{-\infty}^{\infty} p'(x,y)\, \vec{\nabla} h\, dx\, dy \quad , \qquad (8.1)$$

where $\vec{f}'=(d',t')$ is the force per unit crosswind length.

Using (3.21) and (3.19) (with the + sign) to determine the pressure field, one has

$$\vec{F}' = i\, \bar{\rho}_o \bar{U}\, \bar{N} \int_{-\infty}^{\infty}\int_{-\infty}^{\infty}\int_{-\infty}^{\infty}\int_{-\infty}^{\infty} \frac{k\, \hat{h}(k,\ell)}{(k^2+\ell^2)^{\frac{1}{2}}} \vec{\nabla} h\, e^{i(kx+\ell y)}\, dk\, d\ell\, dx\, dy \quad , \qquad (8.2)$$

where $\hat{h}(k,\ell)$ is the Fourier transform of the terrain height, defined by (3.17). Integration by parts, with respect to x and y, in the integrals for D' and T', respectively, assuming the terrain height vanishes as $|x|\to\infty$ and $|y|\to\infty$, one obtains

$$\vec{F}' = (D',T') = 4\pi^2\, \bar{\rho}_o \bar{U}\, \bar{N} \int_{-\infty}^{\infty}\int_{-\infty}^{\infty} \frac{k\, \vec{k}}{(k^2+\ell^2)^{\frac{1}{2}}} \left|\hat{h}(k,\ell)\right|^2 dk\, d\ell \quad , \qquad (8.3)$$

where $\vec{k}=(k,\ell)$.

In a similar manner, one can show that the force per unit crosswind length is given by

$$\vec{f}' = (d',t') = 2\pi \bar{\rho}_o \bar{U}\, \bar{N} \int_{-\infty}^{\infty}\int_{-\infty}^{\infty} \frac{k\, \hat{h}}{(k^2+\ell^2)^{\frac{1}{2}}} \left(k\tilde{h}^*,\ i\,\frac{\partial \tilde{h}^*}{\partial y}\right) e^{i\ell y}\, dk\, d\ell, \qquad (8.4)$$

where $\tilde{h}=\tilde{h}(k;y)$ is the Fourier transform of $h(x,y)$ with respect to x alone, defined by (3.26), and * denotes the complex conjugate.

As in Chapter 5, the three-dimensional flow results can be compared to those that would be obtained if the flow were confined to vertical planes parallel to the mean wind. In the latter case, the pressure perturbation in (8.1) is replaced with the 'two-dimensional slice' form, given in (3.25). After some manipulation, the resulting expression for the total force on the barrier is

$$\vec{F}'_{2S} = (D'_{2S}, T'_{2S}) = 2\pi\bar{\rho}_o\bar{U}\,\bar{N}\int_{-\infty}^{\infty}\int_{-\infty}^{\infty}\tilde{h}\,\left(|k|\tilde{h}^*,\ i\ \mathrm{sign}(k)\,\frac{\partial\tilde{h}^*}{\partial y}\right)dk\,dy, \quad (8.5)$$

and the force per unit crosswind length is

$$\vec{f}'_{2S} = (d'_{2S}, t'_{2S}) = 2\pi\bar{\rho}_o\bar{U}\,\bar{N}\int_{-\infty}^{\infty}\tilde{h}\,\left(|k|\tilde{h}^*,\ i\ \mathrm{sign}(k)\,\frac{\partial\tilde{h}^*}{\partial y}\right)dk\quad. \quad (8.6)$$

CHAPTER 9

DRAG PER UNIT CROSSWIND LENGTH

9.1 Drag per unit crosswind length for infinitely-extended ridges

The relation between the shape of a barrier and the resistance it presents to the air is a complicated one. Before discussing aspects of this relation which depend on three-dimensional flow, first consider the two-dimensional flow over a uniform ridge which extends to infinity along the y axis, perpendicular to the mean wind. In this case, from (8.5), it is seen that the total drag on the air is infinite and the transverse force component is zero, since $\tilde{h}(k;y)$ becomes independent of y. However, the drag per unit crosswind length, $d_2'=d_{2S}'(y=0)$, is non-zero and finite. Scaling the terrain height by h_o and the x coordinate by a (see Appendix B), a non-dimensional measure of d_2' is

$$d_2 = d_2'/(\overline{\rho}_o \overline{U}\ \overline{N}\ h_o^2) = 2\pi \int_{-\infty}^{\infty} |\kappa|\ |\tilde{H}(\kappa)|^2\ d\kappa \quad , \qquad (9.1)$$

where $\tilde{H}(\kappa)=\tilde{h}(k;y=0)/(ah_o)$ and $\kappa=ka$. Primary determinants of the wave drag are the wind speed, $\overline{U}$, stability, $\overline{N}$, and the square of the terrain amplitude, h_o^2, incorporated in the normalization factor, $\overline{\rho}_o\overline{U}\ \overline{N}\ h_o^2$.

Note that the wave drag per unit crosswind length is independent of the parameter, a, the length scale along the direction parallel to the incident flow over an infinitely-long ridge. This implies that the value of d_2 is the same for a barrier $H(X)$ and for one related to it by changing the horizontal scale through a dimensionless factor, α, to give $H(X/\alpha)$. See Appendix C for the effect of this scale transformation on other variables. The invariance of d_2 with respect to α complicates the discussion of the relation between drag and terrain shape. At first thought, one might suppose that the maximum terrain slope would be a relevant parameter in the determination of d_2. However, it is not, at least in the most straightforward interpretation. For example, if the parameter, α, is increased, the magnitude of the terrain slope decreases everywhere. As a consequence, the pressure field falls off more gradually with distance from the ridge. The result is that the net force on the barrier is unchanged. Hence, it is terrain shape effects which are more subtle than the maximum height gradient that determine the wave drag.

In order to investigate other geometrical factors affecting the drag, the pressure perturbation and drag per unit length were calculated for a wide variety of terrain shapes. Three barrier types were considered: a single symmetrical ridge for which the height decreases monotonically away from the crest; a ridge on which a sinusoidal roughness has been superimposed; and, finally, a combination of two single ridges displaced from one another by an arbitrary separation. The main analytical results are derived in Appendices L, M, and N.

The single ridge cases will be discussed first. Barriers were considered with dimensionless terrain height, $H(X)=h(x)/h_0$, normalized in each case to give a maximum value of $H=1$ at $X=0$. The specific examples used are:

$$H = \begin{cases} (1+\chi^2)^{-\mu} & ;\ \alpha^2 = 2\mu+1 \ , \\[2ex] e^{-\chi^2} & ;\ \alpha^2 = 2 \ , \\[2ex] (1-\chi^2)^{\nu}\theta(1-\chi^2) & ;\ \alpha^2 = \begin{cases} 1 & ,\ \nu\le 1 \\ 2\nu-1 & ,\ \nu\ge 1 \end{cases} \ , \\[2ex] \dfrac{\ln\left(\dfrac{\delta^2+\chi^2}{1+\chi^2}\right)}{\ln(\delta^2)} & ;\ \alpha^2 = \dfrac{6}{\left((1+\delta^2)^2+12\delta^2\right)^{\frac{1}{2}} - (1+\delta^2)} \ , \\[2ex] \dfrac{1}{2\omega}\operatorname{arccot}\left(\dfrac{\chi^2+\cos 2\omega}{\sin 2\omega}\right) & ;\ \alpha^2 = \left(\cos^2 2\omega + 3\right)^{\frac{1}{2}} + \cos 2\omega \ , \end{cases} \tag{9.2}$$

where $\chi^2=X^2/\alpha^2$. Here α, μ, ν, δ, and ω are dimensionless real parameters which determine various characteristics of the vertical cross-section of the terrain. Although α can be an arbitrary number (see Appendix C), the particular values of α given in (9.2) are those for which the extreme terrain slopes occur at $X^2=1$. θ is a step function, which is 0 or 1 according to whether its argument is negative or positive, respectively. Limited results were also obtained for several other terrain forms, as indicated in Appendix K.

The terrain shapes were chosen primarily because they give rise to analytically tractable integrals for the drag. However, they turn out to be closely related. For example, replacing α^2 by $\alpha^2\mu$ in the μ-type terrain and taking the limit $\mu\to\infty$ leads to the exponential (Gaussian) form. Similarly, $\nu\to\infty$ gives an exponential form if α^2 is chosen as a linear function of ν. The logarithmic and arccot ridges both tend to a 'Witch of Agnesi' profile ($\mu=1$) in appropriate limits, namely, $\delta\to1$ and $\omega\to0$. A rectangular barrier, $H=\theta(1-X^2/\alpha^2)$, is obtained for both the $\nu=0$ and $\omega\to\pi/2$ cases. If the parameters are allowed to take on imaginary values, further connections between these terrain shapes are seen. For example, replacing α by $i\alpha$ and ν by $-\mu$, the ν-type terrain goes over into the μ-type. Noting that the arccot form can be written as

$$\frac{1}{4\omega i}\ln\left(\frac{X^2+e^{2\omega i}}{X^2+e^{-2\omega i}}\right) , \qquad (9.3)$$

one sees that, for imaginary values of ω, the arccot terrain shape is equivalent to the logarithmic one. These relations between the various barrier cross-sections provide useful checks on the analytical results.

In Fig. 19, the terrain height is plotted as a function of the dimensionless coordinate, X, for the μ, ν, and exponential type barriers. The examples shown have values of 1/2 and 3/2 for both μ and ν. To provide a basis for comparing the barriers, the parameter, α, which determines the overall horizontal scale, has been chosen, as in (9.2), to make the extremes of the terrain slope occur at $X^2=1$. As suggested by previous discussion, the choice of α has no effect on the drag per unit length, d_2. Values of d_2 are indicated beside each curve, increasing from $2/\pi\simeq.637$ for the $\mu=1/2$ case, to 1.0 for the exponential case (corresponding to $\mu=\infty$ and $\nu=\infty$), and continuing to increase to infinity

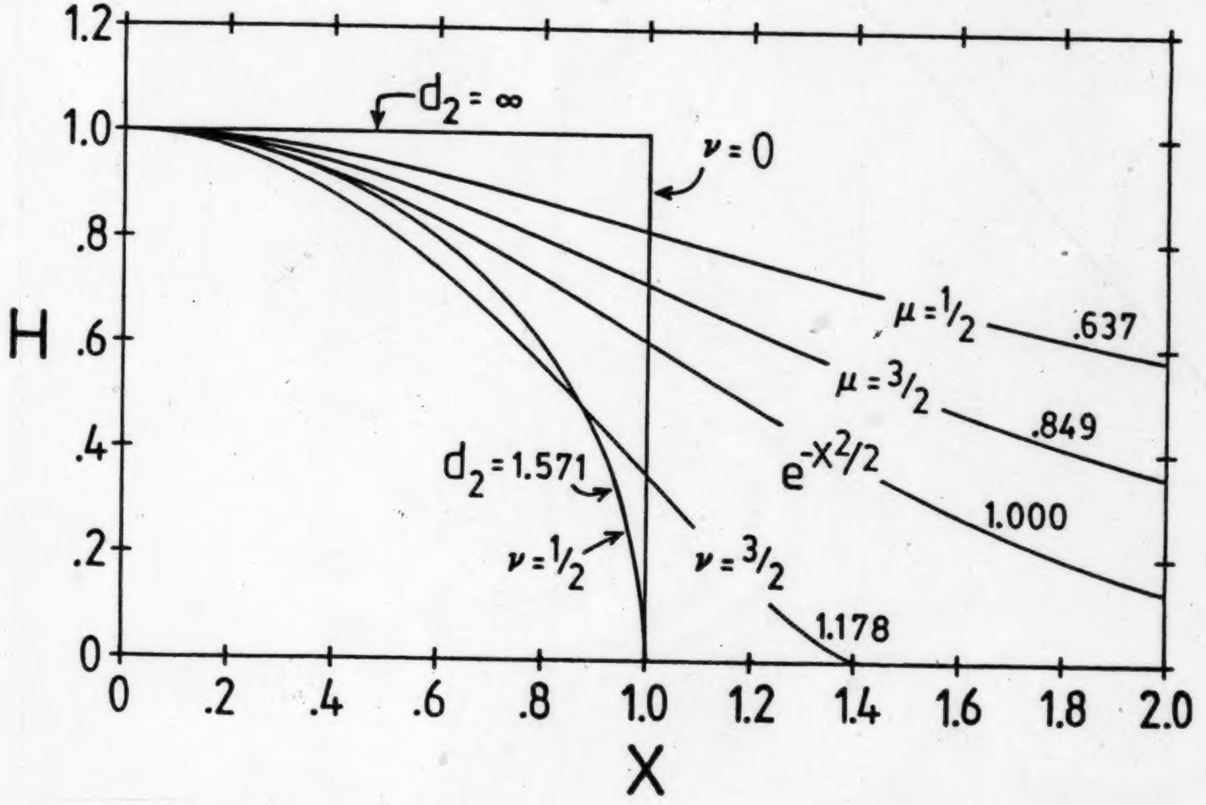

Figure 19. Normalized terrain height, H, as a function of the dimensionless coordinate, X, for the μ, ν and exponential type barriers defined in (9.2). The normalized drag per unit length, d_2, is marked beside each curve.

as ν decreases to 0. The analytical results in Appendix K (Y=0 in Table 8) show that the drag per unit length for the μ-type terrain is just the reciprocal of that for the ν-type, if $\mu=\nu$.

With the value of α fixed in the manner described, the variation in d_2 is seen to be closely related to the maximum steepness of the terrain. However, note that while the $\nu=1/2$ and $\nu=0$ ridges both have infinite slope at $X^2=1$, the wave drag per unit length is infinite only in the latter case. Similarly, examination of the pressure field for these cases (Appendix D) shows that, in spite of sharp corners at $X^2=1$, the maximum pressure perturbation for the $\nu=1/2$ case is finite, while that for $\nu=0$ is not. It is not only the relative steepness of the barrier, but also its smoothness, that determines the drag. The μ-type and Gaussian height fields are infinitely differentiable, giving Fourier transforms, $\tilde{H}(\kappa)$, which decrease exponentially fast for large wave number, κ. The resulting drag is relatively small. On the other hand, the ν-type terrain is not so smooth, having a zero-order discontinuity in the $\nu=0$ case, and having at most a finite number of continuous derivatives for larger ν. Consequently, the corresponding $\tilde{H}(\kappa)$ decreases only algebraically for large κ, leading to relatively large values of drag per unit length.

Fig. 20 illustrates a similar family of curves, composed of the logarithmic and arccot forms introduced earlier. The specific parameters for this example are $\delta=10$,

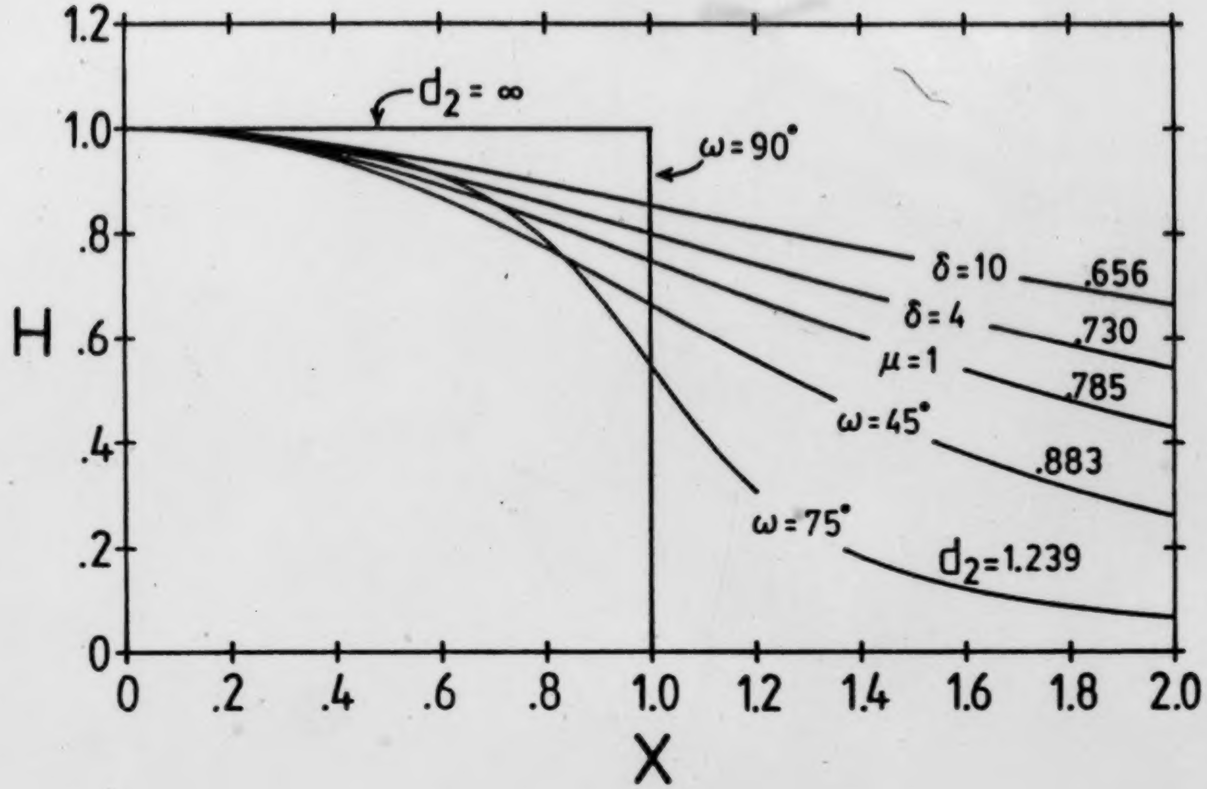

Figure 20. Normalized terrain height, H, as a function of the dimensionless coordinate, X, for the logarithmic (δ) and arccot (ω) barriers defined in (9.2). The curve marked $\mu=1$ corresponds to $\delta=1$ and $\omega=0$. The normalized drag per unit length, d_2, is marked beside each curve.

4, and 1 in the logarithmic case and $\omega=0$, 45°, 75° and 90° for the inverse trigonometric case (with $\delta=1$ and $\omega=0$ corresponding to the curve marked $\mu=1$). As in Fig. 19, the scale parameter, α, is given by (9.2) so that the extreme terrain slopes occur at $X^2=1$ for each curve. With this constraint on α, the drag increases with increasing terrain steepness, as in the examples of Fig. 19. Barriers with the logarithmic height profile have relatively small drag for all values of δ. However, the trigonometric form gives large drag per unit length as $\omega\to 90°$. While the limits $\nu\to 0$ and $\omega\to 90°$ both lead to the same barrier, $H=\theta(1-X^2)$, having infinite drag, the arccot profile is continuously differentiable for all $\omega\neq 90°$, whereas the ν-type terrain is not. Therefore, a discontinuity in the height field or its derivatives is not a necessary condition for a high-drag barrier.

Conversely, there are barriers with a sharp corner that have a relatively low drag. One example is a ridge with a triangular cross-section: $H=(1-|X|/\alpha)\theta(1-|X|/\alpha)$. In Appendix K, the drag per unit length for this type of ridge is shown to be $d_2=(4/\pi)\ln 2\simeq .8825$. In Fig. 21, the triangular height profile is plotted as a function of X for $\alpha=1/2$ and $\alpha=2$. Several other barriers having the same value of drag per unit length are also shown, corresponding to $H=\text{sech}(X/\alpha)$, with $\alpha=1/\ln(1+\sqrt{2})$, the $\mu\simeq 1.981$ case in (9.2) and the $\omega=45°$ ridges having $\alpha^2=\sqrt{3}$ and $1/\sqrt{3}$. These examples illustrate that an experienced eye or a keen grasp of Fourier transforms would be required to judge the magnitude of

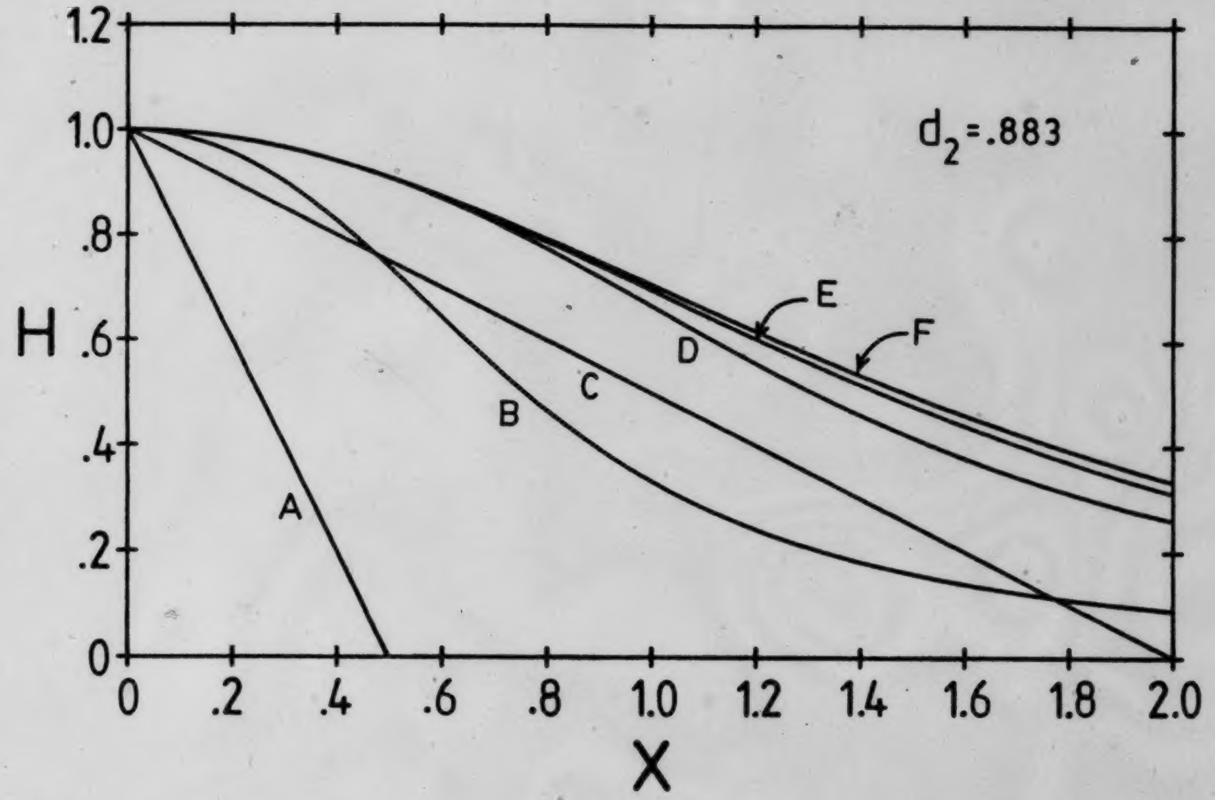

Figure 21. Normalized terrain height, H, as a function of the dimensionless coordinate, X, for several barriers having the same normalized drag per unit length, $d_2=0.883$. The terrain shapes are H=

A) $(1-2|X|)\ \theta(1-2|X|)$, B) $(2/\pi)\arctan(1/(X^2\sqrt{3}))$,
C) $(1-|X|/2)\ \theta(1-|X|/2)$, D) $(2/\pi)\arctan(X^2/\sqrt{3})$,
E) $(1+X^2/4.962)^{-1.98}$, F) $\mathrm{sech}(X\ln(1+\sqrt{2}))$.

the wave drag from a visual inspection of the vertical profile of the terrain height.

In Fig. 22, the drag per unit length is summarized for the various single-ridge cases by plotting it versus the corresponding maximum normalized pressure perturbation, P_{2m} for flow over the ridge. This form of presentation was chosen because, like d_2, P_{2m} is independent of the scale parameter, α. For details on the pressure field calculations refer to Appendix D. Simple closed-form expressions for the maximum pressure and drag exist for the logarithmic and arccot barriers, so a continuous curve of d_2 versus P_{2m} is shown for these cases. However, for the μ- and ν-type terrain, such expressions for the maximum pressure are not available. Therefore, only a few representative values are plotted. A strong positive correlation is seen between the drag per unit length and the maximum pressure perturbation. In fact, if the formula

$$d_2 = \frac{\pi}{2} P_{2m} + \Delta \;, \tag{9.4}$$

is used to summarize the results for $P_{2m}<1$, then $|\Delta|$ is less than 0.1 for all the single-ridge cases studied. One should use caution in applying this formula for $P_{2m}>1$ or to other barrier shapes. For example, in the limit $\omega \rightarrow 90°$, as the arccot terrain approaches the rectangular form, $H=\theta(1-X^2)$, the ratio of d_2 to P_{2m} tends to 2, rather than the value of $\pi/2$ that would be obtained from (9.4). Also, for barriers which do not have a simple monotonic decrease of height away

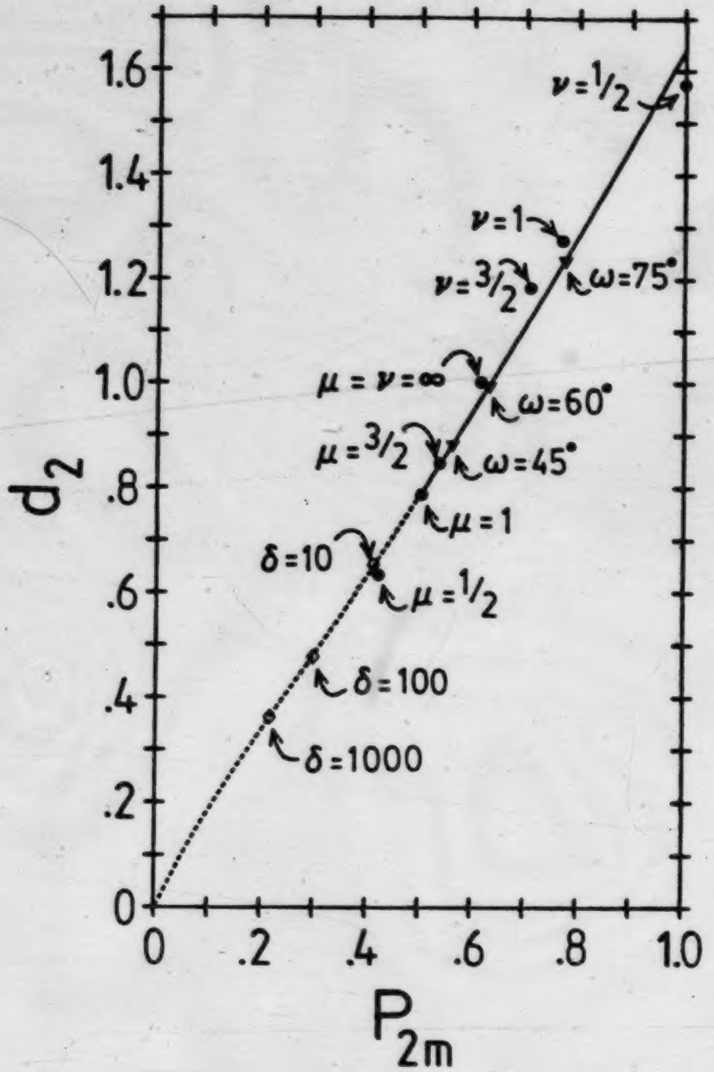

Figure 22. Normalized drag per unit crosswind length, d_2, versus the normalized maximum pressure perturbation, P_{2m}, for various barriers defined in (9.2). The dashed curve, labelled by δ values, corresponds to the logarithmic height profile, while the solid curve, labelled by ω values, is the result for the arccot terrain. The point denoted by $\mu=\nu=\infty$ is the exponential barrier.

from the ridgeline, the relation between d_2 and P_{2m} can be far from linear. The double ridges considered in Section 9.3 illustrate this point.

9.2 Drag per unit crosswind length for sinusoidally modulated ridges

Because of the κ factor in the integrand in the expression (9.1) for d_2, the contribution to the drag from the low wave number (or spatial frequency) components of the height field is suppressed. It is primarily the high frequency components that lead to large drag values. To some extent this idea was illustrated by the relatively slow decay of $\tilde{H}(\kappa)$ with increasing κ for the ν-type terrain as compared to the μ-type. To demonstrate this in a more explicit manner, barrier shapes were considered having a single smooth ridge upon which a sinusoidal variation, of frequency Ω, was superimposed. The specific examples studied are the Agnesi case (μ=1), $H = (A+B\cos\Omega X)/(1+X^2)$, and the Gaussian case, $H = (A+B\cos\Omega X)\exp(-X^2)$. The analytical results are derived in Appendix L.

In Figs. 23a and 23b, the drag per unit length is plotted against the spatial frequency, Ω, for the Agnesi and Gaussian shapes, respectively. The numerical values are based on (L.3) and (L.5). The barriers considered all have unit height at X=0 (A+B=1), but the amplitude of the cosine term varies from B=0 to B=0.5 in increments of 0.1. Direct

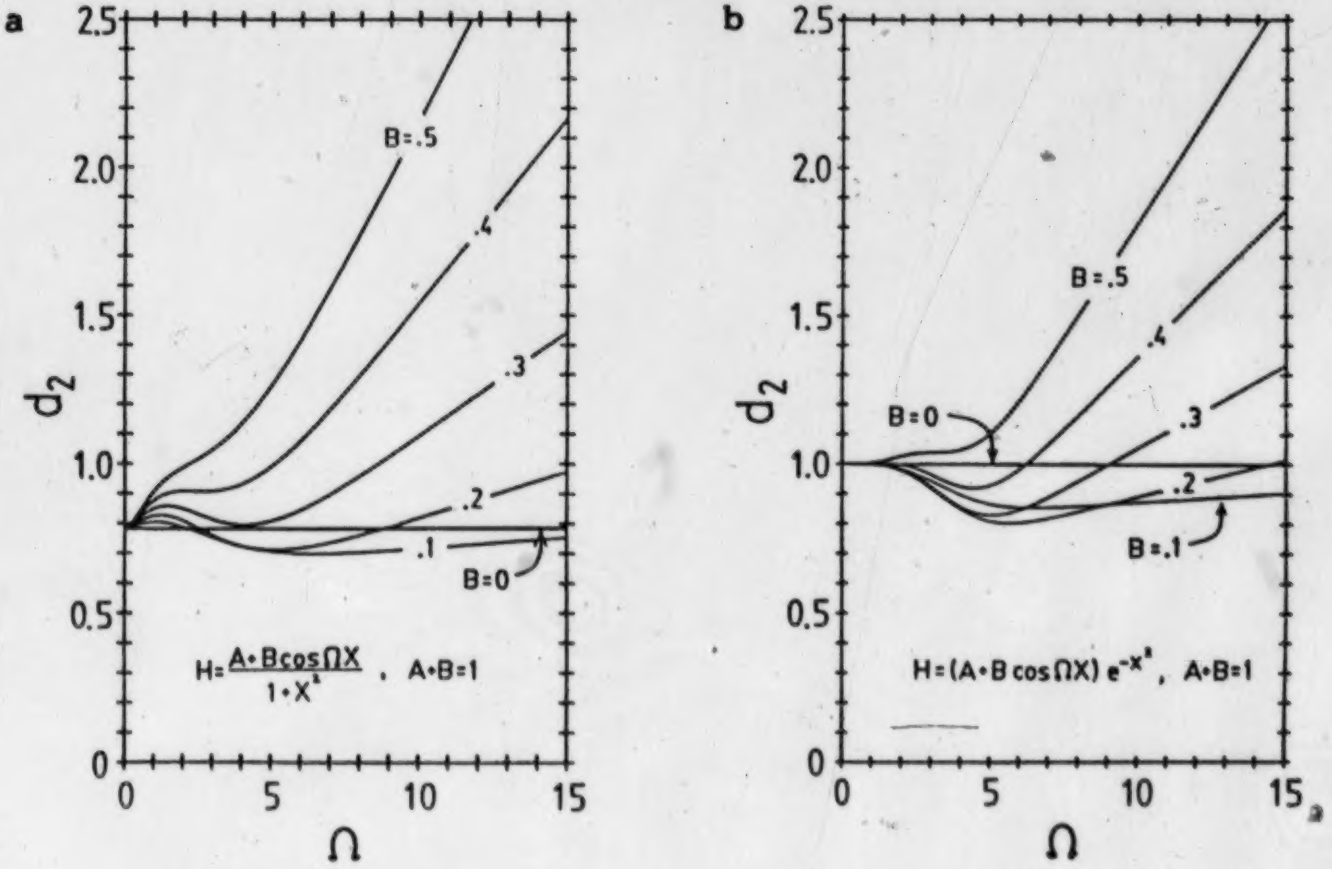

Figure 23. Normalized drag per unit crosswind length, d_2, as a function of the spatial frequency, Ω, for sinusoidally modulated barriers. Figs. 23a and 23b correspond to the Agnesi and Gaussian cases, respectively.

attention to the left hand portion of the figures. For $\Omega<1$, the relatively low-frequency modulation has a wavelength which is large in comparison to the length scale of the single ridge (B=0), so the oscillations are quickly damped away from the barrier peak. Referring to the figure, one sees that for the Gaussian ridge, d_2 is almost independent of Ω for low frequencies, whereas in the Agnesi case the drag increases with Ω and B. Expanding (L.3) and (L.5) for $|\Omega|<<1$ (GR, p. 931, for the latter equation), gives, for the Agnesi case:

$$d_2 = \frac{\pi}{4}\left(1+B\Omega^2\right) + O(|\Omega|^3) \quad , \tag{9.5}$$

and for the Gaussian case:

$$d_2 = 1 + \frac{B(3B-1)}{48}\,\Omega^4 + O(\Omega^6) \quad . \tag{9.6}$$

The vanishing of the low-order terms in Ω in (9.6) accounts for the difference in the low-frequency behaviour of the two cases. This can be understood from a more physical point of view by looking at the barrier shapes themselves. If $|\Omega X|<<1$ and A+B=1, then one can write the Gaussian terrain height as

$$(A+B\cos\Omega X)\, e^{-X^2} \approx e^{-\left(1 + \frac{1}{2}B\Omega^2\right)X^2} \quad , \tag{9.7}$$

as can be shown by expanding the Ω-dependent terms on both sides. Therefore, for sufficiently small Ω, the effect of the cosine modulation on the Gaussian hill is merely to change its scale while retaining the same basic shape. As mentioned previously, such a change does not affect d_2. Considering the Agnesi case in a similar manner, for $|\Omega X| << 1$ and $A+B=1$, one can write

$$\frac{A+B\cos\Omega X}{1+X^2} \approx \frac{1}{(1+X^2)(1+\frac{1}{2}B\Omega^2X^2)} \quad . \qquad (9.8)$$

Here, the sinusoidal term is seen to lead to a more sharply peaked barrier. However, since this is not caused by a simple change of horizontal scale, there is a stronger dependence of d_2 on Ω than in the Gaussian case.

As Ω increases, there is a transition region where the interaction of the sinusoidal and simple ridge contributions is more complicated. This will not be discussed here. However, for Ω larger than about 5, things appear to be simpler, with the curves in Fig. 23 showing a linear relation between d_2 and Ω and a strong dependence on the amplitude of the cosine term, B. This can also be seen by considering (L.3) and (L.5) in the range $\Omega >> 1$. One finds the drag per unit length for the Agnesi ridge becomes

$$d_2 \approx \frac{\pi}{4}\left(A^2+|\Omega|B^2\right) \quad , \qquad (9.9)$$

and that for the exponential one is

$$d_2 \approx A^2 + (\pi/8)^{\frac{1}{2}}|\Omega|B^2 \quad . \qquad (9.10)$$

If the horizontal scale of the simple ridge is large enough to contain several wavelengths of the cosine modulation, then these formulae imply that the drag contributions from the single ridge (A^2 terms) and the oscillation (B^2 terms) add independently to give the total, d_2. Therefore, if $\Omega >> 1$ and A is fixed, the cosine term always leads to increased drag. However, if the terrain is normalized to unit height, as in the examples of Fig. 23, so that $A+B=1$, then for sufficiently small B, there is a range of Ω such that d_2 is less than it would be for the unmodulated ridge ($B=0$). Nevertheless, for any non-zero value of B, the cosine term will dominate for sufficiently high frequency.

This importance of the high-frequency components of the terrain-height spectrum in determining the drag per unit length is the most significant result of the preceding analysis. One should remain aware, however, that nonhydrostatic and nonlinear turbulent processes, that are not included in the present model, become more important as the spatial scale decreases. Blocking of the flow upstream of mountain ranges, stagnation of air in valleys, and boundary layer separation in the lee of steep barriers are all processes which would tend to screen the upper flow from some of the high-frequency content of the terrain-height spectrum. In applying linear theory to real atmospheric cases, it might be necessary to mimic the effect of such processes by altering the terrain shape used in the model. The lee-wave model of Vergeiner (1971) is an example in which the low-level flow is artificially blocked. Also, Pearse et al. (1981) suggest the change in the effective terrain shape associated with boundary layer separation as an explanation of some features of the velocity amplification in the flow over laboratory model hills.

9.3 Drag per unit crosswind length for double ridges

The third type of infinitely-extended barrier for which the drag per unit length has been calculated is the superposition of two identical ridges, which have been displaced symmetrically from the origin, in opposite directions, by an amount, ϵ. If h(X) is the terrain height of a single ridge, then the double ridge is defined by

$$H(X) = h(X+\varepsilon) + h(X-\varepsilon) \quad . \tag{9.11}$$

The drag per unit length, d_2, is evaluated for a variety of single ridge shapes, h(X), in Appendix M. The specific forms considered are the $\mu=1$ (Agnesi) case: $h=1/(1+X^2)$, the triangular case: $h=(1-|X|)\theta(1-|X|)$, and the logarithmic and arccot cases given in (9.2). The pressure field can be calculated from

$$P(X) = p(X+\varepsilon) + p(X-\varepsilon) \quad , \tag{9.12}$$

where p(X) is the pressure perturbation for the single ridge, h(X). For these single ridge cases the pressure field consists of one windward high and one lee low, with these extrema each being displaced from the origin by a distance, X_m (see Appendix D). The pressure perturbation for a double ridge is more complicated, but, the extreme perturbation, P_{2m}, can be determined by solving dP/dX=0 (a cubic equation in X^2).

In Fig. 24a, the drag per unit length is plotted as a function of the maximum pressure perturbation for double ridges of the logarithmic form with $\delta=10$ (dashed curve), and the arccot form for a selection of ω values (including $\omega=0$, the Agnesi case). Fig. 24b is similar, but, on an expanded scale, shows results for the $\omega=45°$ and triangular barrier cases. The curves are parameterized in terms of the ratio of the ridge displacement to the position of the extreme pressure perturbation for a single ridge, ϵ/X_m.

For $\epsilon=0$, at the upper right of each curve, the two single ridges overlap completely, giving a barrier twice as high. The corresponding drag per unit length is four times that of a single ridge while the pressure perturbation is twice as large. If the ridges are separated ($\epsilon>0$), then d_2 and P_{2m} decrease rapidly. For $\epsilon/X_m=1$, the line of minimum low pressure associated with the upstream ridge overlaps with the line of maximum high pressure associated with the downstream ridge. For the arccot barriers, if the parameter, ω, is near 90°, this cancellation of the pressure field in the neighbourhood of $X=0$ leads to a sharp minimum in the drag near $\epsilon/X_m=1$. (Note the position of the diamond, marking $\epsilon/X_m=1$, near the minimum of the curve for ω larger than about 75° in Fig. 24a). However, for ω values near 0, or in the logarithmic case, the cancellation of the pressure field between the superimposed ridges is less complete because the pressure field for a single ridge has a less

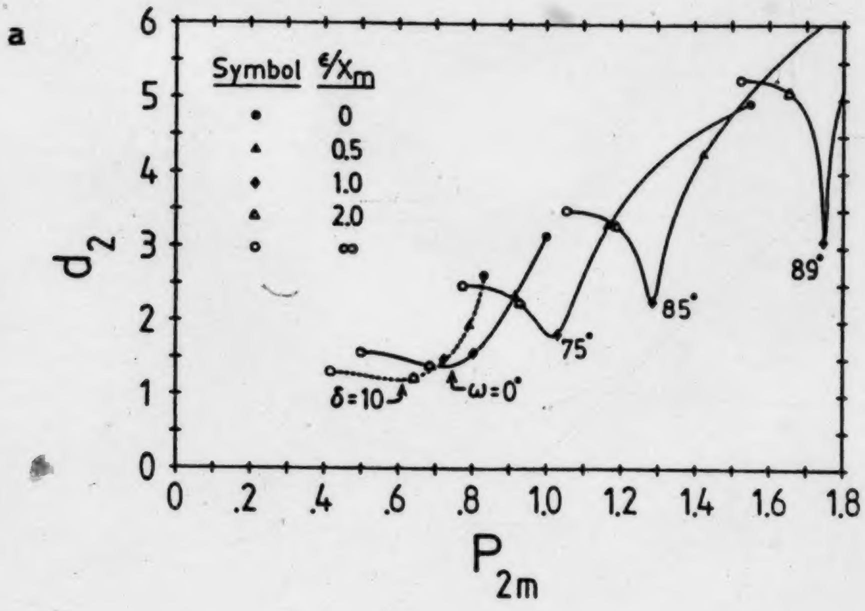

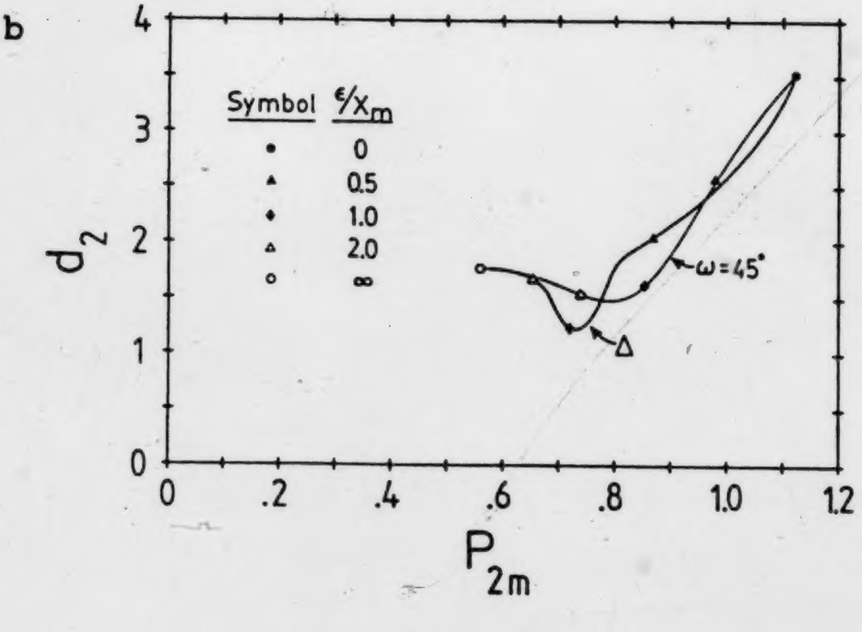

Figure 24. Drag per unit length, d_2, versus the maximum pressure perturbation, P_{2m}, for double ridge terrain shapes of the logarithmic (dashed curve) and arccot (solid curves) types (Fig. 24a), and the ω=45° and triangular types (Fig. 24b). Symbols mark the ratio of the ridge displacement to the position of the extreme pressure perturbation for a single ridge, ϵ/X_m.

pronounced maximum near $X=X_m$. Therefore, the minimum in d_2 is less sharp and occurs at larger values of ϵ/X_m. A similar behavior is seen in Fig. 24b. Although the two cases shown there have the same maximum pressure and drag per unit length values when $\epsilon=0$ or ∞, the triangular case shows a fairly sharp minimum in d_2 at $\epsilon/X_m \simeq .92$, whereas the $\omega=45°$ barrier gives a broader minimum with the extreme value at $\epsilon/X_m=\sqrt{3}\simeq 1.73$. These differences are consistent with the fact that the pressure field for a single ridge in the $\omega=45°$ case falls off as $-(\sqrt{8}/\pi)\cdot(X_m/X)$ as $X\to\infty$, whereas that for the triangular ridge goes as $-(\sqrt{2}/\pi)\cdot(X_m/X)$, with the numerical coefficient only half as large. This implies that the region of significant pressure perturbation in the triangular case is smaller, leading to a more effective cancellation when two ridges are superimposed with $\epsilon/X_m \simeq 1$.

As $\epsilon/X_m \to \infty$ (left side of each curve in Fig. 24), the interference between the ridges disappears. The maximum pressure reduces to that for a single ridge, but the total drag per unit length is double the single ridge value, because of independent contributions from the two ridges.

Fig. 25 shows the drag per unit length, explicitly as a function of ϵ/X_m, for some of the arccot types of barrier. From this diagram one can see many of the features mentioned in discussing the other figures. There is a sharp decrease in drag as ϵ increases from 0, associated with a rapid decrease in the height of the double ridge. There is a minimum of d_2 in the region of $\epsilon/X_m=1$ due to cancellation of

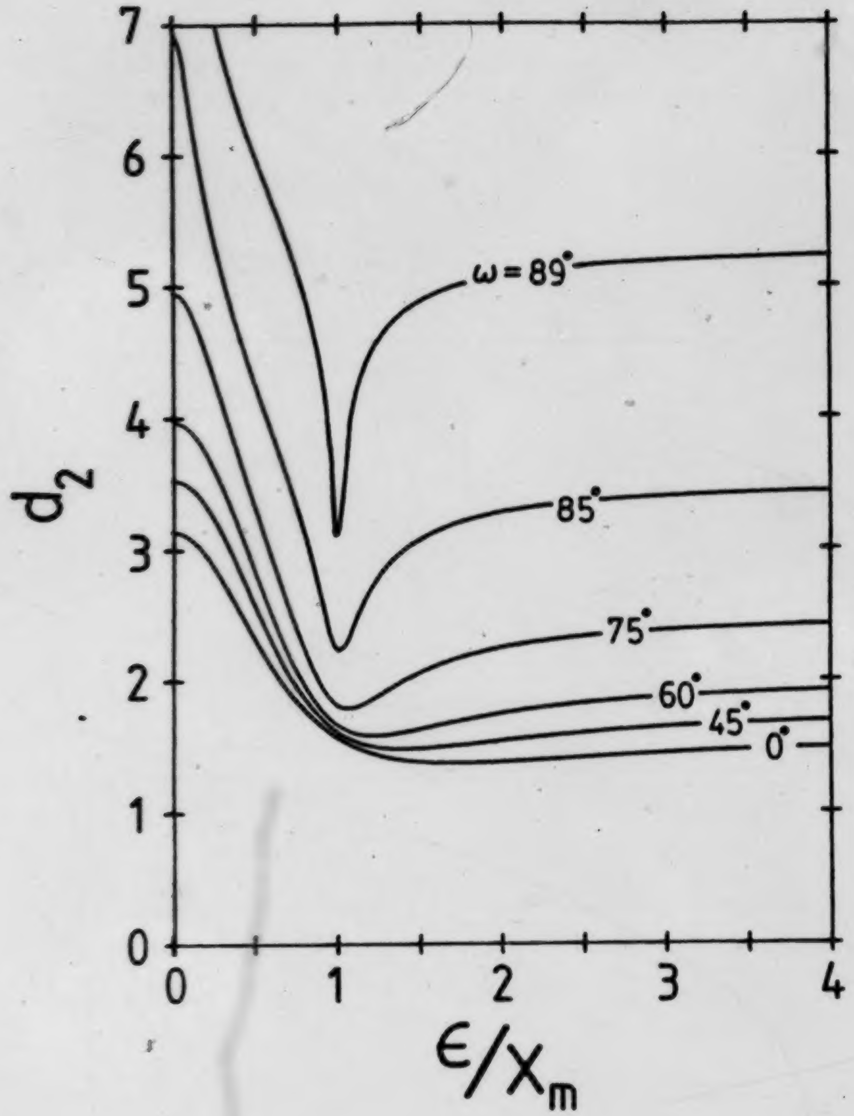

Figure 25. Normalized drag per unit crosswind length, d_2, for the superposition of two arccot ridges, as a function of the ratio of the ridge displacement to the position of the extreme pressure perturbation for a single ridge, ϵ/X_m.

the pressure perturbation between the barriers. Finally, there is a recovery to drag values twice that of a single ridge as $\epsilon \to \infty$. The curves become rather flat at the right edge of Fig. 25, with the d_2 value at $\epsilon/X_m=4$ differing from the value obtained at infinite separation by only 5.2% for $\omega=0$ and less than 1% for $\omega=89°$.

9.4 Drag per unit crosswind length for isolated three-dimensional barriers

For flow over the infinitely-extended barriers treated in preceding sections, the drag per unit length is uniform, being independent of the y coordinate. Now consider the more complicated case of three-dimensional flow over an elliptical hill with a non-zero ratio, $\gamma=a/b$, of horizontal length scales, a and b, along and perpendicular to the upstream flow, respectively.

Analytical treatment of the integral (8.4) for the drag per unit length in the three-dimensional case, in general, proves to be much more difficult than for the corresponding two-dimensional flow. However, the ν-type elliptical terrain, $H(R)=(1-R^2/\alpha^2)\ \theta(1-R^2/\alpha^2)$, with $R^2=X^2+Y^2$ ($X=x/a$, $Y=y/b$), is tractable for arbitrary γ if ν is half an odd integer. The results for $\nu=1/2$ and $3/2$ are derived in Appendix K, with the explicit formulae given by (K.11) and (K.14) in the $\alpha=1$ case. For $\alpha\neq1$, one can use the transformations in Appendix C. For the μ-type terrain with

$H=(1+R^2/\alpha^2)^{\mu}$, progress was made in the $\mu=1/2$ and 3/2 cases, but only for $\gamma=1$ (a circular hill). The normalized drag per unit length for the circular case, d_{3C}, is calculated in Appendix K, with the result given by (K.5). In Fig. 26 (solid curves), d_{3C} is plotted as a function of Y for the $\mu=3/2$ and $\nu=1/2$ cases (putting $\gamma=1$ in (K.11)). The horizontal scale parameter, α, has been chosen as $\sqrt{2}$ and 1, for the $\mu=3/2$ and $\nu=1/2$ cases, respectively, which implies that the maximum terrain slope occurs at R=1. With α fixed in this manner, the drag per unit length is non-zero for the $\nu=1/2$ hill only for $|Y|<1$, with a maximum at Y=0. The $\mu=3/2$ hill gives a much smaller value for d_{3C} at Y=0, but falls off more gradually away from the peak.

For comparison, the normalized drag per unit length, $d_{2S}=d'_{2S}/\bar{\rho}_0\bar{U}\ \bar{N}\ h_0^2$, that would result from flow in vertical planes, has been calculated from (8.6) (see Table 8 is Appendix K) and included in Fig. 26 (dashed lines). The relatively larger pressure field along Y=0 under the two-dimensional flow assumption leads to large values of $d_{2S}(Y)$ compared to $d_{3C}(Y)$ at Y=0. Specifically, $d_{2S}(0)/d_{3C}(0)=1.44$ for $\mu=3/2$ and 1.27 for $\nu=1/2$. For the hemispherical barrier, $\nu=1/2$, the value of d_{2S} exceeds that of d_{3C} for all Y for which the drag per unit length is non-zero. On the other hand, for the broader $\mu=3/2$ barrier, $d_{2S}(Y)\sim Y^{-6}$ for large Y (see Table 8), whereas $d_{3C}(Y)\sim Y^{-5}$ (from (K.5)), so d_{3C} exceeds d_{2S} for sufficiently large Y (Y>2.1). However, as will be discussed in Chapter 10, the total drag for these

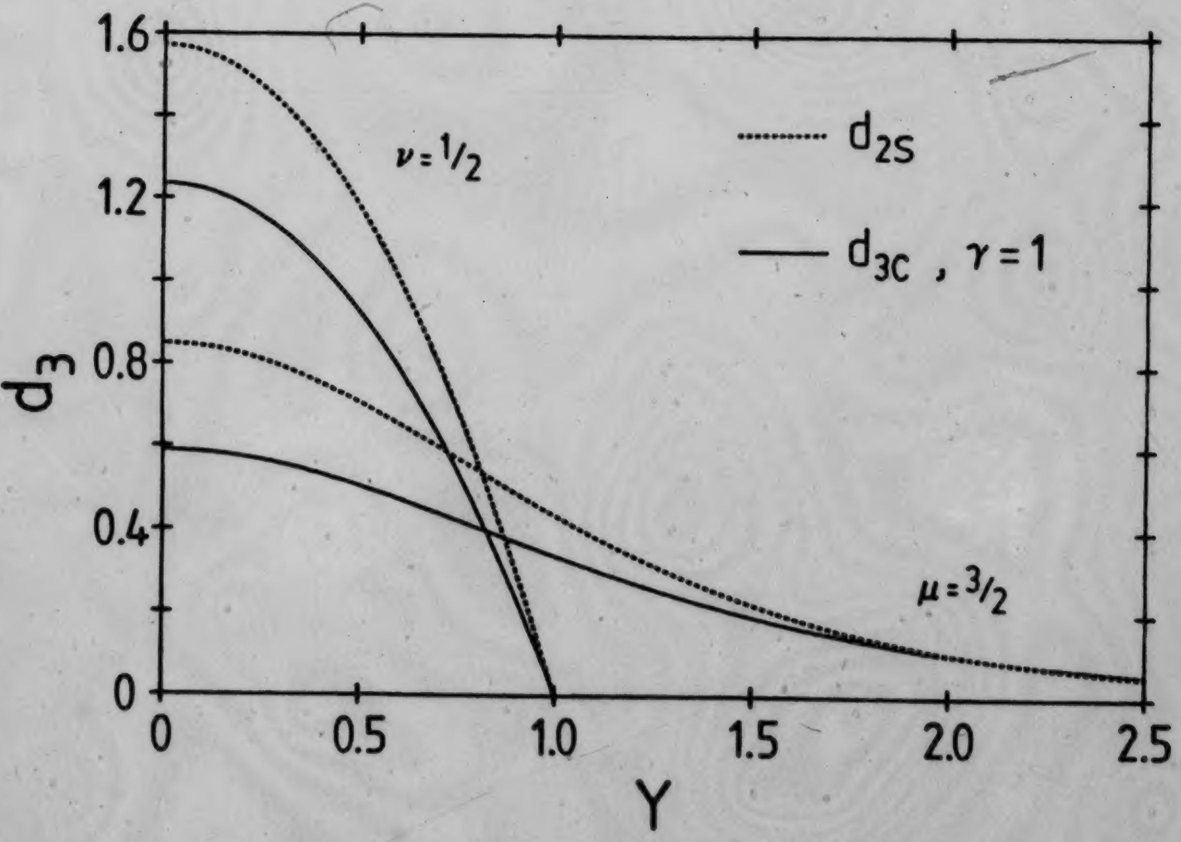

Figure 26. Normalized drag per unit crosswind length as a function of the crosswind coordinate, Y, for three-dimensional flow over a circular barrier (solid curves) and two-dimensional slice flow for the $\nu=1/2$ and $\mu=3/2$ barriers defined in Table 3 in Appendix D.

elliptical barriers, found by integrating the drag per unit length over Y, is always larger under the assumption of flow in vertical planes than it is for the three-dimensional flow solution.

In Fig. 27, the maximum drag per unit length, which occurs at $Y=0$, is shown as a function of the elliptical shape parameter, γ, for the terrain cross-sections $\nu=1/2$ and $3/2$, $\mu=1/2$ and $3/2$, and the Gaussian case ($\mu=\nu=\infty$). For the ν cases the results were obtained using (K.11) and (K.14). A closed form result (K.8) was found for the Gaussian hill, whereas in the μ cases, a truncated infinite series was used, given by (K.3). In all cases, d_3 is seen to decrease smoothly as the crosswind length scale decreases relative to the terrain width parallel to the mean wind (that is, as γ increases).

In Fig. 27, a diamond marks the position on each curve at which the drag per unit length for two-dimensional flow over an infinite ridge, $d_2=d_3(\gamma=0)$ exceeds that for the three-dimensional flow by 10% of $d_3(\gamma)$. The corresponding value of $1/\gamma$ ranges from about 2.2 in the $\nu=1/2$ case to 4.3 for $\mu=1/2$. Therefore, as far as calculations of drag per unit length are concerned, approximating an isolated three-dimensional barrier ($\gamma>0$) with an infinitely-extended ridge of the same cross-section ($\gamma=0$) is reasonable as long as the hill is several times wider across the mean wind than along it.

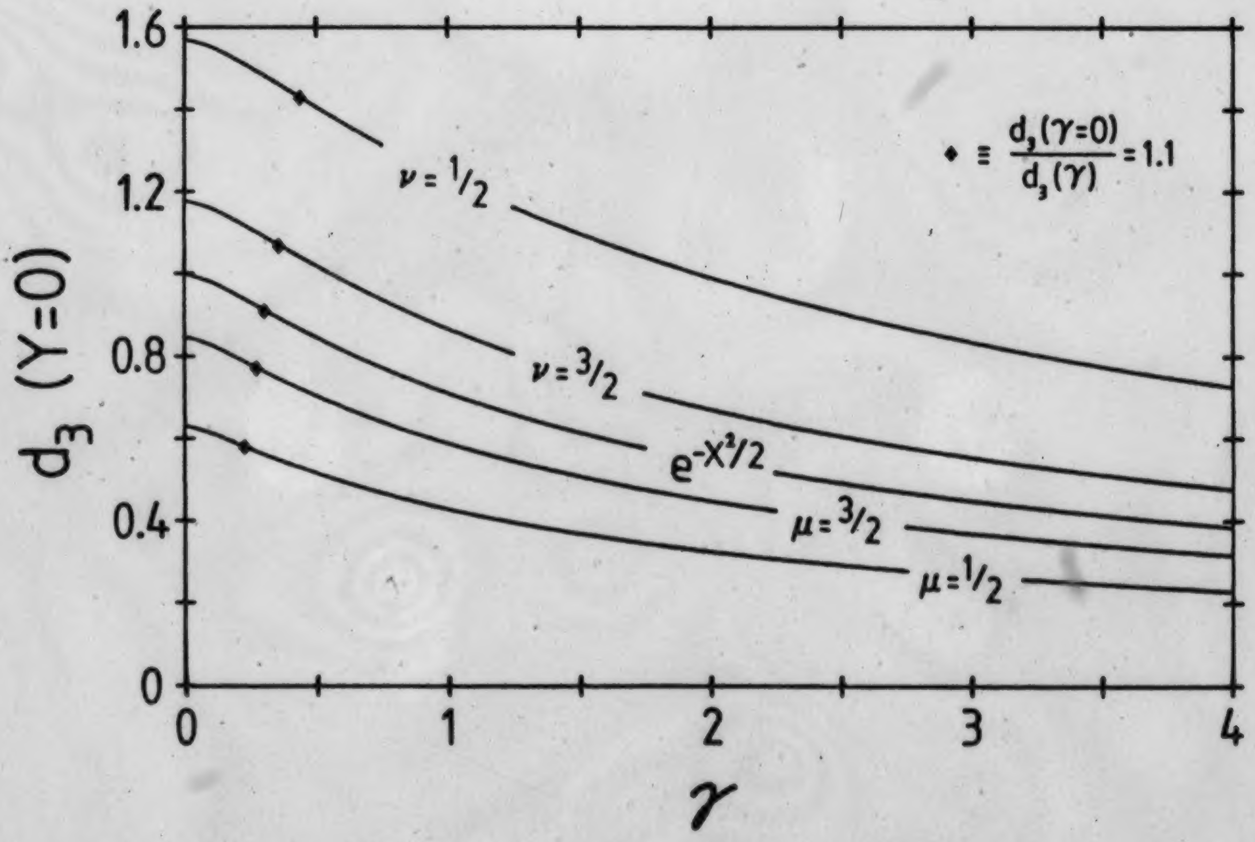

Figure 27. Normalized drag per unit length at Y=0 for three-dimensional flow over elliptical terrain as a function of the ratio of horizontal length scales, γ, for various terrain cross-sections defined in Table 3 in Appendix D. The diamond on each curve marks the position at which the drag per unit length for two-dimensional flow exceeds that for three-dimensional flow by 10%.

CHAPTER 10

TOTAL FORCE ON THE BARRIER

Integrating the force per unit crosswind length, $\vec{f}'$, with respect to y, as in (8.1), one obtains the total force, $\vec{F}'$, exerted by the air on the barrier. Even if the integral for the force per unit length proves difficult to evaluate, it is often the case that one can find the total force directly from (8.3). Some results concerning the dependence of $\vec{F}'$ on the shape and orientation of the barrier will now be presented.

Let $h(x,y;\psi)$ be the height field for a barrier rotated counterclockwise through an angle, ψ, from the barrier with height $h(x,y)=h(x,y;\psi=0)$ (see (0.1)). One can show that the Fourier transform of h, for the rotated case, is given by

$$\hat{h}(k,\ell;\psi) = \hat{h}(k',\ell';\psi=0) \quad , \tag{10.1}$$

where

$$\left.\begin{aligned} k' &= k\cos\psi + \ell\sin\psi \quad , \\ \ell' &= -k\sin\psi + \ell\cos\psi \quad . \end{aligned}\right\} \tag{10.2}$$

Substituting from (10.1) into (8.3), changing the integration variables to k' and ℓ', and noting that $k^2+\ell^2=k'^2+\ell'^2$, one finds that the components of $\vec{F}'$ are simple quadratic forms in $\cos\psi$ and $\sin\psi$. For example, in the case where $h(x,y)$ is an elliptical terrain form having a symmetry axis perpendicular to the mean flow, after some simplification, one obtains the normalized total force on the barrier,

$$\vec{F}_3 = (D_3, T_3) = \vec{F}'/(\overline{\rho}_o \overline{U}\, \overline{N}\, h_o^2\, b) \quad , \qquad (10.3)$$

with components

$$\left.\begin{aligned} D_3 &= G\ (B\cos^2\psi + C\sin^2\psi) \quad , \\ T_3 &= G\ (B-C)\sin\psi\cos\psi \quad . \end{aligned}\right\} \qquad (10.4)$$

Here

$$G = 16\pi^2 \int_0^\infty \rho^2 \left[\hat{H}(\rho)\right]^2 d\rho \quad , \qquad (10.5)$$

where $\hat{H}(\rho)$ is the normalized Fourier transform of the height field, defined in (B.4). $B=B_o(\gamma)$ and $C=C_o(\gamma)$, which are elliptical integrals defined in Appendix Q, are functions of the ratio of the horizontal length scales, $\gamma=a/b$.

As was the case for the drag per unit length, the total force, $\vec{F}'$, is seen to be proportional to the mean flow speed, $\overline{U}$, the stability, $\overline{N}$, and the square of the barrier amplitude. However, an additional geometrical factor, b, the unrotated terrain crosswind length scale, also appears. If the horizontal scale of a hill is changed, so as to present a greater cross-section to the wind, the force on the barrier increases in proportion.

The quantity G incorporates the influence of the vertical cross-section of the barrier, that is, the spacing of the elliptical terrain height contours, on the drag and lateral force on the air. G has been calculated in Appendix N for a variety of terrain forms with the results summarized in Table 9. For the particular mountain shape,

$h(x,y)=h_0/(1+R^2/\alpha^2)^{\mu}$, one finds, using (C.6), that

$$G = 4\,\Gamma(3/2)\,\frac{\Gamma(2\mu-1/2)}{\Gamma(2\mu+1)}\left[\frac{\Gamma(\mu+1/2)}{\Gamma(\mu)}\right]^2 \alpha\ .. \qquad (10.6)$$

If $\alpha=1$, G is a monotonically decreasing function of μ, having the value 2 for the relatively broad barrier with $\mu=1/2$ and decreasing to about 0.9 for the more sharply peaked case of $\mu=2$. Thus, the drag could vary by a factor of two or more, depending on how quickly the terrain height falls off from its hilltop value. If $\alpha=(2\mu+1)^{\frac{1}{2}}$, as in Fig. 19, the drag still decreases with increasing μ, but at a slower rate. Recall that the drag per unit length for the ridge $H(X)=(1+X^2)^{-\mu}$ showed the opposite trend with μ. As μ increases and the barrier becomes steeper, the maximum pressure perturbation becomes greater, tending to increase the drag. However, the crosswind profile of the barrier also becomes more sharply peaked. The reduced cross-section that the hill presents to the incoming flow tends to reduce the drag. It is this second effect that dominates the value of G in the present example, so that the net result is a decrease in the total force on the barrier as μ increases.

An interesting property of elliptical barriers is that the dependence of D_3 and T_3 on the orientation and eccentricity of the height contours separates completely from the dependence, through G, on the vertical cross-section. The former effects enter through the terms involving $B(\gamma)$, $C(\gamma)$, and ψ. The functional form of the dependence on γ and ψ is exactly the same as in the evaluation of the pressure gradient maximum that occurs over the barrier (see Appendix F). One finds

$$\vec{F}' = -h_o ab \frac{G}{I} \vec{\nabla} p' \Big|_{R=0} \quad , \tag{10.7}$$

where I, given by

$$I = 4 \int_0^\infty \rho^2 \hat{H}(\rho)\, d\rho \quad , \tag{10.8}$$

like G, is an integral independent of γ and ψ. Thus, the direction of the net force on an elliptical barrier is determined by the pressure gradient at the mountain top.

The dimensionless drag and lateral force, normalized by G, are plotted as functions of $\gamma=a/b$ for various barrier orientation angles, ψ, in Figs. 28a and 28b, respectively. Since $\vec{F}'$ is proportional to b, the graphs can be regarded as showing the variation of the force on the barrier as a is varied, holding b fixed. The maximum normalized drag is obtained for a long ridge, with its axis perpendicular to the incoming flow ($\gamma=0$, $\psi=0$). A circular barrier, corresponding to $\gamma=1$, gives a drag which is lower than this maximum by a factor $\pi/4$. As should obviously be the case, the drag is independent of ψ for a circular barrier. However, for an extended barrier, with $\gamma<1$, the orientation of the ridge, relative to the incoming flow, has a considerable effect on the drag, as is seen by comparing the $\psi=0$ and $\psi=90°$ curves in Fig. 28a. As was indicated by Blumen (1965), the drag is much less if the long axis of a ridge is aligned with the mean flow than if it is perpendicular to

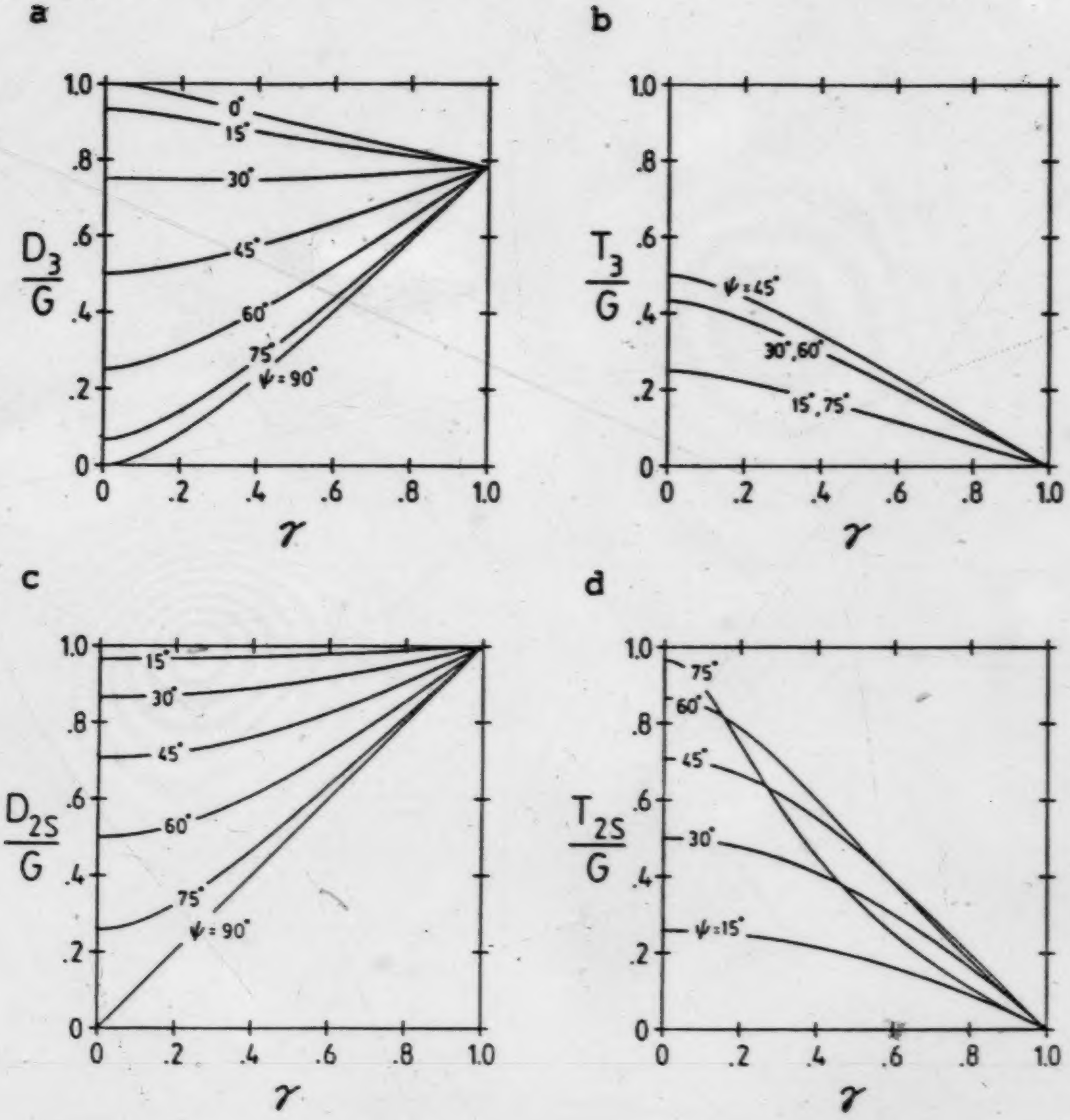

Figure 28. (a) and (b): Drag and transverse force components, D_3 and T_3, respectively, for three-dimensional flow, normalized by the factor, G (defined by (10.5)), as a function of the scaling ratio, γ, for various barrier orientation angles, ψ.

(c) and (d): As in (a) and (b), except showing force components, D_{2S} and T_{2S}, for two-dimensional slice flow.

the stream. This is confirmed by the present results. From (10.4), it is found that the ratio of the drag in the parallel (ψ=90°), to that in the perpendicular case (ψ=0), is equal to C_0/B_0. This is a function of γ alone, being independent of the vertical cross-section of the terrain. Evaluating B_0 and C_0 from their expressions in terms of elliptic integrals given in (Q.3), one finds the drag ratio, C_0/B_0, to be about 0.35 for $\gamma=1/2$ and 0.12 for $\gamma=1/4$. Thus, a 90° change in wind direction can result in a change in drag of more than a factor of eight for an elliptical barrier four times as long as wide.

Next, refer to Fig. 28b, which shows the force exerted on the mountain, in a direction normal to the mean flow. For the ψ=0 and ψ=90° cases, or for arbitrary ψ in the circular case (γ=1), the incoming flow is parallel to an axis of symmetry of the mountain, giving a pressure field which is symmetric about the x axis. Thus, there is no net force component on the barrier in the lateral direction ($T_3=0$). However, for an intermediate orientation of an extended barrier ($0<\psi<90°$; $\gamma<1$) this symmetry is lost, leading to a non-zero value for T_3. For any fixed value of γ, the maximum transverse force occurs for a barrier inclined at a 45° angle to the mean flow. Comparing Figs. 28a and 28b, it is seen that the transverse force is an appreciable fraction of the drag force, except when the mountain is almost circular ($0.8<\gamma\leq 1$, say), or has its long axis nearly perpendicular to the incoming flow ($\psi<10°$, say). For an extended ridge with its long axis nosing into the incident flow ($\psi > 45°$), T_3 can exceed D_3 for sufficiently small γ. This is seen more clearly in Fig. 29, which shows isopleths of the ratio, T_3/D_3, in a (γ, ψ) plane. For ridges more than about three times wider across the wind than along it, the lateral force can be larger than the drag. Even for a barrier with a horizontal cross-section as round as $\gamma = .5$, T_3/D_3 exceeds .5 for a limited range of orientation angle.

The surface drag and lateral force corresponding to the three-dimensional flow pressure perturbation are now compared to the force, $\vec{F}'_{2S}$, that would arise if the motion were confined to the x-z plane, as if the barrier were infinitely long, with a uniform vertical cross-section. A general expression for $\vec{F}'_{2S}$ has already been given in (8.5). For an elliptical barrier, with scale lengths, a and b, along the x and y axes, respectively, which has been rotated counterclockwise by an angle ψ, it is shown in Appendix O that the components of the normalized force, $\vec{F}'_{2S} = (D'_{2S}, T'_{2S}) = \vec{F}'_{2S}/(\bar{\rho}_o \bar{U}\ \bar{N}\ h_o^2\ b)$ are

$$\left.\begin{aligned} D_{2S} &= G\ (\cos^2\psi + \gamma^2 \sin^2\psi)^{\frac{1}{2}} \quad , \\ T_{2S} &= G\ \frac{(1-\gamma^2)\cos\psi \sin\psi}{(\cos^2\psi + \gamma^2 \sin^2\psi)^{\frac{1}{2}}} \quad , \end{aligned}\right\} \qquad (10.9)$$

where $\gamma = a/b$, and G is given by (10.5). The dimensional factor, $\bar{\rho}_o \bar{U}\ \bar{N}\ h_o^2\ b$, and the dependence on the vertical cross-section of the barrier, implicit in G, are exactly the same as in the calculation based on the three-dimensional

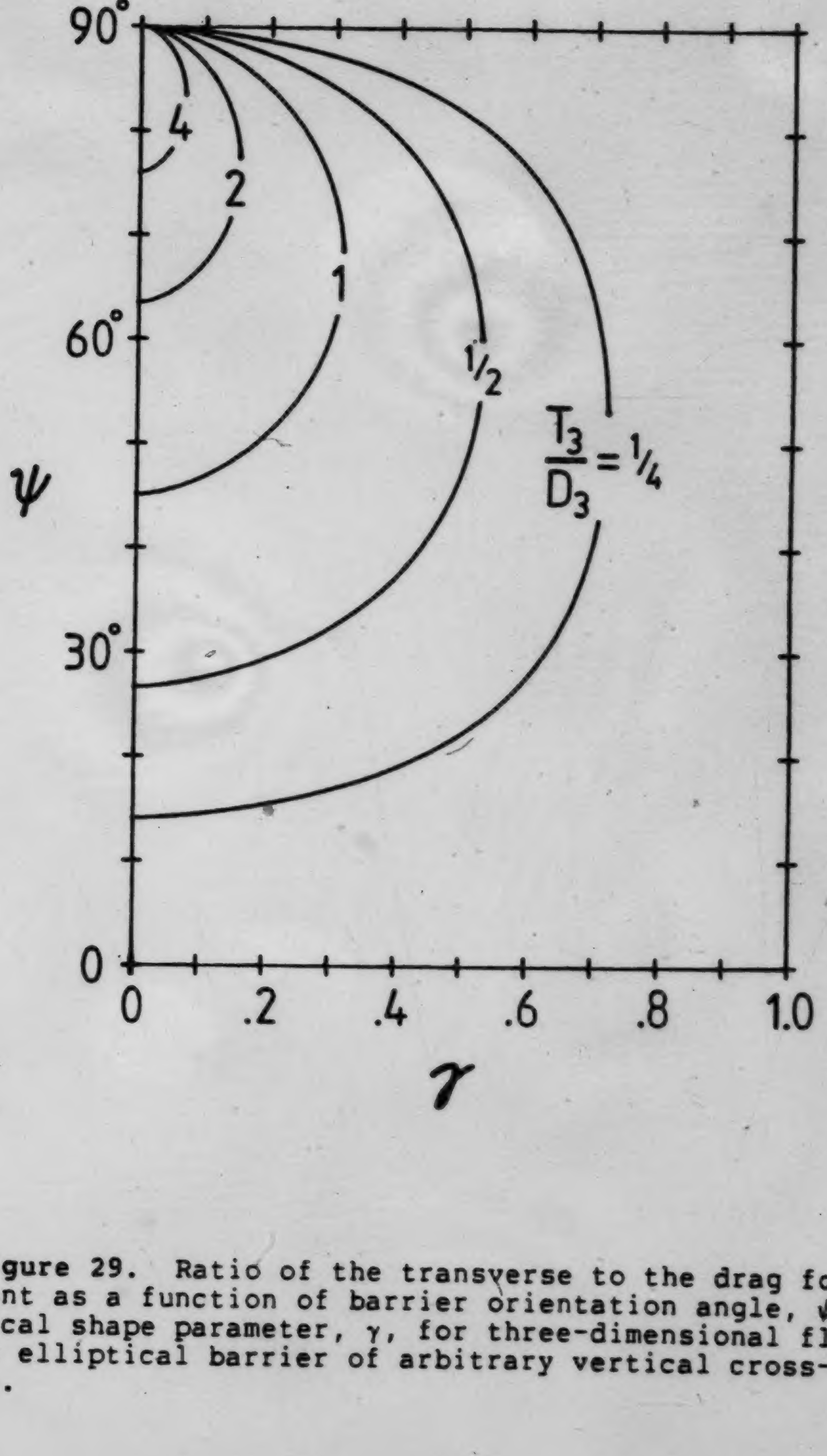

Figure 29. Ratio of the transverse to the drag force component as a function of barrier orientation angle, ψ, and elliptical shape parameter, γ, for three-dimensional flow over an elliptical barrier of arbitrary vertical cross-section.

flow pressure perturbation.

Figs. 28c and 28d illustrate the dependence of D_{2S} and T_{2S} (normalized by the factor G), respectively, on γ and ψ. Careful comparison of Figs. 28a and 28c shows that the two-dimensional slice flow approximation overestimates the drag for all values of γ, except the case of an infinitely-extended barrier, perpendicular to the wind (γ=0, ψ=0). For a circular barrier, the assumption of flow over the barrier in vertical planes, leads to a calculated drag which is too high by a factor of $4/\pi$. The maximum of the normalized absolute difference, $(D_{2S}-D_3)/G$ is 0.25, which occurs for a long ridge, rotated 60° from the perpendicular to the airstream (γ=0, ψ=60°). For ψ in the range from 35° to 80°, one finds $(D_{2S}-D_3)/G$ to be only a weak function of the eccentricity of the elliptical terrain, with 0.2 being a typical value.

One can ask how small the ratio of the barrier cross-wind to downwind length scales has to be for the two-dimensional slice flow solution to approach the three-dimensional one to a given precision. For the unrotated barrier case (ψ=0), for example, one finds that D_{2S} exceeds D_3 by 10% for γ=0.44 and by 5% for γ=0.27. These γ values are larger than the corresponding ones related to estimation of the maximum pressure perturbation discussed in Chapter 5 ($\gamma \approx 1/3$ and 1/5 for the 10% and 5% precisions, respectively). Thus, the total drag is somewhat less sensitive to the flow around the barrier than is the maximum pressure perturbation.

Next, concerning the force acting perpendicular to the mean flow, comparison of Figs. 28b and 28d shows that, like the drag, it is larger under the two-dimensional slice flow assumption. Other than correctly predicting zero lateral force in the $\psi=0$ and $\psi=90°$ cases, and in the circular hill case ($\gamma=0$), the two-dimensional slice flow approximation, T_{2S} is not particularly useful for quantitative estimates of T_3.

In this chapter, it has been shown that the orientation and eccentricity of an elliptical mountain have a large effect on the force exerted by the barrier on the air, in association with linear, hydrostatic mountain waves in a model atmosphere having a simple vertical structure.

CHAPTER 11

EFFECT OF SMOOTHING ON SURFACE DRAG AND TRANSVERSE FORCE

11.1 Introduction to terrain smoothing

The mountain barriers represented in numerical models of atmospheric flow are necessarily smoothed versions of the real terrain. This idealization may be introduced because of limitations on computing resources, to control a numerical instability, or to ensure that the motion satisfies constraints particular to the model, such as being quasi-geostrophic or hydrostatic. Although there has been some recognition of the need to maintain the effect of adequate mountain steepness in numerical models (for example, Egger, 1972; Tibaldi et al., 1980; Fawcett, 1969; and Bettge, 1983), there has been relatively little quantitative exploration of how smoothing affects the predicted flow fields. In view of this, the present section is devoted to illustrating the effect of terrain smoothing on surface pressure and mountain wave drag in the context of the linear hydrostatic model used in this paper. Two different smoothing operations are considered: differentiation and spectral truncation.

11.2 Differential smoothing

First, suppose that the smoothing can be represented by applying a linear differential operator, S, to the unsmoothed terrain height field, $h(x,y)$ to yield

$$<h(x,y)> = S\, h(x,y) \quad . \qquad (11.1)$$

For example, one might choose a smoother based on the Laplacian, with $S=1+\sigma\nabla^2$, or $S=1+\sigma\nabla^4$, where $|\sigma|<<1$, is a parameter controlling the degree of smoothing. The latter form was used by Hoskins (1980) in preparing a terrain field for possible input to numerical models of atmospheric motion.

An example of the effect of the $S=1+\sigma\nabla^2$ operator on the height field is shown in Fig. 30, for the unsmoothed barrier $H=(1+R^2)^{-\mu}$, with $\mu=3/2$. Figs. 30a and 30c show contours of the unsmoothed terrain for the $\gamma=1/2$ and $\gamma=2$ cases, respectively, while Figs. 30b and 30d show the corresponding height fields smoothed with the parameter $\sigma=.06a^2$, where a is the length scale of the terrain along the x axis. The effect of the smoothing operator on the height field is to reduce the maximum height of the barrier, for example, from 1.0 to 0.775 in the case of Fig. 30b. Far from the peak the terrain is changed relatively little. The value of σ is four times larger in Fig. 30d than in Fig. 30b because of a doubling of the length, a. While having been somewhat circularized near the origin, the terrain contours in Fig. 30b maintain a quasi-elliptical shape under the smoothing operation. The larger σ parameter of Fig. 30d leads to considerable distortion of the basic mountain shape. In the latter case, the main barrier has been split into two peaks

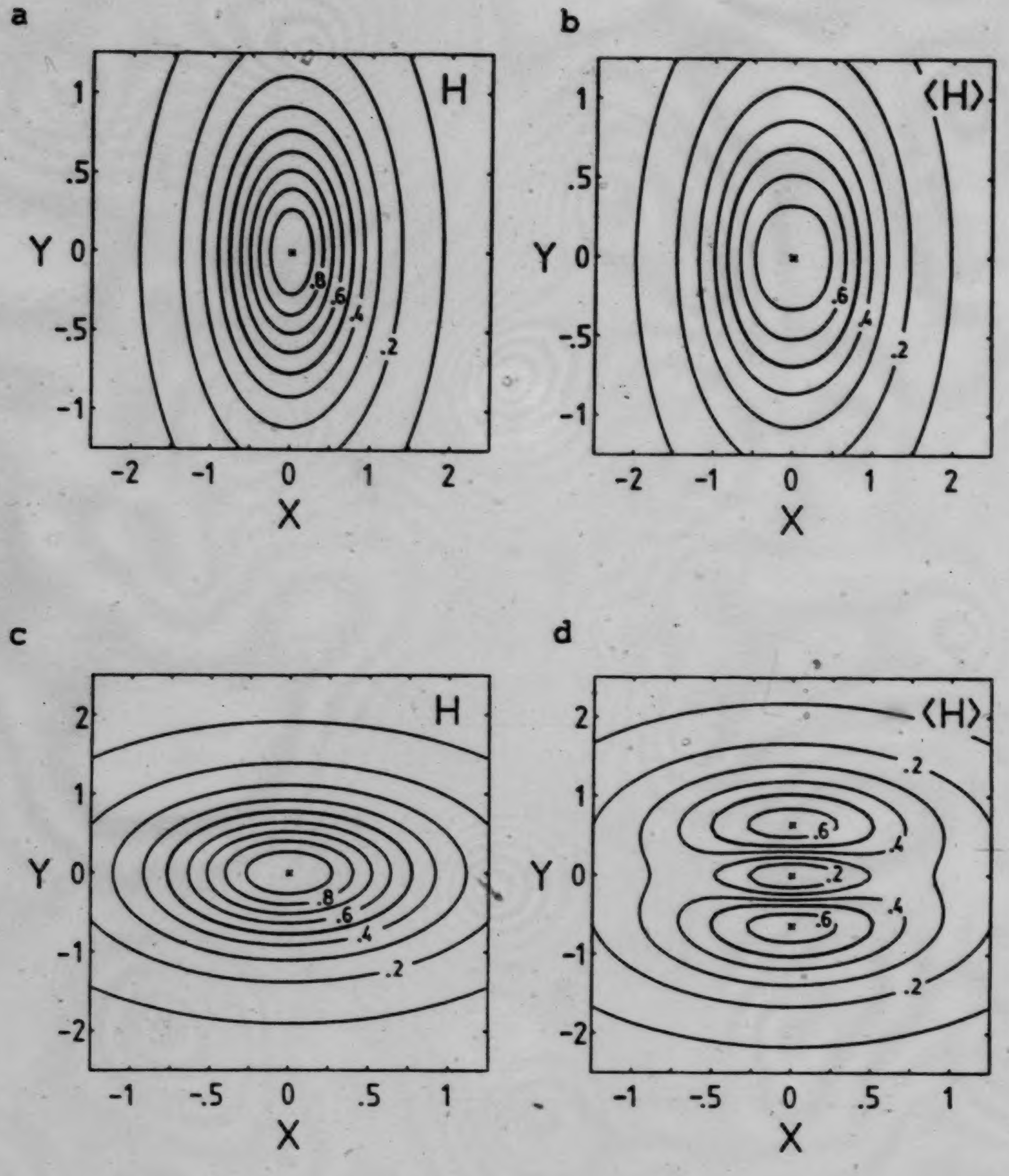

Figure 30. Contours of terrain height $H=(1+R^2)^{-\mu}$, with $\mu=3/2$, and smoothed height $\langle H\rangle=(1+\sigma\nabla^2)H$, with $\sigma=.06a^2$, for horizontal length scale ratio $\gamma=1/2$ (Figs. 30a and 30b) and $\gamma=2$ (Figs. 30c and 30d). Figs. 30a and 30c are the unsmoothed cases and Figs. 30b and 30d are the smoothed ones. In Fig. 30d, the parameter, a, is twice as large as in Fig. 30b.

with height 0.655, with the value at the origin being only 0.1.

The Fourier transforms, $\langle\hat{h}(k,\ell)\rangle$ and $\hat{h}(k,\ell)$, of the smoothed and unsmoothed height, are defined by integrals of the form given in (3.17). Assuming that S is represented in the general form

$$S = \sum_{m=0}^{M} \sum_{n=0}^{N} \sigma_{mn} \frac{\partial^m}{\partial x^m} \frac{\partial^n}{\partial y^n} , \qquad (11.2)$$

and that the relevant derivatives exist, then

$$\langle\hat{h}(k,\ell)\rangle = \hat{S}(k,\ell)\, \hat{h}(k,\ell) , \qquad (11.3)$$

where

$$\hat{S}(k,\ell) = \sum_{m=0}^{M} \sum_{n=0}^{N} \sigma_{mn} (ik)^m (i\ell)^n . \qquad (11.4)$$

This is shown by integration by parts in the integral defining $\langle\hat{h}\rangle$.

Substituting (11.3) into (3.20) for the pressure perturbation, assuming operations of differentiation and integration can be interchanged, one obtains the pressure field for the smoothed terrain as

$$\langle p'(x,y,z)\rangle = S\, p'(x,y,z) . \qquad (11.5)$$

Due to the linearity of the model, the pressure perturbation corresponding to the smoothed barrier is obtained simply by applying the same operator, S, to the unsmoothed pressure field as was applied to the terrain height.

The force, $\langle\vec{F}\rangle=(\langle D\rangle,\langle T\rangle)$, that the air exerts on the smoothed mountain, can be found by replacing $\hat{h}(k,\ell)$ by $\langle\hat{h}(k,\ell)\rangle$ in (8.3). As in Chapter 10, one can consider the effect on the force of changing the orientation of the barrier relative to the incoming wind. If the barrier is rotated from its initial position by a counterclockwise angle, ψ, and subsequently smoothed, then the Fourier transform of the resulting height field is given by

$$\langle\hat{h}(k,\ell;\psi)\rangle = \hat{S}(k,\ell)\ \hat{h}(k',\ell';\psi=0) \quad , \qquad (11.6)$$

where k' and ℓ' are defined in (10.2). On the other hand, if the terrain is rotated after smoothing, then its Fourier transform is

$$\langle\hat{h}(k,\ell)\rangle(\psi) = \hat{S}(k',\ell')\ \hat{h}(k',\ell';\psi=0) \quad . \qquad (11.7)$$

If the smoothing operator, S, is isotropic, that is, depends only on the Laplacian, ∇^2, then S will depend only on the combination $k^2+\ell^2=k'^2+\ell'^2$. This relation implies that $\hat{S}(k,\ell)=\hat{S}(k',\ell')$. Comparison of (11.6) and (11.7) then shows that the resulting height field is independent of the order of the smoothing and rotation operations. The remainder of the discussion will be restricted to such cases, for which S can be written as

$$S = \sum_{n=0}^{N} \sigma_n\ (\nabla^2)^n \quad . \qquad (11.8)$$

As a further restriction, consider elliptical terrain, $h(x,y)=h_0H(R)$, having normalized Fourier transform, $\hat{H}(\rho)$, given by (B.4). Transforming to elliptical polar coordinates, defined by (B.2), one finds from (11.4) that

$$\hat{S}(k,\ell) = \sum_{n=0}^{N} \left(\frac{-\rho^2\Delta^2}{a^2}\right)^n \sigma_n \quad , \tag{11.9}$$

where

$$\Delta = \left(\cos^2\phi+\gamma^2\sin^2\phi\right)^{\frac{1}{2}} \quad ; \gamma=a/b \quad . \tag{11.10}$$

First consider the effect of smoothing an infinitely-extended crosswind ridge, H(X), with the operator (11.8). The Laplacian effectively reduces to $\partial^2/\partial X^2$ for this case and $\gamma\rightarrow 0$ in (11.10). The Fourier transform of the height field becomes $\hat{h}(k,\ell) = \tilde{h}(k)\ \delta(\ell)$, where δ is a Dirac delta function. Substituting from (11.3) into (9.1), one finds that the drag per unit length due to the smoothed terrain is

$$\langle d_2\rangle = d_2 \sum_{n=0}^{2N} \omega_n\, s_n \quad , \tag{11.11}$$

where

$$\omega_n = \left(\frac{-1}{a^2}\right)^n \sum_{m=0}^{n} \sigma_m\, \sigma_{n-m} \quad ; \sigma_m=0 \text{ if } m>N \quad , \tag{11.12}$$

and

$$s_n = \frac{2\pi}{d_2} \int_{-\infty}^{\infty} |\kappa^{2n+1}|\ |\tilde{H}(\kappa)|^2\, d\kappa \quad . \tag{11.13}$$

Here d_2 and $\tilde{H}(\kappa)$ are the normalized drag and Fourier transform of the unsmoothed terrain. Note, from (9.1), that $s_0=1$. The higher order s_n terms are evaluated for the μ, ν and exponential type ridges, defined in (9.2), in Appendix P, with the results summarized in Table 10.

In the more general case of an isolated three-dimensional hill, the components of the force (normalized as in (10.3)) acting on the smoothed barrier with orientation angle, ψ, are found to be

$$\left.\begin{aligned} \langle D_3 \rangle &= G\,(B\cos^2\psi + C\sin^2\psi) \quad , \\ \langle T_3 \rangle &= G\,(B-C)\sin\psi\cos\psi \quad . \end{aligned}\right\} \qquad (11.14)$$

Here

$$\left.\begin{aligned} B &= \sum_{n=0}^{2N} \omega_n\, S_n\, B_n \quad , \\ C &= \sum_{n=0}^{2N} \omega_n\, S_n\, C_n \quad . \end{aligned}\right\} \qquad (11.15)$$

The factors, S_n, defined by

$$S_n = \frac{16\pi^2}{G}\int_0^\infty \rho^{2+2n} \left[\hat{H}(\rho)\right]^2 d\rho \quad , \qquad (11.16)$$

where G is defined by (10.5), incorporate the effect of the vertical cross-section of the barrier, while $B_n = B_n(\gamma)$ and $C_n = C_n(\gamma)$, defined in Appendix Q, give the dependence on the eccentricity of the horizontal cross-section of the mountain. The weighting factors, ω_n, are defined in (11.12). The expressions (11.14) reduce to those for the unsmoothed case, given by (10.4), when $\sigma_0 = 1$ and $\sigma_n = 0$ for $n > 0$. Comparing (11.14) and (10.4), it is seen that the structure of the dependence on the barrier orientation angle, ψ, is the same in the smoothed and unsmoothed cases.

To illustrate the preceding formulae, some numerical examples of the force on a smoothed barrier have been calculated for the case of the smoothing operator, $S=1+\sigma\nabla^2$, applied to several of the terrain forms defined in (9.2) (with X^2 replaced by R^2 to give three-dimensional barriers). The specific cases considered are $\mu=5/2$ with $\alpha^2=6$, the exponential case with $\alpha^2=2$, and $\nu=5/2$ with $\alpha^2=4$. The relevant integrals (11.16) are evaluated in Appendix P, with the results shown in Table 11. In Fig. 31, the ratio, R_D, defined by

$$R_D(\sigma) = \frac{\langle D_3 \rangle}{D_3} \left(\frac{H}{\langle H \rangle}\right)^2_{R=0} , \tag{11.17}$$

is plotted as a function of $\langle H(\sigma)\rangle(R=0)$, the smoothed terrain height at R=0, for each of the three terrain shapes. Here, $\langle D_3\rangle=\langle D_3(\sigma)\rangle$ is the drag force component for the smoothed barrier and $D_3=\langle D_3(\sigma=0)\rangle$ is the corresponding drag for the unsmoothed case. Fig. 31a shows an elliptical barrier case, $\gamma=1/2$, while Fig. 31b is the circular case, $\gamma=1$. The right hand edge of each figure corresponds to the unsmoothed hill, $\sigma=0$. Proceeding to the left, the value of σ increases along each curve, with a corresponding decrease in the terrain height.

An explicit relation between $\langle H\rangle(R=0)$ and σ is given below. By expressing the unsmoothed height field, H, in terms of its Fourier transform, it turns out to be possible to calculate derivatives of H at R=0 without explicitly doing the differentiation. For example, if $S=1+\sigma\nabla^2$, as in the case under study, one finds

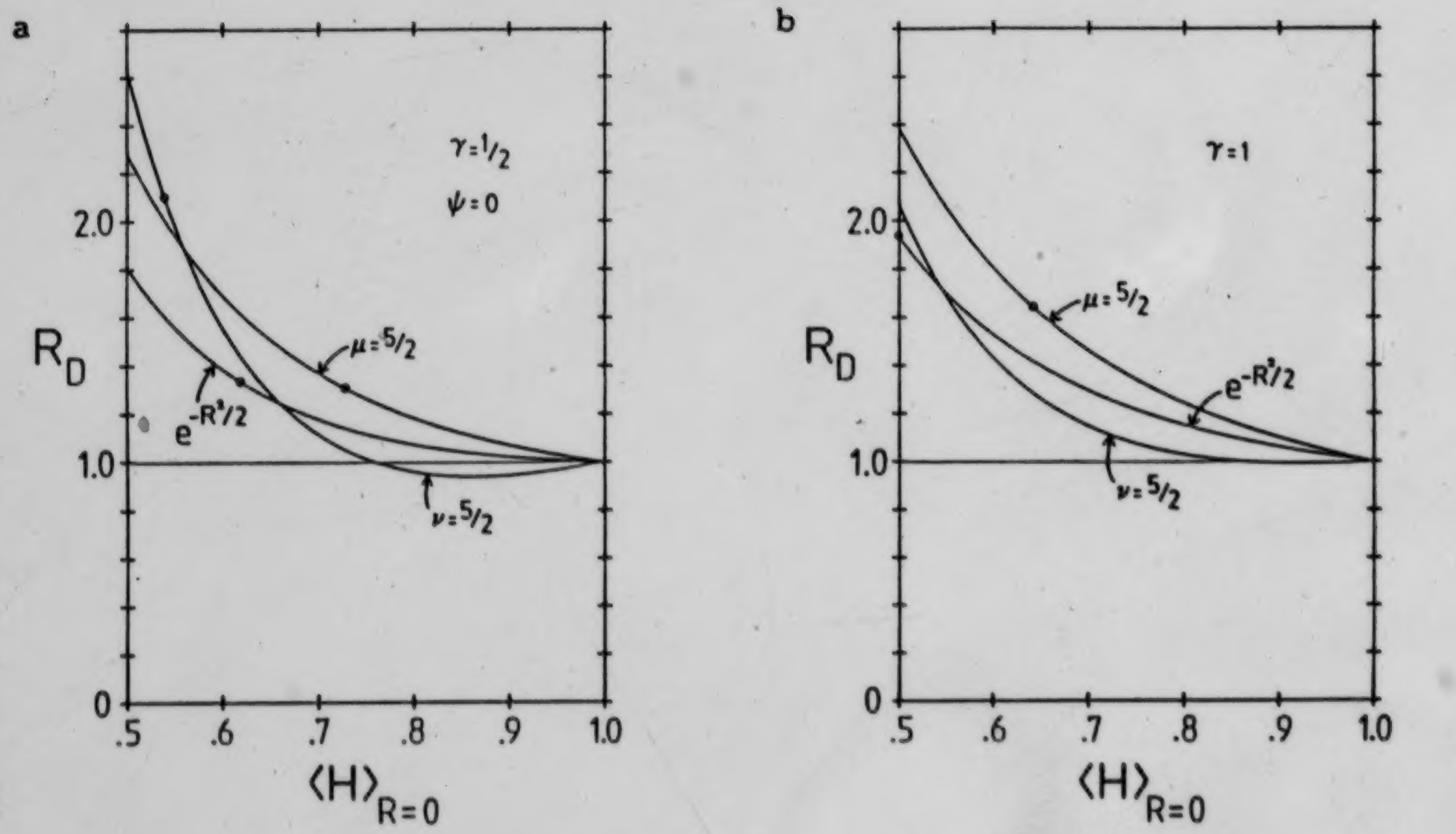

Figure 31. Normalized total drag, R_D, defined by (11.17), for a barrier with smoothed terrain height $\langle H\rangle=(1+\sigma\nabla^2)H$, as a function of $\langle H\rangle(R=0)$. Unsmoothed shapes, $H(R)$, are defined by replacing X by R in (9.2), with Fig. 31a showing an elliptical case ($\gamma=1/2$) and Fig. 31b a circular one ($\gamma=1$). For sufficiently large σ (points to the left of the circle on each curve), the maximum terrain height does not occur at $R=0$, due to changes in the mountain shape.

$$<H>_{R=0} = 1 - \frac{\sigma}{a^2}\frac{1+\gamma^2}{2} J \quad , \qquad (11.18)$$

where

$$J = 2\pi \int_0^\infty \rho^3 \hat{H}(\rho)\, d\rho \quad . \qquad (11.19)$$

$J=4\mu/\alpha^2$, $4/\alpha^2$, and $4\nu/\alpha^2$, for the μ, exponential, and ν cases, respectively (GR, p. 684). <H>(R=0) was chosen instead of σ for the abscissa in Fig. 31 because it is a readily comprehensible measure of the degree of smoothing.

If the smoothing simply reduced the barrier height, without changing its shape, then R_D would be equal to 1 (independent of σ). This corresponds to the thin horizontal line in Fig. 31. In Fig. 31a, it is seen that for an amount of smoothing which reduces the inital height by less than 25%, the ν=5/2 terrain shape produces a drag force which is less than would be expected from the height change alone. The exponential and μ=5/2 cases both show drag values which are larger than predicted from the square of the height at the origin, with the μ case showing the greater effect. For heavy smoothing, such that <H>(R=0) is only .5, the value of R_D ranges from 1.81 for the exponential case to 2.63 for ν=5/2. The variation of the drag force with the degree of smoothing is qualitatively similar for the γ=1 example shown in Fig. 31b.

The large values of R_D seen in the cases of relatively large smoothing are associated with correspondingly great changes in the shape of the original mountain. As an example, contours of the smoothed terrain field for the $\nu=5/2$, $\gamma=1/2$ case, with $\langle H\rangle(R=0)=.5$ (obtained with $\sigma=.32a^2$), are shown in Fig. 32. The unsmoothed barrier is of unit height at the origin and decreases away from the peak, reaching zero along the dashed elliptical contour, $R=2$. The smoothing has produced a ridge at about $R=1.6$ and a concentration of topographic contours between the ridge and the $R=2$ ellipse. The resulting barrier, with a relatively flat top and steep sides, has a larger drag in relation to its height than the original terrain (compare the progression to larger ω values in Fig. 20).

For sufficiently small smoothing parameters, the smoothed terrain height decreases monotonically from the peak. The σ values for which this condition obtains in Fig. 31 are those to the right of the circle on each curve. The left portion of each curve corresponds to a smoothing parameter large enough to appreciably distort the terrain shape, by introducing secondary maxima on the shoulders of the unsmoothed barrier. No circle appears on the $\nu=5/2$, $\gamma=1$ curve (Fig. 31b) because the corresponding dividing point is off-scale, to the left, at $\langle H\rangle(R=0)=7/15$.

Calculations were also performed for rotated barriers with $\psi=45°$ and $\gamma=1/2$. A plot of R_D versus $\langle H\rangle(R=0)$ (not shown) was found to be very similar to the $\psi=0$ case in Fig. 31a. The corresponding ratio for the transverse force on the barrier is defined by

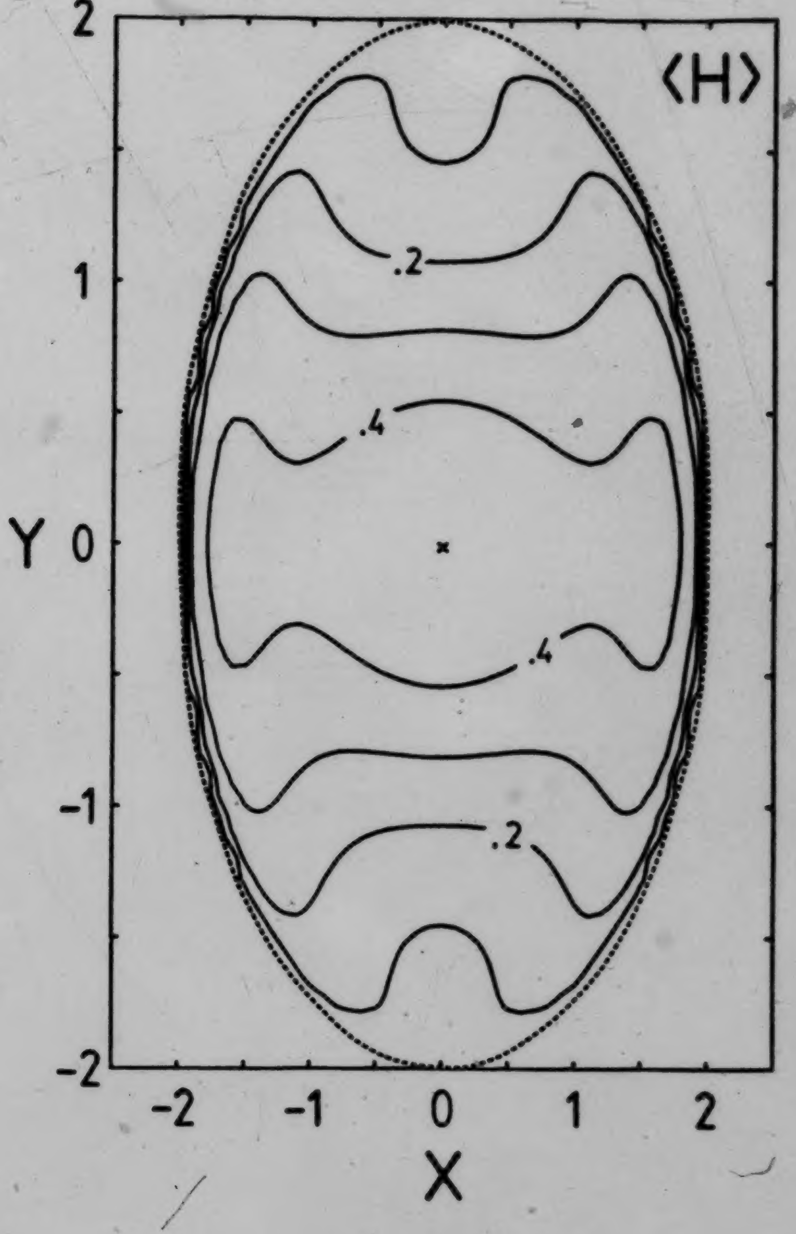

Figure 32. Terrain height contours (interval 0.1) for a smoothed elliptical barrier $<H>=(1+\sigma\nabla^2)H$, with H(R) defined by replacing X by R in (9.2), with $\nu=5/2$ and $\gamma=1/2$. The smoothing parameter, $\sigma=.32a^2$, is chosen so that $<H>(X=Y=0)=0.5$. <H> is zero outside the dashed contour, R=2.

$$R_T(\sigma) = \frac{\langle T_3\rangle}{T_3}\left(\frac{H}{\langle H\rangle}\right)^2_{R=0} \quad . \tag{11.20}$$

R_T is shown as a function of <H>(R=0) in Fig. 33. The curves for R_T are rather similar to those previously discussed for R_D, although R_T is less than R_D over almost the entire range shown.

11.3 Smoothing by spectral truncation

In recent years, many mathematical models of meteorological phenomena have been formulated in terms of expansions in a complete set of basis functions. However, to limit the amount of calculation these series are truncated at a finite number of terms. This truncation can be interpreted as a type of smoothing because it is usual to discard terms from the high, rather than the low frequency end of the spectrum. As an example of the smoothing effect of spectral truncation, the normalized drag per unit length, d_2, defined by (9.1), is calculated in the following for two-dimensional flow over an infinitely-extended crosswind ridge.

Suppose that H=H(X) is the unsmoothed terrain shape. For the sake of this example, let the smoothed terrain, <H>, be an approximation to H of the form

$$\langle H\rangle = e^{-X^2/2\beta^2} \sum_{n=0}^{N} h_n H_n(X/\beta) \quad , \tag{11.21}$$

where h_n are constant coefficients multiplying Hermite

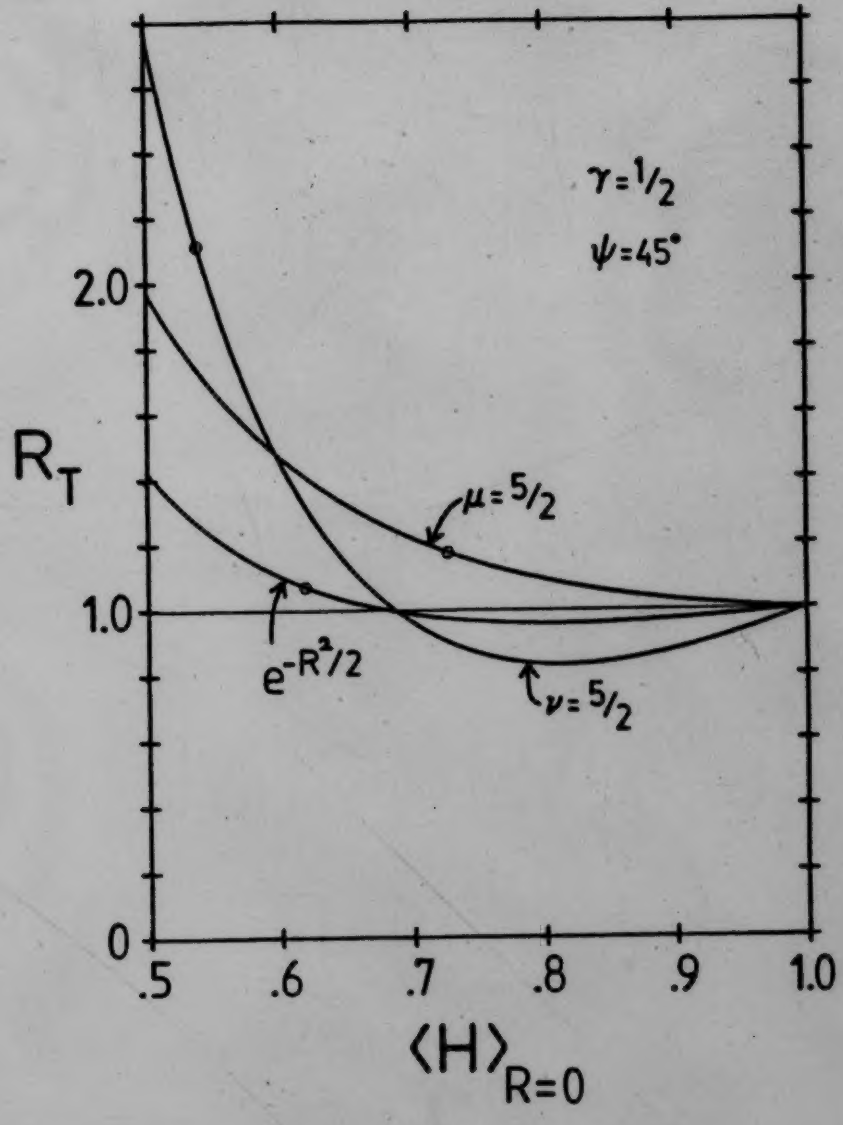

Figure 33. Normalized total transverse force, R_T, defined by (11.20), for a barrier with smoothed terrain height $\langle H \rangle = (1+\sigma\nabla^2)H$, as a function of $\langle H \rangle (R=0)$. Unsmoothed shapes, $H(R)$, are defined by replacing X by R in (9.2), with $\gamma = 1/2$, but rotated by 45°. For sufficiently large σ (points to the left of the circle on each curve) the maximum terrain height does not occur at R=0, due to changes in the mountain shape.

polynomials, H_n. The parameter, β, has been introduced to increase the flexibility of the expansion. To determine h_n, the total squared difference, E^2, between H and <H> is minimized, by requiring $\partial E^2/\partial h_n = 0$, where

$$E^2 = \int_{-\infty}^{\infty} \left(H - \langle H \rangle\right)^2 dX \quad . \tag{11.22}$$

Using the orthogonality property of Hermite polynomials (GR, p. 837), one finds

$$h_n = \frac{1}{\beta\ \Gamma(\frac{1}{2})\ 2^n\ \Gamma(n+1)} \int_{-\infty}^{\infty} H(X)\ H_n(X/\beta)\ e^{-X^2/2\beta^2} dX \quad . \tag{11.23}$$

See Appendix P for evaluation of (11.23) for specific terrain shapes, H(X). Given h_n, the approximate height field (11.21) can be efficiently summed for a specific X using recursion relations for Hermite polynomials (GR, p. 1033).

To evaluate the pressure field or drag per unit length for the smoothed terrain, its Fourier transform, $\langle \tilde{H}(\kappa) \rangle$, is required. Using GR (p. 838), one finds from (11.21) and (B.3), that

$$\langle \tilde{H}(\kappa) \rangle = \frac{\beta\, e^{-\kappa^2\beta^2/2}}{\Gamma(\frac{1}{2})\ 2^{\frac{1}{2}}} \sum_{n=0}^{N} h_n\ i^n\ H_n(-\kappa\beta) \quad . \tag{11.24}$$

The pressure field could then be evaluated by substituting (11.24) into the last integral in (B.5) (at Y=0). However, as the emphasis in this section is on the drag per unit length, examples were not calculated for the pressure perturbation.

Substituting (11.24) into (9.1), one obtains the drag per unit length due to the smoothed terrain:

$$\langle d_2 \rangle = \sum_{m=0}^{N} \sum_{n=0}^{N} h_m \, h_n \, d_{mn} \quad , \tag{11.25}$$

where

$$\begin{aligned} d_{mn} &= (-i)^m i^n \int_{-\infty}^{\infty} |\kappa| \, H_m(\kappa) \, H_n(\kappa) \, e^{-\kappa^2} \, d\kappa \quad , \\ &= \begin{cases} 0 \quad ; \; m+n \text{ odd} \quad , \\ \dfrac{m+n-1}{1-(m-n)^2} \, \dfrac{\Gamma(m+1)}{\Gamma(m/2+1)} \, \dfrac{\Gamma(n+1)}{\Gamma(n/2+1)} \quad ; \; m, \, n \text{ both even} \quad , \\ \dfrac{4}{1-(m-n)^2} \, \dfrac{\Gamma(m+1)}{\Gamma\left(\dfrac{m+1}{2}\right)} \, \dfrac{\Gamma(n+1)}{\Gamma\left(\dfrac{n+1}{2}\right)} \quad ; \; m, \, n \text{ both odd} \quad . \end{cases} \end{aligned} \tag{11.26}$$

Numerical values for the integrals, d_{mn}, were initially found using recursion relations for Hermite polynomials. The explicit expressions appearing in (11.26) were obtained subsequently, by inspection, and can be verified by induction in combination with the recursion formulae. The summation (11.25) can be interpreted as a product of the form

$$\langle d_2 \rangle = \mathbf{h}^T \mathbf{d} \, \mathbf{h} \quad , \tag{11.27}$$

where, $\mathbf{h}^T = (h_0, h_1, \ldots h_n)$ is a vector of coefficients describing the height field, **h** is the corresponding column vector and **d** is a positive-definite symmetric matrix with elements, d_{mn}. Note that **d** is characteristic of the choice of basis functions in the spectral expansion (11.21) of the height field, but is independent of the particular terrain shape.

Therefore, even if one examines several different barriers, the d_{mn} values need be calculated only once. For the symmetrical terrain forms considered in this paper, it is only the case of m and n both even that has non-zero coefficients in the drag sum (11.25).

Two examples were chosen to illustrate the mathematical results of this section. The first of these is the Agnesi case ($\mu=1$ in (9.2), but with $\alpha^2=1$), $H=(1+X^2)^{-1}$. In Fig. 34, H (dashed curve, $N=\infty$) is plotted as a function of X, along with the approximation, $\langle H\rangle$, provided by (11.21), with $\beta=1$, for truncations N=2 and 4. The expansion coefficients, h_n, appearing in (11.21) are given by (P.7) and (P.8). Because the unsmoothed terrain is already relatively smooth, the spectral expansion gives a reasonably good approximation to H, even for N as low as 4. The effect on the drag per unit length of truncating the series at different values of N is seen in Fig. 35. The ratio, $R_d(N)$, defined by

$$R_d(N) = \frac{\langle d_2\rangle}{d_2}\left(\frac{H}{\langle H\rangle}\right)^2_{X=0} , \qquad (11.28)$$

is plotted as a function of the smoothed height at the origin, $\langle H\rangle(X=0)$. Here $d_2=\pi/4$ and $H(X=0)=1$ are the values corresponding to the unsmoothed terrain. The definition (11.28) is analogous to (11.17) for the total drag used in the discussion of differential smoothing, with the truncation limit, N, replacing the parameter, σ. From the points at the upper right in Fig. 35, it is seen that including only one or two terms (N=0 or 2) in the spectral expansion

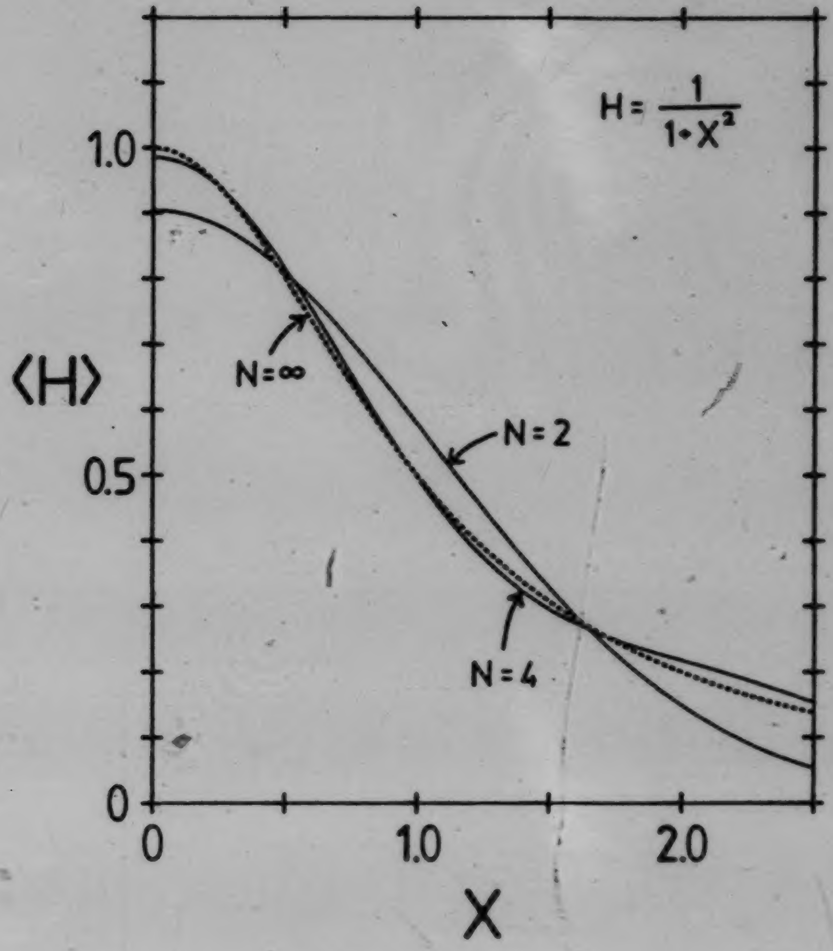

Figure 34. Terrain height, $H=1/(1+X^2)$ versus X (dashed curve labelled N=∞) and a truncated spectral series approximation to H, <H>, for truncation limits N=2 and 4 (solid curves), with $\beta=1$ in (11.21).

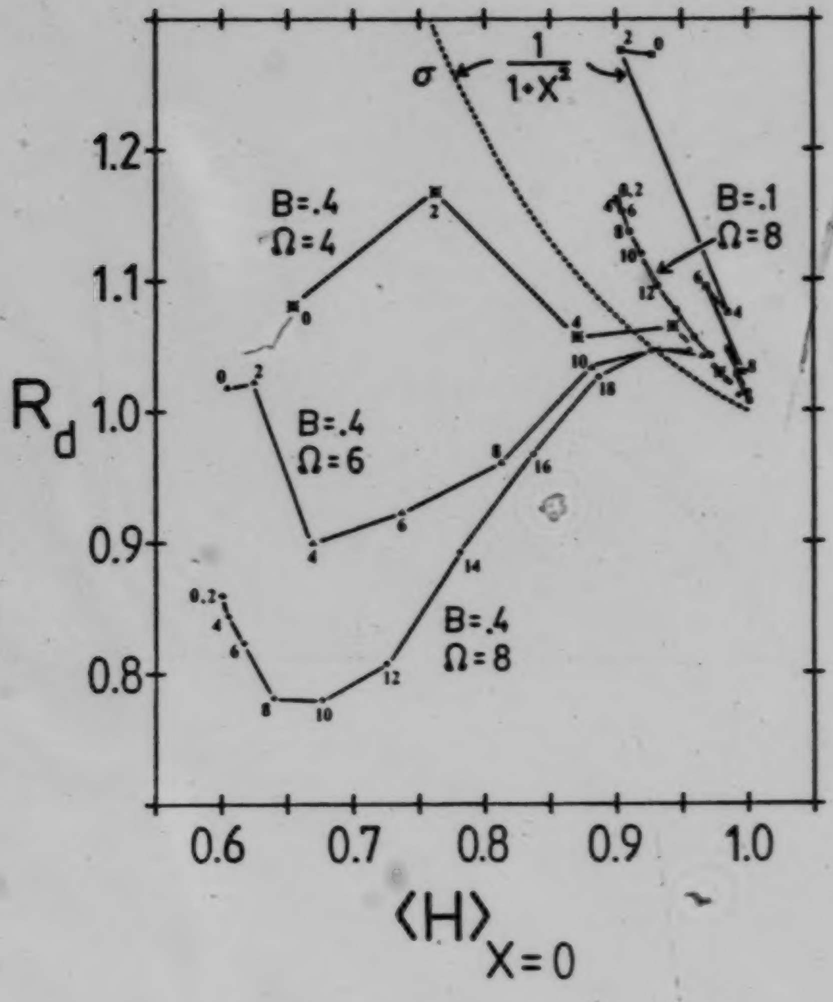

Figure 35. Normalized drag per unit crosswind length, R_d, defined by (11.28), for a barrier represented by a truncated spectral series. Examples shown are for the Agnesi barrier with height $H=1/(1+X^2)$ and the sinusoidally modulated case with $H=(1-B+B\cos\Omega X)\exp(-X^2)$. Points correspond to successive even values of the series truncation limit, N (indicated in small type). Line segments joining the points are for visualization purposes only. The dashed curve gives the result for the barrier $\langle H\rangle=(1+\sigma\nabla^2)(1/(1+X^2))$.

leads to R_d values which are significantly greater than 1 (1.27 and 1.28, respectively). Including the N=4 term in the series leads to a large change in R_d, so that the drag per unit length for the smoothed terrain is less than 10% larger than the value expected from the reduced height at the origin. Studying numerical results for $<d_2>$ it was found that it steadily decreases to the value for unsmoothed terrain as N increases. However, oscillation in the value of $<H>(X=0)$ causes R_d to approach 1 along a zigzag path in Fig. 35.

For comparison, the drag per unit length for terrain smoothed with the operator, $1+\sigma\nabla^2$, was calculated for the Agnesi barrier, using the formula (11.11). The result is plotted as the dashed curve, labelled σ, in Fig. 35. Although both the spectral truncation and differential smoothing operations lead to R_d values greater than 1 for this terrain shape, the degree to which the drag per unit length is near the value expected from the height at the origin differs in the two cases. In spite of the fact that the differential smoothing operation can lead to larger changes in the height of the barrier, it apparently preserves the shape of the mountain more precisely than the spectral truncation. This leads to smaller R_d values in the former case, for a given value of $<H>(X=0)$.

A second example chosen for study is the sinusoidally modulated Gaussian terrain, $H=(A+B\cos\Omega X)\exp(-X^2)$, with $\beta=1/\sqrt{2}$ in (11.21). The expansion coefficients for this case are given in (P.10). The R_d and $\langle H\rangle(X=0)$ values for several cases of this type are shown in Fig. 35. If only the $N=0$ term is included in the series for $\langle H\rangle$, then $\langle d_2\rangle=h_0^2$ and $\langle H\rangle(X=0)=h_0$ so R_d reduces to $1/d_2$. Thus, the position of the $N=0$ end of each curve in Fig. 35 can be determined from the drag per unit length for the unsmoothed terrain plotted in Fig. 23b. From the latter figure, one can see that R_d for the $N=0$ truncation should be near 1 for small values of Ω. However, for Ω larger than about 2, R_d can differ appreciably from unity, either on the high or low side, depending on the particular combination of frequency, Ω, and amplitude, B. For sufficiently large Ω, $R_d<1$ for all non-zero B.

Now consider the effect of additional terms in the series for $\langle H\rangle$. For example, including the $N=2$ term changes the drag and height by a relatively large amount for the $B=.4$, $\Omega=4$ case, but by progressively smaller amounts as Ω increases. For the $\Omega=8$ curves in Fig. 35, the $N=2$ contribution to R_d and $\langle H\rangle(X=0)$ is negligible. This is the case for both $B=.4$ and $B=.1$, even though R_d and $\langle H\rangle(X=0)$ themselves are much different for the the two B values. Because of the comparative smoothness of the terrain in the low Ω cases, the inclusion of just a few terms in the spectral series leads to rapid convergence of the drag value to the unsmoothed result. More terms must be added to represent the terrain accurately as the frequency of the sinusoidal variation increases. As an example, the terrain height, H, with

$A=.6$, $B=.4$ and $\Omega=8$ is plotted as a function of X in Fig. 36 (dashed curve), along with $\langle H \rangle$ for $N=10$ and $N=20$. For $X<1$, the $N=20$ curve follows the variation in H reasonably well, although the extrema for larger X have greater magnitude for the $\langle H \rangle$ case. This may account for the fact that $R_d>1$ for the $N=20$ truncation. By comparison, the height field for the $N=10$ series follows the peaks and valleys of the unsmoothed terrain very poorly, leading to $R_d<.8$ for this case, as is seen from the bottom curve in Fig. 35.

In this study of the effects of terrain smoothing on the drag associated with mountain waves, two rather different smoothing processes have been considered. In both the differential operator and spectral truncation approaches, the maximum terrain height is reduced by the smoothing, leading to a reduction in drag. The main point to be made, however, is that the smoothing not only changes the barrier height, but also changes its shape. As a consequence, the drag on a flow over the smoothed mountain can be either larger or smaller than one would predict from a quadratic dependence on height. For the Laplacian smoothing examples the drag and transverse forces were predominantly larger than expected. However, in the series expansion case, the drag per unit length was seen to differ from a height-squared dependence by as much as 20% in either direction. The specific numerical results for the effect of smoothing on the drag are rather sensitive functions of the initial terrain shape and the type of smoothing operation.

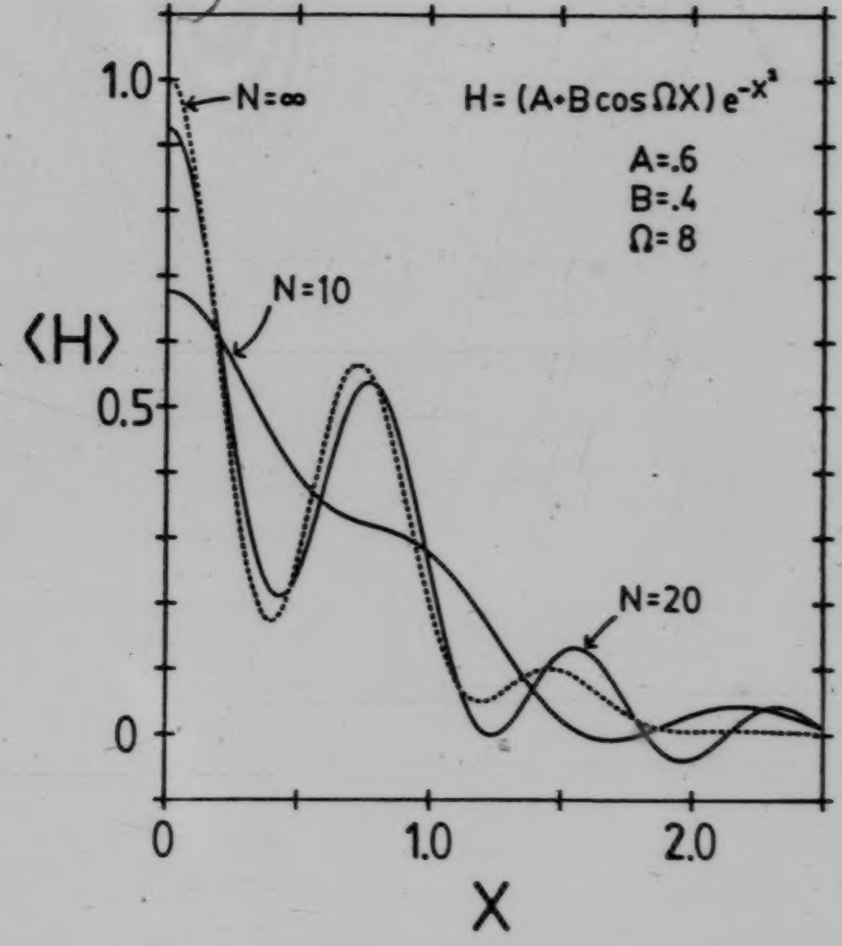

Figure 36. Terrain height, H=(A+BcosΩX) exp($-X^2$), with A=.6, B=.4 and Ω=8 (dashed curve labelled N=∞) and a truncated spectral series approximation to H, <H>, for truncation limits N=10 and 20 (solid curves), with $\beta=1/\sqrt{2}$ in (11.21).

CHAPTER 12

APPLICATION OF THE LINEAR MODEL TO REALISTIC TERRAIN

12.1 Model limitations

In this chapter, the linear model introduced in Chapter 3 is applied to the flow of air over a representation of the Rocky Mountains in Western Canada. This calculation was undertaken to determine if topographic factors can be used to explain the double maximum in the pattern of lee cyclone formation in Southern Alberta that was discussed in Chapter 2. However, the relationship between the fine details of the terrain shape and of the cyclogenesis location maps is not sufficiently definite to permit more than speculation about the origin of the frequency maximum. This result is not surprising in view of the simple nature of the model and the limited sample of cyclogenesis events.

The linearity constraint and the neglect of the Coriolis force are two shortcomings of the model which require that the results presented in this chapter be regarded with caution. As discussed by Smith (1980, 1982), the Froude number based on mountain height, $F=\overline{U}/h\overline{N}$, can be used as an indicator of the extent to which linear theory is valid. Nonlinear effects are expected to become important for F less than about 1. For the Rocky Mountain case, with h in the 2-3 km range, the flow will be in the nonlinear regime for typical values of wind speed and stability. However, for situations in which the mountain wave amplitude is small enough that streamlines do not become vertical in the lee (that is, the wave does not 'break'), Smith (1982) comments that 'the qualitative nature of the flow is not greatly changed by nonlinear effects'. Whether or not wave breaking occurs depends on the vertical structure of the wind and temperature. For example, if the wind speed decreases with height, an upwardly propagating wave might overturn as it encounters a region of lower Froude number. Such a case is presented by Durran and Klemp (1983).

The Rossby number, $Ro=\overline{U}/Lf$, based on a streamwise horizontal scale, L, is the appropriate dimensionless ratio for discussing the role of the Coriolis parameter, f, in mountain airflow. Rotational effects could be important for Ro less than about 1. Taking L=100 km as a typical length scale for an individual mountain range in Western Canada, $Ro\simeq 1$ for $\overline{U}=10$ m s^{-1}. For cases of relatively strong cross-barrier flow, with $\overline{U}>>10$ m s^{-1}, the air has less time to be accelerated by the Coriolis force, so the influence of the Earth's rotation is reduced. By studying an expansion of the equations of motion in terms of 1/Ro, Smith (1982) showed that the pressure perturbation is affected by rotation at second order in 1/Ro, whereas the horizontal wind fields require first-order corrections. The main effect of a non-zero Coriolis parameter on the wind perturbation is an increase in the air speed on the high-latitude side of the barrier and a decrease on the low-latitude side. Parish (1982) has studied the role of the Coriolis force in the development of a low-level jet parallel to a long ridge, on the windward side. Because of its quadratic dependence on 1/Ro, the pressure perturbation field is relatively unaffected by rotation, compared to the horizontal wind components, if Ro >> 1. This condition on Ro is not satisfied for the case of flow over the Rocky Mountains in Western Canada, unless $\overline{U}$>>10 m s^{-1}. In spite of this, some results of the application of a linear model excluding rotation will be presented, if only to provide a basis for comparison with more appropriate models.

Even if the effect of rotation is neglected in the calculation of the perturbation fields, it can be incorporated into $\overline{U}$, the mean flow. Supposing that a mean flow of speed $\overline{U}$ is geostrophically balanced, it is related to a mean pressure field $\overline{P}$, by

$$\overline{P} = -\overline{\rho}_o\overline{U}\, f\, (y\cos\overline{\psi} - x\sin\overline{\psi}) + \overline{P}_o \quad , \qquad (12.1)$$

where $\overline{P}_o$ is an arbitrary constant and $\overline{\psi}$ is the angle measured counterclockwise from the +x axis (due east) to the direction of the wind vector. Fig. 37 shows the total pressure field, P_T, found by adding the pressure perturbation of Fig. 8a (multiplied by the dimensional factor, $\overline{\rho}_o\overline{U}\ \overline{N}\ h_o$) to the mean pressure given by (12.1). Values of the horizontal length scales used for this figure are a=25 km and b=50 km. The other parameters were chosen as $\overline{U}$=10 m s^{-1}, h_o=1 km, $\overline{\rho}_o$=1 kg m^{-3}, f=.0001 s^{-1}, $\overline{N}$=.01 s^{-1}, $\overline{\psi}$=0 and $\overline{P}_o$=0. The contour interval is 0.1 mb. The dashed curve is the terrain

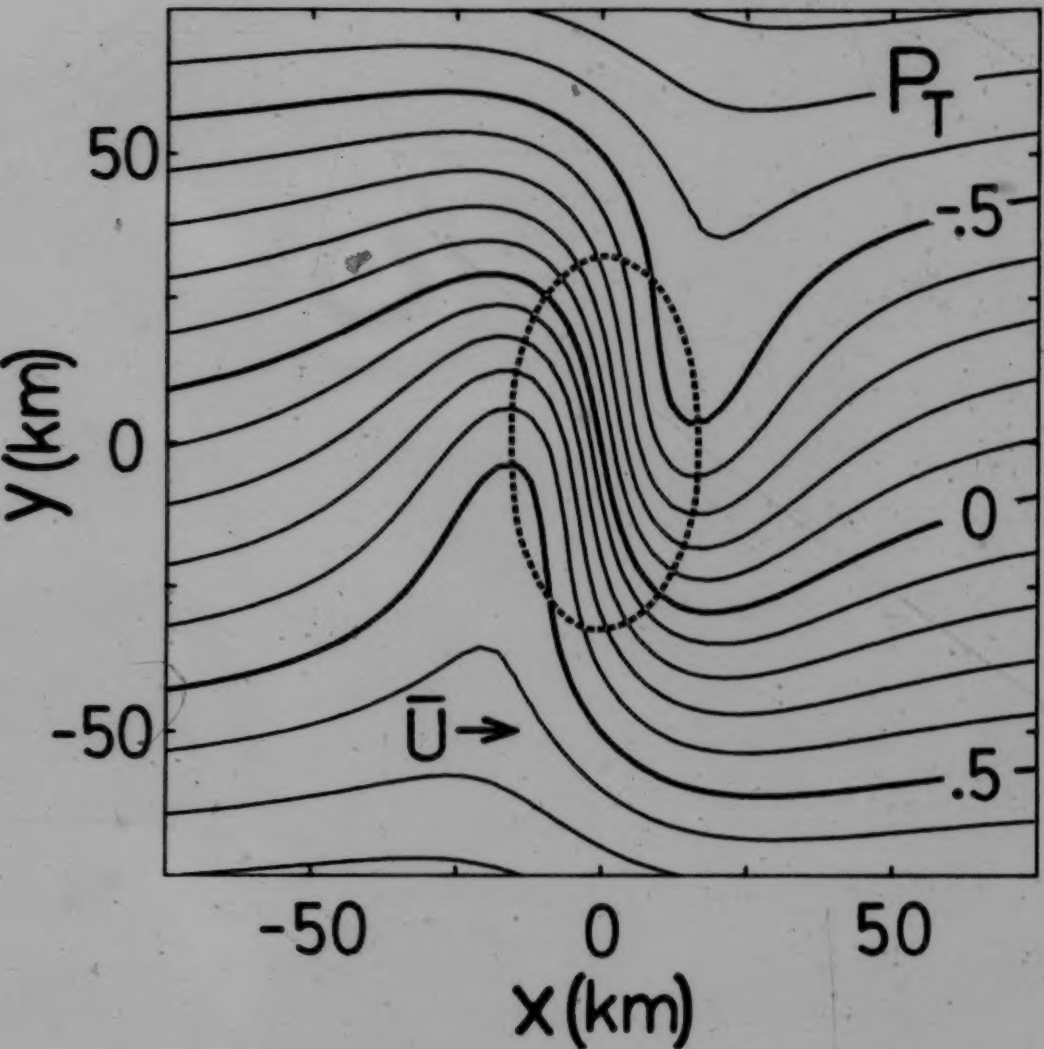

Figure 37. Contour plot of the total pressure, P_T, defined by adding the mean pressure defined by (12.1) to the dimensional form of the $\mu=2$ perturbation from Fig. 8a. Mean flow parameters are $\overline{U}=10$ m s^{-1}, $\overline{\rho}_0=1.0$ kg m^{-3}, $\overline{N}=0.01$ s^{-1}, $\overline{\psi}=0$, and $\overline{P}_0=0$. Also, $f=0.0001$ s^{-1} and $h_0=1$ km. The contour interval is 0.1 mb. The dashed curve is the 500 m terrain height contour.

surface at the 500 m level. Because the total pressure is directly proportional to $\bar{\rho}_0$ and $\bar{U}$, the figure would be unchanged if $\bar{\rho}_0$ or $\bar{U}$ were varied, except for the labelling of the contours. Note that physical coordinates have been used in Fig. 37 rather than the dimensionless ones used in Fig. 8.

If one were to look for the pressure signature of a hydrostatic mountain wave using real data, one would expect to find a pattern similar to Fig. 37. Smith (1981, 1982) has reported several cases of this type, including flow over the Olympic Mountains in Washington state, and over islands such as New Zealand and Iceland. Although surface pressure is one of the best resolved meteorological fields, a finer network of observing stations would be very helpful in the present context.

12.2 Realistic Terrain

Now consider the application of the linear model (with no Coriolis force) to flow over a representation of the topography in Western Canada. Through the Canadian Meteorological Centre, terrain height data on magnetic tape was obtained for the entire Northern Hemisphere. The data originated at the European Centre for Medium-Range Weather Forecasting. The terrain heights were nominally given to the nearest 100 ft as averages over 10′ latitude by 10′ longitude quadrangles (approximately 19 km by 11 km at 55°N). However, a frequency analysis of the reported heights showed an excessive number of certain values, suggesting that the heights had been rounded to the nearest 500 or 1000 ft in some regions of higher terrain. This is not unreasonable in view of the large variation in surface elevation that can occur in a 200 km^2 region.

To illustrate the complex structure of the barrier presented to the prevailing winds in Western North America, cross-sections of the terrain height are shown in Fig. 38. The vertical scale on each portion of the figure extends from sea level to 3000 m. The divisions in the horizontal direction correspond to 100 km intervals, measured along great circle arcs on a sphere of radius 6371 km at sea-level. The arcs chosen are inclined at an angle of 55° east of north at the midpoints of the sections. The latitude and longitude of the midpoints of each section are marked on the corresponding diagrams. The profiles are roughly perpendicular to the main ridge of the Rocky Mountains. They extend approximately from the Continental Divide to the west coast of North America and about an equal distance on the east side of the Divide. For reference, the cross-sections are indicated on Fig. 39. In Fig. 38, the northernmost cross-section appears in (a) with a southward progression through to (l). The most southerly terrain profile shows the greatest degree of symmetry. In the other cross-sections, there is a marked difference between the western and eastern sides of the Continental Divide. The western (left) side of the barrier is rather chaotic, with numerous ranges, and

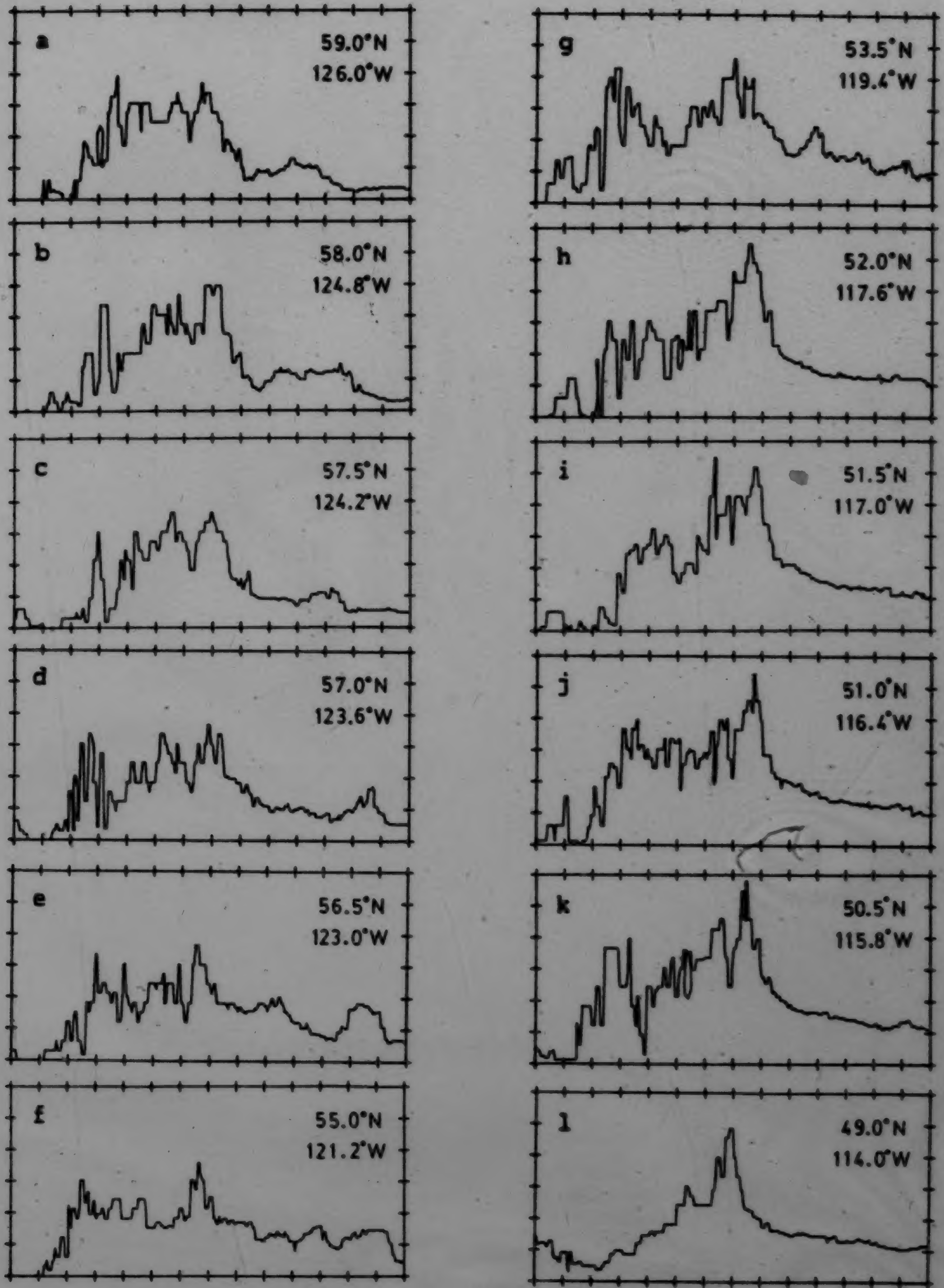

Figure 38. Average terrain height cross-sections in Western Canada, as shown in Fig. 39, centered about the latitude and longitude marked on each profile. Tick marks are separated by 100 km on the abscissa and 500 m on the ordinate.

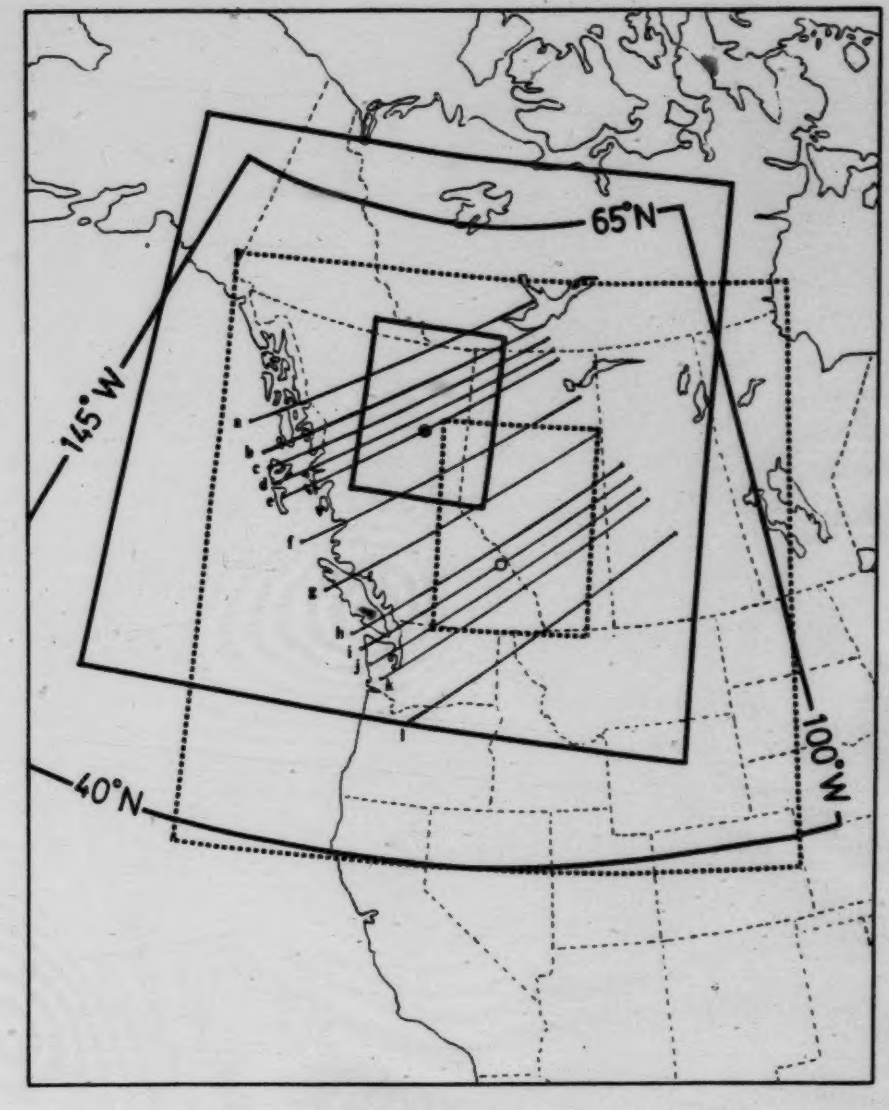

Figure 39. Map showing positions of the cross-sections in Fig. 38 and the areas for which the pressure perturbation was calculated (large boxes, approximately centered about the marked circles) and displayed (small boxes) in Figs. 40-44. In these calculations, the terrain height was set equal to zero outside the sector from 40°N to 65°N and 100°W to 145°W.

shows large changes in appearance between cross-sections separated by only 0.5° latitude. In contrast, the eastern (right) side of the barrier is much smoother. This is especially true of panels (h) through (l), which show cross-sections passing through the southern half of Alberta. For these sections, the average terrain height drops from a maximum of 2500-3000 m to about 1000 m, in a distance of about 100 km, and then falls off much more gradually to the east. For the mountains of Northeastern B.C., shown in (a) through (e), the average height is only 1500-2000 m and there is a less uniform decrease with eastward displacement than for the Southern Alberta cases.

To calculate the pressure perturbation, p', resulting from flow over this terrain, a Fast Fourier Transform method was used to evaluate the Fourier transform of the height field (B.3) and the first integral in (B.5). The numerical procedure is outlined in Appendix J. In the model used, the motion is assumed to occur on a plane surface, rather than a sphere. Therefore, one must map the terrain height field on to a plane. The method used to accomplish this was likely more complicated than necessary, in view of the many limitations of the model, so the full development of the equations will not be presented here. It suffices to state that the following transformation was made to associate a point on the Earth's surface at latitude, ϕ, and longitude, λ, with a point in the (x,y) plane :

$$\left.\begin{aligned} x &= R_e \arcsin\left(\cos\phi\sin(\lambda-\lambda_o)\right) \;, \\ y &= R_e \arcsin\left(\sin\phi\cos\phi_o-\cos\phi\sin\phi_o\cos(\lambda-\lambda_o)\right) \;. \end{aligned}\right\} \qquad (12.2)$$

Here R_e=6371 km is the mean radius of the Earth. The parameters ϕ_0 and λ_0 specify the latitude and longitude of the origin x=y=0. For ϕ near ϕ_0 and λ near λ_0, x and y given by (12.2) are similar to coordinates defined by projection from the center of the Earth on to a tangent plane. One reason for choosing the coordinates (12.2) instead of the tangent-plane coordinates, is that distance measured along the x or y axis is equal to distance along the curved surface of the Earth.

The Fast Fourier Transform procedure requires that the height field be sampled on a uniform grid of points in the (x,y) plane. Given a point (x,y), the corresponding latitude and longitude can be found from (12.2) and, subsequently, the average terrain height. A matrix of 256 by 256 height values was generated in this way, with a resolution of 10 km in x and in y. Two separate regions were considered, one centered approximately at (ϕ_0=51.5°N, λ_0=117°W), which will be termed the Southern Alberta case, and the other at (ϕ_0=56.5°N, λ_0=123°W), the Northeastern B.C. case. The pressure field was then calculated for each area, with values given at the same 256 by 256 points. However, to avoid contamination from edge effects and the periodicity implicit in the discrete Fourier transform method (see Appendix J), results are presented for only a small interior portion of the grid. In Fig. 39, the regions covered by the 256 x 256 grids are shown on a polar stereographic map, true at 60°N. The areas for which the Southern Alberta and Northeastern B.C. results will be displayed are also outlined.

At the start of this project, to limit computer storage requirements, the terrain heights were extracted from the magnetic tape for a limited sector, extending from 40°N to 65°N and 100°W to 145°W. However, when the calculations were extended from an initially planned grid of 128 x 128 points to the 256 x 256 points ultimately used, the new grid extended beyond the boundary of the sector just described. For convenience, the terrain height at these external points was set equal to zero. However, it is expected that using the actual terrain heights for these points would have little effect on the pressure perturbation in the display windows in the interior of the grid.

First consider the results for the Southern Alberta region. In Fig. 40a, topographic contours are plotted at an interval of 250 m. The darkest level of shading highlights regions where the mean height is greater than 2250 m. Within the innermost dashed contours, the terrain height exceeds 2500 m. In Fig. 40b, the corresponding pressure field is shown for a mean wind at an angle, $\overline{\Psi}=35°$ north (counterclockwise) of east. The contour interval is 0.25 mb (25 Pa) assuming that $\overline{U}=10$ m s^{-1}, $\overline{N}=.01$ s^{-1} and $\overline{\rho}_0=1.0$ kg m^{-3}. The darkest shading indicates a perturbation of less than

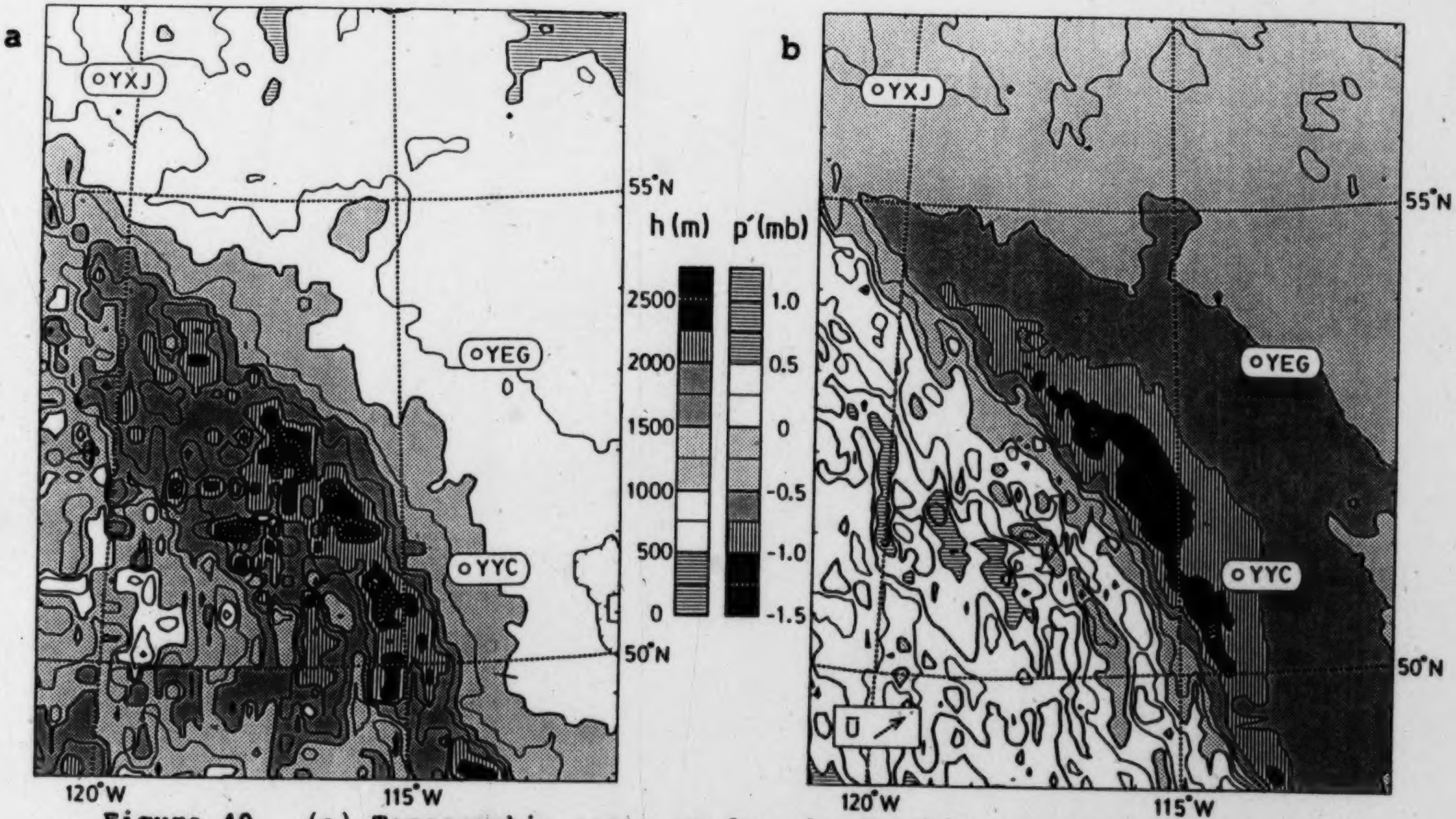
a
b
○YXJ
○YEG
○YYC
55°N
50°N
120°W
115°W
h (m)
p′(mb)
2500
2000
1500
1000
500
0
1.0
0.5
0
-0.5
-1.0
-1.5
Ū

Figure 40. (a) Topographic contours for the Southern Alberta case at an interval of 250 m, with shading as indicated in the legend. Dashed contours indicate regions with an average height greater than 2250 m.

(b) Pressure perturbation calculated for a wind vector directed at an angle of $\overline{\psi}=35^\circ$ north of east, over the terrain shown in (a). The isobars are spaced at 0.25 mb, assuming mean flow parameters to be $\overline{U}=10$ m s^{-1}, $\overline{\rho}_0=1.0$ kg m^{-3}, and $\overline{N}=0.01$ s^{-1}. Dashed isobars inside the region of darkest shading indicate a pressure less than -1.25 mb.

-1.0 mb, with the small dashed contours denoting a pressure of less than -1.25 mb. The shading indicates the region in which the pressure perturbation is negative, except for the areas with horizontal lines. These denote positive perturbations greater than 0.50 mb. This pressure field was constructed from an appropriate linear superposition of the fields due to the westerly and southerly flows shown in Figs. 41a and 41b, respectively. This superposition is similar in principle to (5.15) except that here the wind vector is rotated rather than the barrier. Similarly, Fig. 42b illustrates the case of a flow directed 35° south (clockwise) of east ($\bar{\psi}=-35°$). The height field has been repeated in Fig. 42a, for convenience. Comparing the pressure fields shown in these figures, it is seen that the area of significant pressure perturbation is much greater on the lee side of the barrier if the flow is directed nearly perpendicular to the mountain range, as in Fig. 40b. Because of interference between the pressure fields due to the many individual ridges on the British Columbia side of the Continental Divide, the pressure perturbation field is generally disorganized and weak in the lower left portions of the figures. The most extensive areas of positive pressure perturbation occur for westerly (Fig. 41a) and northwesterly (Fig. 42b) flow.

Comparison of the height and pressure maps shows that the minima in the pressure typically occur 50 to 100 km downstream of the major topographic features. This is

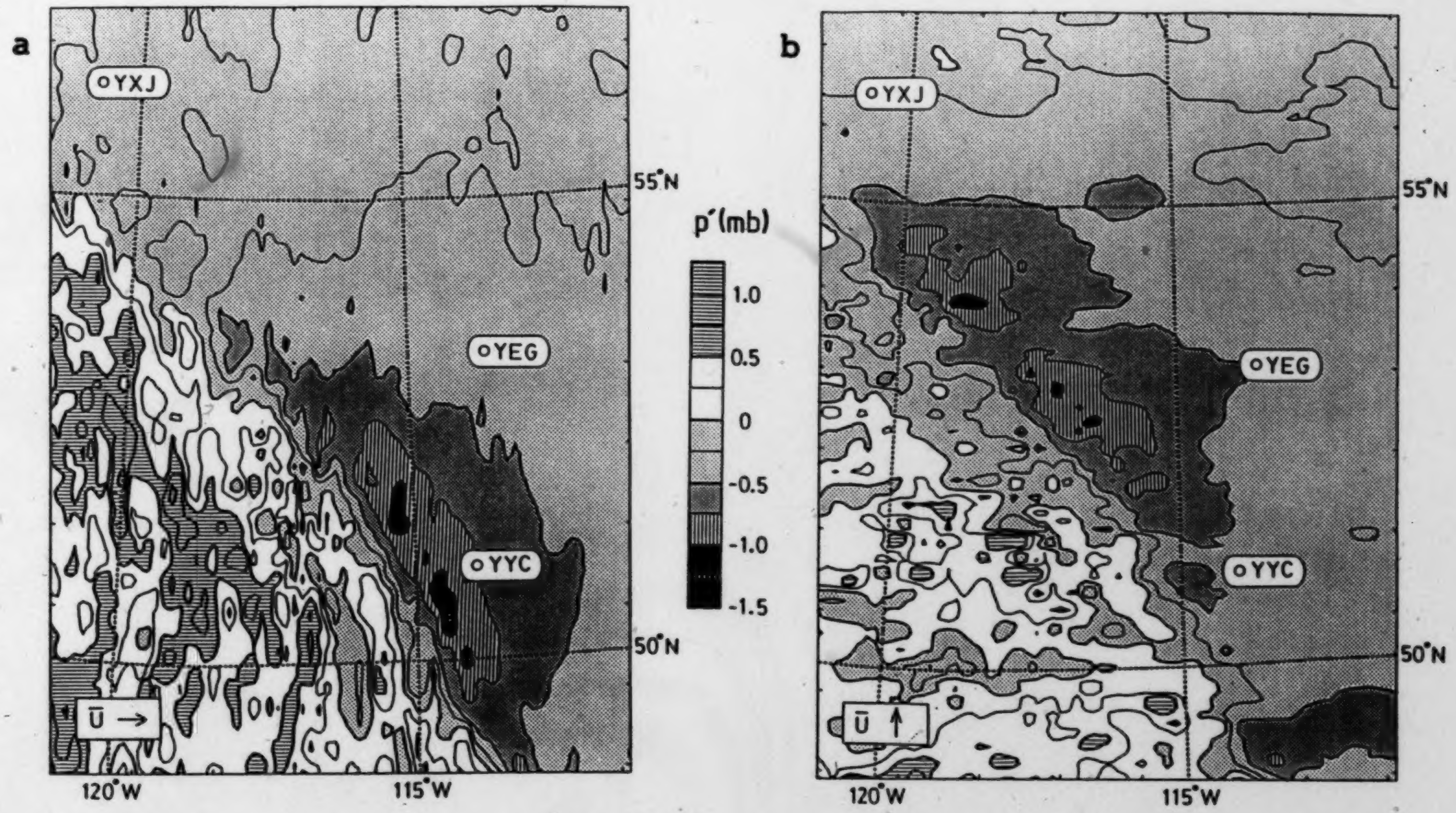
a
oYXJ
oYEG
oYYC
55°N
50°N
120°W
115°W
Ū →
p′(mb)
1.0
0.5
0
-0.5
-1.0
-1.5
b
oYXJ
oYEG
oYYC
55°N
50°N
120°W
115°W
Ū ↑

Figure 41. (a) As in Fig. 40b, except $\overline{\psi}=0°$ (westerly flow).
(b) As in Fig. 40b, except $\overline{\psi}=90°$ (southerly flow).

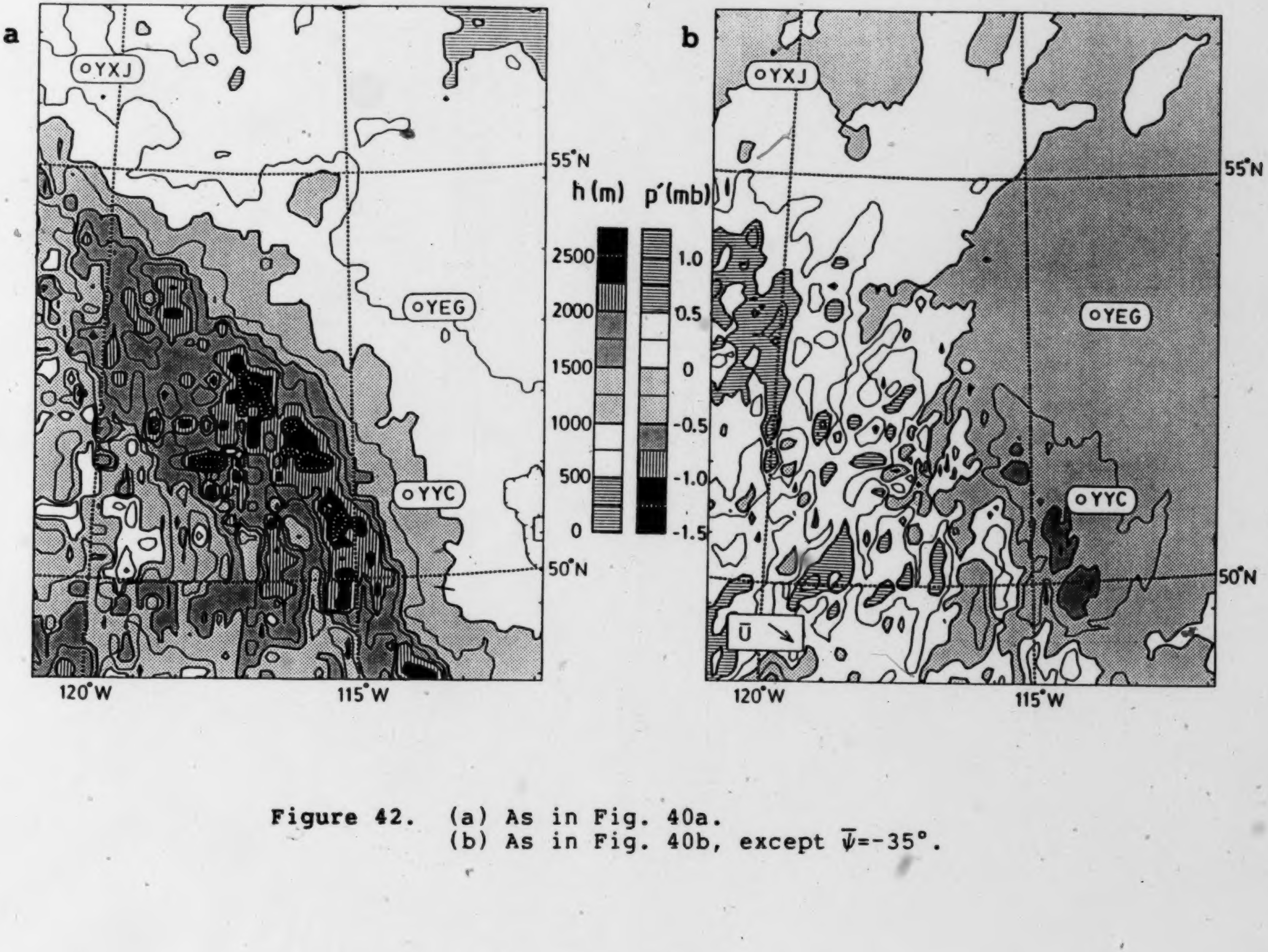
a
b
oYXJ
oYEG
oYYC
55°N
50°N
120°W
115°W
h (m)
p′(mb)
2500
2000
1500
1000
500
0
1.0
0.5
0
-0.5
-1.0
-1.5
Ū

Figure 42. (a) As in Fig. 40a.
(b) As in Fig. 40b, except $\overline{\psi}$=-35°.

coincident with the length scale over which the mountains show a large slope in the cross-sections of Fig. 38 (panels (h) through (l)). The magnitude of the extreme pressure in the lee is not uniform along the length of the ridge. The distribution of negative pressure perturbation is similar to the pattern of terrain-induced descending motion described by Charette (1971, p. 58). For all of the wind directions shown here, there is a small region ofrelatively weak perturbation near 51°N and 115°W, which is associated with the Bow River Valley. Although this gap in the mountains is directly upstream (in the $\overline{\psi}$=35° case) of the break between the two maxima in the areal density of cyclogenesis frequency seen in Fig. 1, it would be unwise, at this point, to suggest any causal link between the two.

Next consider the Northeastern B.C. region. Topographic contours are shown in Fig. 43a. The display window chosen for this case is slightly smaller than for the Southern Alberta case, but the figures are plotted using the same map scale to facilitate comparison. As can be seen by looking at the intersection of 55°N and 120°W, there is a region of overlap between Figs. 43a and 40a. Considering that the grid of points upon which the contouring is based has a slightly different orientation in the two figures, the correspondence between the two contour maps is reasonable.

As already seen in the cross-section plots (Fig. 38), the mountains are significantly lower in the Northeastern B.C. ranges than in Southern Alberta. Nevertheless, the

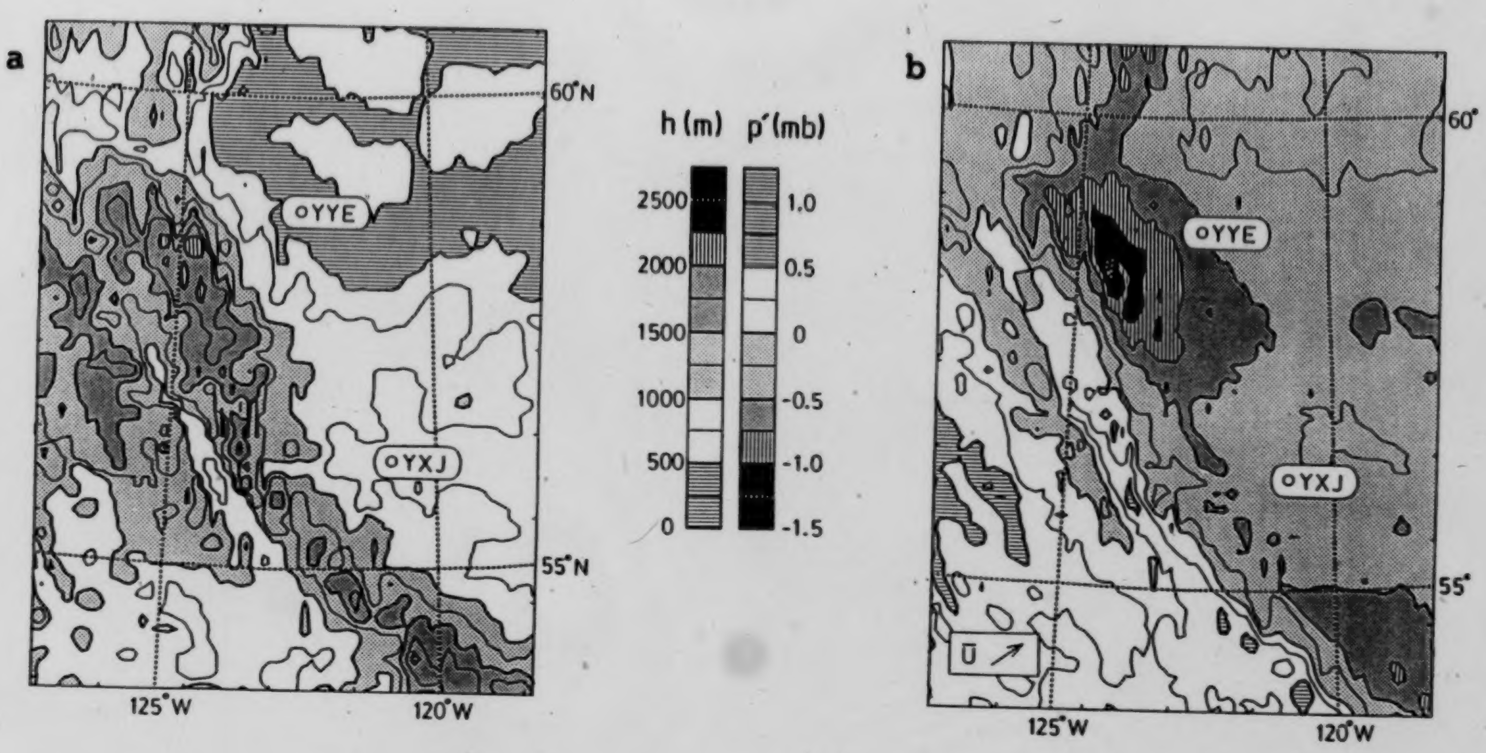
a
60°N
55°N
125°W
120°W
oYYE
oYXJ
h (m)
p′(mb)
2500
2000
1500
1000
500
0
1.0
0.5
0
-0.5
-1.0
-1.5
b
60°
55°
125°W
120°W
Ū

Figure 43. As in Fig. 40, except showing the Northeastern B.C. region ($\overline{\Psi}=35°$).

steepness of the lee slope is comparable along at least some cross-sections (for example, see Fig. 38b). This is reflected in the pressure perturbation field for the $\overline{\Psi}$=35° case, shown in Fig. 43b. Although the area of significant perturbation is smaller than in the Southern Alberta cases, the magnitude of the extreme perturbation is about the same. There is a close correspondence between the position of the minimum in the pressure field in Fig. 43b, and a maximum of lee cyclogenesis frequency per unit area in Fig. 1.

In Figs. 44a and 44b, the pressure perturbations are shown for westerly ($\overline{\Psi}$=0) and southerly flow ($\overline{\Psi}$=90°), respectively. The most significant pressure perturbations are seen with a wind from the west or southwest, with a relatively weak perturbation being produced by a southerly flow.

To conclude this section, a brief comparison will be made between the total pressure field (perturbation plus mean) and a lee trough analyzed from real weather data. In Fig. 45, a mean pressure field corresponding to a geostrophic wind of 10 m s^{-1} has been added to the perturbation field of Fig. 40b. Contours are shown at 1 mb intervals. A constant Coriolis parameter of value $f=1.15\times10^{-4}$ s^{-1} was used. Fig. 45a corresponds to the choice $\overline{N}$=.01 s^{-1} for the buoyancy frequency. In Fig. 45b, $\overline{N}$=.02 s^{-1}, so that the amplitude of the pressure perturbation is twice as large. One of the problems in trying to apply a model with such a simple vertical structure is choosing a value for $\overline{N}$. $\overline{N}$=.01 s^{-1} is more representative of the real atmosphere than

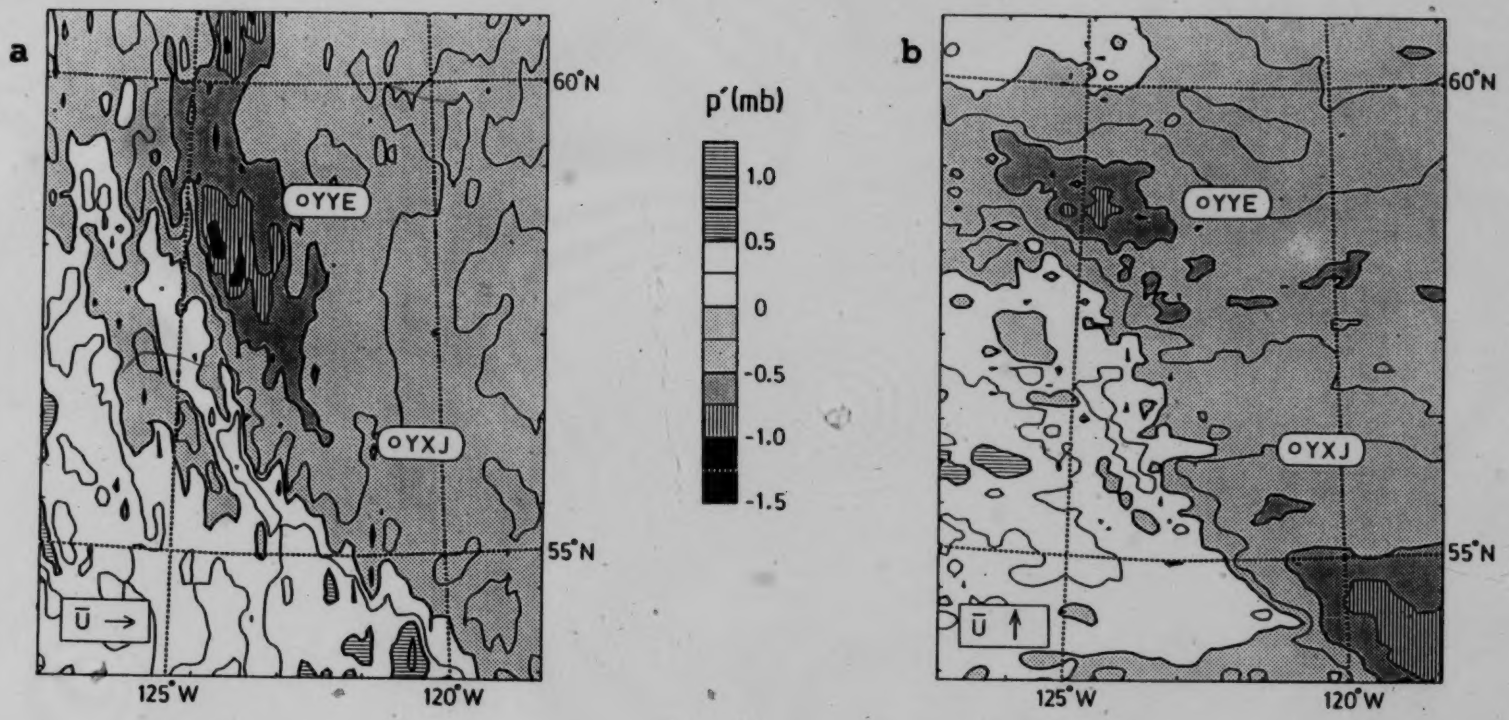
a
b
p′(mb)
1.0
0.5
0
-0.5
-1.0
-1.5
60°N
55°N
125°W
120°W
oYYE
oYXJ
$\overline{U}$ →
$\overline{U}$ ↑

Figure 44. As in Fig. 40b, except showing the Northeastern B.C. region for (a) $\overline{\psi}=0^\circ$ and (b) $\overline{\psi}=90^\circ$.

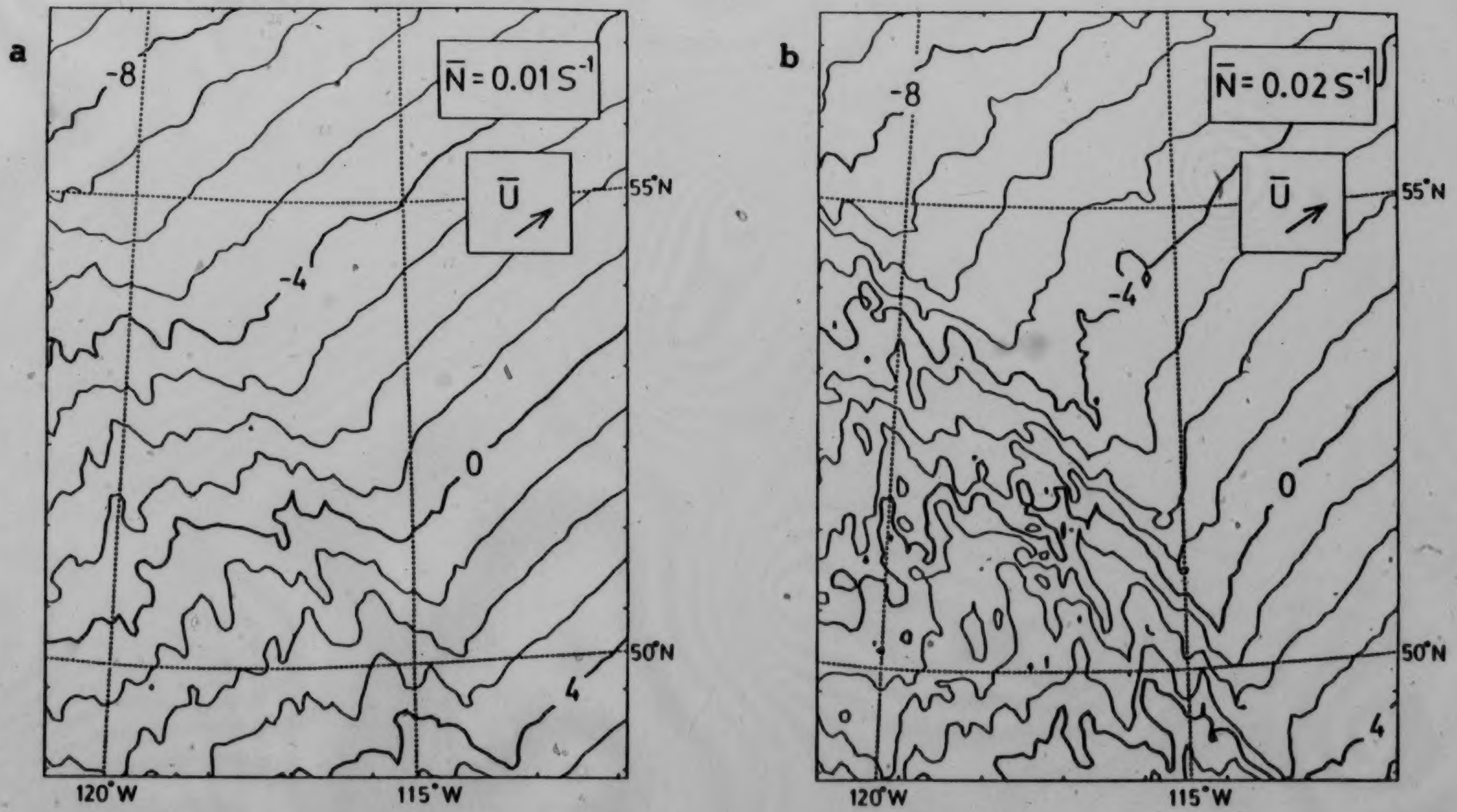
a
-8
$\bar{N}$=0.01 S^{-1}
$\bar{U}$
55°N
-4
0
50°N
4
120°W
115°W
b
-8
$\bar{N}$=0.02 S^{-1}
$\bar{U}$
55°N
-4
0
50°N
4
120°W
115°W

Figure 45. (a) Total pressure field, contoured at 1 mb intervals, for the Southern Alberta case (mean flow corresponding to a geostrophic wind of $\overline{U}=10$ m s^{-1} plus perturbation field of Fig. 40a). Parameters are $f=1.15\times10^{-4}$ s^{-1}, $\overline{\psi}=35°$, $\overline{\rho}_0=1.2$ kg m^{-3} and $\overline{N}=.01$ s^{-1}.
(b) As in (a), except $\overline{N}=.02$ s^{-1}.

$.02\ s^{-1}$. However, putting a realistic temperature in the model, such as $\bar{T}=260°K$, leads to a value of $\bar{N}$, calculated from (3.13), of $.019\ s^{-1}$.

For comparison, Fig. 46 shows a weather map with surface isobars (solid curves, labelled in millibars) and contours of geopotential height at 500 mb (dashed curves, labelled in tens of geopotential metres) based on an analysis by the Canadian Meteorological Centre for 1200 UTC on 2 February 1984. The region depicted in Fig. 45 is shaded in Fig. 46. Wind barbs, in standard notation, show the 500 mb wind in knots. The flow at 500 mb, of about 20 m s^{-1} upstream of the Continental Divide, is nearly perpendicular to the main range of the Rocky Mountains. The contours at 700 mb (not shown) show a similar configuration. The surface analysis indicates a windward ridge and lee trough which are vaguely similar to the corresponding features in Fig. 45. However, the width of the trough calculated from the simple theory is significantly less than that seen in Fig. 46 and occurs closer to the barrier. In application of a more complicated linear model, which included rotation, to flow over the Bavarian Hills, Somieski (1981) also found the observed pressure field to be characterized by a larger horizontal scale than seen in the model. As noted by Somieski, the network of synoptic stations is inadequate to properly verify the mesoscale details of a numerical model.

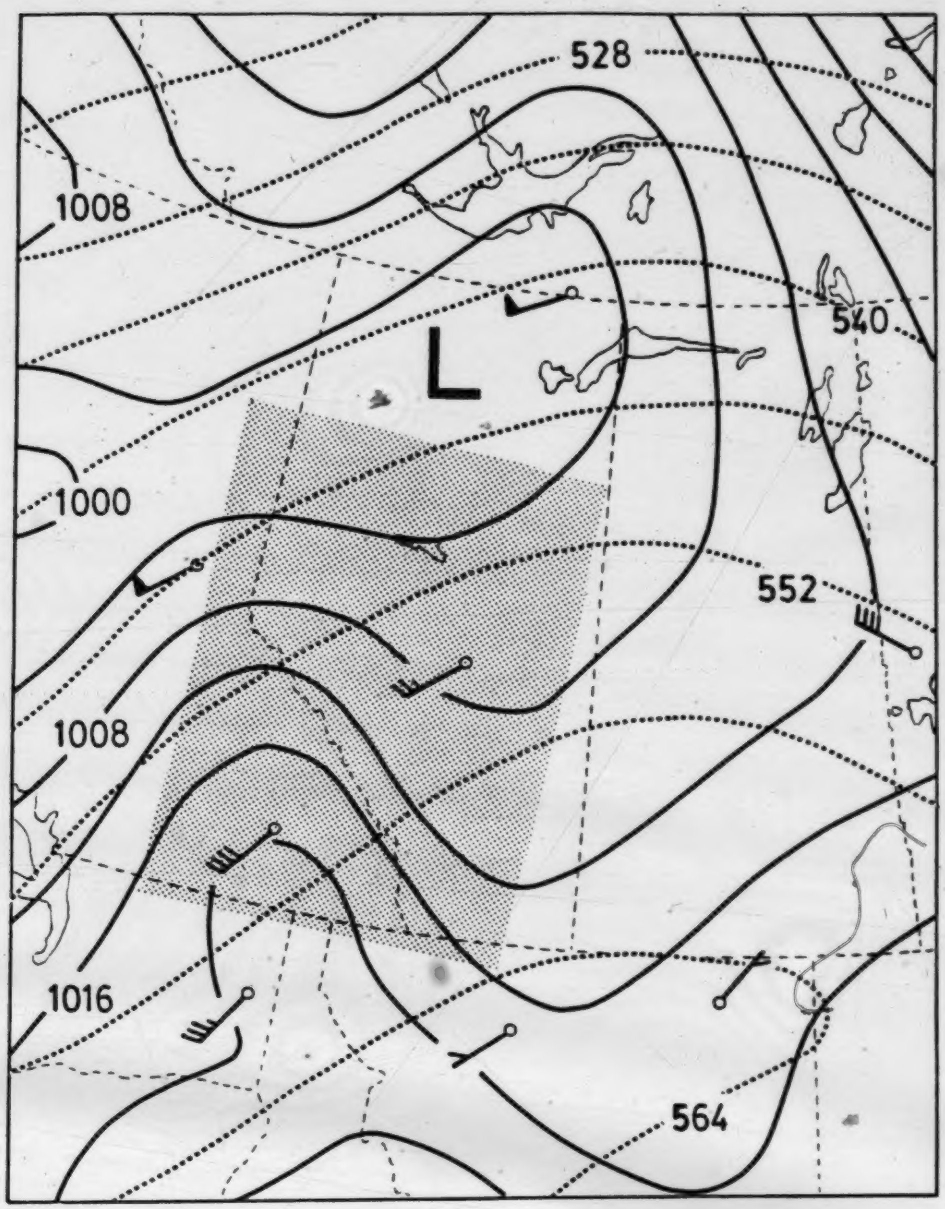
528
1008
540
1000
552
1008
1016
564

Figure 46. Surface isobars (solid curves, in mb) and 500 mb geopotential height contours (dashed curves, in tens of gpm) at 1200 UTC on 2 February 1984. Wind barbs show 500 mb wind speed in knots. Shaded region corresponds to Fig. 45.

CHAPTER 13

SUMMARY AND POSSIBILITIES FOR FUTURE STUDY

13.1 Summary

The research that is summarized in this thesis consisted primarily of three components: a review of theory and observations of lee cyclogenesis; application of a simple model to the determination of the surface pressure perturbation due to an isolated three-dimensional barrier; and, the calculation of the net force exerted on the terrain surface by the air in the same linear model. Some of the main results from these three areas will now be summarized.

In the review of lee cyclogenesis, given in Chapter 2, the discussion centered on conservation of potential vorticity. Typical sequences of lee cyclone formation were considered for Alpine and Rocky Mountain regions. In both cases, a two-step process may be involved, with the development of an area of enhanced low-level vorticity in the lee which is subsequently overtaken by an advancing upper trough. In Chapter 3, a study was made of the data compiled by Chung (1972) on the formation of lows in the lee of the Rocky Mountains in Western Canada. It was found that the areal density of cyclogenesis frequency is a sensitive function of the area over which cyclone counts are averaged, at least for the small sample size considered. Attention was focussed on the existence of two maxima of cyclogenesis frequency per unit area in the southern half of Alberta. Of these maxima, the northern one showed a deficiency, and the southern one an excess, of lee cyclones that were classified as having relatively short trajectories. A similar pattern was noted for lee lows that were not associated with upstream parent cyclones.

In Chapters 3, 4, 5, and 7, linear, hydrostatic theory was applied to the airflow over a class of three-dimensional elliptical mountains, with an emphasis on departures from two-dimensional flow. Because of the unsheared, isothermal structure of the upstream flow, analytical solutions for several surface fields of interest could be obtained. The results have been discussed mainly in terms of the dependence of these fields on three geometric parameters: 1) the ratio of two horizontal terrain length scales, $\gamma=a/b$; 2) the terrain height exponent, μ, which is related to the maximum barrier slope and its behavior away from the peak; and 3) the barrier orientation angle, ψ.

To indicate the role of the parameter γ, some of the characteristics of flow over three-dimensional barriers ($\gamma>0$) were compared to those of flow in vertical planes, over infinitely-long ridges having the same cross-section ($\gamma=0$). The surface pressure perturbation in a three-dimensional case, with $\gamma=1$, has an extreme value which is typically about 30% less than the two-dimensional one, and occurs closer to the barrier peak. Also, for a given exponent, μ, the perturbation falls off more rapidly with distance from the top of an isolated barrier than from an extended ridge. The maximum pressure perturbation in the case of flow in vertical planes is found to be within 10% of that for the full three-dimensional flow solution, if the crosswind width of the terrain is more than about three times the length of the barrier in the direction parallel to the mean wind ($\gamma<1/3$). For $\gamma<1/5$, the relative difference between the maximum surface pressure perturbation in the two- and three-dimensional flows is reduced to less than 5%. For an unrotated barrier ($\psi=0$), the greatest difference in surface pressure between the two- and three-dimensional cases occurs on the symmetry axis parallel to the mean wind, rather than off to the sides where the air is deflected laterally by a three-dimensional barrier.

The variation of the maximum pressure with γ is qualitatively similar for different values of the terrain exponent, μ. However, as μ increases, implying a barrier with a sharper peak, the maximum pressure perturbation increases and shifts closer to the terrain top. Far from the barrier, the asymptotic decay of the pressure field is found to be closely related to the terrain volume, which, in turn, is a function of μ. For an isolated barrier with finite volume, the pressure field falls off as X^{-2}. However, for sufficiently small μ, the volume is infinite and the pressure field decays more gradually.

The final geometrical parameter involved in the solution is the angle, ψ, defining the orientation of the elliptical barrier with respect to the undisturbed stream. The pressure perturbation is greatest when the long axis of the barrier is perpendicular to the mean flow. For a ridge with $\mu=2$ and $\gamma=1/2$, the maximum perturbation is about 1.5 times larger when the long axis is across the wind ($\psi=0$), than when it is along the wind ($\psi=90°$). The maximum gradient of pressure is a more sensitive function of ψ, with the $\psi=0$ result being about 2.8 times that for $\psi=90°$, in the $\gamma=1/2$ case. On the other hand, the maximum horizontal divergence is independent of the barrier orientation.

In general, the surface fields considered in this paper have a rather complicated functional dependence on the parameters μ, γ and ψ. However, the calculations in Appendix F show that, at R=0, the pressure gradient, horizontal divergence, and other quantities, take a simpler form, in which the dependence on μ factors out from that on the parameters γ and ψ. As a consequence, for example, the ratio of the maximum horizontal divergence for flow over a circular hill to that over an infinitely-extended ridge (both with the same horizontal scale, a), has the value $\pi/2$, independent of the shape of the vertical cross-section of the barriers (i.e., independent of μ).

Another geometrical feature of the terrain was studied in Chapter 6, where the pressure perturbation was calculated for flow over infinitely-extended crosswind ridges that were curved in a horizontal plane. Parabolic and sinusoidal types of curvature were considered. The perturbation was found to be enhanced on the convex side of the ridge and reduced in magnitude on the concave side, relative to a straight ridge. The absolute change in pressure, due to the effect of curvature, was greatest in the concave regions.

The force exerted on a mountain by the air streaming over it was studied in Chapters 8 through 12, again using a simple linear model. The drag per unit length was calculated for the two-dimensional flow over a variety of uniform crosswind ridges. Symmetrical single ridges, a superposition of two separate ridges and sinusoidally modulated barriers were all considered. The presence of sharp corners or steep slopes tends to increase the drag per unit length, d_2, although discussion of such effects is complicated by the invariance of d_2 with respect to a change of horizontal scale in the direction parallel to the incoming flow. The discussion of the sinusoidally modulated terrain in Section 9.2 emphasized that it is the high spatial frequency components of the terrain height spectrum that contribute to the drag force. The drag per unit crosswind length for flow over a barrier constructed from the juxtaposition of two identical ridges was found to be smaller than the value expected from the maximum pressure perturbation, for some values of the ridge separation distance. This result is associated with the cancellation of the lee low of the upwind ridge with the windward high of the downwind ridge. These examples serve to illustrate the complexity of predicting wave drag from mountain shape, even in this simple model.

The drag per unit crosswind length is independent of y for the ridge case discussed above. The calculations are more difficult for three-dimensional flow over isolated hills, but some results have been presented in Chapter 9. The drag values for three-dimensional barriers differ from the two-dimensional flow results along the Y=0 axis by 10% if the crosswind dimension of the mountain is from about 2 to 4 times the length scale parallel to the mean wind, depending on the shape of the vertical profile of the barrier.

The total force exerted by the air on the terrain proved to be relatively easy to calculate for barriers with an elliptical horizontal cross-section of arbitrary eccentricity and orientation. For an elongated barrier the force varies considerably as the orientation of the mountain is changed relative to the incident wind. For example, a hill with a major to minor axis ratio of 4 experiences a force which is over 8 times larger if the long axis of the barrier is across, compared to along, the mean flow. If the upstream flow is not parallel to an axis of symmetry of the barrier, it experiences a transverse force which can be an appreciable fraction of, or even exceed, the drag force component. Conditions are particularly favourable for a large transverse force (relative to the drag force) if the barrier is highly eccentric, with the long axis inclined to the mean flow by less than 45°.

In Chapter 11, the effect of smoothing a terrain shape was determined, either by applying a differential operator or by truncating a spectral series. The drag and drag per unit crosswind length were found to differ from values determined from a scaling based on the square of the maximum terrain height. This result is due to the fact that the terrain shape is not preserved as the height is reduced through the smoothing procedure. The extent of the departure from a quadratic height dependence varies with the initial barrier shape and which smoothing operation is performed.

It should be noted that the wave drag is a function of many other factors of equal or potentially greater importance than the geometrical factors considered here. For example, the sensitivity of the wave structure to vertical shear in the mean wind and stability has been studied by Klemp and Lilly (1975). Peltier and Clark (1979) emphasized the importance of the time evolution of the flow and of nonlinear processes (for sufficiently steep barriers). The surface drag for a nonlinear flow exceeds the linear theory result by a factor of three or more in some of their calculations. As shown by Jusem and Barcilon (1981), introduction of terrain asymmetry also tends to increase the drag, particularly in a nonlinear model (Lilly and Klemp, 1979). On the other hand, Barcilon et al. (1979) find that the inclusion of moisture reduced the drag by 40% in a typical case.

All of the studies mentioned here refer to two-dimensional models. In three-dimensional flows, the extra degree of freedom introduces new complications (in addition to the role of barrier orientation and shape, discussed in this paper). For barriers of slightly larger scale than those to which the present theory is applicable, Smith (1979b) has studied the reduction in drag that occurs if one introduces a Coriolis force. As another example, Blumen and McGregor (1976) find a 30% increase in drag is possible when lateral shear of the horizontal wind is included in the upstream flow. Further work is required to uncover how these varied factors interact when several of them are allowed to act simultaneously, especially in three-dimensional models.

Finally, in Chapter 12, some consideration was given to the application of a linear model to air flow over a realistic representation of the Rocky Mountains. In the model, the minimum pressure in the lee trough occurs 50-100 km downstream of the major topographic ridge. A typical surface-pressure analysis based on synoptic data, however, placed the lee trough significantly further downwind, perhaps 200-300 km from the mountain peaks.

13.2 Possibilities for future study

In this section, some possible directions for future research on lee cyclogenesis and related aspects of mountain airflow will be outlined.

In the course of the discussion of lee cyclogenesis in Chapter 1, it was noted that Speranza (1975) made a distinction between lee-side low-pressure areas in general and those low-pressure regions with cyclonic vorticity. Clarification of these differences might lead to insight into the initial stages of lee cyclone development. As previously noted in Chapter 3, the simple model used in the current work cannot describe the formation of regions of enhanced vorticity. Therefore, further exploration is needed of the ways in which vorticity can be generated by mountain induced circulations. This requirement was also seen in the discussion of potential vorticity conservation in Chapter 1. To what extent is a lee cyclogenesis event the formation of a new weather system? Is it simply the regeneration of cyclonic vorticity that was present on the windward side of the barrier? Smith (1979a, p. 165) suggested that trajectory analysis could be used to determine whether 'the lee cyclone is composed of the same fluid particles as the parent cyclone'. Cyclolysis on the windward side of a barrier is an inadequately documented process, but is a part of the overall interaction of a low-pressure center with a mountain range.

It is suggested that in future studies of the formation of lee cyclones that the surface pressure field be analyzed at contour intervals of no greater than 2 mb, and at as fine a temporal resolution as possible. This would allow one to investigate the possible interaction of diurnal mountain circulations or tides (Longley, 1968, 1969; Hamilton, 1980) with other processes affecting the pressure distribution in the lee. Hourly surface pressure data are available, but, to restrict the amount of data to be handled to manageable proportions, it might be necessary to limit study to a small region, such as the southern half of Alberta. By collecting additional data on cyclogenesis in this area, with particular attention to classifying the lows according to the criteria used by Schallert (1962) and Chung (1972), it might be possible to clarify whether or not the double maximum in cyclogenesis frequency seen in Chung's data is due to his limited sample size. It could also be useful to note the degree of association between a lee cyclone and features in the upstream flow, such as the presence or absence of an advancing trough, or a parent surface low. Numerical modelling could also be used to test for the existence of preferred regions of cyclone formation. If the model were sufficiently simple to allow it, one could execute many integrations under slightly different initial conditions to compile statistics on regions of cyclogenesis.

One of the major limitations of the model used in the present work, is its steady-state nature. Time-dependent models of mountain waves have been used in past research, but, often not for the study of time-dependent phenomena. For example, Durran and Klemp (1983) initialize their model by gradually increasing the mean wind speed, up to some constant value, and then continue the integration with this constant upstream forcing. No attempt is made to study the wave response under conditions of variable upstream flow. Other recent papers, which deal explicitly with time-dependent phenomena that may be of relevance to lee cyclogenesis, include the work of Bannon (1983) on the interaction of a front with a topographic barrier, and the baroclinic instability studies of Farrell (1982) and Grotjahn (1980). Although the introduction of the time variable increases the complexity of the mathematical development considerably, it opens interesting possibilities for future research.

Although the many limitations of the model used in this thesis preclude detailed comparison with real atmospheric flows, it is hoped that the analytical results that have been presented will serve to provide useful checks on more realistic models. The main emphasis has been on the differences between flow over infinitely-extended ridges and that over isolated hills. As technological developments allow more extensive calculations to be performed, increased understanding of the three-dimensional aspects of mountain airflow will surely result.

BIBLIOGRAPHY

Abramowitz, M., and I. A. Stegun, 1965: *Handbook of Mathematical Functions.* Dover Publications, Inc., New York, 1046 pp.

Ballentine, R. J., 1980: A numerical investigation of New England coastal frontogenesis. *Mon. Weather Rev.*, 108, 1479-1497.

Bannon, P. R., 1983: Quasi-geostrophic frontogenesis over topography. *J. Atmos. Sci.*, 40, 2266-2277.

Barcilon, A., J. C. Jusem, and P. G. Drazin, 1979: On the two-dimensional hydrostatic flow of a stream of moist air over a mountain ridge. *Geophys. Astrophys. Fluid Dyn.*, 13, 125-140.

Barcilon, A., J. C. Jusem, and S. Blumsack, 1980: Pseudo-adiabatic flow over a two-dimensional ridge. *Geophys. Astrophys. Fluid Dyn.*, 16, 19-33.

Bettge, T. W., 1983: A systematic error comparison between the ECMWF and NMC prediction models. *Mon. Weather Rev.*, 111, 2385-2389.

Blumen, W., 1965: A random model of momentum flux by mountain waves. *Geofys. Publ.*, 26, 1-33.

Blumen, W., and S. C. Dietze, 1981: An analysis of three-dimensional mountain lee waves in a stratified shear flow. *J. Atmos. Sci.*, 38, 1949-1963.

Blumen, W., and C. D. McGregor, 1976: Wave drag by three-dimensional mountain lee-waves in nonplanar shear flow. *Tellus*, 28, 287-298.

Bolin, B., 1950: On the influence of the Earth's orography on the general character of the westerlies. *Tellus*, 2, 184-195.

Bretherton, F. P., 1969: Momentum transport by gravity waves. *Q. J. Roy. Meteorol. Soc.*, 95, 213-243.

Brinkmann, W., and I. Y. Ashwell, 1968: The structure and movement of the chinook in Alberta. *Atmosphere*, 6, 1-10.

Buzzi, A., and S. Tibaldi, 1977: Inertial and frictional effects on rotating stratified flow over topography. *Q. J. Roy. Meteorol. Soc.*, 103, 135-150.

Byrd, P. F., and M. D. Friedman, 1971: *Handbook of Elliptic Integrals for Engineers and Scientists.* Second Edition, Revised, Springer-Verlag, Berlin, 358 pp. (Denoted by BF in this thesis).

Byron, F. W., Jr., and R. W. Fuller, 1969: *Mathematics of Classical and Quantum Physics. Volume One.* Addison-Wesley, Reading, Mass., 310 pp.

Carlson, T. N., 1961: Lee-side frontogenesis in the Rocky Mountains. *Mon. Weather Rev.*, 89, 163-172.

Carpenter, A. B., 1945: Cyclogenetic arcs on the Pacific coast. *Bull. Am. Meteorol. Soc.*, 26, 72-73.

Charette, C. O., 1971: Streamline patterns and terrain-induced vertical velocities in the Canadian Cordillera. M. Sc. Thesis, Univ. of Alberta, Edmonton, 117 pp.

Charney, J. G., and A. Eliassen, 1949: A numerical method for predicting the perturbations of the middle latitude westerlies. *Tellus*, 1, 38-54.

Chung, Y.-S., 1972: Lee cyclogenesis in the Canadian Rockies. M. Sc. Thesis, Univ. of Alberta, 156 pp.

Chung, Y.-S., 1977a: On the orographic influence and lee cyclogenesis in the Andes, the Rockies, and the East Asian Mountains. *Arch. Met. Geoph. Biokl., Ser. A.*, 26, 1-12.

Chung, Y.-S., 1977b: An observational study of the influence of large-scale mountains on air flow and lee cyclogenesis. *Arch. Met. Geoph. Biokl., Ser. A.*, **26**, 109-126.

Chung, Y.-S., K. D. Hage, and E. R. Reinelt, 1976: On lee cyclogenesis and airflow in the Canadian Rocky Mountains and the East Asian Mountains. *Mon. Weather Rev.*, **104**, 879-891.

Chung, Y.-S., and E. R. Reinelt, 1973: On cyclogenesis in the lee of the Canadian Rocky Mountains. *Arch. Met. Geoph. Biokl., Ser. A.*, **22**, 205-226.

Clark, T. L., and R. Gall, 1982: Three-dimensional numerical model simulations of airflow over mountainous terrain: a comparison with observations. *Mon. Weather Rev.*, **110**, 766-791.

Clark, T. L., and W. R. Peltier, 1977: On the evolution and stability of finite-amplitude mountain waves. *J. Atmos. Sci.*, **34**, 1715-1730.

Cook, A. W., and A. G. Topil, 1952: Some examples of chinooks east of the mountains in Colorado. *Bull. Am. Meteorol. Soc.*, **33**, 42-47.

Crapper, G. D., 1959: A three-dimensional solution for waves in the lee of mountains. *J. Fluid Mech.*, **6**, 51-76.

Crapper, G. D., 1962: Waves in the lee of a mountain with elliptical contours. *Philos. Trans. R. S. London, Ser. A.* **254**, 601-623.

Dickinson, R. E., 1980: Planetary waves: theory and observation. Chapter 2 of Orographic Effects on Planetary Flows, *GARP Publication Series*, **23**, WMO - ICSU, pp. 51-84.

Durran, D. R., and J. B. Klemp, 1983: A compressible model for the simulation of moist mountain waves. *Mon. Weather Rev.*, **111**, 2341-2361.

Egger, J., 1972: Incorporation of steep mountains into numerical forecasting models. *Tellus*, **24**, 324-335.

Egger, J., 1974: Numerical experiments on lee cyclogenesis. *Mon. Weather Rev.*, 102, 847-860.

Farrell, B. F., 1982: The initial growth of disturbances in a baroclinic flow. *J. Atmos. Sci.*, 39, 1663-1686.

Fawcett, E. B., 1969: Systematic errors in operational baroclinic prognoses at the National Meteorological Center. *Mon. Weather Rev.*, 97, 670-682.

Fawcett, E. B., and H. K. Saylor, 1965: A study of the distribution of weather accompanying Colorado cyclogenesis. *Mon. Weather Rev.*, 93, 359-367.

Fons, M. C., 1979: Cyclogénèses du Bassin Méditerraneén Occidental. *Monographie N'109 de la Météorologie Nationale Ministère des Transports*, Direction de la Météorologie, 54 pp.

Gerald, C. F., 1978: *Applied Numerical Analysis*. Second Edition, Addison-Wesley, Reading, Mass., 518 pp.

Gerbier N., and M. Berenger, 1961: Experimental studies of lee waves in the French Alps. *Q. J. Roy. Meteorol. Soc.*, 87, 13-23 and Plates I-III.

Godev, N., 1971: The cyclogenetic properties of the Pacific coast: possible source of errors in numerical prediction. *J. Atmos. Sci.*, 28, 968-972.

Godson, W. L., 1948: A new tendency equation and its application to the analysis of surface pressure changes. *J. Meteorol.*, 5, 227-235.

Gossard, E. E., and W. H. Hooke, 1975: *Waves in the Atmosphere*, Elsevier, Amsterdam, 456 pp.

Gradshteyn, I. S., and I. M. Ryzhik, 1965: *Table of Integrals, Series, and Products*, Academic Press Inc., New York, 1086 pp. (Denoted by GR in this thesis).

Grotjahn, R., 1981: Stability properties of an arbitrarily oriented mean flow. *Tellus*, 33, 188-200.

Hage, K. D., 1961: On summer cyclogenesis in the lee of the Rocky Mountains. *Bull. Am. Meteorol. Soc.*, 42, 20-33.

Hamilton, K., 1980: Observations of the solar diurnal and semidiurnal surface pressure oscillations in Canada. *Atmosphere-Ocean*, 18, 89-97.

Hess, S. L., and H. Wagner, 1948: Atmospheric waves in the northwestern United States. *J. Meteorol.*, 5, 1-19.

Holton, J. R., 1972: *An Introduction to Dynamic Meteorology*. Academic Press, Inc., New York, 319 pp.

Hopkinson, R. F., 1972: A study of orographically-induced vertical velocity and precipitation in western Canada. M. Sc. Thesis, Univ. of Alberta, Edmonton, 79 pp.

Hoskins, B. J., 1980: Representation of the Earth topography using spherical harmonics. *Mon. Weather Rev.*, 108, 111-115.

Hovanec, R. D., and L. H. Horn, 1975: Static stability and the 300 mb isotach field in the Colorado cyclogenetic area. *Mon. Weather Rev.*, 103, 628-638.

Jurčec, V., 1981: On the problem of oreigenic lee cyclogenesis by means of isentropic analysis. Paper presented at the Second Conference on Mountain Meteorology of the American Meteorological Society, Nov. 9-12, 1981, Steamboat Springs, Colorado, U.S.A.

Jusem, J. C., and A. Barcilon, 1981: Hydrostatic mountain waves produced by asymmetric ridges. *Geophys. Astrophys. Fluid Dyn.*, 17, 3-14.

Kasahara, A., 1966: The dynamical influence of orography on the large-scale motion of the atmosphere. *J. Atmos. Sci.*, 23, 259-271.

Kasahara, A., 1980: Influence of orography on the atmospheric general circulation. Chapter 1 of Orographic Effects in Planetary Flows, *GARP Publication Series*, 23, WMO - ICSU, pp. 1-49.

Kasahara, A., T. Sasamori, and W. M. Washington, 1973: Simulation experiments with a 12-layer stratospheric global circulation model. I. Dynamical effect of the Earth's orography and thermal influence of continentality. *J. Atmos. Sci.*, 30, 1229-1251.

Klemp, J. B., and D. K. Lilly, 1975: The dynamics of wave-induced downslope winds. *J. Atmos. Sci.*, 32, 320-339.

Klemp, J. B., and D. K. Lilly, 1978: Numerical simulation of hydrostatic mountain waves. *J. Atmos. Sci.*, 35, 78-107.

Klemp, J. B., and D. K. Lilly, 1980: Mountain waves and momentum flux. Chapter 4 of Orographic Effects in Planetary Flows, *GARP Publication Series*, 23, WMO - ICSU, pp. 115-141.

Kuettner, J. P., and H. R. O'Neill, 1981: ALPEX, the GARP mountain subprogram. *Bull. Am. Meteorol. Soc.*, 62, 793-805.

Lang, H. A., and D. F. Stevens, 1960: On the evaluation of certain complex elliptic integrals. *Math. Computat.*, 14, 195-199.

Lester, P., 1976: Evidence of long lee waves in southern Alberta. *Atmosphere*, 14, 28-36.

Lilly, D. K., and J. B. Klemp, 1979: The effects of terrain shape on nonlinear hydrostatic mountain waves. *J. Fluid Mech.*, 95, Part 2, 241-261.

Longley, R. W., 1968: The diurnal variation of wind direction at Calgary. *Atmosphere*, 6, 23-38.

Longley, R. W., 1969: The diurnal pressure wave in western Canada. *J. Appl. Meteorol.*, 8, 754-761.

Lyra, G., 1943: Theorie der stationären Leewellenströmung in freier Atmosphäre. *Z. Angew. Math. Mech.*, 23, 1-28.

Manabe, S., and T. B. Terpstra, 1974: The effects of mountains on the general circulation of the atmosphere as identified by numerical experiments. *J. Atmos. Sci.*, 31, 3-42.

Marthinsen, T., 1980: Three-dimensional lee waves. *Q. J. Roy. Meteorol. Soc.*, 106, 569-580.

Mathews, J., and R. L. Walker, 1970: *Mathematical Methods of Physics*. Second Edition, W. A. Benjamin, Inc., New York, 501 pp.

McClain, E. P., 1952: Synoptic investigation of a typical chinook situation in Montana. *Bull. Am. Meteorol. Soc.*, 33, 87-94.

McClain, E. P., 1960: Some effects of the western Cordillera of North America on cyclonic activity. *J. Meteorol.*, 17, 105-115.

McGinley, J., 1982: A diagnosis of Alpine lee cyclogenesis. *Mon. Weather Rev.*, 110, 1271-1287.

McKay, G. A., (undated): Climatic maps of the prairie provinces for agriculture. Climatological Studies No. 1, Dept. of Transport, Meteorological Branch, Toronto.

Newton, C. W., 1956: Mechanisms of circulation change during a lee cyclogenesis. *J. Meteorol.*, 13, 528-539.

Palm, E., 1958: Two-dimensional and three-dimensional mountain waves. *Geofys. Publ.*, 20, 1-25.

Palmén, E., and C. W. Newton, 1969: *Atmospheric Circulation Systems*, Academic Press Inc., New York, 603 pp.

Parish, T. R., 1982: Barrier winds along the Sierra Nevada Mountains, *J. Appl. Meteorol.*, 21, 925-930.

Pearse, J. R., D. Lindley and D. C. Stevenson, 1981: Wind flow over ridges in simulated atmospheric boundary layers. *Boundary-Layer Meteorol.*, 21, 77-92.

Pedlosky, J., 1979: *Geophysical Fluid Dynamics.* Springer-Verlag New York Inc., New York, 624 pp.

Peltier, W. R., and T. L. Clark, 1979: The evolution and stability of finite-amplitude mountain waves. Part II: Surface wave drag and severe downslope windstorms. *J. Atmos. Sci.*, **36**, 1498-1529.

Petterssen, S., 1955: A general survey of factors influencing development at sea level. *J. Meteorol.*, 12, 36-42.

Petterssen, S., 1956: Weather Analysis and Forecasting. Second Edition, Volume 1, McGraw-Hill Book Company, Inc., New York, 428 pp.

Petterssen, S., G. E. Dunn and L. L. Means, 1955: Report of an experiment in forecasting of cyclone development. *J. Meteorol.*, 12, 58-67.

Peyrefitte, A. G. Jr. and E. G. Astling, 1981: Comments on 'The climatology of cyclones and anticyclones over N. America and surrounding ocean environs for January and July 1950-77'. *Mon. Weather Rev.*, **109**, 1356-1357.

Queney, P., 1947: Theory of perturbations in stratified currents with applications to air flow over mountain barriers. Dept. of Meteorol., Univ. of Chicago, Misc. Reports No. 23, 81 pp.

Queney, P., 1948: The problem of air flow over mountains: A summary of theoretical studies. *Bull. Am. Meteorol. Soc.*, 29, 16-26.

Queney, P., G. A. Corby, N. Gerbier, H. Koschmieder, and J. Zierep, 1960: The airflow over mountains. *WMO Tech. Note No. 34*, 135 pp.

Radinović, D., 1965: Cyclonic activity in Yugoslavia and surrounding areas. *Arch. Met. Geoph. Biokl., Ser. A.*, 14, 391-408.

Reitan, C. R., 1974: Frequencies of cyclones and cyclogenesis for N. America, 1951-1970. *Mon. Weather Rev.*, 102, 861-868.

Sampson, R. J., 1978: Surface II Graphics System, Revised Ed., Kansas Geological Survey, Lawrence, Kansas, 240 pp.

Sawyer, J. S., 1959: The introduction of the effects of topography into methods of numerical forecasting. *Q. J. Roy. Meteorol. Soc.*, 85, 31-43.

Sawyer, J. S., 1962: Gravity waves in the atmosphere as a three-dimensional problem. *Q. J. Roy. Meteorol. Soc.*, 88, 412-425.

Schallert, W. L., 1962: An investigation of Colorado cyclones. Univ. of Chicago, Dept. of the Geophysical Sciences, Scientific Report No. 7, Contract No. AF 19(604)-7230, 68 pp.

Schram, G. R., 1974: The influence of orography and surface friction on synoptic scale vertical motions over Western Canada. M. Sc. Thesis, Univ. of Alberta, Edmonton, 83 pp.

Smith, R. B., 1976: The generation of lee waves by the Blue Ridge. *J. Atmos. Sci.*, 33, 507-519.

Smith, R. B., 1979a: The influence of mountains on the atmosphere. *Adv. Geophys.*, 21, 87-230.

Smith, R. B., 1979b: The influence of the Earth's rotation on mountain wave drag. *J. Atmos. Sci.*, 36, 177-180.

Smith, R. B., 1979c: Some aspects of the quasi-geostrophic flow over mountains. *J. Atmos. Sci.*, 36, 2385-2393.

Smith, R. B., 1980: Linear theory of stratified hydrostatic flow past an isolated mountain. *Tellus*, 32, 348-364.

Smith, R. B., 1981: An alternative explanation for the destruction of the Hood Canal bridge. *Bull. Am. Meteorol. Soc.*, **62**, 1319-1320.

Smith, R. B., 1982: Synoptic observations and theory of orographically disturbed wind and pressure. *J. Atmos. Sci.*, **39**, 60-70.

Smith, R. B., and Y.-L. Lin, 1982: The addition of heat to a stratified airstream with application to the dynamics of orographic rain. *Q. J. Roy. Meteorol. Soc.*, **108**, 353-378.

Somieski, F., 1981: Linear theory of three-dimensional flow over mesoscale mountains. *Contrib. Atmos. Phys.*, **54**, 315-334.

Speranza, A., 1975: The formation of baric depressions near the Alps. *Ann. Geofis.* , Rome, **28**, 177-217.

Sutcliffe, R. C., 1951: Mean upper contour patterns of the northern hemisphere - the thermal synoptic view-point. *Q. J. Roy. Meteorol. Soc.*, 77, 435-440.

Sutherland, C. D., 1965: Footnote to the evaluation of certain complex elliptic integrals. *Math. Computat.*, **19**, 132-133.

Tibaldi, S., 1979: Lee cyclogenesis and its numerical simulation, with special attention to the Alpine region: a review. *Geophys. Astrophys. Fluid Dynamics*, **13**, 25-49.

Tibaldi, S., 1980: Cyclogenesis in the lee of orography and its numerical modelling, with special reference to the Alps. Chapter 7 of Orographic Effects on Planetary Flows, *GARP Publication Series*, **23**, WMO - ICSU, pp. 207-232.

Tibaldi, S., A. Buzzi, and P. Malguzzi, 1980: Orographically induced cyclogenesis: analysis of numerical experiments. *Mon. Weather Rev.*, **108**, 1302-1314.

Vergeiner, I., 1971: An operational linear lee wave model for arbitrary basic flow and two-dimensional topography. *Q. J. Roy. Meteorol. Soc.*, 97, 30-60.

Vickers, G. G., 1975: Diffluence and cyclogenesis in the lee of the Rocky Mountains. M. Sc. Thesis, Univ. of Alberta, Edmonton, 126 pp.

Wurtele, M. G., 1957: The three-dimensional lee wave. *Contrib. Atmos. Phys.*, 29, 242-252.

Zehnder, J. A., and P. R. Bannon, 1983: Some aspects of linear mountain wave drag. Unpublished manuscript. Dept. of the Geophysical Sciences, Univ. of Chicago, 39 pp.

Zishka, K. M., and P. J. Smith, 1980: The climatology of cyclones and anticyclones over N. America and surrounding ocean environs for January and July 1950-77. *Mon. Weather Rev.*, 108, 387-401.

Zishka, K. M., and P. J. Smith, 1981: Reply. *Mon. Weather Rev.*, 109, 1358.

APPENDIX A

JUSTIFICATION OF THE NEGLECT OF CERTAIN EFFECTS OF THE VERTICAL VARIATION OF DENSITY

In this appendix an analytical solution is found for the pressure perturbation due to an infinitely-extended ridge, retaining all the terms in the governing equations (3.1-3.5). This exact solution is then used to determine whether certain terms, involving compressibility and the vertical variation of density, can be neglected, in a type of Boussinesq approximation.

First, express the pressure perturbation, p', in terms of the vertical displacement, η, by multiplying (3.12) by $\exp(-\delta_3 g z/\bar{c}^2)$ and integrate with respect to z to give

$$p'(x,y,z) = e^{-\delta_3 g z/\bar{c}^2}\, \bar{N}^2 \int_z^{\infty} e^{\delta_3 g z/\bar{c}^2}\, \bar{\rho}(z')\, \eta(x,y,z')\, dz' \quad , \qquad (A.1)$$

assuming $\lim\limits_{z\to\infty} \left(e^{\delta_3 g z/\bar{c}^2}\, p' \right) = 0$.

Substituting for the density, $\bar{\rho}$, from (3.14), one can then do the integration over z' to give

$$p'(x,y,z) = -\,\bar{\rho}\, \bar{N}^2 \int_{-\infty}^{\infty}\int_{-\infty}^{\infty} \frac{\hat{h}(k,\ell)\, e^{i(kx+\ell y+mz)}}{\left(i\, m(k,\ell) + \frac{g}{\bar{c}^2}\delta_3 - \frac{\delta_4}{\bar{H}_o} \right)}\, dk\, d\ell \quad , \qquad (A.2)$$

where the Brunt-Väisälä frequency, $\bar{N}$, is given by (3.13), and the height-field Fourier transform, $\hat{h}(k,\ell)$, is defined by (3.17). The vertical wave number, $m(k,\ell)$, determined by substituting (3.18) into (3.16), is the root, with real part having the same sign as k, of the equation

$$m^2 + i \left[\frac{\delta_4(1+\delta_2)-\delta_1}{\overline{H}_o} + (\delta_1-\delta_3) \frac{g}{\bar{c}^2} \right] m$$

$$+ \frac{\delta_4}{\overline{H}_o} \left[\frac{(\delta_1-\delta_2\delta_4)}{\overline{H}_o} + (\delta_2\delta_3-\delta_1) \frac{g}{\bar{c}^2} \right] = m_o^2 \left[1 + \frac{\ell^2}{k^2}\right] \quad . \qquad (A.3)$$

where

$$m_o = m_o(k) = \frac{\overline{N}}{\overline{U}} \operatorname{sign}(k) \quad . \qquad (A.4)$$

If the terrain is a ridge of uniform cross-section, infinitely-extended in the crosswind direction, then $\hat{h}(k,\ell)$ simplifies to (3.22). As a consequence, the integration over ℓ in (A.2) can be done immediately. Setting z=0 then gives the surface pressure perturbation:

$$p'(x) = -\bar{\rho}_o\overline{N}^2 \int_{-\infty}^{\infty} \frac{\tilde{h}(k)\, e^{ikx}}{\left[i\, m(k,0) + \frac{g}{\bar{c}^2}\delta_3 - \frac{\delta_4}{\overline{H}_o} \right]} dk \quad . \qquad (A.5)$$

To simplify this result, introduce the pressure perturbation, $p_o'(x)$, that would be obtained with the approximation $\delta_1=\delta_2=\delta_3=\delta_4=0$:

$$p_o'(x) = -\bar{\rho}_o\overline{N} \int_{-\infty}^{\infty} \frac{\tilde{h}(k)}{i\, m_o(k)}\, e^{ikx}\, dk \quad . \qquad (A.6)$$

Defining a Froude number,

$$F_o = \frac{\overline{U}}{\overline{H}_o\overline{N}} \quad , \qquad (A.7)$$

writing $g/\bar{c}^2 = 1/\gamma_o\overline{H}_o$, and using the fact that m_o^2 is independent of k, one finds that the pressure perturbation (A.3) can be expressed as

$$p'(x) = \frac{\left[1 - (\alpha^2+\beta)F_o^2\right]^{\frac{1}{2}} p_o'(x) - \alpha\bar{\rho}_o\bar{U}^2 \frac{h(x)}{\bar{H}_o}}{1 - \beta F_o^2} , \qquad (A.8)$$

where

$$\left.\begin{aligned} \alpha &= \frac{1}{2}\left[\delta_1\left(\frac{1}{\gamma_o} - 1\right) + \delta_2(\delta_4-1) + \frac{\delta_3}{\gamma_o}\right] , \\ \beta &= \frac{\delta_1\delta_3}{\gamma_o}\left(1 - \frac{1}{\gamma_o}\right) . \end{aligned}\right\} \qquad (A.9)$$

The exact pressure perturbation, p', is seen to be obtained from the simplified version, p_o', by an amplitude correction involving the Froude number and by a dynamic pressure correction involving the barrier height. The compressibility and stratification effects are seen to enter the dimensionless coefficients, α and β, in a complicated way. Retaining all the terms in the original equations, so that $\delta_1=\delta_2=\delta_3=\delta_4=1$, gives $\alpha\simeq\beta\simeq0.2$. For typical atmospheric values of $\bar{U}=10$ m s^{-1}, $\bar{H}_o=8$ km, $g=9.8$ m s^{-2}, and $\gamma_o=1.4$, giving $\bar{N}=0.02$ s^{-1} (from (3.13)), one finds $F_o=0.06$ so that the quadratic terms in F_o can be neglected, introducing a relative error of much less than 1%. Dropping these terms, and normalizing by the factor $\bar{\rho}_o\ \bar{U}\ \bar{N}\ h_o$, where h_o is the maximum mountain height, gives

$$\frac{p'(x)}{\bar{\rho}_o\bar{U}\ \bar{N}\ h_o} = \frac{p_o'(x)}{\bar{\rho}_o\bar{U}\ \bar{N}\ h_o} - \alpha\,\frac{h(x)}{h_o}\,F_o \ . \qquad (A.10)$$

Analytical results show that the maximum value of the first term on the right is typically about 1/2 and occurs on the slope of the barrier where $h/h_0 \simeq 1/2$. With $F_0 \simeq 0.06$, as above, the dynamic pressure correction to the maximum value of p_0' amounts to only 1-2%. However, directly over the barrier peak, where $h/h_0=1$, with a stronger wind speed, and weaker stability, the correction term could be as large as 5-10% of the maximum pressure perturbation. It is interesting to note that the height-dependent correction to the pressure does not affect the wave drag for two-dimensional flow over any barrier having the same height at $x=\infty$ and $x=-\infty$ (see Eq. 8.1). The drag is changed only by the weak amplitude correction to p_0', involving F_0^2.

As a result of this analysis it is seen that the approximation, $p_0'(x)$, given by (A.6), for the pressure perturbation due to an infinitely-extended ridge, is accurate to within a few percent for typical flow conditions. This form for the pressure field arises directly from the governing equations of the model if one neglects the compressibility terms in the continuity equation ($\delta_1=\delta_2=0$), the acoustic pressure term in the adiabatic equation ($\delta_3=0$), and the vertical variation of density ($\delta_4=0$), except in the buoyancy frequency, $\overline{N}$.

A similar analysis is possible for flow over isolated three-dimensional barriers, but the corrections to the pressure field involving the vertical variation of density do not take the simple form given by (A.8). It will be assumed without further justification that the pressure perturbation determined from (3.20) and (3.19) provides an adequate description if the Froude number (A.7) is not too large.

APPENDIX B

DIMENSIONLESS VARIABLES AND INTEGRAL FORMULAE

In this appendix, definitions of dimensionless variables are summarized for the coordinates in the space and wave number domains, the height field and its Fourier transforms, the pressure field and the wave drag per unit crosswind length of barrier. Expressions for some of these variables are given for the special cases of flow over infinitely-extended crosswind ridges and for flow over barriers with elliptical horizontal cross-sections. If (x,y) are Cartesian coordinates in the physical domain, dimensionless Cartesian coordinates, (X,Y), and elliptical polar coordinates, (R,θ), are defined in (4.3) as

$$\left.\begin{array}{c} R = (X^2+Y^2)^{\frac{1}{2}} \quad , \\ X = \dfrac{x}{a} = R\cos\theta \quad , \quad Y = \dfrac{y}{b} = R\sin\theta \quad . \end{array}\right\} \qquad (B.1)$$

If the corresponding wave number coordinates are (k,ℓ), the dimensionless variables are (κ,λ) and (ρ,ϕ), and are defined in (4.9) as

$$\left.\begin{array}{c} \rho = (\kappa^2+\lambda^2)^{\frac{1}{2}} \quad , \\ \kappa = ka = \rho\cos\phi \quad , \quad \lambda = \ell b = \rho\sin\phi \quad . \end{array}\right\} \qquad (B.2)$$

If h(x,y) is the terrain height field, having Fourier transform $\tilde{h}$ with respect to x, as in (3.26), and $\hat{h}$ with respect to x and y, as in (3.17), then the non-dimensional forms are defined by

$$\left.\begin{aligned}
H(X,Y) &= h(x,y)/h_o \quad , \\
\tilde{H}(\kappa;Y) &= \frac{\tilde{h}}{h_o a} = \frac{1}{2\pi}\int_{-\infty}^{\infty} H(X,Y)\, e^{-i\kappa X}\, dX \quad , \\
\hat{H}(\kappa,\lambda) &= \frac{\hat{h}}{h_o ab} = \frac{1}{4\pi^2}\int_{-\infty}^{\infty}\int_{-\infty}^{\infty} H(X,Y)\, e^{-i(\kappa X+\lambda Y)}\, dX\, dY \quad .
\end{aligned}\right\} \qquad (B.3)$$

For convenience, denote $\tilde{H}(\kappa;Y=0)$ by $\tilde{H}(\kappa)$, a normalized form of (3.22). In the special case of flow over elliptical terrain, $H=H(R)$, from (4.10), one has

$$\hat{H}(\kappa,\lambda) = \hat{H}(\rho) = \frac{1}{2\pi}\int_0^{\infty} R\, H(R)\, J_o(\rho R)\, dR \quad . \qquad (B.4)$$

For the remaining quantities to be discussed, a prime denotes the physical variable and particular cases of dimensionless variables are indicated by appropriate subscripts. If V is an arbitrary variable, then V_3 denotes the special case of three-dimensional flow over an elliptical barrier, V_{3C} is used for circular barriers, $V_{2S}(Y)$ for two-dimensional slice flow (see Chapter 3) over an isolated three-dimensional barrier, and $V_2=V_{2S}(Y=0)$ for two-dimensional flow over an infinite ridge.

From (5.1) and (3.25), the normalized pressure field, P, and particular cases are

$$\left.\begin{aligned}
P &= p'/(\bar{\rho}_o \bar{U}\, \bar{N}\, h_o) = i\int_{-\infty}^{\infty}\int_{-\infty}^{\infty} \frac{\kappa\, e^{i(\kappa X+\lambda Y)}}{(\kappa^2+\gamma^2\lambda^2)^{\frac{1}{2}}}\, \hat{H}(\kappa,\lambda)\, d\kappa\, d\lambda \quad , \\
P_3(X,Y) &= i\int_0^{2\pi}\int_0^{\infty} \frac{\cos\phi\, e^{i\rho R\cos(\phi-\theta)}}{(\cos^2\phi+\gamma^2\sin^2\phi)^{\frac{1}{2}}}\, \rho\, \hat{H}(\rho)\, d\rho\, d\phi \quad ; \; \gamma=a/b \quad , \\
P_{2S}(X,Y) &= i\int_{-\infty}^{\infty} \mathrm{sign}(\kappa)\, \tilde{H}(\kappa;Y)\, e^{i\kappa X}\, d\kappa \quad .
\end{aligned}\right\} \qquad (B.5)$$

As shown in Chapter 5, (B.5) simplifies in the circular case to give

$$P_{3C}(X,Y) = -2\pi \frac{X}{R} \int_0^\infty \rho \, J_1(\rho R) \, \hat{H}(\rho) \, d\rho \quad . \tag{B.6}$$

Also, from (5.4)

$$P_2(X) = -2\pi \int_0^\infty \rho \, H_o(\rho X) \, \hat{H}(\rho) \, d\rho \quad . \tag{B.7}$$

where H_o is a Struve function.

The drag per unit crosswind length of the barrier is denoted by d. From Chapter 8 (Eqs. 8.4 and 8.6), the dimensionless variables are :

$$\left.\begin{aligned} d = d'/(\bar{\rho}_o \bar{U} \, \bar{N} \, h_o^2) &= 2\pi \int_{-\infty}^{\infty} \int_{-\infty}^{\infty} \frac{\kappa^2 e^{i\lambda Y}}{(\kappa^2+\gamma^2\lambda^2)^{\frac{1}{2}}} \hat{H}(\kappa,\lambda) \, \tilde{H}(\kappa;Y)^* \, d\kappa \, d\lambda \quad , \\ d_{2S}(Y) &= 2\pi \int_{-\infty}^{\infty} |\kappa| \, |\tilde{H}(\kappa;Y)|^2 \, d\kappa \quad . \end{aligned}\right\} \tag{B.8}$$

To obtain the form, d_3, for elliptical terrain, substitute $\hat{H}(\kappa,\lambda)=\hat{H}(\rho)$ in the expression for d and use elliptical polar coordinates (B.2).

For the normalized total force, $\vec{F}_3=(D_3,T_3)$, in the elliptical barrier case, the reader is referred to (10.3) and (10.4). The two-dimensional slice flow solution, being less straightforward to derive, is considered in Appendix O.

APPENDIX C

HORIZONTAL SCALE TRANSFORMATION

Given a barrier, H=H(X,Y), one can increase the horizontal scale to form a new barrier, H_α, which has the same shape. Although the effects of such a transformation are implicit in the expressions Appendix B, they are summarized here :

$$H(X,Y)_\alpha = H(\frac{X}{\alpha},\frac{Y}{\alpha}) \quad , \qquad (C.1)$$

$$\tilde{H}(\kappa;Y)_\alpha = \alpha\ \tilde{H}(\kappa\alpha;\frac{Y}{\alpha}) \quad , \qquad (C.2)$$

$$\hat{H}(\kappa,\lambda)_\alpha = \alpha^2\ \hat{H}(\kappa\alpha,\lambda\alpha) \quad ; \quad \hat{H}(\rho)_\alpha = \alpha^2\ \hat{H}(\rho\alpha) \quad , \qquad (C.3)$$

$$P(X,Y)_\alpha = P(\frac{X}{\alpha},\frac{Y}{\alpha}) \quad , \qquad (C.4)$$

$$d(Y)_\alpha = d(\frac{Y}{\alpha}) \quad ; \quad d_{2\alpha} = d_2 \quad , \qquad (C.5)$$

$$D_\alpha = \alpha\ D \quad . \qquad (C.6)$$

Quantities such as the drag per unit length at Y=0 and the maximum pressure perturbation are unchanged by the scale transformation.

APPENDIX D

ANALYTICAL RESULTS FOR SINGLE RIDGES AND ELLIPTICAL HILLS

D.1 Terrain-height Fourier transforms

Analytical results are presented in this section for the terrain-height Fourier transform and pressure perturbation for single ridges and elliptical hills.

In Table 2, the normalized terrain-height Fourier transform for two-dimensional slice flow, $\tilde{H}(\kappa;Y)$, defined in Appendix B, is given for a variety of terrain forms. In each case, a reference is made to the page in GR where the $\tilde{H}$ integral, or a closely related form, can be found. An exception is the barrier with a triangular profile, for which case integration by parts gives the result without resorting to tables. For the last two entries in the table, only the Y=0 solution was found. In Table 3, $\hat{H}(\rho)$, the Fourier transform appearing in the three-dimensional flow problem, is given. Special functions appearing in the results are Bessel functions, J_μ, Bessel functions of imaginary argument, K_μ, Struve functions, $\mathbf{H}_n$, and the complete elliptic integrals, K and E. Properties of these functions are summarized in GR.

Table 2. Normalized terrain-height Fourier transform, $\tilde{H}(\kappa;Y)$, for elliptical terrain, $H(R)$. See Appendix B for definitions.

$H(R)$	$\tilde{H}(\kappa;Y)$	Reference
$(1+R^2)^{-\mu}$	$\frac{1}{\Gamma(\frac{1}{2})\,\Gamma(\mu)}\left(\frac{\lvert\kappa\rvert}{2(1+Y^2)^{\frac{1}{2}}}\right)^{\mu-\frac{1}{2}} K_{\mu-\frac{1}{2}}\left(\lvert\kappa\rvert(1+Y^2)^{\frac{1}{2}}\right)$	GR, p. 959
e^{-R^2}	$\frac{1}{2\,\Gamma(\frac{1}{2})}\, e^{-Y^2}\, e^{-\kappa^2/4}$	GR, p. 480
$(1-R^2)^{\nu}\,\theta(1-R^2)$	$\frac{\Gamma(\nu+1)}{2\,\Gamma(\frac{1}{2})}\left(\frac{2(1-Y^2)^{\frac{1}{2}}}{\lvert\kappa\rvert}\right)^{\nu+\frac{1}{2}} J_{\nu+\frac{1}{2}}\left(\lvert\kappa\rvert(1-Y^2)^{\frac{1}{2}}\right)\theta(1-Y^2)$	GR, p. 953
$\frac{\ln\left(\frac{\delta^2+R^2}{1+R^2}\right)}{\ln(\delta^2)}$	$\frac{e^{-\lvert\kappa\rvert(1+Y^2)^{\frac{1}{2}}}-e^{-\lvert\kappa\rvert(\delta^2+Y^2)^{\frac{1}{2}}}}{\ln(\delta^2)}$	GR, p. 583
$\frac{\mathrm{arccot}\left(\frac{R^2+\cos2\omega}{\sin2\omega}\right)}{2\omega}$	$e^{-\lvert\kappa\rvert\eta\cos\xi}\sin(\kappa\eta\sin\omega)/(2\omega\kappa)$ where $\eta^2\cos2\xi=Y^2+\cos2\omega$ and $\eta^2\sin2\xi=\sin2\omega$	GR, p. 411
e^{-R}	$\frac{\lvert Y\rvert}{\pi(1+\kappa^2)^{\frac{1}{2}}} K_1\left(\lvert Y\rvert(1+\kappa^2)^{\frac{1}{2}}\right)$; $\frac{1}{\pi(1+\kappa^2)}$ at $Y=0$	GR, p. 482, p. 477
$K_o(R)$	$\frac{e^{-\lvert Y\rvert(1+\kappa^2)^{\frac{1}{2}}}}{2\,(1+\kappa^2)^{\frac{1}{2}}}$	GR, p. 736
$(1-R)\,\theta(1-R)$	$\frac{2\sin^2\left(\frac{\kappa}{2}\right)}{\pi\kappa^2}$ at $Y=0$	integrate by parts
$\mathrm{sech}(R)$	$\frac{1}{2}\,\mathrm{sech}\left(\frac{\pi\kappa}{2}\right)$ at $Y=0$	GR, p. 503

Table 3. Normalized terrain-height Fourier transform, $\hat{H}(\rho)$, for elliptical terrain, H(R). See Appendix B for [illegible]ions.

H(R)	$\hat{H}(\rho)$	Reference
$(1+R^2)^{-\mu}$	$\frac{\rho^{\mu-1}}{\pi\ 2^{\mu}\ \Gamma(\mu)} K_{\mu-1}(\rho)$	GR, p. 686
e^{-R^2}	$\frac{1}{4\pi} e^{-\rho^2/4}$	GR, p. 480
$(1-R^2)^{\nu}\ \theta(1-R^2)$	$\frac{\Gamma(\nu+1)}{4\pi} \left(\frac{2}{\rho}\right)^{\nu+1} J_{\nu+1}(\rho)$	Put R=sinθ in GR, p. 740
$\frac{\ln\left(\frac{\delta^2+R^2}{1+R^2}\right)}{\ln(\delta^2)}$	$\frac{K_1(\rho) - \delta K_1(\delta\rho)}{\pi\ \rho\ \ln(\delta^2)}$	GR, p. 768
$\frac{\operatorname{arccot}\left(\frac{R^2+\cos 2\omega}{\sin 2\omega}\right)}{2\omega}$	$\frac{i}{4\pi\omega\rho}\left(e^{i\omega}K_1(\rho e^{i\omega}) - e^{-i\omega}K_1(\rho e^{-i\omega})\right)$	Use (9.3) GR, p. 768
e^{-R}	$\frac{1}{2\pi\ (1+\rho^2)^{3/2}}$	GR, p. 712
$K_0(R)$	$\frac{1}{2\pi\ (1+\rho^2)}$	GR, p. 672
$(1-R)\ \theta(1-R)$	$\frac{J_1(\rho)H_0(\rho) - J_0(\rho)H_1(\rho)}{2\rho}$	GR, p. 666

D.2 Pressure fields

Results are now presented for the normalized surface pressure perturbation for flow over various barriers, based on the integrals in Appendix B and the Fourier transforms in Tables 2 and 3. For some of the terrain forms, the absolute value of the extreme perturbation, P_{2m} or P_{3Cm}, is given for the flow over an infinitely-extended ridge or a circular barrier, respectively. The distance from the terrain peak to the position of the extreme pressure is denoted by X_m.

D.2.1 Pressure for a μ-type barrier: $H = (1+R^2)^{-\mu}$

The pressure field, P_2, for flow over an infinitely-extended ridge has been derived in Chapter 5, with the result given in (5.8). Special cases are shown in Table 4. The corresponding two-dimensional slice flow solution, P_{2S} can be obtained from P_2 using (5.10).

The circular hill case, P_{3C} has also been treated in Chapter 5, with the result (5.12). Simplified expressions for specific values of μ are given in Table 5.

Now consider the evaluation of the integral (5.14) for the normalized surface pressure, P_3, for the terrain exponent μ=1/2, 1, 3/2, and 2. Making the change of variable $t=-\mathrm{ctn}\phi$, and introducing the notation

$$\alpha = \frac{XY}{1+X^2} , \tag{D.1}$$

Table 4. Normalized surface pressure perturbation, $P_2(X)$, and the absolute values of the extreme perturbation, $P_{2m}=|P_2(X_m)|$, and its position, X_m, for flow over an infinite ridge with height $H(X) = (1+X^2)^{-\mu}$ as a function of the exponent, μ.

μ	$P_2(X)$	X_m	P_{2m}
1/2	$-\frac{2}{\pi}\frac{\ln\left(X+(1+X^2)^{1/2}\right)}{(1+X^2)^{1/2}}$	1.509	0.422
1	$-\frac{X}{1+X^2}$	1.000	0.500
3/2	$-\frac{2}{\pi}\left[\frac{X}{1+X^2}+\frac{\ln\left(X+(1+X^2)^{1/2}\right)}{(1+X^2)^{3/2}}\right]$	0.797	0.533
2	$-\frac{X(3+X^2)}{2(1+X^2)^2}$	0.681	0.550
μ	$-\frac{\Gamma(\mu+1/2)}{\Gamma(3/2)\,\Gamma(\mu)}\frac{X}{1+X^2}F(1,1-\mu;\frac{3}{2};\frac{X^2}{1+X^2})$		

Table 5. Normalized surface pressure perturbation, $P_{3C}(X,Y)$, and the absolute values of the extreme perturbation, $P_{3Cm}=|P_{3C}(X_m,0)|$, and its position, X_m, for three-dimensional flow over a circular hill with height $H(R) = (1+R^2)^{-\mu}$ as a function of the exponent, μ, where $R^2=X^2+Y^2$.

μ	$P_{3C}(X,Y)$	X_m	P_{3Cm}
1/2	$-\frac{X}{(1+R^2)^{1/2}}\ \frac{1}{1+(1+R^2)^{1/2}}$	1.272	0.300
1	$-\frac{X(K-E)}{R^2(1+R^2)^{1/2}}$ *	0.875	0.360
3/2	$-\frac{X}{(1+R^2)^{3/2}}$	0.707	0.385
2	$-\frac{X(K+(R^2-1)E)}{2R^2(1+R^2)^{3/2}}$ *	0.609	0.399
μ	$-\frac{\Gamma(\mu+1/2)\ \Gamma(3/2)}{\Gamma(\mu)}\ \frac{X}{(1+R^2)^{3/2}}\ F(\frac{3}{2},\frac{3}{2}-\mu\ ;2;\frac{R^2}{1+R^2})$		

* $K = K(k)$ and $E = E(k)$ are complete elliptic integrals of the first and second kinds, respectively, where the modulus, $k = R/(1+R^2)^{\frac{1}{2}}$.

$$\beta = \frac{(1+X^2+Y^2)^{\frac{1}{2}}}{1+X^2} = \frac{(1+R^2)^{\frac{1}{2}}}{1+X^2} \quad , \tag{D.2}$$

$$\Delta = (t^2+\gamma^2)^{\frac{1}{2}}(t^2+1)^{\frac{1}{2}} \quad , \tag{D.3}$$

(5.14) becomes

$$P_3(X,Y) = -\frac{\Gamma(\mu+1/2)}{\Gamma(1/2)\ \Gamma(\mu)} \frac{1}{(1+X^2)^{\mu+\frac{1}{2}}} \int_{-\infty}^{\infty} \frac{t\ (Xt-Y)\ (1+t^2)^{\mu-\frac{1}{2}}}{\Delta\ \left((t-\alpha)^2+\beta^2\right)^{\mu+\frac{1}{2}}}\, dt \quad . \tag{D.4}$$

For $\mu>1/2$ this can be written as

$$P_3(X,Y) = \frac{\Gamma(\mu-1/2)}{4\,\Gamma(3/2)\ \Gamma(\mu)} \frac{\partial}{\partial X} \left[\frac{1}{(1+X^2)^{\mu-\frac{1}{2}}} \int_{-\infty}^{\infty} \frac{(1+t^2)^{\mu-\frac{1}{2}}}{\Delta\ \left((t-\alpha)^2+\beta^2\right)^{\mu-\frac{1}{2}}}\, dt \right] \quad . \tag{D.5}$$

For $\mu>1/2$ the form (D.5) is somewhat simpler to integrate, but for $\mu=1/2$, (D.4) must be used.

First consider the evaluation of (D.4) for the $\mu=1/2$ case. Introducing

$$q_\pm = \alpha \pm i\beta \quad , \tag{D.6}$$

so that

$$(t-\alpha)^2+\beta^2 = (t-q_+)\ (t-q_-) \quad , \tag{D.7}$$

and using $\Gamma(1/2)=\pi^{1/2}$ in (D.4) gives

$$P_3(X,Y)\Big|_{\mu=\frac{1}{2}} = -\frac{1}{\pi\ (1+X^2)} \int_{-\infty}^{\infty} \frac{t\ (Xt-Y)}{\Delta\ (t-q_+)(t-q_-)}\, dt \quad . \tag{D.8}$$

To put the integral into a form found in standard tables, eliminate the odd powers of t by separating into partial fractions and multiplying top and bottom by $t+q_+$ or $t+q_-$ as is appropriate. The result is

$$P_3(X,Y)\Big|_{\mu=\frac{1}{2}} = -\frac{2}{\pi(1+X^2)}\left[X\int_0^\infty \frac{dt}{\Delta} + \frac{1}{\beta}\mathrm{Im}\left(q_+^2(Xq_+-Y)\int_0^\infty \frac{1}{\Delta\ (t^2-q_+^2)}\,dt\right)\right] , \tag{D.9}$$

where Im denotes 'the imaginary part of'. From Byrd and Friedman (1971, 61-64, denoted as BF in the following) one finds

$$\int_0^\infty \frac{dt}{\Delta} = \begin{cases} K(k) & ;\ \gamma<1\ , \\ \frac{\pi}{2} & ;\ \gamma=1\ , \\ \frac{K(k)}{\gamma} & ;\ \gamma>1\ , \end{cases} \tag{D.10}$$

where $K(k)$ is a complete elliptic integral of the first kind with modulus $k=\epsilon(\gamma)$, being equal to the eccentricity of the elliptical barrier as defined by (4.5). Also,

$$\int_0^\infty \frac{dt}{\Delta\ (t^2-q^2)} = \begin{cases} \frac{1}{q^2+1}\left(\Pi(q^2+1,k) - K(k)\right) & ;\ \gamma<1\ , \\ -\frac{\pi}{2}\,\frac{1}{q(q+i)} \qquad (\ \mathrm{Im}(q)>0\ ) & ;\ \gamma=1\ , \\ -\frac{1}{\gamma(q^2+1)}\left[\frac{1}{q^2}\,\Pi\left(\frac{1}{q^2}+1,k\right) + K(k)\right] & ;\ \gamma>1\ , \end{cases} \tag{D.11}$$

where $\Pi(\xi^2,k)$ is the complete elliptic integral of the third kind, with parameter ξ^2, and modulus k, in the standard terminology (see BF).

The literature on the elliptic integral of the third kind is much less extensive than that on the first and second kinds. Unfortunately, some reference materials, including BF, contain omissions and typographical errors in the case where ξ^2 is a complex number, as it is for the integrals encountered above. See Lang and Stevens (1960) and Sutherland (1965) for clarification of the major problems in previous literature. For the purpose of numerical evaluation, $\Pi(\xi^2,k)$, with complex ξ^2, can be expressed as a linear combination of two real complete elliptic integrals of the third kind, each of which can be evaluated in terms of incomplete elliptic integrals of the first and second kinds.

Substituting (D.10) and (D.11) into (D.9) gives the pressure field for the $\gamma<1$ case as

$$P_3(X,Y)\Big|_{\mu=\frac{1}{2}} = -\frac{2}{\pi}\frac{1}{(1+R^2)^{\frac{1}{2}}}\,\mathrm{Im}\left(\frac{q_+}{1+q_+^2}\left[X\left(q_+^2\Pi+K\right) - Yq_+\left(\Pi-K\right)\right]\right) , \quad (D.12)$$

where $\Pi = \Pi(q_+^2+1,k)$ and $K = K(k)$. The expression for P_3 when $\gamma=1$ has already been given in Table 5, and that for $\gamma>1$ is found from (D.10) and (D.11), as in the $\gamma<1$ case.

Note that when $\alpha=0$, which occurs along the X and Y axes (see Eq. D.1), the parameter, ξ^2, becomes real and the calculation of the pressure field becomes considerably simpler. Thus, quantities such as the maximum pressure perturbation, which occur along the Y=0 axis, can be calculated without evaluating elliptic integrals with complex parameters.

Since the integrals arising for the $\mu=3/2$ case are similar to those just considered for $\mu=1/2$, these will be treated next. From (D.5) and (D.7), one has

$$P_3(X,Y)\Big|_{\mu=\frac{3}{2}} = \frac{1}{\pi}\frac{\partial}{\partial X}\left[\frac{1}{1+X^2}\int_{-\infty}^{\infty}\frac{t^2+1}{\Delta\,(t-q_+)(t-q_-)}\,dt\right] . \qquad (D.13)$$

Separating into partial fractions and using (D.10) and (D.11) as before, gives

$$P_3(X,Y)\Big|_{\mu=\frac{3}{2}} = \begin{cases} \dfrac{2}{\pi}\dfrac{\partial}{\partial X}\left[\dfrac{1}{(1+R^2)^{\frac{1}{2}}}\,\mathrm{Im}\left(q_+\Pi(q_+^2+1,k)\right)\right] & ;\ \gamma<1 , \\ \dfrac{\partial}{\partial X}\left[\dfrac{1}{(1+R^2)^{\frac{1}{2}}}\right] & ;\ \gamma=1 , \\ -\dfrac{2}{\pi\gamma}\dfrac{\partial}{\partial X}\left[\dfrac{1}{(1+R^2)^{\frac{1}{2}}}\,\mathrm{Im}\left(\dfrac{1}{q_+}\Pi\left(\dfrac{1}{q_+^2}+1,k\right)\right)\right] & ;\ \gamma>1 . \end{cases} \qquad (D.14)$$

The process of taking the imaginary part and differentiating in (D.14) is rather lengthy so will not be presented here.

Next consider the $\mu=1$ case, for which (D.5) becomes

$$P_3(X,Y)\Big|_{\mu=1} = \frac{1}{2}\frac{\partial}{\partial X}\left[\frac{1}{(1+X^2)^{\frac{1}{2}}}\int_{-\infty}^{\infty}\frac{(t^2+1)^{\frac{1}{2}}}{\Delta\,\left((t-\alpha)^2+\beta^2\right)^{\frac{1}{2}}}\,dt\right] . \qquad (D.15)$$

An integral of this form is tabulated by BF (p. 146), giving the result

$$P_3(X,Y)\Big|_{\mu=1} = \frac{\partial}{\partial X}\left[\frac{\nu\ K(k)}{(1+X^2)^{\frac{1}{2}}}\right] , \qquad (D.16)$$

where

$$\left.\begin{aligned} \nu &= \frac{2}{\zeta_+ + \zeta_-} \ , \\ k &= \nu \left(\zeta_+\zeta_-\right)^{\frac{1}{2}} \ , \\ \zeta_\pm &= \left(\alpha^2+(\beta\pm\gamma)^2\right)^{\frac{1}{2}} \ . \end{aligned}\right\} \quad . \qquad (D.17)$$

Carrying out the differentiation in (D.16) or integrating (D.4) directly gives

$$P_3(X,Y)\Big|_{\mu=1} = - \frac{\nu\ (1+X^2)^{\frac{1}{2}}}{k^2\ (1+R^2)} \left(SB-TC \right) \ , \qquad (D.18)$$

where

$$\left.\begin{aligned} &B = \frac{E-k'^2K}{k^2} \ , \quad C = \frac{k'^2(K-E)}{k^2} \ , \quad k'^2 = 1 - k^2 \ , \\ &S = X\sigma-Y\alpha \ , \quad T = X\tau-Y\alpha \ , \\ &\sigma = \frac{1}{\nu^2} - \gamma^2 \ , \quad \tau = \frac{k'^2}{\nu^2} - \gamma^2 \ . \end{aligned}\right\} \qquad (D.19)$$

Here $K=K(k)$ and $E=E(k)$ are complete elliptic integrals of the first and second kinds, respectively, with k as in (D.17).

The final case to be considered in this section is $\mu=2$. By means of the change of variable $\omega=(\alpha t-\sigma)/(\tau-\alpha t)$, where σ and τ are given in (D.19) and α in (D.1), the integrands of (D.4) and (D.5) become even functions of the integration variable, ω. Then, after separation into partial fractions, one can use integrals tabulated in BF (pp. 61-64), as in the $\mu=1/2$ and 1 cases. The result obtained is

$$P_3(X,Y)\Big|_{\mu=2} = \frac{\partial}{\partial X}\left[\frac{\nu\,(1+X^2)^{\frac{1}{2}}}{2\,\gamma^2\,k^2\,(1+R^2)}\left(sC-k^{\prime 2}tB\right)\right] \tag{D.20}$$

$$= \frac{\nu^5}{2k^4(1+R^2)(1+X^2)^{\frac{5}{2}}}\Bigg[3sTC+3tSB + \frac{(C-B)}{k^2}\Big[(s+t)(k^{\prime 2}T+S)+2(\overset{y}{\cancel{1}}-\gamma^2)(\sigma T+\tau S)\Big]\Bigg] ,$$

where

$$s = \sigma-\gamma^2\tau \quad , \quad t = \frac{\tau-\gamma^2\sigma}{k^{\prime 2}} , \tag{D.21}$$

and the other symbols are defined in (D.17) and (D.19).

Regarding numerical evaluation using the preceding formulae, the $\mu=1/2$ and $3/2$ cases required about 40% more computer time than for $\mu=1$ and 2 because complex elliptic integrals of the third kind, appearing in the former cases, are less straightforward to calculate than the integrals of the first and second kinds.

D.2.2 Pressure for a Gaussian barrier: $H = e^{-R^2}$

The two-dimensional slice flow solution is

$$P_{2S}(X,Y) = -\frac{X\,e^{-R^2}}{\Gamma(3/2)}\,{}_1F_1(1/2;3/2;X^2)$$

$$= -\frac{e^{-Y^2}}{\Gamma(3/2)}\,F(X) , \tag{D.22}$$

where the first form involves a degenerate hypergeometric function (GR, pp. 480, 1063). The second form expresses the result in terms of Dawson's integral, F, which allows one to use tabulated results to obtain the extreme values of P_2

(Abramowitz and Stegun, 1965, p. 298): $P_{2m}=.6105$ at $X_m=.924$.

The result for the circular case, in terms of modified Bessel functions, follows directly from (B.6) using GR (p. 717) :

$$P_{3C}(X,Y) = -\,\Gamma\left(\tfrac{3}{2}\right)\, X \left[I_0\left(\tfrac{R^2}{2}\right)-I_1\left(\tfrac{R^2}{2}\right)\right] e^{-R^2/2} \quad . \qquad (D.23)$$

D.2.3 Pressure for a ν-type barrier: $H = (1-R^2)^{\nu}\,\theta(1-R^2)$

P_{2S} and P_{3C} can be expressed in terms of hypergeometric functions using GR p. 747 and p. 692, respectively. The expressions for general ν and simplified results for $\nu=0$, 1/2, 1 and 3/2 are given in Tables 6 and 7. One can solve for pressure in the elliptical terrain case in terms of elliptic integrals if ν is half an odd integer. Performing the ρ integration in (B.5) using GR (p. 747), gives

$$P_3(X,Y) = -\frac{\Gamma(\nu+1)}{2\,\Gamma(\frac{1}{2})\,\Gamma(\nu+\frac{1}{2})}\int_0^{2\pi}\frac{\xi\,(1-\xi^2)^{\nu-\frac{1}{2}}\theta(1-\xi^2)\,\cos\phi}{\left(\cos^2\phi+\gamma^2\sin^2\phi\right)^{\frac{1}{2}}}\,d\phi \quad , \qquad (D.24)$$

where

$$\xi = X\cos\phi + Y\sin\phi \quad . \qquad (D.25)$$

If $R<1$ then $\theta(1-\xi^2)=1$ and the integral (D.24) can be expressed in terms of complete elliptic integrals. For example, in the $\nu=1/2$ case :

$$P_3(X,Y) = -\,X\,B_o(\gamma) \quad ;\ R<1 \quad , \qquad (D.26)$$

where B_o is defined in Appendix Q. Note that the isobars

Table 6. Normalized surface pressure perturbation, $P_{2S}(X,Y)$, and the absolute values of the extreme perturbation, $P_{2m}=|P_{2S}(X_m,0)|$, and its position, X_m, for two-dimensional slice flow over an elliptical barrier with height $H(R) = (1-R^2)^\nu\theta(1-R^2)$, where $R^2=X^2+Y^2$. Define $\Lambda^2=1-Y^2$. Also, $P_{2S}(X,Y)=0$ for $|Y|\ge1$.

ν	$P_{2S}(X,Y)$; $\lvert Y\rvert\le 1$	X_m	P_{2m}
0	$-\frac{2}{\pi}\operatorname{arctanh}\frac{X}{\Lambda}$; $R\le1$ $-\frac{2}{\pi}\operatorname{arctanh}\frac{\Lambda}{X}$; $R\ge1$	1	∞
$\frac{1}{2}$	$-X$; $R\le1$ $-X+(R^2-1)\operatorname{sign}(X)$; $R\ge1$	1	1
1	$-\frac{2}{\pi}\left[\Lambda X+(1-R^2)\operatorname{arctanh}\left(\frac{X}{\Lambda}\right)\right]$; $R\le1$ $-\frac{2}{\pi}\left[\Lambda X+(1-R^2)\operatorname{arctanh}\left(\frac{\Lambda}{X}\right)\right]$; $R\ge1$	.834	.764
$\frac{3}{2}$	$-\Lambda^2X\left(\frac{3}{2}-\frac{X^2}{\Lambda^2}\right)$; $R\le1$ $-X^3\left[\frac{3\Lambda^2}{2X^2}-1+\left(1-\frac{\Lambda^2}{X^2}\right)\right]^{3/2}$; $R\ge1$	.707	.707
ν	$-\frac{\Gamma(\nu+1)}{\Gamma(\nu+1/2)\,\Gamma(3/2)}\Lambda^{2\nu-1}X\,F(1,1/2-\nu;3/2;\frac{X^2}{\Lambda^2})$; $R\le1$ $-\frac{\Gamma(\nu+1)}{\Gamma(\nu+3/2)\,\Gamma(1/2)}\frac{\Lambda^{2\nu+1}}{X}F(1/2,1;\nu+3/2;\frac{\Lambda^2}{X^2})$; $R\ge1$		

Table 7. Normalized surface pressure perturbation, $P_{3C}(X,Y)$, and the absolute values of the extreme perturbation, $P_{3Cm}=|P_{3C}(X_m,0)|$, and its position, X_m, for three-dimensional flow over a circular hill with height $H(R) = (1-R^2)^{\nu}\theta(1-R^2)$, where $R^2=X^2+Y^2$.

ν	$P_{3C}(X,Y)$	X_m	P_{3Cm}
0	$-\frac{2}{\pi} X\ (K-E)\quad ; R\le 1$ * $-\frac{2}{\pi}\frac{X}{R}\ (K-E)\quad ; R\ge 1$ *	1	∞
$\frac{1}{2}$	$-\frac{\pi}{4} X\quad ; R\le 1$ $-\frac{X}{2}\left[\arcsin\left(\frac{1}{R}\right) - \frac{1}{R}\left(1-\frac{1}{R^2}\right)^{\frac{1}{2}}\right]\quad ; R\ge 1$	1	.785
1	$-\frac{4}{3\pi}\frac{X}{R^2}\left[(1-R^2)K + (2R^2-1)E\right]\quad ; R\le 1$ * $-\frac{4}{3\pi}\frac{X}{R}\left[(2R^2-1)E + 2(1-R^2)K\right]\quad ; R\ge 1$ *	.799	.571
$\frac{3}{2}$	$-\frac{3\pi}{32} X\ (4-3R^2)\quad ; R\le 1$ $-\frac{3X}{16}\left[(4-3R^2)\arcsin\left(\frac{1}{R}\right) + \frac{3R^2-2}{R}\left(1-\frac{1}{R^2}\right)^{\frac{1}{2}}\right]\quad ; R\ge 1$	.667	.524
ν	$-\frac{\Gamma(3/2)\ \Gamma(\nu+1)}{\Gamma(\nu+1/2)} X\ F(3/2,1/2-\nu;2;R^2)\quad ; R\le 1$ $-\frac{1}{2(\nu+1)}\frac{X}{R^3} F(1/2,3/2,\nu+2;\frac{1}{R^2})\quad ; R\ge 1$		

* K=K(k) and E=E(k) are complete elliptic integrals with modulus k, where k=R for R≤1 and k=1/R for R≥1.

for the $\nu=1/2$ case are straight lines parallel to the Y-axis, within the elliptical region $R<1$. At $R=1$ the pressure is continuous but the pressure gradient is not. Therefore, the isobars kink at $R=1$. For $R>1$ the pressure field involves incomplete elliptic integrals, because $\theta(1-\xi^2)$ is zero for part of the region of integration.

D.2.4 Pressure for a logarithmic barrier: $H = \dfrac{\ln\left(\dfrac{\delta^2+R^2}{1+R^2}\right)}{\ln(\delta^2)}$

From GR (p. 489) one obtains

$$P_{2S}(X,Y) = \frac{2}{\ln(\delta^2)}\left\{\arctan\left(\frac{X}{(\delta^2+Y^2)^{\frac{1}{2}}}\right) - \arctan\left(\frac{X}{(1+Y^2)^{\frac{1}{2}}}\right)\right\} \quad . \tag{D.27}$$

Unlike the preceding cases, an explicit formula for the extreme pressure perturbation exists for the infinitely-extended logarithmic ridge. The result is

$$P_{2m} = \frac{2}{\ln(\delta^2)}\left\{\arctan\left(\frac{1}{\delta^{\frac{1}{2}}}\right) - \arctan\left(\delta^{\frac{1}{2}}\right)\right\} \quad \text{at } X_m = \delta^{\frac{1}{2}} \quad . \tag{D.28}$$

The extrema of the pressure field occur at the half-height points, $H=1/2$, and inflection points occur at $X^2=\delta^{\frac{1}{2}}(\delta+\delta^{\frac{1}{2}}+1)$, where $H=1/4$.

Proceeding as with the ν-type terrain (see Section D.2.3) evaluation of the ρ integral (GR, p. 731) in (B.5) leaves a ϕ integral that can be expressed in terms of elliptic integrals. In the circular barrier case one finds from this approach (GR, p. 905), or from (B.6) directly (GR, p. 693), that

$$P_{3C}(X,Y) = \frac{2X}{\ln(\delta^2)} \left[\frac{\gamma_\delta}{\delta} B_o(\gamma_\delta) - \gamma_1 B_o(\gamma_1)\right] , \qquad (D.29)$$

where $\gamma_\delta = \delta/(\delta^2+R^2)^{\frac{1}{2}}$, $\gamma_1 = 1/(1+R^2)^{\frac{1}{2}}$ and $B_o(\gamma)$ is defined in Appendix Q.

D.2.5 Pressure for an arccot barrier: $H = \dfrac{\operatorname{arccot}\left(\dfrac{R^2+\cos 2\omega}{\sin 2\omega}\right)}{2\omega}$

P_3 involves elliptic integrals with complex modulus and will not be discussed here. P_{2S} can be evaluated from GR (p. 491) :

$$P_{2S}(X,Y) = -\frac{1}{2\omega} \operatorname{arctanh}\left(\frac{2X\eta\sin\xi}{X^2+\eta^2}\right) , \qquad (D.30)$$

where

$$\left.\begin{aligned} \eta^2 \cos 2\xi &= Y^2 + \cos 2\omega \\ \eta^2 \sin 2\xi &= \sin 2\omega \quad . \end{aligned}\right\} \qquad (D.31)$$

As with the logarithmic case (see Section D.2.4), the extreme perturbations occur at $H=1/2$. One finds

$$P_{2m} = \frac{1}{2\omega} \operatorname{arctanh}(\sin\omega) \quad \text{at } X_m = 1 \quad . \qquad (D.32)$$

Inflection points of the pressure field are at $X^2=1+2\cos\omega$, where $H=1/4$.

D.2.6 Pressure for a singular barrier: $H = K_0(R)$

Although this case involves a barrier of infinite height at $R=0$, a formal solution for the pressure field can be found for the infinitely-extended ridge and circular barrier cases. From GR (p. 419),

$$P_2(X) = \frac{\pi}{2}\left[L_0|X| - I_0|X|\right] \operatorname{sign}(X) \quad . \tag{D.33}$$

$P_{2S}(X,Y)$ was not found. From (B.6), using a differentiated form of an expression in GR (p. 678), one obtains

$$P_{3C}(X,Y) = \frac{\pi}{2}\frac{X}{R}\left[I_1(R) - L_{-1}(R)\right] \quad . \tag{D.34}$$

For properties of Struve functions of imaginary argument, L_n, see, for example, Abramowitz and Stegun (1965, p. 498).

D.2.7 Pressure for miscellaneous infinite ridge cases

For $H=(1-|X|)\ \theta(1-|X|)$ the pressure perturbation is (GR, p. 433) :

$$P_2(X) = -\frac{1}{\pi}\left[X \ln\left|\frac{1}{X^2} - 1\right| + \ln\left|\frac{1+X}{1-X}\right|\right] \quad . \tag{D.35}$$

The pressure is finite everywhere, but dP_2/dX is singular at $X^2=0$ and 1. The extreme perturbation is $P_{2m}=(2/\pi)\ln(1+\sqrt{2}) \simeq .561$, at $X_m=1/\sqrt{2}\simeq .707$. Note that P_{2m} is exactly the same as for the $\omega=\pi/4$ case of the arccot barrier (see Section D.2.5).

For $H=\exp(-|X|)$, the pressure perturbation can be expressed in terms of the exponential integral function (GR, pp. 406, 925).

For $H=\operatorname{sech}(X)$, it is Euler's ψ function that arises.

APPENDIX E

ANALYTICAL RESULTS FOR A SEPARABLE TERRAIN FORM

E.1 Three-dimensional pressure field

In this appendix, derivations are given for the pressure perturbation and total drag associated with flow over a mountain with normalized height

$$H = \frac{1}{(1+X^2)(1+Y^2)} \quad . \tag{E.1}$$

X and Y are defined by (B.1).

The Fourier transform of H, defined by (B.3), is found from GR (p. 406) to be

$$\hat{H}(\kappa,\lambda) = \frac{1}{4}\, e^{-|\kappa|}\, e^{-|\lambda|} \quad . \tag{E.2}$$

Because the topographic contours are not ellipses, there is no particular advantage to using coordinates defined by (B.2). Instead, define the variables (τ,ξ) by

$$\left.\begin{aligned} \kappa &= \rho\cos\phi = \gamma\tau\cos\xi \quad , \\ \lambda &= \rho\sin\phi = \tau\sin\xi \quad . \end{aligned}\right\} \tag{E.3}$$

Use (E.3) in (B.5), replacing $\hat{H}(\rho)$ with $\hat{H}(k,\ell)$. The τ integration is easily carried out to leave

$$P(X,Y) = -\left(J(X,Y) + J(X,-Y)\right) = \frac{1}{2}\frac{\partial}{\partial X}\left[I(X,Y) + I(X,-Y)\right] \quad , \tag{E.4}$$

where

$$I(X,Y) = \int_0^{\pi/2} \frac{\gamma\cos\xi+\sin\xi}{(\gamma\cos\xi+\sin\xi)^2 + (\gamma X\cos\xi+Y\sin\xi)^2}\, d\xi \quad , \tag{E.5}$$

and

$$J(X,Y) = -\frac{1}{2}\frac{\partial I}{\partial X} \quad . \tag{E.6}$$

After considerable algebraic manipulation, (introducing the integration variable tan($\xi/2$) and using the method of partial fractions, for example) the following results were obtained:

$$I(X,Y) = \frac{1}{(1+X^2)^{\frac{1}{2}}} \left(L\cos(\alpha+\omega) + A\sin(\alpha+\omega)\right) \quad , \tag{E.7}$$

and

$$\begin{aligned} J(X,Y) = \frac{1}{2\ (1+X^2)\ T^2} \Big[& \gamma^2 L\sin(2\alpha+3\omega) - \gamma^2 A\cos(2\alpha+3\omega) \\ & + S\sin(2\alpha+2\omega-\eta) - \gamma\sin(2\alpha+2\omega)\Big] \quad , \end{aligned} \tag{E.8}$$

where

$$\begin{gathered} \eta = \beta-\alpha \quad , \quad \alpha = \arctan X \quad , \quad \beta = \arctan Y \quad , \quad S = \left(\frac{1+Y^2}{1+X^2}\right)^{\frac{1}{2}} \quad , \\ T^2\cos 2\omega = \gamma^2 + S^2\cos 2\eta \quad , \quad T^2\sin 2\omega = S^2\sin 2\eta \quad , \\ P_\pm = S\cos\eta \pm T\cos\omega \quad , \quad Q_\pm = S\sin\eta \pm T\sin\omega \quad , \\ L = \frac{1}{2T}\ln\left[\frac{(\gamma+P_+)^2 + Q_+^2}{(\gamma+P_-)^2 + Q_-^2}\right] \quad , \quad A = \frac{1}{T}\left[\arctan\left(\frac{\gamma+P_-}{Q_-}\right) - \arctan\left(\frac{\gamma+P_+}{Q_+}\right)\right] \quad . \end{gathered} \tag{E.9}$$

To verify (E.8) in all its detail would require considerable study. However, it is not too difficult to show that it leads to the correct result for the pressure field in the limit b→∞ ($\gamma \to 0$ and $Y \to 0$, in which case the pressure reduces to P_2 for the $\mu=1$ case in Table 4 of

Appendix D). As another check, a calculation was done for the $\gamma=1$ case of (E.8). The magnitude of the extreme pressure perturbation was found to be $P_{3Cm} \simeq .365$, occurring at a distance, $X_m \simeq .849$, from the mountain top. These values are reasonable, in light of the results obtained for the circular hill with $\mu=1$ (see Table 5 in Appendix D).

E.2 Total drag

To find the total drag, D (normalized as in Eq. 10.3), for three-dimensional flow over the barrier (E.1), substitute (E.2) into (8.3). Changing the integration variables to (τ,ξ), as in (E.3), the τ integration is found to be elementary, once again. The resulting expression for D is

$$D = \frac{\pi^2\gamma^2}{4}\int_0^{\pi/2} \frac{\cos^2\xi}{(\gamma\cos\xi+\sin\xi)^3}\,d\xi \quad . \tag{E.10}$$

Introducing $\tan\sigma=1/\gamma$ allows the denominator in the integrand to be written as $\cos^3(\xi-\sigma)/\sin^3\sigma$. Finally, changing the integration variable to $\xi-\sigma$ and using GR (pp. 136, 137) gives the result

$$D = \frac{\pi^2}{8(1+\gamma^2)^2}\left\{\frac{\gamma^2(2\gamma^2-1)}{(1+\gamma^2)^{1/2}}\ln\left[\frac{\left(\gamma+(1+\gamma^2)^{1/2}\right)\left(1+(1+\gamma^2)^{1/2}\right)}{\gamma}\right] + 1 + 4\gamma^2 - 3\gamma^3\right\} \quad . \tag{E.11}$$

For example, if $\gamma=1$, then $D \simeq 1.001$. The corresponding value for the $\mu=1$ circular hill case, calculated from (10.4) and

(10.6), is $\pi^3/32 \approx .969$. Zehnder and Bannon (1983) have calculated the total drag for non-hydrostatic flow over the barrier (E.1) in the presence of a constant Coriolis parameter, f. In the hydrostatic limit, with $f=0$, numerical values taken from one of their diagrams agree with the analytical result (E.11).

APPENDIX F

PERTURBATION FIELDS NEAR R=0

An approximation for the surface pressure perturbation directly over the barrier, near $R^2=X^2+Y^2=0$, can be obtained by expanding the complex exponential in (5.1) as

$$e^{i\rho R\cos(\phi-\theta)} = 1 + i\rho R\cos(\phi-\theta) + O(R^2) \quad . \tag{F.1}$$

Substituting this expansion into (5.1), the integation over ϕ can be done, with the terms involving even powers of R vanishing to leave

$$P_3(X,Y) = - X\, B_0\, I + O(R^3) \quad , \tag{F.2}$$

where $B_0=B_0(\gamma)$ is an elliptic integral defined by (Q.1) or (Q.3), and

$$I = 4\int_0^\infty \rho^2\, \hat{H}(\rho)\, d\rho \quad . \tag{F.3}$$

The pressure field is seen to depend on a factor, $B_0(\gamma)$, which is a function only of the eccentricity of the elliptical terrain (that is, on its horizontal cross-section), and a factor, I, which depends only on the spacing of the elliptical terrain height contours (that is, on the vertical cross-section of the terrain). For the barrier (4.1), for example, using (4.11), one obtains from GR (p. 684)

$$I = \frac{\Gamma(\mu+1/2)}{\Gamma(3/2)\,\Gamma(\mu)} \quad . \tag{F.4}$$

The pressure perturbation due to a barrier rotated through an angle, ψ, as introduced in Chapter 5, is found, from (5.15) and (5.16), to be

$$P_{ROT}(X,Y) = -\, I\left(X(B_o\cos^2\psi+C_o\sin^2\psi) + \frac{Y}{\gamma}(B_o-C_o)\sin\psi\,\cos\psi\right) + O(R^3), \tag{F.5}$$

where $C_0=C_0(\gamma)$ is defined in (Q.1).

From (F.5), one can derive various other quantities of interest. For the barriers studied in this paper, for example, the maximum pressure gradient occurs at $R=0$. The magnitude of this maximum, normalized by the dimensional factor $\bar{\rho}_0\bar{U}\,\bar{N}h_0/a$, is

$$\left|\vec{\nabla}P_3\right|_{R=0} = \left(\left(\frac{\partial P_3}{\partial X}\right)^2+\gamma^2\left(\frac{\partial P_3}{\partial Y}\right)^2\right)^{1/2}_{R=0} = I\left(B_o^2\cos^2\psi+C_o^2\sin^2\psi\right)^{1/2}. \tag{F.6}$$

If χ is the counterclockwise angle that the $P_{ROT}(X,Y)=0$ isobar makes with the y axis at the origin in an x-y plot, such as Fig. 8, then from (F.5):

$$\tan\chi = \frac{(B_o-C_o)\tan\psi}{B_o+C_o\tan^2\psi}\ . \tag{F.7}$$

If the terrain is an infinitely-extended ridge ($\gamma=0$), one finds $\chi=\psi$, so that the isobars are parallel to the ridge. For a finite barrier in its standard orientation ($\psi=0$) or rotated a quarter turn ($\psi=\pi/2$), from (F.7) one obtains $\chi=0$, so the isobars are aligned perpendicular to the incoming wind. For some intermediate orientation ($0<\psi<\pi/2$) of an isolated ridge ($0<\gamma<1$, say), the relation of the isobars to the ridge is $0<\chi<\psi$. This result means that the isobars rotate less than the barrier if its orientation is changed relative to the upstream flow. For a given barrier shape, γ=constant, the rotation, χ, of the isobars, is maximized for the barrier orientation angle $\psi=\psi_m$, where

$$\tan^2\psi_m = \frac{B_o}{C_o} \quad . \tag{F.8}$$

If χ_m is this maximum value of χ, then one finds

$$\chi_m = 2\psi_m - \pi/2 \quad . \tag{F.9}$$

For a barrier with $0<\gamma<1$, one finds $B_0 > C_0$, so, (F.8) implies that $\psi_m>\pi/4$. This means that, in the orientation giving the maximum rotation of the isobars, the long axis of the barrier is closer to being aligned with the mean wind than is the short axis.

From the pressure field at R=0 one can also calculate the velocity derivatives, $\partial u'/\partial x$ and $\partial v'/\partial y$, and the horizontal divergence, D_H. As mentioned in Chapter 7, these quantities have extrema at R=0. Using (3.27), (3.31) and (F.5) one obtains

$$\left.\begin{aligned}
\frac{\partial u'}{\partial x} &= \frac{\bar{N}h_o}{a}\, I\, (B_o\cos^2\psi + C_o\sin^2\psi) \quad , \\
\frac{\partial v'}{\partial y} &= \frac{\bar{N}h_o}{a}\, I\, (B_o\sin^2\psi + C_o\cos^2\psi) \quad , \\
D_H &= \frac{\partial u'}{\partial x} + \frac{\partial v'}{\partial y} = \frac{\bar{N}h_o}{a}\, I\, (B_o + C_o) \quad .
\end{aligned}\right\} \tag{F.10}$$

Fig. 17 shows the variation of $\partial u'/\partial x$, $\partial v'/\partial y$ and D_H as a function of γ for $\psi=0$. For a barrier rotated by 45°

($\psi=\pi/4$), one finds $\partial u'/\partial x=\partial v'/\partial y$, independent of γ.

Substituting for B_0 and C_0 in (F.10) from their definitions in (Q.3), gives

$$D_H = \begin{cases} \dfrac{\bar{N}h_o}{a}\ I\ E(k) & ;\ \gamma\leq 1\ , \\[2ex] \dfrac{\bar{N}h_o}{b}\ I\ E(k) & ;\ \gamma\geq 1\ , \end{cases} \tag{F.11}$$

Since $\gamma=a/b$, (F.11) implies that the horizontal divergence at R=0 is inversely proportional to the minor axis length of the elliptical terrain and is independent of its orientation, ψ. As with the pressure gradient, the contribution, I, depending on the vertical cross-section of the terrain, factors out from the dependence on the shape of the horizontal cross-section.

APPENDIX G

PRESSURE PERTURBATION FAR FROM THE BARRIER

In this appendix the rate of decay of the pressure perturbation far from the barrier will be determined. Arguments are made to suggest a close relationship between the asymptotic behaviour of the pressure field and the cross-sectional area and volume of the terrain, in two- and three-dimensional flow situations, respectively.

For flow over an infinitely-extended crosswind ridge, h=h(x), the normalized pressure perturbation, $P_2(X)$, is determined from (3.23) and (3.24) to be

$$P_2(X) = \frac{p'(x)}{\bar{\rho}_o \bar{U} \bar{N} h_o} = \frac{i}{h_o} \int_{-\infty}^{\infty} \mathrm{sign}(k)\, \tilde{h}(k)\, e^{ikx}\, dk \quad . \qquad (G.1)$$

Integrating by parts twice, assuming the height Fourier transform, $\tilde{h}(k)$, and its derivatives vanish as $|k| \to \infty$, one has

$$P_2(X) = -\frac{1}{a h_o X} \int_{-\infty}^{\infty} \frac{d}{dk}\left(\mathrm{sign}(k)\right) \tilde{h}(k)\, e^{ikx}\, dk + O\left(\frac{1}{X^2}\right) \quad . \qquad (G.2)$$

This integral can be evaluated by noting that

$$\frac{d}{dk}\left(\mathrm{sign}(k)\right) = 2\delta(k) \quad , \qquad (G.3)$$

where $\delta(k)$ is a Dirac delta function. (See any standard book on mathematical physics, such as Mathews and Walker (1970)). Substituting (G.3) into (G.2) gives

$$P_2(X) = -\frac{2\tilde{h}(0)}{ah_o X} + O\left(\frac{1}{X^2}\right) \quad . \tag{G.4}$$

From (3.22) the Fourier transform at zero wave number is seen to be related to the x-z cross-sectional area, A, of the ridge, by $\tilde{h}(0)=A/2\pi$, so

$$P_2(X) = -\frac{A}{\pi a h_o X} + O\left(\frac{1}{X^2}\right) \quad . \tag{G.5}$$

For the particular terrain $h=h_o/(1+X^2)^\mu$, the formula (G.5) can be verified directly from the solution (5.8) with the transformation (5.9), using the properties of the hypergeometric function. It is found to hold for all values of μ for which the area, A, given by (4.6) with Y=0, is finite. However, for $\mu \leq 1/2$, A is infinite and the pressure field falls off more slowly. Specifically, one finds

$$P_2(X) \sim \begin{cases} -\dfrac{2}{\pi}\dfrac{\ln|X|}{X} & ; \quad \mu = \frac{1}{2} \ , \\ -\dfrac{\tan(\pi\mu)}{X^{2\mu}} & ; \quad \mu < \frac{1}{2} \ . \end{cases} \tag{G.6}$$

Proceeding similarly, but with even less mathematical rigor, the behaviour of the pressure at large distances from an isolated three-dimensional barrier will now be found. For convenience, the present discussion will be limited to the Y=0 case, in the limit as $X\to\infty$. The normalized pressure field along Y=0, from (3.19) and (3.20) is

$$P_3(X,0) = \frac{p'(x,0)}{\bar{\rho}_o \bar{U} \bar{N} h_o} = \frac{1}{h_o}\frac{\partial}{\partial x}\left(\int_{-\infty}^{\infty}\int_{-\infty}^{\infty} \frac{\hat{h}(k,\ell)}{(k^2+\ell^2)^{\frac{1}{2}}} e^{ikx}\, dk\, d\ell \right) \quad . \tag{G.7}$$

If $\hat{h}(k,\ell)$ vanishes sufficiently fast as $|k|\to\infty$, then integration by parts in (G.7) gives

$$P_3(X,0) = \frac{1}{h_o}\frac{\partial}{\partial x}\left(\frac{i}{x}\int_{-\infty}^{\infty}\int_{-\infty}^{\infty}\frac{\partial}{\partial k}\left(\frac{\hat{h}(k,\ell)}{(k^2+\ell^2)^{\frac{1}{2}}}\right)e^{ikx}\,dk\,d\ell\right) . \tag{G.8}$$

For the smooth terrain fields under consideration in this paper, the Fourier transform, $\hat{h}(k,\ell)$, has no singularities away from the origin, so that the major contribution to the integral (G.8) is expected to come from the region about $k=\ell=0$. Approximating $\hat{h}(k,\ell)$ by $\hat{h}(0,0)$ and performing the integrations over k and ℓ (GR pp. 296, 405), leads to the result

$$P_3(X,0) = -\frac{V}{2\pi a^2 h_o}\frac{\mathrm{sign}(X)}{X^2} + O\left(\frac{1}{X^3}\right) , \tag{G.9}$$

where $V=4\pi^2\hat{h}(0,0)$ is the terrain volume (see Eq. 4.7). The expression (G.9) is found to give the correct result for the terrain $h=h_o/(1+R^2)^{\mu}$, whenever the volume, as given by (4.8), is finite. This is the case for $\mu>1$. For $\mu\leq 1$, the volume is infinite and the pressure falls off more slowly than X^{-2}. This can be illustrated by examining analytical solutions for the pressure field. For a circular barrier, for example, from (5.12) one obtains

$$P_{3C}(X,Y) \sim \begin{cases} -\dfrac{\Gamma(\mu+1/2)\ \Gamma(1-\mu)}{\Gamma(\mu)\ \Gamma(3/2-\mu)}\dfrac{X}{R^{2\mu+1}} & ;\ 0<\mu<1 \ , \\ -\dfrac{X\left(\ln(4R)-1\right)}{R^3} & ;\ \mu=1 \ . \end{cases} \tag{G.10}$$

Expansions for the elliptical terrain cases with $\mu=1/2$, 1, 3/2, and 2 were developed from the analytical solutions presented is Appendix D, using properties of elliptic integrals, with the results:

$$P_3(X,0) = -\frac{1}{X}\cdot\left\{\begin{array}{lll} S - \frac{1}{\chi} + \frac{T}{\chi^2} + \frac{Q}{\chi^3} + O\left(\frac{1}{\chi^4}\right) & ; \mu=1/2 \\ \frac{L-1}{\chi} - \frac{(3L-4)Q}{2\chi^3} + O\left(\frac{\ln\chi}{\chi^5}\right) & ; \mu=1 \\ \frac{1}{\chi} - \frac{2T}{\chi^2} - \frac{3Q}{\chi^3} + O\left(\frac{1}{\chi^4}\right) & ; \mu=3/2 \\ \frac{1}{2\chi} + \frac{(6L-11)Q}{4\chi^3} + O\left(\frac{\ln\chi}{\chi^5}\right) & ; \mu=2 \end{array}\right\} , \qquad (G.11)$$

where $\chi=\gamma|X|$ and $L=\ln(4\chi)$. The expansion coefficients depend on the barrier eccentricity through the parameters

$$S = \frac{2K}{\pi} \ , \quad T = \frac{2}{\pi}(E-\gamma^2K) \quad ; \gamma\leq1 \ ,$$

$$S = \frac{2K}{\pi\gamma} \ , \quad T = \frac{2\gamma}{\pi}(E-K) \quad ; \gamma\geq1 \ ,$$

and $Q=\gamma^2-1/2$.

Note that the pressure far from the barrier, along $Y=0$, decays as X^{-1} for both the flow over an isolated three-dimensional barrier ($\gamma\neq0$) with $\mu=1/2$, and for the two-dimensional flow over an infinitely-extended crosswind ridge with $\mu=1$. This indicates that the rate at which the pressure perturbation decreases downstream of the mountain peak is not solely determined by whether the flow is two- or three-dimensional.

APPENDIX H

LIMIT OF AN INFINITELY-EXTENDED CROSSWIND RIDGE

In this appendix, an approximation, P_{3A}, to the pressure field for a three-dimensional flow, P_3, is derived to show how the two-dimensional slice field, P_{2S}, is approached as the mountain barrier becomes infinitely-extended in the crosswind direction. This is the limit $\gamma \to 0$.

The starting point for the calculation to be outlined here is the integral (5.1) for P_3. A binomial expansion of the γ-dependent factor in the integrand, as

$$\left(\cos^2\phi + \gamma^2\sin^2\phi\right)^{-\frac{1}{2}} = \frac{1 - \frac{1}{2}\gamma^2\tan^2\phi}{|\cos\phi|} + O(\gamma^4) \quad , \tag{H.1}$$

fails to give a useful result because the $\tan^2\phi$ factor becomes infinitely large at $\phi=\pi/2$ and $3\pi/2$. The approach used instead is to expand the complex exponential in the numerator of the integrand as

$$\begin{aligned} e^{i\rho R\cos(\phi-\theta)} &= e^{i\rho(X\cos\phi+Y\sin\phi)} \\ &= \sum_{q=0}^{\infty}\sum_{r=0}^{\infty} \frac{(i\rho X\cos\phi)^q}{q!}\,\frac{(i\rho Y\sin\phi)^r}{r!} \quad . \end{aligned} \tag{H.2}$$

The ϕ integration can then be carried out and the series resummed. Although this method is very cumbersome, it will be shown to give reasonable results.

Substituting (H.2) into (5.1), the ϕ integral to be evaluated, denoted here by S for brevity, takes the form

$$S = S(\rho) = \int_0^{2\pi} \frac{\cos\phi \; e^{i\rho(X\cos\phi + Y\sin\phi)}}{\left(\cos^2\phi + \gamma^2\sin^2\phi\right)^{\frac{1}{2}}} \, d\phi \tag{H.3}$$

$$= \int_0^{2\pi} \frac{\cos\phi}{\left(\cos^2\phi + \gamma^2\sin^2\phi\right)^{\frac{1}{2}}} \sum_{q=0}^{\infty} \sum_{r=0}^{\infty} \frac{(i\rho X\cos\phi)^q}{q!} \frac{(i\rho Y\sin\phi)^r}{r!} \, d\phi \quad .$$

From symmetry considerations, the integral reduces to

$$S = 4i\rho X \sum_{m=0}^{\infty} \sum_{n=0}^{\infty} \frac{(-\rho^2X^2)^m}{(2m+1)!} \frac{(-\rho^2Y^2)^n}{(2n)!} D_{m+1\;n}(\gamma) \quad , \tag{H.4}$$

where D_{mn} defined by (Q.7), can be evaluated in terms of elliptic integrals. However, for the present purposes, the exact form of D_{mn} is not required, but only the terms up to second order in γ. These can be determined by making use of the following expansions for the complete elliptic integrals, K and E (GR, pp. 905, 906):

$$\left.\begin{aligned} K &= \Lambda + \tfrac{1}{4}(\Lambda-1)\gamma^2 + O(\Lambda\gamma^4) \quad , \\ E &= 1 + \tfrac{1}{4}(2\Lambda-1)\gamma^2 + O(\Lambda\gamma^4) \quad , \end{aligned}\right\} \tag{H.5}$$

where $\Lambda = \ln(4/\gamma)$. Substituting (H.5) into recursion relations for D_{mn}, similar to (Q.9) and those given in Byrd and Friedman (1971, pp. 191-193), an explicit result can be obtained to second order in γ:

$$\left.\begin{aligned} D_{mn}(\gamma) &= \frac{\Gamma(m)\;\Gamma(n+\frac{1}{2})}{2\;\Gamma(m+n+\frac{1}{2})} \left[1 - \frac{(2n+1)}{4(m-1)}\gamma^2\right] + O(\Lambda\gamma^4) \quad ; \quad m\geq 2,\; n\geq 0 \quad , \\ D_{1n}(\gamma) &= \frac{1}{2n+1} + \frac{\gamma^2}{4}\left[3 - 2\Lambda + 2\sum_{r=1}^{n} \frac{1}{2r+1}\right] + O(\Lambda\gamma^4) \quad ; \quad n\geq 0 \quad . \end{aligned}\right\} \tag{H.6}$$

where the summation in D_{1n} is taken to be zero for n=0.

Perhaps an easier derivation could be found, based on the theory of hypergeometric functions, using (Q.8).

Substituting from (H.6) into (H.3) and summing portions of the resulting series gives

$$S(\rho) = i\rho X \left(\frac{4\sin\rho Y}{\rho Y} + \gamma^2(3-2\Lambda)\cos\rho Y + 2\gamma^2 \sum_{n=1}^{\infty} \left(\frac{(-\rho^2 Y^2)^n}{(2n)!} \sum_{r=1}^{n} \frac{1}{2r+1} \right) \right.$$

$$\left. + \pi \sum_{m=1}^{\infty} \sum_{n=0}^{\infty} \left(\frac{-\rho^2 X^2}{4} \right)^m \left(\frac{-\rho^2 Y^2}{4} \right)^n \frac{\left(1 - \frac{(2n+1)}{4m}\gamma^2 \right)}{n!\, \Gamma(m+3/2)\, \Gamma(m+n+3/2)} + O(\Lambda\gamma^4) \right) . \tag{H.7}$$

From (5.3), $S(\rho) = 2\pi i H_0(\rho X)$, when $Y=\gamma=0$. This result is consistent with (H.7) because

$$H_n(\rho X) = \left(\frac{\rho X}{2} \right)^{n+1} \sum_{m=0}^{\infty} \frac{\left(\frac{-\rho^2 X^2}{4} \right)^m}{\Gamma(m+3/2)\, \Gamma(m+n+3/2)} , \tag{H.8}$$

(GR p. 982).

In terms of S, the pressure perturbation (5.1) is given by

$$P_3(X,Y) = i \int_0^{\infty} \rho\, S(\rho)\, \hat{H}(\rho)\, d\rho \quad . \tag{H.9}$$

In the specific case $h(x,y)=h_0/(1+R^2)^{\mu}$, substituting $\hat{H}(\rho)$ from (4.11), some of the remaining integrations can be done, using results from GR (pp. 684, 747, 749). Neglecting terms of order $\Lambda\gamma^4$ leaves an approximation to P_3, given by

$$\begin{aligned} P_{3A}(X,Y) = -\frac{\Gamma(\mu+1/2)}{\Gamma(3/2)\,\Gamma(\mu)}\,\frac{X}{(1+Y^2)^{\mu+\frac{1}{2}}} \Bigg\{ & 1 + G(\nu) \\ & + \frac{\gamma^2}{4(1+Y^2)} \Bigg[2Y^2G(\nu) - 2G(\omega) \\ & + (1-2\mu Y^2)\left[3-2\Lambda-\left(\int_0^{\nu}+\int_0^{\omega}\right)\frac{G(\lambda)}{\lambda}\,d\lambda\right]\Bigg]\Bigg\} \quad . \end{aligned} \tag{H.10}$$

where
$$\nu = -\frac{X^2}{1+Y^2} \quad , \quad \omega = \frac{Y^2}{1+Y^2} \quad ,$$

and
$$G(\lambda) = F(1,\mu+\tfrac{1}{2};\tfrac{3}{2};\lambda) - 1 \quad .$$

Note that the terms in (H.10) that are independent of γ give the two-dimensional slice solution, $P_{2S}(X,Y)$, defined by (5.10) and (5.8).

The leading order correction to P_{2S} in (H.10) arises from the term in Λ and is seen to be proportional to

$$\frac{X(1-2\mu Y^2)}{(1+Y^2)^{\mu+3/2}}\,\gamma^2 \ln\gamma \quad . \tag{H.11}$$

Since the correction term is linear in X, the approximation will fail for sufficiently large X. This is illustrated in Fig. 47, which shows the height field for a barrier with $\mu=3/2$ and $\gamma=1/4$ in the region $X\geq0$, $Y\geq0$, along with the corresponding three-dimensional flow pressure field, P_3, the approximation, P_{3A}, given by (H.10), and the two-dimensional slice approximation, P_{2S}. Also shown are the differences, P_3-P_{3A} and P_3-P_{2S}, in Figs. 47e and 47f, respectively. From

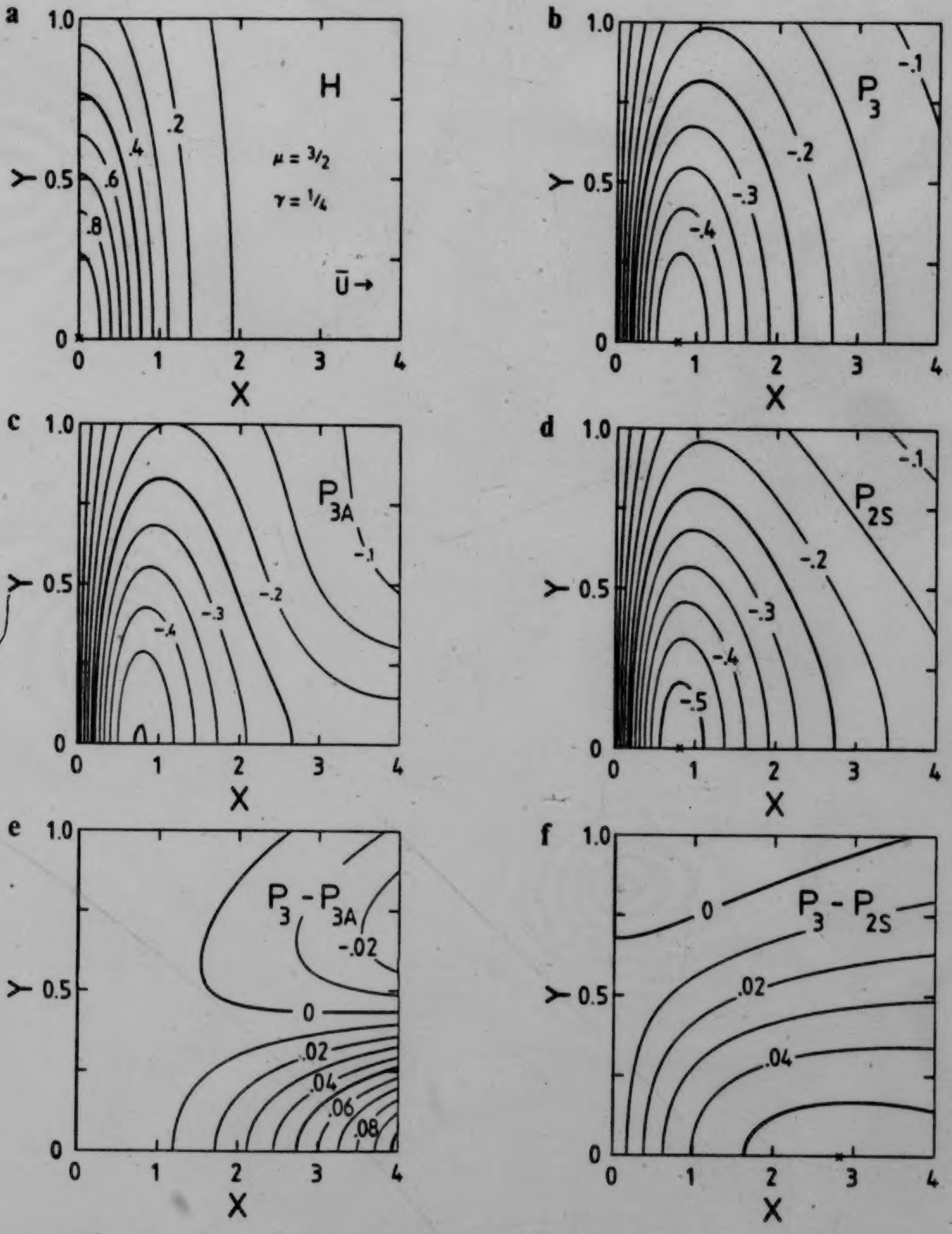

Figure 47. Contours of normalized terrain height, H, for $\mu=3/2$ and $\gamma=1/4$ (Fig. 47a), three-dimensional flow pressure perturbation, P_3 (Fig. 47b), its approximation, P_{3A}, given by Eq. H.10 (Fig. 47c), the two-dimensional slice flow approximation, P_{2s} (Fig. 47d), and the differences, P_3-P_{3A} (Fig. 47e) and P_3-P_{2s} (Fig. 47f).

Figs. 47b, 47c and 47d, it is seen that there is a qualitative similarity between the P_3, P_{3A} and P_{2S} fields near the $Y=0$ axis. However, the concentration of lines in the lower right corner of Fig. 47e shows that the approximate solution, along $Y=0$, rapidly loses accuracy as X increases. At $X=0.8$, for example, the magnitude of the relative error, $|(P_3-P_{3A})/P_3|$ is only 1%, whereas for $X=2.0$ the error is 9.4%. At these positions the values of $|(P_3-P_{2S})/P_3|$ are 7.1% and 18.4%, respectively. Therefore, P_{3A} provides a better description of the pressure field than does P_{2S} in the region of the maximum perturbation and for some distance downstream. Compare the lower left portions of Figs. 47e and 47f.

In the cases $\mu=1/2$, 1, 3/2, and 2, the hypergeometric function and its integral appearing in (H.10) have been evaluated, as in Table 4 of Appendix D, to give the results:

$$P_{3A}(X,Y) = -\frac{2}{\pi}\left\{\left[1+\frac{(1+R^2-X^2Y^2)}{2(1+Y^2)^2}\gamma^2\right]L + \frac{X\gamma^2}{(1+Y^2)^2}\left[\frac{(1-2\Lambda)(1-Y^2)}{4} - Y\arctan Y\right]\right\} \; ; \mu=1/2 \quad ,$$

$$= -\frac{X}{(1+Y^2)^{3/2}}\left\{\left[1+\frac{Y^2\gamma^2}{2(1+Y^2)}\right]\frac{(1+Y^2)}{(1+R^2)} - \frac{Y^2\gamma^2}{1+Y^2} + \frac{\gamma^2(1-2Y^2)(3-2\bar{\Lambda})}{4(1+Y^2)}\right\} \; ; \mu=1 \quad ,$$

$$= -\frac{2}{\pi}\left(\frac{1}{1+R^2}\left[1 + \frac{Y^2}{1+Y^2}\gamma^2\right]\left[\frac{X}{1+Y^2} + L\right]\right.$$

$$+ \frac{X\gamma^2}{(1+Y^2)^3}\left[(1-\Lambda)(1-3Y^2) + Y(2Y^2-3)\arctan Y\right]$$

$$\left. + \frac{\gamma^2(1-3Y^2)(1-Y^2+2R^2)L}{2(1+Y^2)^3} \right) \quad ; \ \mu=3/2 \quad ,$$

$$= -\frac{X}{2(1+Y^2)^{5/2}}\left(\left[1 + \frac{Y^2\gamma^2}{2(1+Y^2)}\right]\frac{(1+Y^2)(3+2Y^2+R^2)}{(1+R^2)^2}\right.$$

$$+ \frac{3\gamma^2(1-4Y^2)}{4(1+Y^2)}\left[3-2\overline{\Lambda}+\frac{2X^2}{3(1+R^2)}\right]$$

$$\left. + \frac{\gamma^2Y^2(2Y^2-9)}{2(1+Y^2)} \right) \quad ; \ \mu=2 \quad ,$$

(H.12)

where $$L = \frac{1}{(1+R^2)^{\frac{1}{2}}}\operatorname{arctanh}\left[\frac{X}{(1+R^2)^{\frac{1}{2}}}\right] \quad ,$$

$$\overline{\Lambda}(X,Y) = \Lambda + \ln\left[\frac{1+Y^2}{(1+R^2)^{\frac{1}{2}}}\right] \quad ,$$

$R=(X^2+Y^2)^{1/2}$ and $\Lambda=\ln(4/\gamma)$.

APPENDIX I

LIMIT OF AN INFINITELY-EXTENDED RIDGE PARALLEL TO THE WIND

In this appendix the pressure field is examined in the limit as $\gamma\to\infty$. This corresponds to an infinitely-long ridge aligned with the direction of the mean wind. As discussed in Chapter 7, this also gives information about the transverse velocity in the $\gamma\to 0$ limit (an infinite crosswind ridge).

The method used is the same as in Appendix H, with the pressure field being determined from (H.9) and (H.4), except that an approximation for $D_{mn}(\gamma)$ valid for $\gamma\to\infty$ is developed, rather than for $\gamma\to 0$. However, there is a close connection between these two limits because of the relation

$$D_{mn}(\gamma) = \frac{1}{\gamma} D_{nm}\left(\frac{1}{\gamma}\right) \quad , \tag{I.1}$$

which follows easily from (Q.7). Using (I.1) in (H.4) gives

$$S(\rho) = \frac{4i\rho X}{\gamma} \sum_{m=0}^{\infty} \sum_{n=0}^{\infty} \frac{(-\rho^2 X^2)^m}{(2m+1)!} \frac{(-\rho^2 Y^2)^n}{(2n)!} D_{n\ m+1}\left(\frac{1}{\gamma}\right) \quad . \tag{I.2}$$

For $n\neq 0$, the factors $D_{n\ m+1}(1/\gamma)$ are given by (A5.7). $D_{o\ m+1}(1/\gamma)$ can also be obtained from (H.6) with (H.5), using the identity

$$D_{o\ m+1}\left(\frac{1}{\gamma}\right) = D_{oo}\left(\frac{1}{\gamma}\right) - \sum_{r=0}^{m} D_{1r}\left(\frac{1}{\gamma}\right) \quad , \tag{I.3}$$

where $D_{oo}(1/\gamma)=K(k)$, with $k^2=1-1/\gamma^2$. One finds

$$D_{o\;m+1}\left(\frac{1}{\gamma}\right) = \left(\tilde{\Lambda} - \sum_{r=0}^{m} \frac{1}{2r+1}\right)\left(1 + \frac{(2m+3)}{4\gamma^2}\right) - \frac{1}{4\gamma^2} + 0\left(\frac{\tilde{\Lambda}}{\gamma^4}\right) \quad , \qquad (I.4)$$

where $\tilde{\Lambda}=\ln(4\gamma)$. Substituting (H.6) and (I.4) into (I.2) and simplifying some of the terms, gives

$$S(\rho) = \frac{4i\rho X}{\gamma}\left[\tilde{\Lambda}\frac{\sin\rho X}{\rho X} - \sum_{m=0}^{\infty}\left(\frac{(-\rho^2X^2)^m}{(2m+1)!}\sum_{r=0}^{m}\frac{1}{2r+1}\right)\right. \qquad (I.5)$$

$$\left. + \frac{\pi}{4}\sum_{m=0}^{\infty}\sum_{n=1}^{\infty}\frac{\left(\frac{-\rho^2X^2}{4}\right)^m\left(\frac{-\rho^2Y^2}{4}\right)^n}{m!\;n\;\;\Gamma(m+n+3/2)\;\Gamma(n+1/2)}\right] + 0\left(\frac{\tilde{\Lambda}}{\gamma^3}\right) \quad .$$

For the particular terrain $h(x,y)=h_0/(1+R^2)^{\mu}$, the integrals to be evaluated, after putting (I.5) into (H.9), are very similar to those considered in Appendix H. The resulting surface pressure perturbation for $\gamma>>1$ is

$$P_3(X,Y) = -\frac{\Gamma(\mu+1/2)}{\Gamma(3/2)\;\Gamma(\mu)}\frac{X}{\gamma(1+X^2)^{\mu+\frac{1}{2}}}\left[\tilde{\Lambda} - 1 + G(\nu')\right. \qquad (I.6)$$

$$\left. + \frac{1}{2}\left(\int_0^{\nu'} + \int_0^{\omega'}\right)\frac{G(\lambda)}{\lambda}\,d\lambda\right] + 0\left(\frac{\tilde{\Lambda}}{\gamma^3}\right) \quad ,$$

where

$$\nu' = -\frac{Y^2}{1+X^2} \quad , \quad \omega' = \frac{X^2}{1+X^2} \quad ,$$

and

$$G(\lambda) = F(1,\mu+\tfrac{1}{2};\tfrac{3}{2};\lambda) - 1 \quad .$$

Since the term in $\tilde{\Lambda}$ dominates the pressure for sufficiently large γ, one can obtain some information about the pressure field without evaluating the hypergeometric function. For example, retaining only the $\tilde{\Lambda}$ term, one finds that the extreme pressure perturbation occurs at a distance

$X_m = (2\mu)^{-1/2}$ from the terrain peak. See Fig. 11.

Evaluation of (I.6) in the specific cases $\mu = 1/2$, 1, 3/2, and 2, gives:

$$P_3(X,Y) = \left\{ \begin{array}{ll} -\frac{2}{\pi\gamma}\frac{X}{1+X^2}\left[\tilde{\Lambda} - \frac{\arctan X}{X} - \zeta \operatorname{arctanh}\zeta\right] + O\left(\frac{\tilde{\Lambda}}{\gamma^3}\right) & ;\ \mu = 1/2\ , \\ -\frac{X}{\gamma(1+X^2)^{3/2}}\left[\tilde{\Lambda} - \ln\beta - 1 - \zeta^2\right] + O\left(\frac{\tilde{\Lambda}}{\gamma^3}\right) & ;\ \mu = 1\ , \\ -\frac{2}{\pi\gamma}\frac{X}{(1+X^2)^2}\left[2\tilde{\Lambda} + \frac{(X^2-1)}{X}\arctan X - 1 - \zeta^2\right. & \\ \qquad\qquad \left. - \zeta(3+\zeta^2)\operatorname{arctanh}\zeta\right] + O\left(\frac{\tilde{\Lambda}}{\gamma^3}\right) & ;\ \mu = 3/2\ , \\ -\frac{X}{2\gamma(1+X^2)^{5/2}}\left[3(\tilde{\Lambda} - \ln\beta - 1) + X^2 - 6\zeta^2 + 2\zeta^4\right] + O\left(\frac{\tilde{\Lambda}}{\gamma^3}\right) & ;\ \mu = 2\ , \end{array} \right\} \tag{I.7}$$

where $$\beta = \frac{(1+R^2)^{\frac{1}{2}}}{1+X^2}\ ,$$

and $$\zeta = \frac{Y}{(1+R^2)^{\frac{1}{2}}}\ .$$

APPENDIX J

FAST FOURIER TRANSFORM CALCULATION OF THE PRESSURE FIELD

Following Smith (1980), the Fast Fourier Transform method can be used to calculate the integrals for the terrain-height Fourier transform and pressure appearing in (B.3) and (B.5).

First consider evaluation of $\tilde{H}(\kappa;Y)$. The height field, $H(X,Y)$, is sampled at M evenly spaced points, X_r, along a line of constant Y:

$$X_r = (r - M/2)\,\Delta X \quad ; \quad r=1,\ 2,\ \ldots\ M \ , \tag{J.1}$$

where Δx is the constant sampling interval. For greatest efficiency, M is chosen to be an integer power of 2. The integral for $\tilde{H}$ is approximated at the points

$$\kappa_s = (s - M/2)\,\Delta\kappa \quad ; \quad s=1,\ 2,\ \ldots\ M \ , \tag{J.2}$$

where

$$\Delta\kappa = \frac{2\pi}{M\ \Delta X} \ , \tag{J.3}$$

by

$$\tilde{H}(\kappa_s;Y) = \frac{\Delta X}{2\pi} \sum_{r=1}^{M} H(X_r,Y)\, e^{-iX_r\kappa_s} \quad ; \quad s=1,\ 2,\ \ldots\ M \ . \tag{J.4}$$

In actual calculation using the Fast Fourier Transform procedure, the height field is assumed to be defined on the interval from $X=0$ to $(M-1)\Delta X$, rather than $X=(1-M/2)\Delta X$ to $M\Delta X/2$ as in (J.1). The expression (J.4) can be cast into the required form by introducing the new summation variable, $t=r+M/2$ for $r\le M/2-1$ and $t=r-M/2$ for $r\ge M/2$. One obtains

$$\tilde{H}(\kappa_s;Y) = \frac{\Delta X}{2\pi} \sum_{t=0}^{M-1} H_t \, e^{-it\Delta X \kappa_s} \quad ; \quad s=1,\ 2,\ \ldots\ M \ , \tag{J.5}$$

where

$$H_t = \begin{cases} H(X_{t+M/2},Y) & ; \quad t=0,\ 1,\ \ldots\ M/2 \ , \\ H(X_{t-M/2},Y) & ; \quad t=M/2+1,\ M/2+2,\ \ldots\ M-1 \ . \end{cases} \tag{J.6}$$

Performing similar operations in the wave number domain, making use of (J.3), leads to the expression

$$\tilde{H}_u = \frac{\Delta X}{2\pi} \sum_{t=0}^{M-1} H_t \, e^{-2\pi itu/M} \quad ; \quad u=0,\ 1,\ \ldots\ M-1 \ , \tag{J.7}$$

where

$$\tilde{H}_u = \begin{cases} H(\kappa_{u+M/2};Y) & ; \quad u=0,\ 1,\ \ldots\ M/2 \ , \\ H(\kappa_{u-M/2};Y) & ; \quad u=M/2+1,\ M/2+2,\ \ldots\ M-1 \ . \end{cases} \tag{J.8}$$

The form (J.7) is suitable for direct application of computer packages for Fast Fourier Transforms.

A consistent approximation for the inverse transform, which regenerates the height field, then takes the form

$$H(X_r,Y) = \Delta\kappa \sum_{s=1}^{M} \tilde{H}(\kappa_s;Y) \, e^{iX_r\kappa_s} \quad ; \ r=1,\ 2,\ \ldots\ M \ . \tag{J.9}$$

Similarly, the two-dimensional slice pressure field, P_{2S}, defined in (B.5), is estimated to be

$$P_{2S}(X_r,Y) = i\ \Delta\kappa \sum_{s=1}^{M} \mathrm{sign}(\kappa_s)\ \tilde{H}(\kappa_s;Y) \, e^{iX_r\kappa_s} \quad ; \quad r=1,\ 2,\ \ldots\ M \ . \tag{J.10}$$

Manipulations such as those leading to (J.7) are used in calculating the pressure field as well.

Note that the pressure field is essentially that due to a periodic train of hills found by infinitely extending the height values, sampled at the points (J.1), in the positive and negative X directions. This periodicity is seen in the representation of the height field (J.9). In the calculation of the pressure by the discrete Fourier transform technique, one must ensure that the periodically repeating hills are widely separated. If they are not, then the windward high associated with one ridge will partially cancel with the lee-side low of the next upstream ridge. To show this effect, a test was done for the Agnesi terrain shape, $H=1/(1+X^2)$. With the total number of points fixed at $M=128$, the pressure, $P_2(X)=P_{2S}(X,Y=0)$, was calculated from (J.10) using $\Delta X=1/32$, 1/16, 1/8, 1/4, 1/2, and 1. In Fig. 48, P_2 is plotted as a function of X, for the various ΔX values and for the exact result, $P_2=-X/(1+X^2)$. A Fast Fourier Transform program from IMSL, Inc. was used in the evaluation. The Fourier transform method provides estimates of P_2 only at the discrete points, but, for clarity, a smooth curve has been drawn through the points for the $\Delta X\leq 1/4$ cases. Values for $\Delta X=1/2$ are indicated with circles, while the diamonds correspond to $\Delta X=1$.

For the $\Delta X=1/32$ case, the terrain height is very well resolved, but, the separation between successive ridges in the infinite succession is only 4 units. There is a significant interference between the ridges which reduces the amplitude of the pressure perturbation. As ΔX is increased,

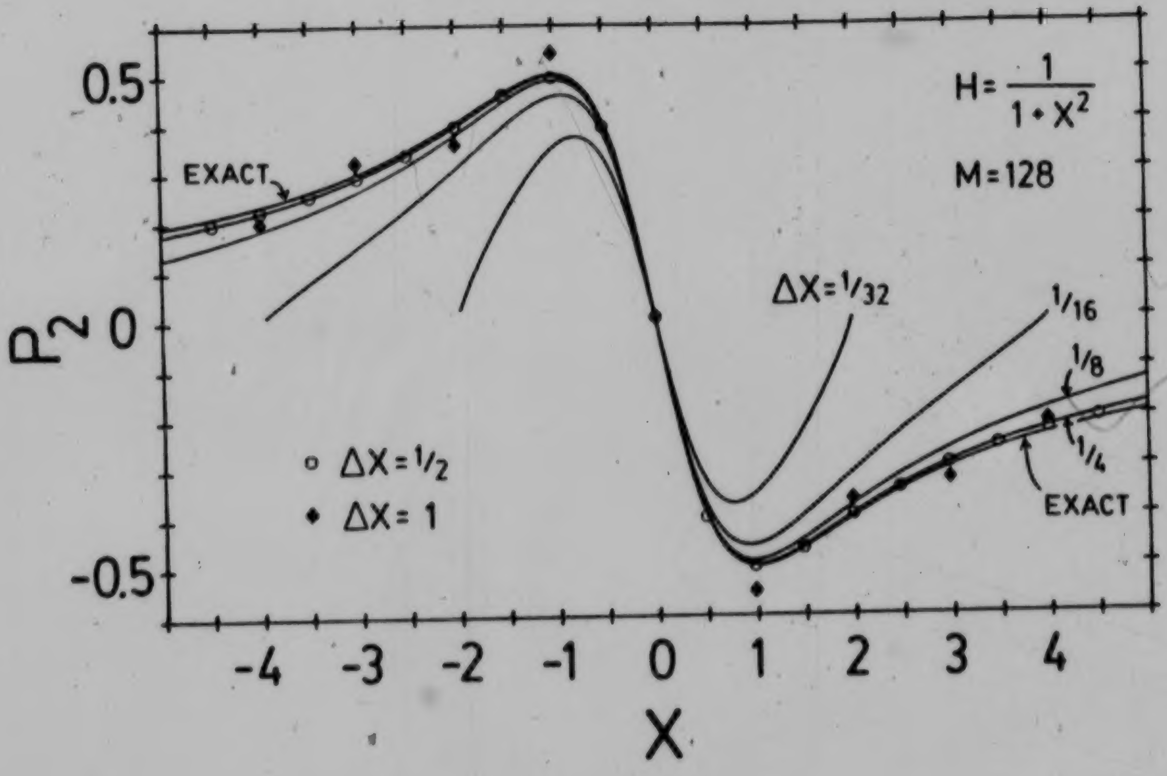

Figure 48. Discrete Fourier transform result for normalized pressure, P_2, vs. distance X, for flow over an Agnesi barrier, H, sampled at M=128 uniformly spaced points at intervals $\Delta X=1/32$, 1/16, 1/8, 1/4, 1/2 and 1. Also shown is the exact result ($\Delta X \rightarrow 0$, $M \rightarrow \infty$).

up to $\Delta X=1/2$, the approximation to the exact pressure field becomes progressively better because the interference between the ridges decreases. However, for $\Delta X=1$, the terrain-height field is sampled so coarsely that the accuracy of the pressure field determination begins to suffer. Appropriate choices of M and ΔX represent a compromise between resolving the height field and minimizing the effect of periodicity implicit in the Fast Fourier Transform method.

The discrete Fourier transform approach can be extended to the evaluation of the multiple integrals that arise in the three-dimensional flow problem. For example, to calculate the Fourier transform of the terrain height, $\hat{H}(\kappa,\lambda)$, defined in (B.3), the double integral can be written as

$$\hat{H}(\kappa,\lambda) = \frac{1}{2\pi} \int_{-\infty}^{\infty} \tilde{H}(\kappa;Y)\, e^{-i\lambda Y}\, dY \quad . \tag{J.11}$$

An approximation to this integral can be determined at a discrete number of points in exactly the same manner as outlined in this appendix for $\tilde{H}(\kappa;Y)$.

APPENDIX K

DRAG PER UNIT CROSSWIND LENGTH

The drag per unit crosswind length, d_{2S}, for two-dimensional slice flow over various elliptical barriers, is presented in Table 8. Most of the results can be obtained by substituting $\tilde{H}(\kappa;Y)$ from Table 2 into (B.8) and using the appropriate tabulated integral from GR. The case of $H=\exp(-R)$ is slightly more involved. Changing the integration variable in (B.8) to $z=|Y|(1+\kappa^2)^{\frac{1}{2}}$ and using relations between K_0 , K_1 and their derivatives (GR, p. 970), one finds that the integrand can be manipulated into the form of an exact derivative. The integration is then easily performed to give the result in the table. For the Bessel function barrier, $K_0(R)$, the change of variable $z=2|Y|(1+\kappa^2)^{\frac{1}{2}}$ allows GR (p. 925) to be used to give the expression for d_{2S} in terms of the exponential integral function, Ei. For the final two entries in the table, the drag per unit length was evaluated only at $Y=0$.

Analytical progress in finding the drag per unit length, d_3, for three-dimensional flow over elliptical terrain was much more limited. First consider the terrain, $H=(1+R^2)^{-\mu}$. Substitute for $\tilde{H}(\kappa;Y)$ and $\hat{H}(\kappa,\lambda)=\hat{H}(\rho)$ in (B.8) from Tables 2 and 3 respectively, and use elliptical polar coordinates (ρ,ϕ) defined in (B.2). The ρ integral can be evaluated in the special case of $Y=0$ (GR, p. 693) to give

Table 8. Normalized drag per unit crosswind length, $d_{2S}(Y)$, for two-dimensional slice flow over an elliptical barrier with height $H(R)$.

$H(R)$	$d_{2S}(Y)$	Reference
$(1+R^2)^{-\mu}$	$\frac{\{\Gamma(\mu+\frac{1}{2})\}^2}{\Gamma(\mu)\ \Gamma(\mu+1)} \frac{1}{(1+Y^2)^{2\mu}}$	GR, p. 693
e^{-R^2}	e^{-2Y^2}	elementary
$(1-R^2)^{\nu}\ \theta(1-R^2)$	$\frac{\Gamma(\nu)\ \Gamma(\nu+1)}{\{\Gamma(\nu+\frac{1}{2})\}^2} (1-Y^2)^{2\nu}\ \theta(1-Y^2)$	GR, p. 693
$\frac{\ln\left(\frac{\delta^2+R^2}{1+R^2}\right)}{\ln(\delta^2)}$	$\frac{4\pi}{\{\ln(\delta^2)\}^2} \ln\left(\frac{(\delta^2+Y^2)^{\frac{1}{2}} + (1+Y^2)^{\frac{1}{2}}}{4\ (\delta^2+Y^2)^{\frac{1}{2}}\ (1+Y^2)^{\frac{1}{2}}}\right)$	GR, p. 328
$\frac{\operatorname{arccot}\left(\frac{R^2+\cos 2\omega}{\sin 2\omega}\right)}{2\omega}$	$-\frac{\pi}{4\omega^2} \ln\left(\frac{1}{2}\left(1 + \frac{Y^2+\cos 2\omega}{\{Y^4+2Y^2\cos 2\omega+1\}^{\frac{1}{2}}}\right)\right)$ $= \frac{\pi}{4\omega^2} \ln\left(\frac{1}{\cos^2\xi}\right)$, where $\tan 2\xi = \frac{\sin 2\omega}{Y^2+\cos 2\omega}$	GR, p. 491
e^{-R}	$\frac{2}{\pi} Y^2 \left(\{K_1 \lvert Y \rvert\}^2 - \{K_0 \lvert Y \rvert\}^2\right)$	see text
$K_0(R)$	$-\pi\ \mathrm{Ei}(-2\lvert Y\rvert)$	see text
$(1-R)\ \theta(1-R)$	$\frac{4\ \ln 2}{\pi}$ at $Y=0$.	GR, p. 449
$\mathrm{sech}(R)$	$\frac{4\ \ln 2}{\pi}$ at $Y=0$.	GR, p. 353

$$d_3(Y=0) = \frac{\Gamma(2\mu+1)}{\Gamma(2\mu+3/2)} \frac{\Gamma(\mu+1/2)}{\Gamma(\mu)} \int_0^{\pi/2} \frac{\cos^2\phi \; F(3/2,\mu+1/2;2\mu+3/2;\sin^2\phi)}{(\cos^2\phi+\gamma^2\sin^2\phi)^{\frac{1}{2}}} \, d\phi \quad . \tag{K.1}$$

(Here, a transformation formula for hypergeometric functions has also been used (GR, p. 1043)). In special cases, the hypergeometric function can be expressed in terms of elementary functions. For example, when $\mu=1/2$, the relevant relation is (GR, p. 1045 and p. 1041)

$$F(3/2,1;5/2;\sin^2\phi) = \frac{3}{\sin^2\phi} \left(\frac{\operatorname{arctanh}(\sin\phi)}{\sin\phi} - 1 \right) \quad . \tag{K.2}$$

A closed-form result for $d_3(Y=0)$ was not obtained, even in the $\mu=1/2$ case. However, expanding the hypergeometric series in $\sin^2\phi$ and interchanging the order of summation and integration, one finds

$$d_3(Y=0) = \frac{\Gamma(2\mu+1)}{\Gamma(3/2)\,\Gamma(\mu)} \sum_{n=0}^{\infty} \frac{\Gamma(n+3/2)\;\Gamma(n+\mu+1/2)}{\Gamma(n+2\mu+3/2)\; n!} D_{1n}(\gamma) \quad , \tag{K.3}$$

where D_{1n} are elliptic integrals defined by (Q.7). As a check on this expression, consider the $\gamma=0$ case. Using $D_{1n}(\gamma=0)=1/(2n+1)$, from (Q.8), one finds that the summation in (K.3) reduces to a hypergeometric function with unit argument. Evaluating this series (GR, p. 1042), it can be verified that the result expected from Table 8 is recovered.

For $Y\neq0$, the drag per unit length was obtained for the μ-type terrain only in the circular hill cases with $\mu=1/2$ and 3/2. Rather than using (B.8), the easiest way to proceed appears to be to calculate d_{3C} directly from the pressure field:

$$d_{3C}(Y) = \int_{-\infty}^{\infty} P_{3C}(X,Y)\,\frac{\partial H}{\partial X}\,dX \quad . \tag{K.4}$$

Substituting for P_{3C} from Table 5 in Appendix D, (K.4) can be evaluated using standard methods for algebraic integrands if μ is half an odd positive integer. The specific results obtained are:

$$d_{3C}(Y) = \begin{cases} 2\left[1 + Y\arctan Y - \frac{\pi}{4}\,\frac{1+2Y^2}{(1+Y^2)^{\frac{1}{2}}}\right] & ; \mu=1/2 \ , \\ \frac{3\pi}{16}\,\frac{1}{(1+Y^2)^{5/2}} & ; \mu=3/2 \ . \end{cases} \tag{K.5}$$

These expressions have been checked by integrating with respect to Y to give the total drag, $D_{3C}=G\pi/4$, where G is defined by (10.5). G values from Table 9 in Appendix N are found to be consistent with (K.5).

Next, consider the exponential terrain shape, $H=\exp(-R^2)$. Only the drag per unit length at Y=0 was found. Substituting from Tables 2 and 3 into (B.8) and performing the integration over ρ (GR, p. 495), one finds

$$d_3(Y=0) = 2\int_0^{\pi/2} \frac{\cos^2\phi}{(1+\cos^2\phi)^{3/2}(\cos^2\phi+\gamma^2\sin^2\phi)^{1/2}}\,d\phi \quad . \tag{K.6}$$

Making the substitution $\cos^2\phi=\cos^2\xi/(1+\sin^2\xi)$ gives

$$d_3(Y=0) = \int_0^{\pi/2} \frac{\cos^2\xi}{(\cos^2\xi+2\gamma^2\sin^2\xi)^{\frac{1}{2}}}\,d\xi \quad . \tag{K.7}$$

Comparing this expression to the definition of B_0 in (Q.1), the final result is obtained:

$$d_3(Y=0) = B_o(\gamma 2^{\frac{1}{2}}) \quad , \tag{K.8}$$

The terrain shape for which the most analytical progress was made is $H=(1-R^2)^\nu \theta(1-R^2)$. Substituting from Tables 2 and 3 into (B.8) gives

$$d_3 = Z\Lambda^{\nu+\frac{1}{2}}\theta(\Lambda^2) \int_0^\infty \int_0^{\pi/2} \frac{(\cos\phi)^{3/2-\nu} \cos(\rho Y\sin\phi)\ J_{\nu+1}(\rho)\ J_{\nu+\frac{1}{2}}(\rho\Lambda\cos\phi)}{(\cos^2\phi+\gamma^2\sin^2\phi)^{\frac{1}{2}}\ \rho^{2\nu-\frac{1}{2}}}\, d\rho d\phi \ , \tag{K.9}$$

where

$$\Lambda^2 = 1 - Y^2 \quad ; \quad Z = \frac{2^{2\nu+3/2}\{\Gamma(\nu+1)\}^2}{\Gamma(\frac{1}{2})} \quad . \tag{K.10}$$

In the $\nu=1/2$ case, after evaluating the ρ integral using GR (p. 749), the ϕ integral reduces to an elliptic type considered in Appendix Q. The explicit result is

$$d_3(Y) = \frac{\pi}{2}\,(1-Y^2)\ \theta(1-Y^2)\ B_0(\gamma) \quad . \tag{K.11}$$

The drag per unit length corresponding to the $\nu=3/2$ barrier was also evaluated, although some manipulation was required to bring (K.9) into a form allowing the use of tabulated integrals. The ρ integral for this case is

$$I = \int_0^\infty \frac{\cos(\rho\beta)\ J_{5/2}(\rho)\ J_2(\rho\Lambda\cos\phi)}{\rho^{5/2}}\, d\rho \quad , \tag{K.12}$$

where $\beta=Y\sin\phi$, and Λ is as in (K.10). I can be found by writing

$$I = I(\beta=0) + \int_0^{\beta} \frac{\partial I}{\partial \beta}\, d\beta \quad . \qquad (K.13)$$

$I(\beta=0)$ is given by GR (p. 692) and $\partial I/\partial\beta$ can be determined from GR (p. 695) by noting that $\cos(\rho\beta)$ can be expressed in terms of $J_{-\frac{1}{2}}(\rho\beta)$. Since $\partial I/\partial\beta$ turns out to be a simple linear function of β, the integral in (K.13) is easily evaluated. The resulting drag per unit length is

$$d_3(Y) = \frac{9\pi}{32}\,(1-Y^2)\;\theta(1-Y^2)\left[2(1-3Y^2)D_{10} - (1-7Y^2)D_{20}\right] \qquad (K.14)$$

where D_{10} and D_{20} are elliptic integrals defined in (Q.10).

For the case of general ν, an expression analogous to the μ-type terrain result (K.3) can be derived (GR, pp. 692, 1039) for the Y=0 limit. However, this was not employed in calculations.

The final terrain shape for which the drag per unit length was evaluated is H=exp(-R). It turns out that the value of d_3 at Y=0 is exactly the same as that for μ=1/2, given in (K.3).

APPENDIX L

ANALYTICAL RESULTS FOR SINUSOIDALLY MODULATED RIDGES

If $\tilde{H}(\kappa)$ is the normalized Fourier transform for the terrain $H(X)$, then the Fourier transform for the sinusoidally modulated ridge, $H(X;A,B,\Omega) = (A+B\cos\Omega X)\,H(X)$ is

$$\tilde{H}(\kappa;A,B,\Omega) = A\,\tilde{H}(\kappa) + \frac{B}{2}\left[\tilde{H}(\kappa-\Omega) + \tilde{H}(\kappa+\Omega)\right] \quad . \qquad (L.1)$$

This result follows directly from the definition of $\tilde{H}(\kappa)$ ($=\tilde{H}(\kappa;Y=0)$ in (B.3)) upon writing $\cos\Omega X$ in terms of exponentials. Although $\tilde{H}(\kappa)$ is given in Table 2 in Appendix D for a variety of terrain shapes, only the Agnesi case, $H=1/(1+X^2)$, and the Gaussian case, $H=\exp(-X^2)$, are treated here.

For the Agnesi barrier, putting $\mu=1$ in Table 2 gives $\tilde{H}(\kappa)=\exp(-|\kappa|)/2$ (GR, p. 967). After substitution into (L.1) and (B.5), straightforward but lengthy calculation gives the pressure perturbation

$$P_2(X;A,B,\Omega) = -\frac{X}{1+X^2}\left[A + B\left(e^{-|\Omega|} + \frac{\sin|\Omega|X}{X}\right)\right] \quad . \qquad (L.2)$$

The drag per unit length, d_2, can also be evaluated in terms of elementary functions, by integrating the pressure times the terrain slope, or more easily, by using (L.1) in (9.1). The result is

$$d_2 = \frac{\pi}{4}\left[\,(1+|\Omega|+\Omega^2)\{A+Be^{-|\Omega|}\}^2 + |\Omega|\{B^2-(1+|\Omega|)A^2\}\,\right] \quad , \qquad (L.3)$$

For the Gaussian ridge, substitution of $\tilde{H}(\kappa)$ from Table 2 into (L.1) gives

$$\tilde{H}(\kappa;A,B,\Omega) = \frac{e^{-\kappa^2/4}}{2\,\Gamma(\frac{1}{2})}\left[A + B\,e^{-\Omega^2/4}\cosh\left(\frac{\kappa\Omega}{2}\right)\right] \quad . \qquad \text{(L.4)}$$

The pressure field was not evaluated for this case, but, from (9.1) the drag per unit length was found to be (GR, p. 365)

$$d_2 = \left(A+Be^{-2\Lambda^2}\right)^2 + \pi^{\frac{1}{2}}\Lambda B\left(2\Phi(\Lambda)e^{-\Lambda^2}A + \Phi(2\Lambda)B\right) \quad , \qquad \text{(L.5)}$$

where $\Lambda=|\Omega|/\sqrt{8}$ and Φ is the error function (GR, p. 930). In obtaining this result, the relation $2\cosh^2(z)=1+\cosh(2z)$ was used.

APPENDIX M

ANALYTICAL RESULTS FOR DOUBLE RIDGES

In this appendix, the drag per unit length, d_2 , is calculated for a barrier, H(X), formed from the juxtaposition of two identical ridges, which have been displaced from the origin in opposite directions by an amount ϵ. From (B.3), the terrain height, defined by (9.11), has Fourier transform, $\tilde{H}(\kappa)$, given by

$$\tilde{H}(\kappa) = 2 \cos\kappa\varepsilon\ \tilde{h}(\kappa) \quad , \tag{M.1}$$

where $\tilde{h}(\kappa)$ is the Fourier transform for a single, undisplaced ridge, h(X). Substituting (M.1) into (9.1), using Fourier transforms from Table 2 in Appendix D, gives d_2. When interpreting the results for d_2, it is convenient to compare the magnitude of ϵ to X_m, the horizontal distance from the ridge top to the position of the maximum pressure perturbation for a single ridge. Therefore, values of X_m are given in the following, along with those for d_2.

The first of four ridge shapes considered is the Agnesi barrier, $h=1/(1+X^2)$, for which case, $X_m=1$. One finds from GR (p. 490) that

$$d_2 = \frac{\pi}{2}\left[1 + \frac{1-\varepsilon^2}{(1+\varepsilon^2)^2}\right] \quad . \tag{M.2}$$

Here, as in the following case, the relation $2\cos^2(\kappa\epsilon)=\cos(2\kappa\epsilon)+1$, has been used. The minimum value of d_2 is $7\pi/16 \simeq 1.374$, which occurs at $\epsilon=\sqrt{3}\simeq 1.732$.

For the logarithmic barrier, defined in (9.2) or Table 2, GR (p. 493) gives

$$d_2 = \frac{4\pi}{\left(\ln(\delta^2)\right)^2} \ln\left(\frac{\left(\frac{1+\delta}{2}\right)^4 \left[\varepsilon^2+\left(\frac{1+\delta}{2}\right)^2\right]^2}{\delta^2\ (\varepsilon^2+1)\ (\varepsilon^2+\delta^2)}\right) . \tag{M.3}$$

$X_m=\delta^{\frac{1}{2}}$ and the minimum of d_2 occurs at $\epsilon^2=(\delta^2+4\delta+1)/2$.

For the arccot barrier (see Table 2 or (9.2)), using GR (p. 492) gives

$$d_2 = \frac{\pi}{4\omega^2} \ln\left(\frac{(1-\varepsilon^2)^2 + 4\varepsilon^2\cos^2\omega}{(\varepsilon^2+\cos^2\omega)^2\ \cos^4\omega}\right) . \tag{M.4}$$

$X_m=1$ and the minimum drag per unit length occurs at $\epsilon^2=1+2\cos^2\omega$.

The final terrain shape considered in this section, is the triangular barrier, $h = (1-|X|)\ \theta(1-|X|)$. Substituting for the Fourier transform from Table 2, into (M.1) and (9.1) gives

$$d_2 = \frac{64}{\pi} \int_0^\infty \frac{\cos^2(\kappa\varepsilon)}{\kappa^3} \sin^4\left(\frac{\kappa}{2}\right) d\kappa \ . \tag{M.5}$$

Integration by parts, to reduce the power of κ in the denominator, followed by reference to GR (pp. 452-453), leads to the result

$$\begin{aligned} d_2 = \frac{4}{\pi} \Big(& 4(1+2\varepsilon^2)\ln 2 + 6\varepsilon^2\ln|\varepsilon| + (1+\varepsilon)^2\ln|1+\varepsilon| + (1-\varepsilon)^2\ln|1-\varepsilon| \\ & - (1+2\varepsilon)^2\ln|1+2\varepsilon| - (1-2\varepsilon)^2\ln|1-2\varepsilon|\Big) . \end{aligned} \tag{M.6}$$

Numerical analysis indicates that the minimum value of d_2 is about 1.223, occurring at $\epsilon \approx .648$. The maximum pressure for a single triangular ridge occurs at $X_m = 1/\sqrt{2} \approx .707$.

APPENDIX N

TOTAL DRAG

The integral, G, defined by (10.5), appears as a factor in the total force on an elliptical barrier in three-dimensional (10.4) and in two-dimensional slice (10.9) flow. G has been evaluated for various terrain shapes, with the results summarized in Table 9. Since G is equal to the total drag for the two-dimensional slice flow over an unrotated barrier (see Appendix O), it can be calculated by integrating the drag per unit length in Table 8, $d_{2S}(Y)$, with respect to Y. For many of the examples, this approach proved easier than using the expression (10.5). Except for the logarithmic and arccot barriers, the integrals for G appear directly in GR. A derivation for these two cases will now be given.

First consider the logarithmic terrain. Substituting in (10.5) for $\hat{H}(\rho)$ from Table 3, one has

$$G = \frac{16\,L}{\left\{\ln(\delta^2)\right\}^2} \quad , \tag{N.1}$$

where

$$L = \int_0^\infty \left\{K_1(\rho) - \delta K_1(\delta\rho)\right\}^2 d\rho \quad . \tag{N.2}$$

The integral, L, can be evaluated in a manner similar to that employed for (K.12), using the identity

$$L(\delta) = L(\delta{=}1) + \int_1^\delta \frac{\partial L}{\partial \delta}\, d\delta \quad . \tag{N.3}$$

Table 9. Normalized total drag, $D_{2S} = G$, for two-dimensional slice flow over an elliptical barrier with height H(R).

H(R)	G	Reference
$(1+R^2)^{-\mu}$	$\frac{\Gamma(\frac{1}{2})\,\Gamma(2\mu-\frac{1}{2})}{\Gamma(2\mu)}\,\frac{\{\Gamma(\mu+\frac{1}{2})\}^2}{\Gamma(\mu)\,\Gamma(\mu+1)}$	GR, p. 295
e^{-R^2}	$\left(\frac{\pi}{2}\right)^{\frac{1}{2}}$	GR, p. 337
$(1-R^2)^{\nu}\,\theta(1-R^2)$	$\frac{\Gamma(\frac{1}{2})\,\Gamma(2\nu+1)}{\Gamma(2\nu+3/2)}\,\frac{\Gamma(\nu)\,\Gamma(\nu+1)}{\{\Gamma(\nu+\frac{1}{2})\}^2}$	GR, p. 294
$\frac{\ln\left(\frac{\delta^2+R^2}{1+R^2}\right)}{\ln(\delta^2)}$	$\frac{16\pi}{\{\ln(\delta^2)\}^2}\left[E(k)-\frac{\pi}{4}(1+\delta)\right]$; $k=(1-\delta^2)^{\frac{1}{2}}$, $\delta<1$ $\frac{\pi^2}{8}$; $\delta=1$ $\frac{16\pi}{\{\ln(\delta^2)\}^2}\left[\delta E(k)-\frac{\pi}{4}(1+\delta)\right]$; $k=(1-\frac{1}{\delta^2})^{\frac{1}{2}}$, $\delta>1$	see text
$\frac{\operatorname{arccot}\left(\frac{R^2+\cos 2\omega}{\sin 2\omega}\right)}{2\omega}$	$\frac{\pi}{\omega^2}\left[\frac{\pi}{2}\cos\omega - 2E(k) + K(k)\right]$; $k=\sin\omega$	see text
e^{-R}	$\frac{\pi}{4}$	GR, p. 295
$K_0(R)$	$\frac{\pi}{4}$	GR, p. 294

Note, from (N.2), that $L(\delta=1)=0$. By expressing $\partial K_1(\delta\rho)/\partial\delta$ in terms of K_1 and K_0 (GR, p. 970), $\partial L/\partial\delta$ can be written as

$$\frac{\partial L}{\partial\delta} = 2\delta\int_0^\infty \rho\left(K_1(\rho) - \delta K_1(\delta\rho)\right) K_0(\delta\rho)\, d\rho \quad . \qquad \text{(N.4)}$$

Integrals of this form are tabulated in GR (p. 693), giving

$$\begin{aligned}\frac{\partial L}{\partial\delta} &= \frac{\pi^2}{4}\left(\delta F(3/2,1/2;2;1-\delta^2) - 1\right) \\ &= \frac{\pi^2}{4}\left(2\frac{\partial}{\partial\delta}\left(F(1/2,-1/2;1/1-\delta^2)\right) - 1\right) \quad .\end{aligned} \qquad \text{(N.5)}$$

Using (N.5) in (N.3) then gives

$$L(\delta) = \frac{\pi^2}{4}\left(2F(1/2,-1/2;1;1-\delta^2) - 1 - \delta^2\right) \quad . \qquad \text{(N.6)}$$

Expressing the hypergeometric function in terms of a complete elliptic integral (GR, pp. 905, 1043) leads to the expression shown in Table 9. An alternate derivation, based on integration by parts in an integral of d_{2S} with respect to Y, was used to check the result.

This latter type of derivation was used to generate the result for the arccot barrier. From Table 8,

$$G = \int_{-\infty}^{\infty} d_{2S}(Y)\, dY = -\frac{\pi}{2\omega^2}\int_0^\infty \ln\left[\frac{1}{2}\left(1 + \frac{Y^2+\cos 2\omega}{\Delta}\right)\right] dY \quad , \qquad \text{(N.7)}$$

where

$$\Delta = \left(Y^4 + 2Y^2\cos 2\omega + 1\right)^{\frac{1}{2}} \quad . \qquad \text{(N.8)}$$

Integration by parts gives

$$G = \frac{\pi}{\omega^2} \int_0^\infty \frac{Y^2}{\Delta} \left(1 - \frac{Y^2+\cos 2\omega}{\Delta}\right) dY \quad . \tag{N.9}$$

The two terms in (N.9) are separately infinite. However, subtracting 1 and integrating by parts in the first term, and adding 1 to the second term, eliminates the singularities :

$$G = \frac{\pi}{\omega^2} \int_0^\infty \frac{1+Y^2\cos 2\omega}{\Delta^2} \left(1 - \frac{2Y^2}{\Delta}\right) dY \quad . \tag{N.10}$$

The term in (N.10) involving $1/\Delta^2$ can be evaluated by contour integration or partial fraction methods. This gives

$$G = \frac{\pi}{\omega^2} \left(\frac{\pi}{2} \cos\omega + \cos 2\omega \int_0^\infty Y \frac{d}{dY}\left(\frac{1}{\Delta}\right) dY \; + \; \sin^2 2\omega \int_0^\infty \frac{Y^2}{\Delta^3} dY\right) \quad , \tag{N.11}$$

where the integral involving $1/\Delta^3$ in (N.10) has been split into two more terms. Finally, integration by parts in the first integral in (N.11) reduces it to a form found in GR (p. 260). Simplification then gives the result shown in Table 9.

The result has been checked by a different integration procedure, started by using ξ, defined in Table 8, as the integration variable. Straightforward manipulation then gives G in terms of an elliptic integral of the third kind with complex parameter. However, considerable algebra is required to simplify the answer to the form given in Table 9.

APPENDIX O

FORCE ON THE BARRIER IN TWO-DIMENSIONAL SLICE FLOW

In this appendix, the expression (10.9) is derived for the normalized force, (D_{2S}, T_{2S}), on a rotated elliptical barrier in two-dimensional slice flow. The height field, $h(x,y;\psi)$, for a barrier which has been rotated counterclockwise through an angle ψ from the barrier $h(x,y)=h(x,y;\psi=0)$ is

$$h(x,y;\psi) = h(x',y') \quad , \tag{O.1}$$

where x' and y' are defined in (5.16). For an elliptical barrier, h depends only on $R^2=x^2/a^2+y^2/b^2$, so that $h(x',y')$ is a function of

$$R'^2 = x'^2/a^2 + y'^2/b^2 = \left(x\Delta + \frac{y}{\Delta}(1-\gamma^2)\cos\psi\sin\psi\right)^2/a^2 + \left(\frac{y}{\Delta}\right)^2/b^2 \quad , \tag{O.2}$$

where

$$\Delta = \left(\cos^2\psi+\gamma^2\sin^2\psi\right)^{\frac{1}{2}} \quad ; \quad \gamma = a/b \quad , \tag{O.3}$$

as is shown by regrouping the terms in (O.2). The relations expressed in (O.2) imply that

$$h(x',y') = h\left(x\Delta + \frac{y}{\Delta}(1-\gamma^2)\cos\psi\sin\psi \ , \ \frac{y}{\Delta}\right) \quad . \tag{O.4}$$

This equation can be used to derive a formula for the Fourier transform, $\tilde{h}(k;y;\psi)$, of the rotated terrain in terms of that for the unrotated case. The definition of $\tilde{h}(k;y;\psi)$ is

$$\tilde{h}(k;y;\psi) = \frac{1}{2\pi}\int_{-\infty}^{\infty} h(x,y;\psi)\, e^{-ikx}\, dx \quad . \tag{O.5}$$

Substituting for $h(x,y;\psi)$ from (O.1) and (O.4), and changing the integration variable to the first argument of h on the right side of (O.4), one obtains

$$\tilde{h}(k;y;\psi) = \frac{1}{2\pi\Delta}\int_{-\infty}^{\infty} h(t,\frac{y}{\Delta})\, e^{-i\frac{k}{\Delta}\left(t - \frac{y}{\Delta}(1-\gamma^2)\cos\psi\sin\psi\right)}\, dt$$

$$= \frac{1}{\Delta}\, e^{i\frac{ky}{\Delta^2}(1-\gamma^2)\cos\psi\sin\psi}\, \tilde{h}(\frac{k}{\Delta};\frac{y}{\Delta};\psi=0) \quad . \qquad (O.6)$$

Using (O.6) in (8.6), dividing by the appropriate dimensional factor from (B.8), and noting that $\tilde{h}$ is real for unrotated elliptical terrain, one obtains the normalized components of the force per unit length for the rotated barrier:

$$\left.\begin{aligned} d_{2S}(Y;\psi) &= d_{2S}(\frac{Y}{\Delta};\psi=0) \quad , \\ t_{2S}(Y;\psi) &= \frac{(1-\gamma^2)\cos\psi\sin\psi}{\Delta^2}\, d_{2S}(\frac{Y}{\Delta};\psi=0) \quad . \end{aligned}\right\} \qquad (O.7)$$

Integrating this expression with respect to Y, making a change of variable to Y/Δ, gives the total force components:

$$\left.\begin{aligned} D_{2S}(\psi) &= \Delta\, D_{2S}(\psi=0) \quad , \\ T_{2S}(\psi) &= \frac{(1-\gamma^2)\cos\psi\sin\psi}{\Delta}\, D_{2S}(\psi=0) \quad . \end{aligned}\right\} \qquad (O.8)$$

To complete the derivation of (10.9), it remains to be shown that $D_{2S}(\psi=0)=G$, the integral defined by (10.5). Consider

$$D_{2S}(\psi=0) = 2\pi \int_{-\infty}^{\infty} \int_{-\infty}^{\infty} |\kappa| \, |\tilde{H}(\kappa;Y)|^2 \, d\kappa \, dY \tag{0.9}$$

$$= \frac{1}{2\pi} \int_{-\infty}^{\infty} \int_{-\infty}^{\infty} \int_{-\infty}^{\infty} \int_{-\infty}^{\infty} |\kappa| \, H(X,Y) \, H(X',Y) \, e^{i\kappa(X'-X)} \, dX \, dX' d\kappa \, dY \ .$$

Using the identity

$$H(X',Y) = \int_{-\infty}^{\infty} H(X',Y') \, \delta(Y-Y') \, dY' \ , \tag{0.10}$$

where

$$\delta(Y-Y') = \frac{1}{2\pi} \int_{-\infty}^{\infty} e^{i\lambda(Y'-Y)} \, d\lambda \tag{0.11}$$

is a representation of the Dirac delta function (Byron and Fuller, 1969, pp. 224 and 248), (0.9) becomes

$$D_{2S}(\psi=0) = \tag{0.12}$$

$$\frac{1}{4\pi^2} \int_{-\infty}^{\infty} \cdots \int_{-\infty}^{\infty} |\kappa| \, H(X,Y) \, H(X',Y') \, e^{i(\kappa X'+\lambda Y')-i(\kappa X+\lambda Y)} \, dXdY \, dX'dY' \, d\kappa d\lambda .$$

For elliptical terrain, using the relation (GR, pp. 213 and 402)

$$\int_0^{2\pi} e^{i(A\cos\xi + B\sin\xi)} \, d\xi = 2\pi \, J_o\left((A^2+B^2)^{\frac{1}{2}}\right) \ , \tag{0.13}$$

after introducing polar coordinates, (0.1) and (0.2), one finds that

$$D_{2S}(\psi=0) = \int_0^{2\pi} |\cos\phi| \, d\phi \int_0^{\infty} \int_0^{\infty} \int_0^{\infty} \rho^2 \, R \, R' \, J_o(\rho R) \, J_o(\rho R') \, dR \, dR' \, d\rho \ . \tag{0.14}$$

Evaluating the ϕ integral in (0.14) to give a factor of 4 and using (B.4) for the R and R′ integrals gives the final result:

$$D_{2S}(\psi=0) = 16\pi^2 \int_0^\infty \rho^2 \left(\hat{H}(\rho)\right)^2 d\rho = G \quad . \tag{0.15}$$

Substituting (0.15) into (0.8) verifies (10.9).

APPENDIX P

INTEGRALS ARISING FROM TERRAIN SMOOTHING

P.1 Differential smoothing

In this appendix, integrals arising in the calculation of the drag per unit length for smoothed barriers are evaluated.

If a differential smoothing operator is applied to an infinitely-extended ridge, the integrals to be evaluated are s_n $(n=0,1,...)$, defined by (11.13). Results are summarized for several terrain shapes in Table 10, using terrain-height Fourier transforms from Table 2 and the appropriate reference to GR. Similarly, Table 11 shows the results for the integrals, S_n, defined by (11.16), which appear in expressions for the total force on a smoothed isolated hill. Values for s_n and S_n, for $n>0$, can be found conveniently by using the relation $\Gamma(z+1)=z\Gamma(z)$, starting with $s_0=S_0=1$. Note that the integrals are defined for the ν-type terrain only for $n<\nu$ because of discontinuities in derivatives of the height field of sufficiently high order.

Table 10. Terrain smoothing integrals, s_n $(n=0,1,2,\ldots)$, defined by (11.13), for several terrain shapes, $H(X)$.

$H(X)$	s_n	Reference
$\left(1+\frac{X^2}{\alpha^2}\right)^{-\mu}$	$\left(\frac{4}{\alpha^2}\right)^n \Gamma(n+1)\ \frac{2\mu\ \Gamma(2\mu+n)}{\Gamma(2\mu+2n+1)} \left(\frac{\Gamma(\mu+n+\frac{1}{2})}{\Gamma(\mu+\frac{1}{2})}\right)^2$	GR, p. 693
e^{-X^2/α^2}	$\left(\frac{2}{\alpha^2}\right)^n \Gamma(n+1)$	GR, p. 337
$\left(1-\frac{X^2}{\alpha^2}\right)^{\nu} \theta(\alpha^2-X^2)$	$\left(\frac{4}{\alpha^2}\right)^n \Gamma(n+1)\ \frac{2\nu\ \Gamma(2\nu-2n)}{\Gamma(2\nu-n+1)} \left(\frac{\Gamma(\nu+\frac{1}{2})}{\Gamma(\nu-n+\frac{1}{2})}\right)^2$	GR, p. 692

Table 11. Terrain smoothing integrals, S_n $(n=0,1,2,\ldots)$, defined by (11.16), for several terrain shapes, $H(R)$. See Table 10 for references.

$H(R)$	S_n
$\left(1+\frac{R^2}{\alpha^2}\right)^{-\mu}$	$\left(\frac{4}{\alpha^2}\right)^n \frac{\Gamma(n+3/2)}{\Gamma(3/2)}\ \frac{\Gamma(2\mu+1)}{\Gamma(2\mu+2n+1)}\ \frac{\Gamma(2\mu+n-\frac{1}{2})}{\Gamma(2\mu-\frac{1}{2})} \left(\frac{\Gamma(\mu+n+\frac{1}{2})}{\Gamma(\mu+\frac{1}{2})}\right)^2$
e^{-R^2/α^2}	$\left(\frac{2}{\alpha^2}\right)^n \frac{\Gamma(n+3/2)}{\Gamma(3/2)}$
$\left(1-\frac{R^2}{\alpha^2}\right)^{\nu} \theta(\alpha^2-R^2)$	$\left(\frac{4}{\alpha^2}\right)^n \frac{\Gamma(n+3/2)}{\Gamma(3/2)}\ \frac{\Gamma(2\nu-2n)}{\Gamma(2\nu)}\ \frac{\Gamma(2\nu+3/2)}{\Gamma(2\nu-n+3/2)} \left(\frac{\Gamma(\nu+\frac{1}{2})}{\Gamma(\nu-n+\frac{1}{2})}\right)^2$

P.2 Truncated spectral series

In the section on terrain smoothing by spectral truncation, the expansion coefficients, h_n, in the series for the terrain height are given by (11.23). Here, h_n ($n=0,1,2,\ldots$), are evaluated for the terrain shapes $H=1/(1+X^2)$ and $H=(A+B\cos\Omega X)\exp(-X^2)$.

Because H is an even function of X for these examples, the coefficients with odd index are zero: $h_{2m+1}=0$ ($m=0,1,2,\ldots$). To determine the even coefficients, substitute a power series expansion for the Hermite polynomials (GR, p. 1033) into (11.23). After simplification one obtains

$$h_{2m} = \frac{2}{(-4)^m \, \beta \, \Gamma(\frac{1}{2})} \sum_{j=0}^{m} \left(\frac{-4}{\beta^2}\right)^j \frac{A_j\left(\frac{1}{2\beta^2}\right)}{\Gamma(2j+1)\,\Gamma(m-j+1)} \quad , \qquad (P.1)$$

where β is the parameter appearing in the exponential in the series (11.21) and A_j is defined by

$$A_j(\zeta) = \int_0^{\infty} H(X)\, X^{2j}\, e^{-\zeta X^2}\, dX \quad . \qquad (P.2)$$

Now consider $H=1/(1+X^2)$. For this case (P.2) can be evaluated in terms of a degenerate hypergeometric function (GR, p. 1058). However, for the present purposes it is sufficient to note that

$$A_{j+1}(\zeta) = -A_j(\zeta) + \int_0^\infty X^{2j} e^{-\zeta X^2}\, dX \;,$$

$$= -A_j(\zeta) + \frac{\Gamma(j+\frac{1}{2})}{2\,\zeta^{j+\frac{1}{2}}} \;, \qquad (P.3)$$

where the last integral follows from GR (p. 337). This recursion relation can be used to generate A_j for $j>0$, starting with (GR, pp. 941-942)

$$A_0(\zeta) = \frac{\pi}{2}\, e^{\zeta} \left(1 - \Phi(\zeta^{\frac{1}{2}})\right) \;. \qquad (P.4)$$

where Φ is the error function. A recursion relation for h_{2m} can also be developed by iterating the formula

$$H_{n+1}(z) = 2z\, H_n(z) - 2n\, H_{n-1}(z) \;, \qquad (P.5)$$

from GR (p. 1033), to give

$$H_{n+2}(\chi) = \frac{H_{n+4}(\chi) + (4n+10+4/\beta^2)H_{n+2}(\chi) + 4(n+1)(n+2)H_n(\chi)}{4\;(\chi^2+1/\beta^2)} \;, \qquad (P.6)$$

where $\chi = X/\beta$. Substitution of this relation into (11.23) gives

$$4(2m+4)(2m+3)h_{2m+4} + (8m+10+4/\beta^2)h_{2m+2} + h_{2m} = \frac{2^{\frac{1}{2}}}{\beta^2 4^m \Gamma(m+2)} \;. \qquad (P.7)$$

From (P.1)-(P.4), one finds

$$\left.\begin{aligned} h_0 &= \frac{1}{\beta}\,\Gamma(\tfrac{1}{2})\, e^{\zeta} \left(1-\Phi(\zeta^{\frac{1}{2}})\right) \quad ; \quad \zeta = \frac{1}{2\beta^2} \;, \\ h_2 &= -\frac{1}{4}\left(1 + \frac{2}{\beta^2}\right) h_0 + \frac{1}{\beta^2 2^{\frac{1}{2}}} \;. \end{aligned}\right\} \qquad (P.8)$$

With the starting values provided by (P.8), the recursion formula (P.7) can be used to find higher-order coefficients.

Next consider the modified Gaussian case, $H=(A+B\cos\Omega X)\exp(-X^2)$. Although A_j in (P.2) can be evaluated explicitly in this case (GR, pp. 337,496), it turns out that this is unnecessary because h_{2m} can be obtained directly from (11.23) using GR (pp. 837,840). The result is

$$h_{2m} = \eta \left(\frac{\eta^2-1}{4}\right)^m \left(\frac{A}{\Gamma(m+1)} + \frac{B\ (-1)^m}{\Gamma(2m+1)}\, e^{-\frac{\Omega^2}{4}\left(1-\frac{\eta^2}{2}\right)} H_{2m}\left(\frac{\beta\Omega\eta}{2(\eta^2-1)^{\frac{1}{2}}}\right)\right) \quad , \quad \text{(P.9)}$$

where $\eta=(\beta^2+\frac{1}{2})^{-\frac{1}{2}}$. In the special case of $\beta=1/\sqrt{2}$, (P.9) simplifies to

$$h_{2m} = A\,\delta_{0m} + \frac{B}{\Gamma(2m+1)}\left(\frac{-\Omega^2}{8}\right)^m e^{-\Omega^2/8} \quad , \qquad \text{(P.10)}$$

where $\delta_{0m}=1$ or 0 according to whether $m=0$ or $m\neq 0$, respectively.

APPENDIX Q

ELLIPTIC INTEGRALS

Expressions are given in this appendix for certain integrals which have appeared repeatedly in this study of airflow over elliptical mountains. These quantities are expressible in terms of complete elliptic integrals, K and E, of the first and second kinds, respectively.

Define B_n and C_n (n=0,1,2,...) by

$$\left.\begin{aligned} B_n(\gamma) &= \int_0^{\pi/2} \cos^2\phi\ \Delta^{2n-1}\, d\phi = \gamma^{2n+1} C_n\left(\frac{1}{\gamma}\right) , \\ C_n(\gamma) &= \gamma^2 \int_0^{\pi/2} \sin^2\phi\ \Delta^{2n-1}\, d\phi = \gamma^{2n+1} B_n\left(\frac{1}{\gamma}\right) . \end{aligned}\right\} \qquad (Q.1)$$

where

$$\Delta = (\cos^2\phi+\gamma^2\sin^2\phi)^{\frac{1}{2}} . \qquad (Q.2)$$

Integrals of the preceding forms are tabulated in GR (pp. 158-162) for some small values of n. For example, for $\gamma<1$, with $K=K(k)$ and $E=E(k)$, where $k^2=1-\gamma^2$

$$\left.\begin{aligned} B_0(\gamma) &= \frac{E-\gamma^2 K}{k^2} , \\ C_0(\gamma) &= \frac{\gamma^2(K-E)}{k^2} , \end{aligned}\right\} \qquad (Q.3)$$

and

$$\left.\begin{aligned} B_1(\gamma) &= \frac{-\gamma^2 K+(k^2+1)E}{3k^2} \quad , \\ C_1(\gamma) &= \frac{\gamma^2\{\gamma^2 K+(2k^2-1)E\}}{3k^2} \quad . \end{aligned}\right\} \qquad (Q.4)$$

The results for $\gamma>1$ can be obtained by replacing γ by $1/\gamma$ in (Q.3) and using the relations between B_n and C_n given in (Q.1).

These formulae are not suitable for numerical evaluation if γ is near 1. However, expressions for B_n and C_n in terms of hypergeometric functions resolve this difficulty. Making the change of variable, $t=\sin^2\phi$, in (Q.1) and comparing to an integral representation of the hypergeometric function in GR (p. 1040), one obtains

$$\left.\begin{aligned} B_n(\gamma) &= \frac{\pi}{4}\, F(1/2-n,1/2;2;1-\gamma^2) \quad , \\ C_n(\gamma) &= \frac{\pi}{4}\, \gamma^2\, F(1/2-n,3/2;2;1-\gamma^2) \quad . \end{aligned}\right\} \qquad (Q.5)$$

Putting $\gamma=1$ in (Q.5) gives $B_n(1)=C_n(1)=\pi/4$, while at $\gamma=0$ one finds (GR, p. 1042) $B_n(0)=\Gamma(3/2)\Gamma(n+1)/\Gamma(n+3/2)$ and $C_n(0)=0$.

In addition to being useful near $\gamma=1$, the hypergeometric function representation of B_n and C_n allows recursion relations to be easily developed. From GR (p. 1044) one obtains

$$\left.\begin{aligned} B_n &= \frac{2\{n+(n-1)\gamma^2\}B_{n-1} - \gamma^2(2n-3)B_{n-2}}{2n+1} \quad , \\ C_n &= \frac{2(n-1+n\gamma^2)C_{n-1} - \gamma^2(2n-3)C_{n-2}}{2n+1} \quad . \end{aligned}\right\} \qquad (Q.6)$$

Given the $n=0$ and 1 results from (Q.3) and (Q.4), one can determine the integrals for n≥2 from (Q.6).

Another type of integral that has appeared in this thesis is defined by

$$D_{mn}(\gamma) = \int_0^{\pi/2} \frac{\cos^{2m}\phi \sin^{2n}\phi}{\Delta} d\phi \quad , \tag{Q.7}$$

where Δ is given in (Q.2). Making the change of variable, $t=\sin^2\phi$, gives (GR, p. 1040 or p. 386)

$$D_{mn}(\gamma) = \frac{\Gamma(m+\frac{1}{2})\ \Gamma(n+\frac{1}{2})}{2\ \Gamma(m+n+1)}\ F(\tfrac{1}{2}, n+\tfrac{1}{2}; m+n+1; 1-\gamma^2) \quad . \tag{Q.8}$$

A special case of interest for the current work is m=1. From GR (pp. 1044-1045) one can derive

$$D_{1n} = \frac{2\left(2n-1-(n-1)\gamma^2\right)D_{1\ n-1} - (2n-3)D_{1\ n-2}}{(2n+1)\ (1-\gamma^2)} \quad . \tag{Q.9}$$

This formula applies for n≥2. However, because of the $1-\gamma^2$ factor in the denominator in (Q.9), this recursion relation is not as useful as (Q.6) for numerical evaluation.

Some low order D_{mn} integrals are given by

$$\left.\begin{aligned} D_{10} &= B_0 \ , \\ D_{11} &= \frac{B_0-B_1}{1-\gamma^2} \ , \\ D_{20} &= \frac{B_1-\gamma^2 B_0}{1-\gamma^2} \ . \end{aligned}\right\} \tag{Q.10}$$

To express these results in terms of complete elliptic integrals one can use (Q.3) and (Q.4).